Dirac and Majorana edge states in graphene and topological superconductors

Akhmerov, A.R.

Citation

Akhmerov, A. R. (2011, May 31). *Dirac and Majorana edge states in graphene and topological superconductors*. *Casimir PhD Series*. Retrieved from https://hdl.handle.net/1887/17678

Dirac and Majorana edge states in graphene and topological superconductors

PROEFSCHRIFT

DOOR

Anton Roustiamovich Akhmerov

GEBOREN TE KRASNOOBSK, RUSLAND IN 1984

Promotiecommissie:

Promotor:	Prof. dr. C. W. J. Beenakker
Overige leden:	Prof. dr. E. R. Eliel
	Prof. dr. F. Guinea (Instituto de Ciencia de Materiales de Madrid)
	Prof. dr. ir. L. P. Kouwenhoven (Technische Universiteit Delft)
	Prof. dr. J. M. van Ruitenbeek
	Prof. dr. C. J. M. Schoutens (Universiteit van Amsterdam)
	Prof. dr. J. Zaanen

To my parents.

Contents

II   Majorana edge states in topological superconductors   77

Chapter 1

Introduction

The two parts of this thesis: "Dirac edge states in graphene" and "Majorana edge states in topological superconductors" may seem very loosely connected to the reader. To study the edges of graphene, a one-dimensional sheet of carbon, one needs to pay close attention to the graphene lattice and accurately account for the microscopic details of the system. The Majorana fermions, particles which are their own anti-particles, are on the contrary insensitive to any perturbation and possess universal properties which are insensitive to microscopic details.

Curiously, the history of graphene has parallels with that of Majorana fermions. Graphene was first analysed in 1947 by Wallace [1], and the term "graphene" was invented in 1962 by Boehm and co-authors [2]. However, it was not until 2005, after graphene was synthesized in the group of Geim [3], that there appeared an explosion of research activity, culminating in the Nobel prize five years later. Majorana fermions were likewise described for the first time a long time ago, in 1932 [4], and then were mostly forgotten until the interest in them revived in high energy physics decades later. For the condensed matter physics community Majorana fermions acquired an important role only in the last few years, when they were predicted to appear in several condensed matter systems [5–7], and to provide a building block for a topological quantum computer [8, 9].

There are two other more relevant similarities between edge states in graphene and in topological superconductors. To understand what they are, we need to answer the question "what is special about the edge states in these systems?" Edge states in general have been known for a long time [10, 11] — they are electronic states localized at the interface of a material with vacuum or another material. They may or may not appear, and their presence depends sensitively on microscopic details of the interface.

The distinctive feature of the edge states studied here is that they are protected by a certain physical symmetry of the system. This protection by symmetry ensures that they always exist at a fixed energy: at the Dirac point in graphene and at the Fermi energy in topological superconductors. Additionally, protection by symmetry ensures that the edge states possess universal properties — they occur at a large set of boundaries, and their presence can be deduced from the bulk properties.

Another property shared by graphene and topological superconductors is that both are well described by the Dirac equation, as opposed to the Schrödinger equation suitable for most other condensed matter systems. This is in no respect accidental and is tightly related to the symmetry properties of the two systems. In graphene the symmetry ensuring the presence of the edge states is the so-called sublattice symmetry. Using only this symmetry one may derive that graphene obeys the Dirac equation on long length scales. The appearance of the Dirac equation in topological superconductors is also natural, once one realizes that the phase transition into a topologically nontrivial state is scale invariant, and that the Dirac Hamiltonian is one of the simplest scale-invariant Hamiltonians.

An understanding of the role of symmetry in the study of edge states and familiarity with the Dirac equation are necessary and sufficient to understand most of this thesis. In this introductory chapter we describe both and explain how they apply to graphene and topological superconductors.

1.1   Role of symmetry in the protection of edge states

The concept of symmetry plays a central role in physics. It is so influential because complete theories may be constructed by just properly taking into account the relevant symmetries. For example, electrodynamics is built on gauge symmetry and Lorentz symmetry. In condensed matter systems there are only three discrete symmetries which survive the presence of disorder: time-reversal symmetry (denoted as $\mathcal{T}$), particle-hole symmetry (denoted as $\mathcal{CT}$), and sublattice or chiral symmetry (denoted as $\mathcal{C}$). The time-reversal symmetry and the particle-hole symmetry have anti-unitary operators. These may square either to $+1$ or -1 depending on the spin of particles and on spin-rotation symmetry being present or absent. Chiral symmetry has a unitary operator and always squares to $+1$. Together these three symmetries form ten symmetry classes [12], each class characterized by the type (or absence of) time-reversal and particle-hole symmetry and the possible presence of chiral symmetry.

Sublattice symmetry and particle-hole symmetry require that for every eigenstate $|\psi\rangle$ of the Hamiltonian H with energy ε there is an eigenstate of the same Hamiltonian given by either $\mathcal{C}|\psi\rangle$ or $\mathcal{CT}|\psi\rangle$ with energy $-\varepsilon$. We observe that eigenstates of the Hamiltonian with energy $\varepsilon = 0$ are special in that they may transform into themselves under the symmetry transformation. Time-reversal symmetry implies no such property, and hence is unimportant for what follows. We proceed to discuss in more detail what is the physical meaning of sublattice and particle-hole symmetries and of the zero energy states protected by them.

1.1.1   Sublattice symmetry

Let us consider a set of atoms which one can split into two groups, such that the Hamiltonian contains only matrix elements between the two groups, but not within the same

group. This means that the system of tight-binding equations describing the system is

$$\varepsilon \psi_i^A = \sum t_{ij} \psi_j^B, \tag{1.1a}$$

$$\varepsilon \psi_i^B = \sum t_{ij} \psi_j^A, \tag{1.1b}$$

where we call one group of atoms sublattice A, and another group of atoms sublattice B. Examples of bipartite lattices are shown in Fig. 1.1, with the panel a) showing the honeycomb lattice of graphene.
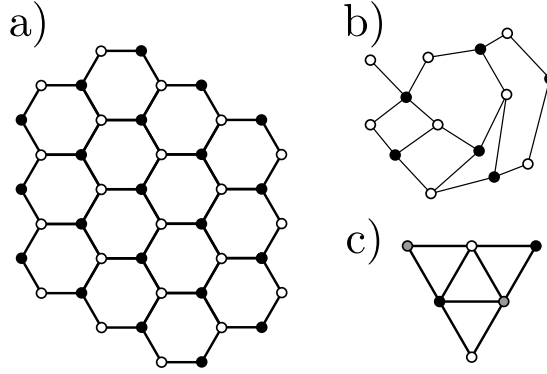
Figure 1.1: Panel a): the bipartite honeycomb lattice of graphene. Panel b): an irregular bipartite lattice. Panel c): an example of a lattice without bipartition. Nodes belonging to one sublattice are marked with open circles, nodes belonging to the other one by black circles, and finally nodes which belong to neither of the sublattices are marked with grey circles.

The Hamiltonian of a system with chiral symmetry can always be brought to a form

$$H = \begin{pmatrix} 0 & T \\ T^\dagger & 0 \end{pmatrix}, \tag{1.2}$$

with T the matrix of hopping amplitudes from one sublattice to another. Now we are ready to construct the chiral symmetry operator. The system of tight-binding equations stays invariant under the transformation $\psi^B \to -\psi^B$ and $\varepsilon \to -\varepsilon$. In terms of the Hamiltonian this translates into a symmetry relation

$$\mathcal{C} H \mathcal{C} = -H, \tag{1.3}$$

$$\mathcal{C} = \text{diag}(1, 1, \ldots, 1, -1, \ldots, -1). \tag{1.4}$$

The number of 1's and -1's in $\mathcal{C}$ is equal to the number of atoms in sublattices A and B respectively.

Let us now consider a situation when the matrix T has vanishing eigenvalues, or in other words when we are able to find $|\psi^A\rangle$ such that $T|\psi^A\rangle = 0$. This means that

$(\psi^A, 0)$ is a zero energy eigenstate of the full Hamiltonian. Moreover since the diagonal terms in the Hamiltonian are prohibited by the symmetry, this eigenstate can only be removed from zero energy by coupling it with an eigenstate which belongs completely to sublattice B. If sublattice A has N more atoms than sublattice B, this means that the matrix T is non-square and always has exactly N more zero eigenstates than the matrix $T^\dagger$. Hence there will be at least N zero energy eigenstates in the system, a result also known as Lieb's theorem [13].

Analogously, if there are several modes localized close to a single edge, they cannot be removed from zero energy as long as they all belong to the same sublattice. One of the central results presented in this thesis is that this is generically the case for a graphene boundary.

1.1.2 Particle-hole symmetry

On the mean-field level superconductors are described by the Bogoliubov-de-Gennes Hamiltonian [14]

$$H_{\text{BdG}} = \begin{pmatrix} H_0 - E_F & \Delta \\ \Delta^\dagger & E_F - \mathcal{T}^{-1} H_0 \mathcal{T} \end{pmatrix}, \tag{1.5}$$

with H_0 the single-particle Hamiltonian, E_F the Fermi energy, and Δ the pairing term. This Hamiltonian acts on a two-component wave function $\psi_{\text{BdG}} = (u, v)^T$ with u the particle component of the wave function and v the hole component. The many-body operators creating excitations above the ground state of this Hamiltonian are $\gamma^\dagger \equiv uc^\dagger + vc$, with $c^\dagger$ and c electron creation and annihilation operators.

This description is redundant; for each eigenstate $\psi_\varepsilon = (u_0, v_0)^T$ of H_{BdG} with energy ε there is another eigenstate $\psi_{-\varepsilon} = (\mathcal{T} v_0, -\mathcal{T} u_0)^T$. The redundancy is manifested in the fact that the creation operator $\gamma^\dagger$ of the quasiparticle in the ψ_ε state is identical to the annihilation operator γ of the quasiparticle in the $\psi_{-\varepsilon}$ state. In other words, the two wave functions ψ_ε and $\psi_{-\varepsilon}$ correspond to a single quasiparticle, and the creation of a quasiparticle with positive energy is identical to the annihilation of a quasiparticle with negative energy. The origin of the redundancy lies in the doubling of the degrees of freedom [15], which has to be applied to bring the many-body Hamiltonian to the non-interacting form (1.5). For the Hamiltonian H_{BdG} this $\mathcal{C}\mathcal{T}$ symmetry is expressed by the relation

$$(i\tau_y \mathcal{T})^{-1} H_{\text{BdG}} (i\tau_y \mathcal{T}) = -H_{\text{BdG}}, \tag{1.6}$$

where τ_y is the second Pauli matrix in the electron-hole space.

Let us now study what happens if there is an eigenstate of H_{BdG} with exactly zero energy, similar to the way we studied the case of the sublattice-symmetric Hamiltonian. This eigenstate transforms into itself after applying $\mathcal{C}\mathcal{T}$ symmetry: $\psi_0 = \mathcal{C}\mathcal{T} \psi_0$, hence it has to have a creation operator $\gamma^\dagger$ which is equal to the annihilation operator γ of its electron-hole partner.

Let us now, similar to the case of sublattice symmetry, study what happens if there is an eigenstate of H_{BdG} with exactly zero energy which transforms into itself after applying $\mathcal{C}\mathcal{T}$ symmetry: $\psi_0 = \mathcal{C}\mathcal{T} \psi_0$. This state has to have a creation operator $\gamma^\dagger$

which is equal to the annihilation operator γ of its electron-hole partner. Since this state is an electron-hole partner of itself, we arrive to $\gamma^\dagger = \gamma$. Fermionic operators which satisfy this property are called *Majorana fermions*. Just using the defining properties we can derive many properties of Majorana fermions. For example let us calculate the occupation number $\gamma^\dagger \gamma$ of a Majorana state. We use the fermionic anticommutation relation

$$\gamma^\dagger \gamma + \gamma \gamma^\dagger = 1. \tag{1.7}$$

Then, by using the Majorana condition, we get $\gamma \gamma^\dagger = \gamma^2 = \gamma^\dagger \gamma$. After substituting this into the anticommutation relation we immediately get $\gamma^\dagger \gamma = 1/2$. In other words, any Majorana state is always half-occupied.

Unlike the zero energy states in sublattice-symmetric systems, which shift in energy if an electric field is applied because the sublattice symmetry is broken, a Majorana fermion can only be moved away from zero energy by being paired with another Majorana fermion, because every state at positive energy has to have a counterpart at negative energy.

1.2 Dirac Hamiltonian

The Dirac equation was originally conceived to settle a disagreement between quantum mechanics and the special theory of relativity, namely to make the Schrödinger equation invariant under Lorentz transformation. The equation in its original form reads

$$i\hbar \frac{d\psi}{dt} = \left(\sum_{i=1}^{3} \alpha_i \, p_i c + \beta m c^2 \right) \psi. \tag{1.8}$$

Here β and α_i form a set of 4×4 Dirac matrices, m and p_i are mass and momentum of the particle, and c is the speed of light. For $p \ll mc$ the spectrum of this equation is conical, and it has a gap between $+m$ and $-m$.

In condensed matter physics the term Dirac equation is used more loosely for any Hamiltonian which is linear in momentum:

$$H = \sum_i \alpha_i \, p_i v_i + \sum_j m_j \beta_j. \tag{1.9}$$

In such a case m_j are called mass terms and v_i velocities. The set of Hermitian matrices α_i, β_i do not have to satisfy the anticommutation relations, unlike the original Dirac matrices. The number of components of the wave function also does not have to be equal to 4: it is even customary to call $H = vp$ a Dirac equation. The symmetry properties of these equations are fully determined by the set of matrices α_i, β_i, making the Dirac equation a very flexible tool in modeling different physical systems. Since the spectrum of the Dirac equation is unbounded both at large positive and large negative energies, this equation is an effective low-energy model.

In this section we focus on two contexts in which the Dirac equation appears: it occurs typically in systems with sublattice symmetry and in particular in graphene; also it allows to study topological phase transitions in insulators and superconductors.

1.2.1 Derivation of Dirac Hamiltonian using sublattice symmetry and its application to graphene

To derive a dispersion relation of a system with sublattice symmetry, we start from the Hamiltonian (1.2). After transforming it to momentum space by applying Bloch's theorem, we get the following Hamiltonian:

$$H = \begin{pmatrix} 0 & Q(\boldsymbol{k}) \\ Q^\dagger(\boldsymbol{k}) & 0 \end{pmatrix}, \tag{1.10}$$

where Q is a matrix which depends on the two-dimensional momentum $\boldsymbol{k}$. Let us now consider a situation when the phase of $\det Q(\boldsymbol{k})$ winds around a unit circle as k goes around a contour Γ in momentum space. Since $\det Q(\boldsymbol{k})$ is a continuous complex function, it has to vanish in a certain point $\boldsymbol{k}_0$ inside this contour. Generically a single eigenvalue of Q vanishes at this point. Since we are interested in the low energy excitation spectrum, let us disregard all the eigenvectors of Q which correspond to the non-vanishing eigenvalues and expand $Q(\boldsymbol{k})$ close to the momentum where it vanishes:

$$Q = v_x \delta k_x + v_y \delta k_y + \mathcal{O}(|\delta k^2|), \tag{1.11}$$

with v_x and v_y complex numbers, and $\boldsymbol{\delta k} \equiv \boldsymbol{k} - \boldsymbol{k}_0$. For Q to vanish only at $\delta k = 0$, $v_x v_y^*$ has to have a finite imaginary part. In that case the spectrum of the Hamiltonian assumes the shape of a cone close to $\boldsymbol{k}_0$, and the Hamiltonian itself has the form

$$H = |v_x|\delta k_x \begin{pmatrix} 0 & e^{i\alpha_x} \\ e^{-i\alpha_x} & \end{pmatrix} + |v_y|\delta k_y \begin{pmatrix} 0 & e^{i\alpha_y} \\ e^{-i\alpha_y} & \end{pmatrix}, \quad \alpha_x \neq \alpha_y. \tag{1.12}$$

We see that the system is indeed described by a Dirac equation with no mass terms. The point $\boldsymbol{k}_0$ in the Brillouin zone is called a Dirac point. Since the winding of $\det Q(\boldsymbol{k})$ around the border of the Brillouin zone must vanish, we conclude that there should be as many Dirac points with positive winding around them, as there are with negative winding. In other words the Dirac points must come in pairs with opposite winding. If in addition time-reversal symmetry is present, then $Q(\boldsymbol{k}) = Q^*(-\boldsymbol{k})$, and the Dirac points with opposite winding are located at opposite momenta.

We are now ready to apply this derivation to graphene. Since there is only one atom of each sublattice per unit cell (as shown in Fig. 1.2), $Q(\boldsymbol{k})$ is a number rather than a matrix. The explicit expression for Q is

$$Q = e^{i\boldsymbol{k}\cdot\boldsymbol{a}_1} + e^{i\boldsymbol{k}\cdot\boldsymbol{a}_2} + e^{i\boldsymbol{k}\cdot\boldsymbol{a}_3}, \tag{1.13}$$

with vectors $\boldsymbol{a}_1, \boldsymbol{a}_2, \boldsymbol{a}_3$ shown in Fig. 1.2. It is straightforward to verify that Q vanishes at momenta $(\pm 4\pi/3a, 0)$. These two momenta are called K and K' valleys of the dispersion respectively. The Dirac dispersion near each valley has to satisfy the three-fold rotation symmetry of the lattice, which leads to $v_x = i v_y$. Further, due to the mirror symmetry around the x-axis, v_x has to be real, so we get the Hamiltonian

$$H = v \begin{pmatrix} \sigma_x p_x + \sigma_y p_y & 0 \\ 0 & \sigma_x p_y - \sigma_y p_y \end{pmatrix}, \tag{1.14}$$
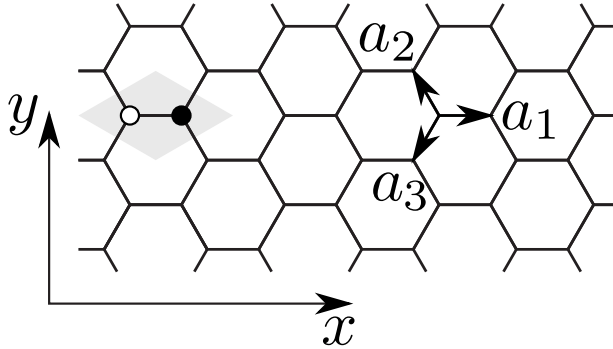
Figure 1.2: Lattice structure of graphene. The grey rhombus is the unit cell, with sublattices A and B marked with open and filled circles respectively.

where the matrices σ_i are Pauli matrices in the sublattice space. The first two components of the wave function in this 4-component equation correspond to the valley K, and the second two to the valley K'. We will find it convenient to perform a change of basis $H \to UHU^\dagger$ with $U = \mathrm{diag}(\sigma_0, \sigma_x)$. This transformation brings the Hamiltonian to the valley-isotropic form:

$$H' = v \begin{pmatrix} \sigma_x p_x + \sigma_y p_y & 0 \\ 0 & \sigma_x p_y + \sigma_y p_y \end{pmatrix}. \tag{1.15}$$

1.2.2 Dirac Hamiltonian close to a phase transition point

Let us consider the one-dimensional Dirac Hamiltonian

$$H = -i\hbar v \sigma_z \frac{\partial}{\partial x} + m(x)\sigma_y. \tag{1.16}$$

The symmetry $H^* = -H$ expresses particle-hole symmetry.[1] We search for eigenstates $\psi(x)$ of this Hamiltonian at exactly zero energy. Expressing the derivative of the wave function through the other terms gives

$$\frac{\partial \psi}{\partial x} = \frac{m(x)}{\hbar v} \sigma_x \psi. \tag{1.17}$$

The solutions of this equation have the form

$$\psi(x) = \exp\left(\sigma_x \int_{x_0}^{x} \frac{m(x')dx'}{\hbar v} \right) \psi(x_0). \tag{1.18}$$

---

[1] Any particle-hole symmetry operator of systems without spin rotation invariance can be brought to this form by a basis transformation.

There is only one Pauli matrix entering the expression, so the two linearly-independent solutions are given by

$$\psi_\pm = \exp\left(\pm\int_{x_0}^{x}\frac{m(x^{'})dx^{'}}{\hbar v}\right)\begin{pmatrix}1\\\pm1\end{pmatrix}.\tag{1.19}$$

At most one of the solutions is normalizable, and it is only possible to find a solution if the mass has opposite signs at $x\to\pm\infty$. In other words a solution exists if and only if there is a domain wall in the mass. The state bound at the interface between positive and negative masses is a Majorana bound state. The wave function corresponding to the Majorana state may change depending on the particular form of the function $m(x)$, but the presence or absence of the Majorana bound state is determined solely by the fact that the mass is positive on one side and negative on the other. An example of a domain wall in the mass and the Majorana bound state localized at the domain wall are shown in Fig. 1.3.
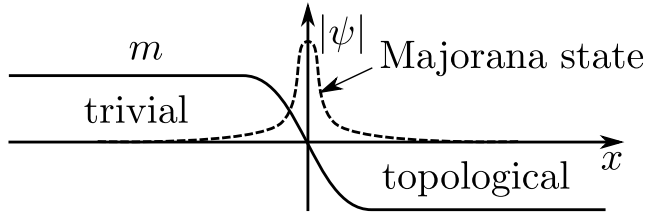
Figure 1.3: A model system with a domain wall in the mass. The domain with positive mass is called topologically trivial, the domain with negative mass is called topologically nontrivial. A Majorana bound state is located at the interface between the two domains.

The property that two domains with opposite mass have a symmetry-protected state at the interface, irrespective of the details of the interface, is called topological protection. Materials with symmetry-protected edge states are called topological insulators and superconductors. By selecting different mass terms in the Dirac equation one can change the symmetry class of the topological insulators or superconductors [16].

1.3   This thesis

We give a brief description of the content of each of the chapters.

1.3.1   Part I: Dirac edge states in graphene

Chapter 2: Boundary conditions for Dirac fermions on a terminated honeycomb lattice

We derive the boundary condition for the Dirac equation corresponding to a tight-binding model of graphene terminated along an arbitrary direction. Zigzag boundary conditions

result generically once the boundary is not parallel to the bonds, as shown in Fig. 1.4. Since a honeycomb strip with zigzag edges is gapless, this implies that confinement by lattice termination does not in general produce an insulating nanoribbon. We consider the opening of a gap in a graphene nanoribbon by a staggered potential at the edge and derive the corresponding boundary condition for the Dirac equation. We analyze the edge states in a nanoribbon for arbitrary boundary conditions and identify a class of propagating edge states that complement the known localized edge states at a zigzag boundary.
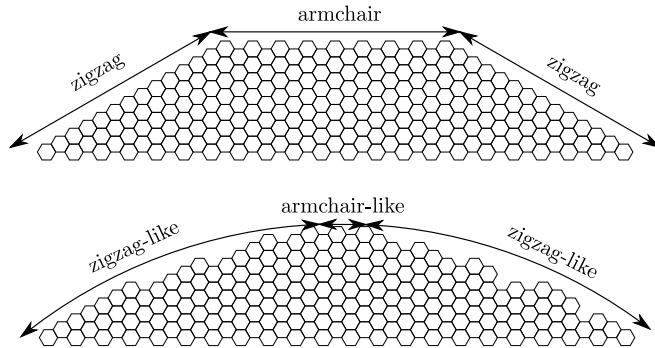
Figure 1.4: Top panel: two graphene boundaries appearing when graphene is terminated along one of the main crystallographic directions are the armchair boundary and the zigzag boundary. Only the zigzag boundary supports edge states. Bottom panel: when graphene is terminated along an arbitrary direction, the boundary condition generically corresponds to a zigzag one, except for special angles.

Chapter 3: Detection of valley polarization in graphene by a superconducting contact

Because the valleys in the band structure of graphene are related by time-reversal symmetry, electrons from one valley are reflected as holes from the other valley at the junction with a superconductor. We show how this Andreev reflection can be used to detect the valley polarization of edge states produced by a magnetic field using the setup of Fig. 1.5. In the absence of intervalley relaxation, the conductance $G_{NS} = 2(e^2/h)(1 - \cos \Theta)$ of the junction on the lowest quantum Hall plateau is entirely determined by the angle Θ between the valley isospins of the edge states approaching and leaving the superconductor. If the superconductor covers a single edge, $\Theta = 0$ and no current can enter the superconductor. A measurement of G_{NS} then determines the intervalley relaxation time.
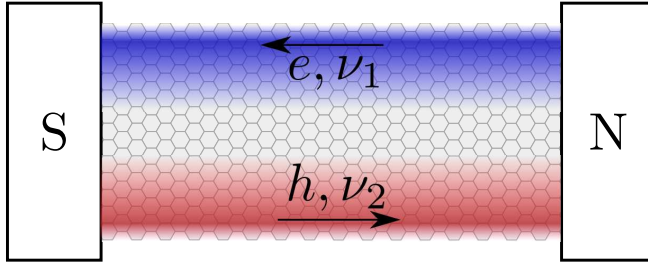
Figure 1.5: A normal metal-graphene-superconductor junction in high magnetic field. The only possibility for electric conductance is via the edge states. The valley polarizations ν_1, ν_2 of the edge states at different boundaries are determined only by the corresponding boundary conditions. The probability for an electron to reflect from the superconductor as a hole, as shown, depends on both ν_1 and ν_2.

Chapter 4: Theory of the valley-valve effect in graphene

A potential step in a graphene nanoribbon with zigzag edges is shown to be an intrinsic source of intervalley scattering – no matter how smooth the step is on the scale of the lattice constant a. The valleys are coupled by a pair of localized states at the opposite edges, which act as an attractor/repellor for edge states propagating in valley K/K'. The relative displacement Δ along the ribbon of the localized states determines the conductance G. Our result $G = (e^2/h)[1 - \cos(N\pi + 2\pi\Delta/3a)]$ explains why the "valley-valve" effect (the blocking of the current by a p-n junction) depends on the parity of the number N of carbon atoms across the ribbon, as shown in Fig. 1.6.
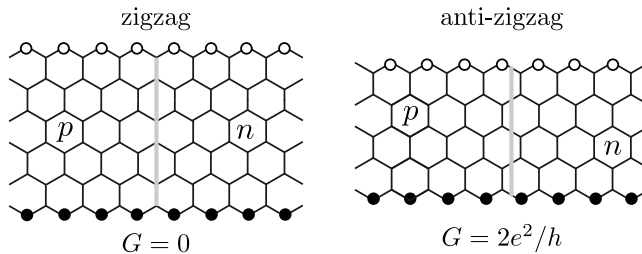
Figure 1.6: A pn-junction in zigzag and antizigzag ribbons (shown as a grey line separating p-type and n-type regions). The two ribbons are described on long length scales by the same Dirac equation, with the same boundary condition, however one ribbon is fully insulating, while the other one is perfectly conducting.

Chapter 5: Robustness of edge states in graphene quantum dots

We analyze the single particle states at the edges of disordered graphene quantum dots. We show that generic graphene quantum dots support a number of edge states proportional to the circumference of the dot divided by the lattice constant. The density of these edge states is shown in Fig. 1.7. Our analytical theory agrees well with numerical simulations. Perturbations breaking sublattice symmetry, like next-nearest neighbor hopping or edge impurities, shift the edge states away from zero energy but do not change their total amount. We discuss the possibility of detecting the edge states in an antidot array and provide an upper bound on the magnetic moment of a graphene dot.
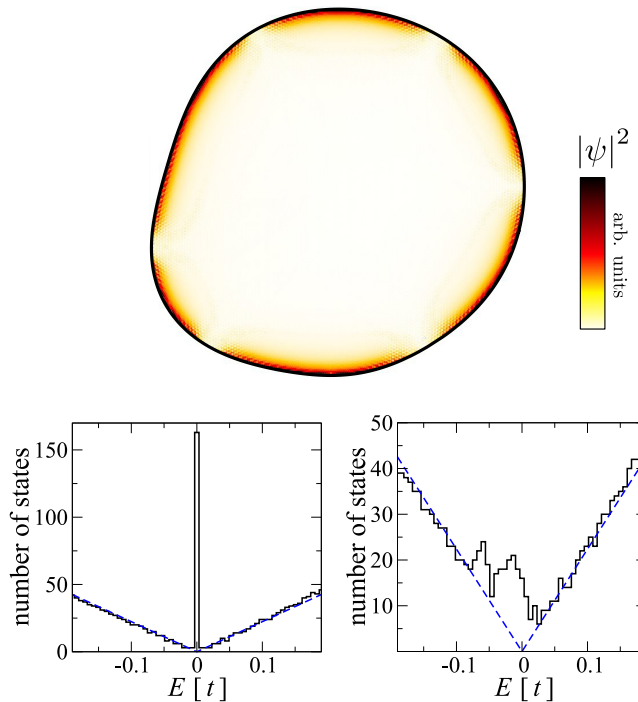
Figure 1.7: Density of low energy states in a graphene quantum dot as a function of position (top panel) or energy (bottom panels). The bottom left panel corresponds to the case when sublattice symmetry is present and the edge states are pinned to zero energy, while the bottom right panel shows the effect of sublattice symmetry breaking perturbations on the density of states.

1.3.2 Part II: Majorana bound states in topological superconductors

Chapter 6: Topological quantum computation away from ground state with Majorana fermions

We relax one of the requirements for topological quantum computation with Majorana fermions. Topological quantum computation was discussed so far as the manipulation of the wave function within a degenerate many-body ground state. Majorana fermions, are the simplest particles providing a degenerate ground state (non-abelian anyons). They often coexist with extremely low energy excitations (see Fig. 1.8), so keeping the system in the ground state may be hard. We show that the topological protection extends to the excited states, as long as the Majorana fermions interact neither directly, nor via the excited states. This protection relies on the fermion parity conservation, and so it is generic to any implementation of Majorana fermions.
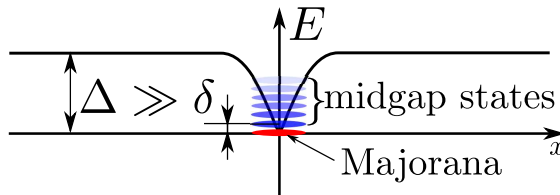
Figure 1.8: A Majorana fermion (red ellipse) coexists with many localized finite energy fermion states (blue ellipses) separated by a minigap δ, which is much smaller than the bulk gap Δ.

Chapter 7: Splitting of a Cooper pair by a pair of Majorana bound states

A single qubit can be encoded nonlocally in a pair of spatially separated Majorana bound states. Such Majorana qubits are in demand as building blocks of a topological quantum computer, but direct experimental tests of the nonlocality remain elusive. In this chapter we propose a method to probe the nonlocality by means of crossed Andreev reflection, which is the injection of an electron into one bound state followed by the emission of a hole by the other bound state (equivalent to the splitting of a Cooper pair over the two states). The setup we use is shown in Fig. 1.9. We have found that, at sufficiently low excitation energies, this nonlocal scattering process dominates over local Andreev reflection involving a single bound state. As a consequence, the low-temperature and low-frequency fluctuations δI_i of currents into the two bound states $i = 1, 2$ are maximally correlated: $\overline{\delta I_1 \delta I_2} = \overline{\delta I_i^2}$.
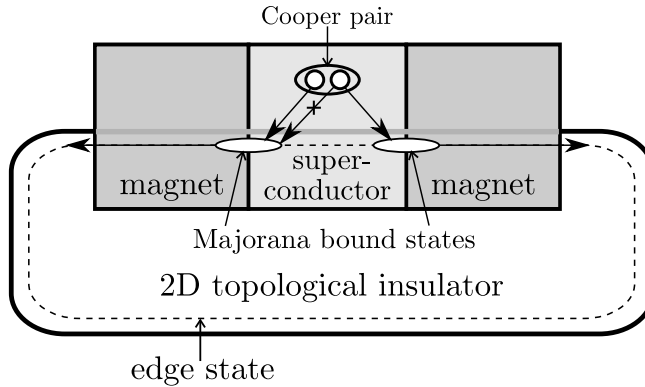
Figure 1.9: An edge of a two-dimensional topological insulator supports Majorana fermions when interrupted by ferromagnetic insulators and superconductors. Majorana fermions allow for only one electron out of a Cooper pair to exit at each side, acting as a perfect Cooper pair splitter.

Chapter 8: Electrically detected interferometry of Majorana fermions in a topological insulator

Chiral Majorana modes, one-dimensional analogue of Majorana bound states exist at a tri-junction of a topological insulator, s-wave superconductor, and a ferromagnetic insulator. Their detection is problematic since they have no charge. This is an obstacle to the realization of topological quantum computation, which relies on Majorana fermions to store qubits in a way which is insensitive to decoherence. We show how a pair of neutral Majorana modes can be converted reversibly into a charged Dirac mode. Our Dirac-Majorana converter, shown in Fig. 1.10, enables electrical detection of a qubit by an interferometric measurement.

Chapter 9: Domain wall in a chiral p-wave superconductor: a pathway for electrical current

Superconductors with $p_x \pm i p_y$ pairing symmetry are characterized by chiral edge states, but these are difficult to detect in equilibrium since the resulting magnetic field is screened by the Meissner effect. Nonequilibrium detection is hindered by the fact that the edge excitations are unpaired Majorana fermions, which cannot transport charge near the Fermi level. In this chapter we show that the boundary between $p_x + i p_y$ and $p_x - i p_y$ domains forms a one-way channel for electrical charge (see Fig. 1.11). We derive a product rule for the domain wall conductance, which allows to cancel the effect of a tunnel barrier between metal electrodes and superconductor and provides a unique signature of topological superconductors in the chiral p-wave symmetry class.

electrons
or holes

Majorana
fermions
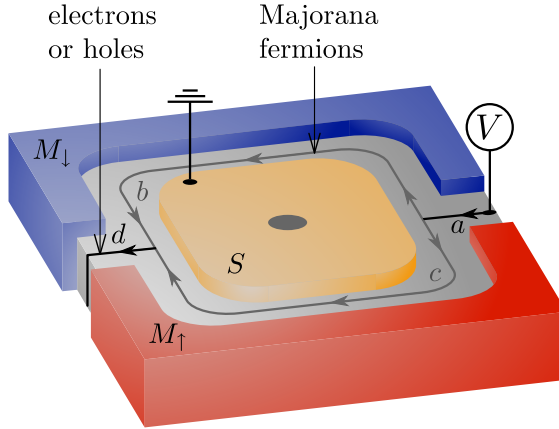
Figure 1.10: A Mach-Zehnder interferometer formed by a three-dimensional topological insulator (grey) in proximity to ferromagnets ($M_\uparrow$ and $M_\downarrow$) of opposite polarizations and a superconductor (S). Electrons approaching the superconductor from the magnetic domain wall are split into pairs of Majorana fermions, which later recombine into either electrones or holes.
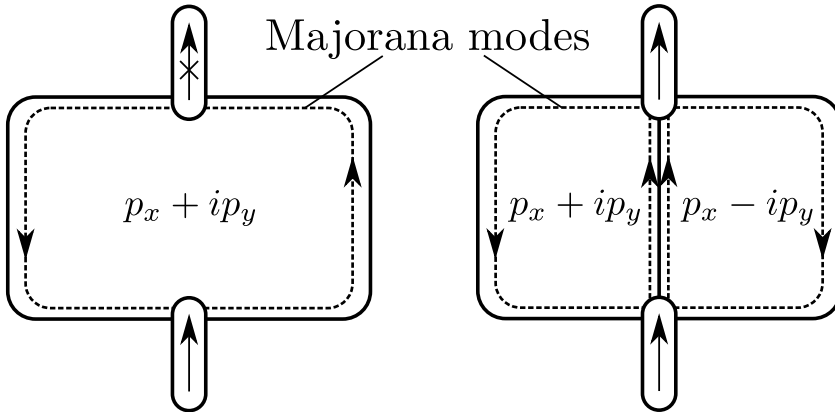
Figure 1.11: Left panel: a single chiral Majorana mode circling around a p-wave superconductor cannot carry electric current due to its charge neutrality. Right panel: when two chiral Majorana modes are brought into contact, they can carry electric current due to interference.

Chapter 10: Quantized conductance at the Majorana phase transition in a disordered superconducting wire

Superconducting wires without time-reversal and spin-rotation symmetries can be driven into a topological phase that supports Majorana bound states. Direct detection of these

zero-energy states is complicated by the proliferation of low-lying excitations in a disordered multi-mode wire. We show that the phase transition itself is signaled by a quantized thermal conductance and electrical shot noise power, irrespective of the degree of disorder. In a ring geometry, the phase transition is signaled by a period doubling of the magnetoconductance oscillations. These signatures directly follow from the identification of the sign of the determinant of the reflection matrix as a topological quantum number (as shown in Fig. 1.12).
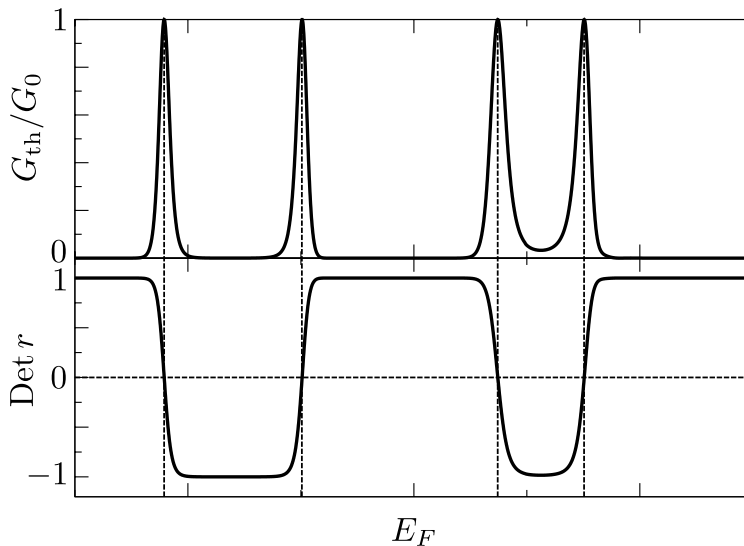
Figure 1.12: Thermal conductance (top panel) and the determinant of a reflection matrix (bottom panel) of a quasi one-dimensional superconducting wire as a function of Fermi energy. At the topological phase transitions (vertical dashed lines) the determinant of the reflection matrix changes sign, and the thermal conductance has a quantized spike.

Chapter 11: Theory of non-Abelian Fabry-Perot interferometry in topological insulators

Interferometry of non-Abelian edge excitations is a useful tool in topological quantum computing. In this chapter we present a theory of non-Abelian edge state interferometry in a 3D topological insulator brought in proximity to an s-wave superconductor. The non-Abelian edge excitations in this system have the same statistics as in the previously studied 5/2 fractional quantum Hall effect and chiral p-wave superconductors. There are however crucial differences between the setup we consider and these systems. The two types of edge excitations existing in these systems, the edge fermions ψ and the edge vortices σ, are charged in fractional quantum Hall system, and neutral in the topological insulator setup. This means that a converter between charged and neutral excitations,

shown in Fig. 1.13, is required. This difference manifests itself in a temperature scaling exponent of $-7/4$ for the conductance instead of $-3/2$ as in the 5/2 fractional quantum Hall effect.
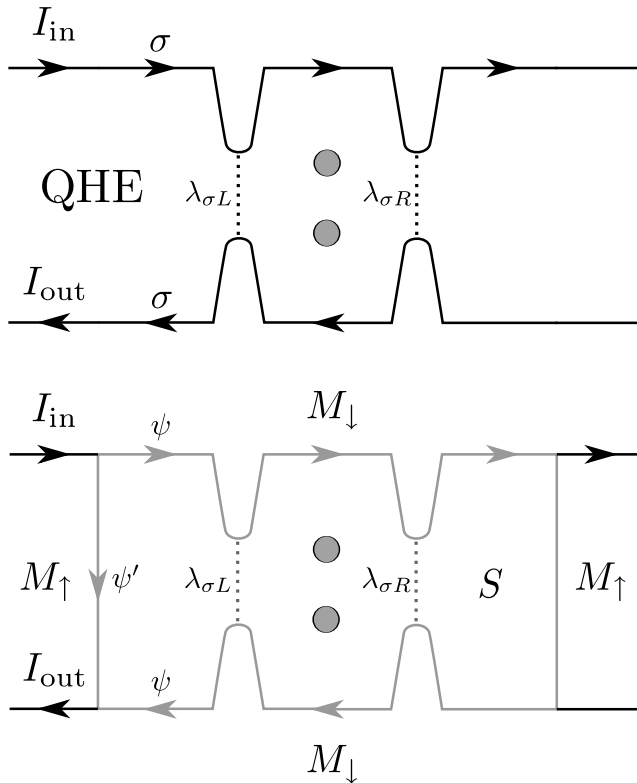
Figure 1.13: Top panel: non-Abelian Fabry-Perot interferometer in the 5/2 fractional quantum Hall effect. The electric current is due to tunneling of σ-excitations with charge $e/4$. Bottom panel: non-abelian Fabry-Perot interferometer in a topological insulator/superconductor/ferromagnet system. The electric current is due to fusion of two ψ-excitations at the exit of the interferometer.

Chapter 12: Probing Majorana edge states with a flux qubit

A pair of counter-propagating Majorana edge modes appears in chiral p-wave superconductors and in other superconducting systems belonging to the same universality class. These modes can be described by an Ising conformal field theory. We show how a superconducting flux qubit attached to such a system couples to the two chiral edge modes via the disorder field of the Ising model. Due to this coupling, measuring the back-action

of the edge states on the qubit allows to probe the properties of Majorana edge modes in the setup drawn in Fig. 1.14.
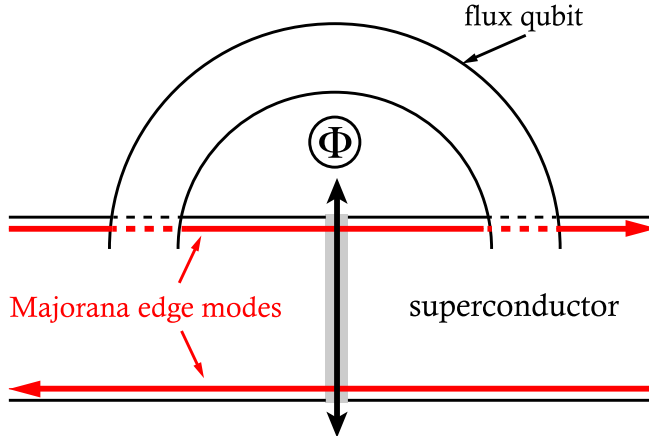
Figure 1.14: Schematic setup of the Majorana fermion edge modes coupled to a flux qubit. A pair of counter-propagating edge modes appears at two opposite edges of a topological superconductor. A flux qubit, consisting of a superconducting ring and a Josephson junction, shown as a gray rectangle, is attached to the superconductor in such a way that it does not interrupt the edge states' flow. As indicated by the arrow across the weak link, vortices can tunnel in and out of the superconducting ring through the Josephson junction.

Chapter 13: Anyonic interferometry without anyons: how a flux qubit can read out a topological qubit

Proposals to measure non-Abelian anyons in a superconductor by quantum interference of vortices suffer from the predominantly classical dynamics of the normal core of an Abrikosov vortex. We show how to avoid this obstruction using coreless Josephson vortices, for which the quantum dynamics has been demonstrated experimentally. The interferometer is a flux qubit in a Josephson junction circuit, which can nondestructively read out a topological qubit stored in a pair of anyons — even though the Josephson vortices themselves are not anyons. The flux qubit does not couple to intra-vortex excitations, thereby removing the dominant restriction on the operating temperature of anyonic interferometry in superconductors. The setup of Fig. 1.15 allows then to create and manipulate a register of topological qubits.
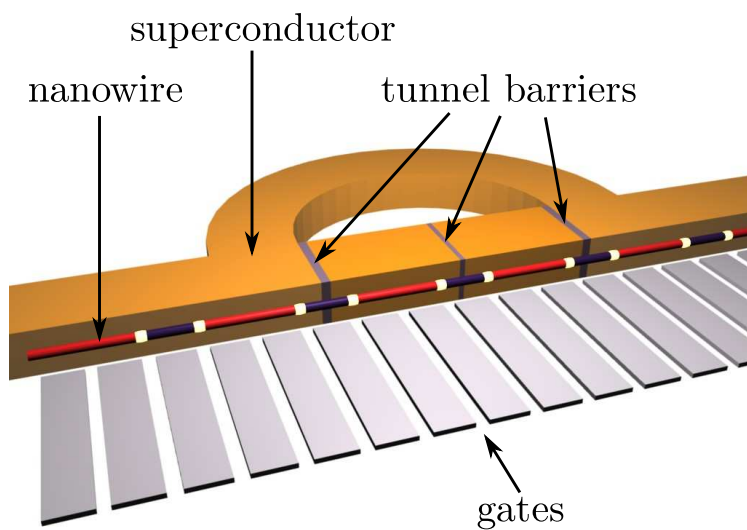
Figure 1.15: Register of topological qubits, read out by a flux qubit in a superconducting ring. The topological qubit is encoded in a pair of Majorana bound states (white dots) at the interface between a topologically trivial (blue) and a topologically nontrivial (red) section of an InAs wire. The flux qubit is encoded in the clockwise or counterclockwise persistent current in the ring. Gate electrodes (grey) can be used to move the Majorana bound states along the wire.

Part I

Dirac edge states in graphene

Chapter 2

Boundary conditions for Dirac fermions on a terminated honeycomb lattice

2.1 Introduction

The electronic properties of graphene can be described by a difference equation (representing a tight-binding model on a honeycomb lattice) or by a differential equation (the two-dimensional Dirac equation) [1, 17]. The two descriptions are equivalent at large length scales and low energies, provided the Dirac equation is supplemented by boundary conditions consistent with the tight-binding model. These boundary conditions depend on a variety of microscopic properties, determined by atomistic calculations [18].

For a general theoretical description, it is useful to know what boundary conditions on the Dirac equation are allowed by the basic physical principles of current conservation and (presence or absence of) time reversal symmetry — independently of any specific microscopic input. This problem was solved in Refs. [19, 20]. The general boundary condition depends on one mixing angle Λ (which vanishes if the boundary does not break time reversal symmetry), one three-dimensional unit vector $\boldsymbol{n}$ perpendicular to the normal to the boundary, and one three-dimensional unit vector $\boldsymbol{\nu}$ on the Bloch sphere of valley isospins. Altogether, four real parameters fix the boundary condition.

In this chapter we investigate how the boundary condition depends on the crystallographic orientation of the boundary. As the orientation is incremented by 30° the boundary configuration switches from armchair (parallel to one-third of the carbon-carbon bonds) to zigzag (perpendicular to another one-third of the bonds). The boundary conditions for the armchair and zigzag orientations are known [21]. Here we show that the boundary condition for intermediate orientations remains of the zigzag form, so that the armchair boundary condition is only reached for a discrete set of orientations.

Since the zigzag boundary condition does not open up a gap in the excitation spectrum [21], the implication of our result (not noticed in earlier studies [22]) is that a terminated honeycomb lattice of arbitrary orientation is metallic rather than insulating. We present tight-binding model calculations to confirm that the gap $\Delta \propto \exp[-f(\varphi)W/a]$ in a nanoribbon at crystallographic orientation φ vanishes exponentially when its width

W becomes large compared to the lattice constant a, characteristic of metallic behavior. The $\Delta \propto 1/W$ dependence characteristic of insulating behavior requires the special armchair orientation (φ a multiple of $60°$), at which the decay rate $f(\varphi)$ vanishes.

Confinement by a mass term in the Dirac equation does produce an excitation gap regardless of the orientation of the boundary. We show how the infinite-mass boundary condition of Ref. [23] can be approached starting from the zigzag boundary condition, by introducing a local potential difference on the two sublattices in the tight-binding model. Such a staggered potential follows from atomistic calculations [18] and may well be the origin of the insulating behavior observed experimentally in graphene nanoribbons [24, 25].

The outline of this chapter is as follows. In Sec. 2.2 we formulate, following Refs. [19, 20], the general boundary condition of the Dirac equation on which our analysis is based. In Sec. 2.3 we derive from the tight-binding model the boundary condition corresponding to an arbitrary direction of lattice termination. In Sec. 2.4 we analyze the effect of a staggered boundary potential on the boundary condition. In Sec. 2.5 we calculate the dispersion relation for a graphene nanoribbon with arbitrary boundary conditions. We identify dispersive (= propagating) edge states which generalize the known dispersionless (= localized) edge states at a zigzag boundary [26]. The exponential dependence of the gap Δ on the nanoribbon width is calculated in Sec. 2.6 both analytically and numerically. We conclude in Sec. 2.7.

2.2   General boundary condition

The long-wavelength and low-energy electronic excitations in graphene are described by the Dirac equation

$$H\Psi = \varepsilon\Psi \tag{2.1}$$

with Hamiltonian

$$H = v\tau_0 \otimes (\boldsymbol{\sigma} \cdot \boldsymbol{p}) \tag{2.2}$$

acting on a four-component spinor wave function Ψ. Here v is the Fermi velocity and $\boldsymbol{p} = -i\hbar\nabla$ is the momentum operator. Matrices τ_i, σ_i are Pauli matrices in valley space and sublattice space, respectively (with unit matrices τ_0, σ_0). The current operator in the direction $\boldsymbol{n}$ is $\boldsymbol{n} \cdot \boldsymbol{J} = v\tau_0 \otimes (\boldsymbol{\sigma} \cdot \boldsymbol{n})$.

The Hamiltonian H is written in the valley isotropic representation of Ref. [20]. The alternative representation $H' = v\tau_z \otimes (\boldsymbol{\sigma} \cdot \boldsymbol{p})$ of Ref. [19] is obtained by the unitary transformation

$$H' = UHU^\dagger, \quad U = \tfrac{1}{2}(\tau_0 + \tau_z) \otimes \sigma_0 + \tfrac{1}{2}(\tau_0 - \tau_z) \otimes \sigma_z. \tag{2.3}$$

As described in Ref. [19], the general energy-independent boundary condition has the form of a local linear restriction on the components of the spinor wave function at the boundary:

$$\Psi = M\Psi. \tag{2.4}$$

The 4×4 matrix M has eigenvalue 1 in a two-dimensional subspace containing Ψ, and without loss of generality we may assume that M has eigenvalue -1 in the orthogonal two-dimensional subspace. This means that M may be chosen as a Hermitian and unitary matrix,

$$M = M^{\dagger}, \; M^2 = 1. \tag{2.5}$$

The requirement of absence of current normal to the boundary,

$$\langle \Psi | \boldsymbol{n}_B \cdot \boldsymbol{J} | \Psi \rangle = 0, \tag{2.6}$$

with $\boldsymbol{n}_B$ a unit vector normal to the boundary and pointing outwards, is equivalent to the requirement of anticommutation of the matrix M with the current operator,

$$\{M, \boldsymbol{n}_B \cdot \boldsymbol{J}\} = 0. \tag{2.7}$$

That Eq. (2.7) implies Eq. (2.6) follows from $\langle \Psi | \boldsymbol{n}_B \cdot \boldsymbol{J} | \Psi \rangle = \langle \Psi | M(\boldsymbol{n}_B \cdot \boldsymbol{J})M | \Psi \rangle = -\langle \Psi | \boldsymbol{n}_B \cdot \boldsymbol{J} | \Psi \rangle$. The converse is proven in App. 2.A.

we are now faced with the problem of determining the most general 4×4 matrix M that satisfies Eqs. (2.5) and (2.7). Ref. [19] obtained two families of two-parameter solutions and two more families of three-parameter solutions. These solutions are subsets of the single four-parameter family of solutions obtained in Ref. [20],

$$M = \sin \Lambda \; \tau_0 \otimes (\boldsymbol{n}_1 \cdot \boldsymbol{\sigma}) + \cos \Lambda \; (\boldsymbol{v} \cdot \boldsymbol{\tau}) \otimes (\boldsymbol{n}_2 \cdot \boldsymbol{\sigma}), \tag{2.8}$$

where $\boldsymbol{v}, \boldsymbol{n}_1, \boldsymbol{n}_2$ are three-dimensional unit vectors, such that $\boldsymbol{n}_1$ and $\boldsymbol{n}_2$ are mutually orthogonal and also orthogonal to $\boldsymbol{n}_B$. A proof that (2.8) is indeed the most general solution is given in App. 2.A. One can also check that the solutions of Ref. [19] are subsets of $M' = UMU^{\dagger}$.

In this work we will restrict ourselves to boundary conditions that do not break time reversal symmetry. The time reversal operator in the valley isotropic representation is

$$T = -(\tau_y \otimes \sigma_y)C, \tag{2.9}$$

with C the operator of complex conjugation. The boundary condition preserves time reversal symmetry if M commutes with T. This implies that the mixing angle $\Lambda = 0$, so that M is restricted to a three-parameter family,

$$M = (\boldsymbol{v} \cdot \boldsymbol{\tau}) \otimes (\boldsymbol{n} \cdot \boldsymbol{\sigma}), \;\; \boldsymbol{n} \perp \boldsymbol{n}_B. \tag{2.10}$$

2.3   Lattice termination boundary

The honeycomb lattice of a carbon monolayer is a triangular lattice (lattice constant a) with two atoms per unit cell, referred to as A and B atoms (see Fig. 2.1a). The A and B atoms separately form two triangular sublattices. The A atoms are connected only to B

atoms, and vice versa. The tight-binding equations on the honeycomb lattice are given
by

$$\varepsilon\psi_A(\boldsymbol{r}) = t[\psi_B(\boldsymbol{r}) + \psi_B(\boldsymbol{r} - \boldsymbol{R}_1) + \psi_B(\boldsymbol{r} - \boldsymbol{R}_2)],$$
$$\varepsilon\psi_B(\boldsymbol{r}) = t[\psi_A(\boldsymbol{r}) + \psi_A(\boldsymbol{r} + \boldsymbol{R}_1) + \psi_A(\boldsymbol{r} + \boldsymbol{R}_2)]. \tag{2.11}$$

Here t is the hopping energy, $\psi_A(\boldsymbol{r})$ and $\psi_B(\boldsymbol{r})$ are the electron wave functions on A
and B atoms belonging to the same unit cell at a discrete coordinate $\boldsymbol{r}$, while $\boldsymbol{R}_1 = (a\sqrt{3}/2, -a/2)$, $\boldsymbol{R}_2 = (a\sqrt{3}/2, a/2)$ are lattice vectors as shown in Fig. 2.1a.

regardless of how the lattice is terminated, Eq. (2.11) has the electron-hole symmetry
$\psi_B \to -\psi_B$, $\varepsilon \to -\varepsilon$. For the long-wavelength Dirac Hamiltonian (2.2) this symmetry
is translated into the anticommutation relation

$$H\sigma_z \otimes \tau_z + \sigma_z \otimes \tau_z H = 0. \tag{2.12}$$

Electron-hole symmetry further restricts the boundary matrix M in Eq. (2.10) to two
classes: zigzag-like ($\boldsymbol{v} = \pm\hat{\boldsymbol{z}}$, $\boldsymbol{n} = \hat{\boldsymbol{z}}$) and armchair-like ($\boldsymbol{v}_z = \boldsymbol{n}_z = 0$). In this
section we will show that the zigzag-like boundary condition applies generically to an
arbitrary orientation of the lattice termination. The armchair-like boundary condition is
only reached for special orientations.

2.3.1   Characterization of the boundary

A terminated honeycomb lattice consists of sites with three neighbors in the interior
and sites with only one or two neighbors at the boundary. The absent neighboring sites
are indicated by open circles in Fig. 2.1 and the dangling bonds by thin line segments.
The tight-binding model demands that the wave function vanishes on the set of absent
sites, so the first step in our analysis is the characterization of this set. We assume
that the absent sites form a one-dimensional superlattice, consisting of a supercell of N
empty sites, translated over multiples of a superlattice vector $\boldsymbol{T}$. Since the boundary
superlattice is part of the honeycomb lattice, we may write $\boldsymbol{T} = n\boldsymbol{R}_1 + m\boldsymbol{R}_2$ with n and
m non-negative integers. For example, in Fig. 2.1 we have $n = 1$, $m = 4$. Without loss
of generality, and for later convenience, we may assume that $m - n = 0$ (modulo 3).

The angle φ between $\boldsymbol{T}$ and the armchair orientation (the x-axis in Fig. 2.1) is given
by

$$\varphi = \arctan\left(\frac{1}{\sqrt{3}}\frac{n-m}{n+m}\right), \quad -\frac{\pi}{6} \leq \varphi \leq \frac{\pi}{6}. \tag{2.13}$$

The armchair orientation corresponds to $\varphi = 0$, while $\varphi = \pm\pi/6$ corresponds to the
zigzag orientation. (Because of the $\pi/3$ periodicity we only need to consider $|\varphi| \leq \pi/6$.)

The number N of empty sites per period T can be arbitrarily large, but it cannot be
smaller than $n + m$. Likewise, the number N' of dangling bonds per period cannot be
smaller than $n + m$. We call the boundary *minimal* if $N = N' = n + m$. For example,
the boundary in Fig. 2.1d is minimal ($N = N' = 5$), while the boundaries in Figs. 2.1b
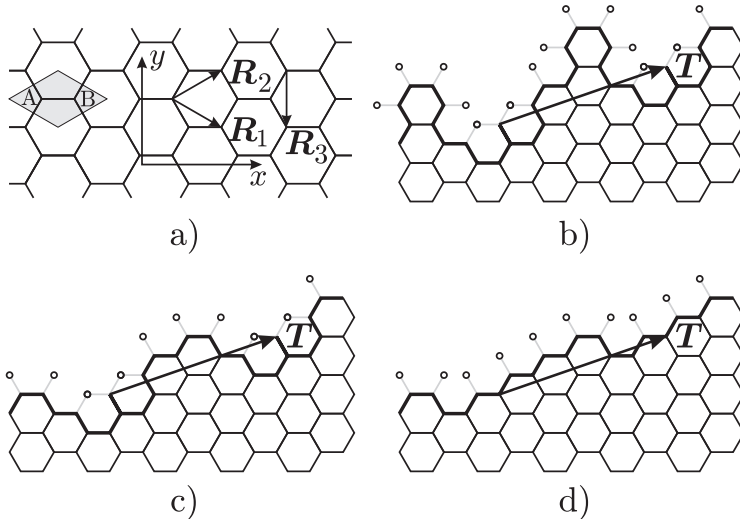
Figure 2.1: (a) Honeycomb latice constructed from a unit cell (grey rhombus) containing two atoms (labeled A and B), translated over lattice vectors $\boldsymbol{R}_1$ and $\boldsymbol{R}_2$. Panels b,c,d show three different periodic boundaries with the same period $\boldsymbol{T} = n\boldsymbol{R}_1 + m\boldsymbol{R}_2$. Atoms on the boundary (connected by thick solid lines) have dangling bonds (thin dotted line segments) to empty neighboring sites (open circles). The number N of missing sites and N' of dangling bonds per period is $\geq n + m$. Panel d shows a *minimal* boundary, for which $N = N' = n + m$.

and 2.1c are not minimal ($N = 7, N' = 9$ and $N = 5, N' = 7$, respectively). In what follows we will restrict our considerations to minimal boundaries, both for reasons of analytical simplicity [1] and for physical reasons (it is natural to expect that the minimal boundary is energetically most favorable for a given orientation).

We conclude this subsection with a property of minimal boundaries that we will need later on. The N empty sites per period can be divided into N_A empty sites on sublattice A and N_B empty sites on sublattice B. A minimal boundary is constructed from n translations over $\boldsymbol{R}_1$, each contributing one empty A site, and m translations over $\boldsymbol{R}_2$, each contributing one empty B site. Hence, $N_A = n$ and $N_B = m$ for a minimal boundary.

2.3.2   Boundary modes

The boundary breaks the two-dimensional translational invariance over $\boldsymbol{R}_1$ and $\boldsymbol{R}_2$, but a one-dimensional translational invariance over $T = n\boldsymbol{R}_1 + m\boldsymbol{R}_2$ remains. The quasimo-

---

[1]The method described in this section can be generalized to boundaries with $N' > n + m$ such as the "strongly disordered zigzag boundary" of Ref. [27]. For these *non-minimal* boundaries the zigzag boundary condition is still generic.

mentum p along the boundary is therefore a good quantum number. The corresponding Bloch state satisfies

$$\psi(r + T) = \exp(ik)\psi(r), \tag{2.14}$$

with $\hbar k = p \cdot T$. While the continuous quantum number $k \in (0, 2\pi)$ describes the propagation along the boundary, a second (discrete) quantum number λ describes how these boundary modes decay away from the boundary. We select λ by demanding that the Bloch wave (2.14) is also a solution of

$$\psi(r + R_3) = \lambda\psi(r). \tag{2.15}$$

The lattice vector $R_3 = R_1 - R_2$ has a nonzero component $a \cos\varphi > a\sqrt{3}/2$ perpendicular to T. We need $|\lambda| \leq 1$ to prevent $\psi(r)$ from diverging in the interior of the lattice. The decay length l_{decay} in the direction perpendicular to T is given by

$$l_{\text{decay}} = \frac{-a\cos\varphi}{\ln|\lambda|}. \tag{2.16}$$

The boundary modes satisfying Eqs. (2.14) and (2.15) are calculated in App. 2.B from the tight-binding model. In the low-energy regime of interest (energies ε small compared to t) there is an independent set of modes on each sublattice. On sublattice A the quantum numbers λ and k are related by

$$(-1 - \lambda)^{m+n} = \exp(ik)\lambda^n \tag{2.17a}$$

and on sublattice B they are related by

$$(-1 - \lambda)^{m+n} = \exp(ik)\lambda^m. \tag{2.17b}$$

For a given k there are N_A roots λ_p of Eq. (2.17a) having absolute value ≤ 1, with corresponding boundary modes ψ_p. We sort these modes according to their decay lengths from short to long, $l_{\text{decay}}(\lambda_p) \leq l_{\text{decay}}(\lambda_{p+1})$, or $|\lambda_p| \leq |\lambda_{p+1}|$. The wave function on sublattice A is a superposition of these modes

$$\psi^{(A)} = \sum_{p=1}^{N_A} \alpha_p \psi_p, \tag{2.18}$$

with coefficients α_p such that $\psi^{(A)}$ vanishes on the N_A missing A sites. Similarly there are N_B roots λ'_p of Eq. (2.17b) with $|\lambda'_p| \leq 1$, $|\lambda'_p| \leq |\lambda'_{p+1}|$. The corresponding boundary modes form the wave function on sublattice B,

$$\psi^{(B)} = \sum_{p=1}^{N_B} \alpha'_p \psi'_p, \tag{2.19}$$

with α'_p such that $\psi^{(B)}$ vanishes on the N_B missing B sites.

2.3.3 Derivation of the boundary condition

To derive the boundary condition for the Dirac equation it is sufficient to consider the boundary modes in the $k \to 0$ limit. The characteristic equations (2.17) for $k = 0$ each have a pair of solutions $\lambda_\pm = \exp(\pm 2i\pi/3)$ that do not depend on n and m. Since $|\lambda_\pm| = 1$, these modes do not decay as one moves away from the boundary. The corresponding eigenstate $\exp(\pm i\boldsymbol{K} \cdot \boldsymbol{r})$ is a plane wave with wave vector $\boldsymbol{K} = (4/3)\pi \boldsymbol{R}_3/a^2$. One readily checks that this Bloch state also satisfies Eq. (2.14) with $k = 0$ [since $\boldsymbol{K} \cdot \boldsymbol{T} = 2\pi(n-m)/3 = 0$ (modulo 2π)].

The wave functions (2.18) and (2.19) on sublattices A and B in the limit $k \to 0$ take the form

$$\psi^{(A)} = \Psi_1 e^{i\boldsymbol{K}\cdot\boldsymbol{r}} + \Psi_4 e^{-i\boldsymbol{K}\cdot\boldsymbol{r}} + \sum_{p=1}^{N_A-2} \alpha_p \psi_p, \qquad (2.20a)$$

$$\psi^{(B)} = \Psi_2 e^{i\boldsymbol{K}\cdot\boldsymbol{r}} + \Psi_3 e^{-i\boldsymbol{K}\cdot\boldsymbol{r}} + \sum_{p=1}^{N_B-2} \alpha'_p \psi'_p. \qquad (2.20b)$$

The four amplitudes $(\Psi_1, -i\Psi_2, i\Psi_3, -\Psi_4) \equiv \Psi$ form the four-component spinor Ψ in the Dirac equation (2.1). The remaining $N_A - 2$ and $N_B - 2$ terms describe decaying boundary modes of the tight-binding model that are not included in the Dirac equation.

We are now ready to determine what restriction on Ψ is imposed by the boundary condition on $\psi^{(A)}$ and $\psi^{(B)}$. This restriction is the required boundary condition for the Dirac equation. In App. 2.B we calculate that, for $k = 0$,

$$N_A = n - (n-m)/3 + 1, \qquad (2.21)$$
$$N_B = m - (m-n)/3 + 1, \qquad (2.22)$$

so that $N_A + N_B = n + m + 2$ is the total number of unknown amplitudes in Eqs. (2.18) and (2.19). These have to be chosen such that $\psi^{(A)}$ and $\psi^{(B)}$ vanish on N_A and N_B lattice sites respectively. For the minimal boundary under consideration we have $N_A = n$ equations to determine N_A unknowns and $N_B = m$ equations to determine N_B unknowns.

Three cases can be distinguished [in each case $n - m = 0$ (modulo 3)]:

1. If $n > m$ then $N_A \leq n$ and $N_B \geq m + 2$, so $\Psi_1 = \Psi_4 = 0$, while Ψ_2 and Ψ_3 are undetermined.

2. If $n < m$ then $N_B \leq n$ and $N_A \geq m + 2$, so $\Psi_2 = \Psi_3 = 0$, while Ψ_1 and Ψ_4 are undetermined.

3. If $n = m$ then $N_A = n + 1$ and $N_B = m + 1$, so $|\Psi_1| = |\Psi_4|$ and $|\Psi_2| = |\Psi_3|$.

In each case the boundary condition is of the canonical form $\Psi = (\boldsymbol{\nu} \cdot \boldsymbol{\tau}) \otimes (\boldsymbol{n} \cdot \boldsymbol{\sigma})\Psi$ with

1. $\boldsymbol{v} = -\hat{\boldsymbol{z}}$, $\boldsymbol{n} = \hat{\boldsymbol{z}}$ if $n > m$ (zigzag-type boundary condition).

2. $\boldsymbol{v} = \hat{\boldsymbol{z}}$, $\boldsymbol{n} = \hat{\boldsymbol{z}}$ if $n < m$ (zigzag-type boundary condition).

3. $\boldsymbol{v} \cdot \hat{\boldsymbol{z}} = 0$, $\boldsymbol{n} \cdot \hat{\boldsymbol{z}} = 0$ if $n = m$ (armchair-type boundary condition).

We conclude that the boundary condition is of zigzag-type for any orientation $\boldsymbol{T}$ of the boundary, unless $\boldsymbol{T}$ is parallel to the bonds [so that $n = m$ and $\varphi = 0$ (modulo $\pi/3$)].

2.3.4 Precision of the boundary condition

At a perfect zigzag or armchair edge the four components of the Dirac spinor Ψ are sufficient to meet the boundary condition. Near the boundaries with larger period and more complicated structure the wave function (2.20) also necessarily contains several boundary modes ψ_p, ψ_p' that decay away from the boundary. The decay length δ of the slowest decaying mode is the distance at which the boundary is indistinguishable from a perfect armchair or zigzag edge. At distances smaller than δ the boundary condition breaks down.

In the case of an armchair-like boundary (with $n = m$), all the coefficients α_p and α_p' in Eqs. (2.20) must be nonzero to satisfy the boundary condition. The maximal decay length δ is then equal to the decay length of the boundary mode ψ_{n-1} which has the largest $|\lambda|$. It can be estimated from the characteristic equations (2.17) that $\delta \approx |\boldsymbol{T}|$. Hence the larger the period of an armchair-like boundary, the larger the distance from the boundary at which the boundary condition breaks down.

For the zigzag-like boundary the situation is different. On one sublattice there are more boundary modes than conditions imposed by the presence of the boundary and on the other sublattice there are less boundary modes than conditions. Let us assume that sublattice A has more modes than conditions (which happens if $n < m$). The quickest decaying set of boundary modes sufficient to satisfy the tight-binding boundary condition contains n modes ψ_p with $p \leq n$. The distance δ from the boundary within which the boundary condition breaks down is then equal to the decay length of the slowest decaying mode ψ_n in this set and is given by

$$\delta = l_{\text{decay}}(\lambda_n) = -a \cos \varphi / \ln |\lambda_n|. \tag{2.23}$$

[See Eq. (2.16).]

As derived in App. 2.B for the case of large periods $|\boldsymbol{T}| \gg a$, the quantum number λ_n satisfies the following system of equations:

$$|1 + \lambda_n|^{m+n} = |\lambda_n|^n, \tag{2.24a}$$

$$\arg(1 + \lambda_n) - \frac{n}{n+m} \arg(-\lambda_n) = \frac{n}{n+m} \pi. \tag{2.24b}$$

The solution λ_n of this equation and hence the decay length δ do not depend on the length $|\boldsymbol{T}|$ of the period, but only on the ratio $n/(n+m) = (1 - \sqrt{3} \tan \varphi)/2$, which is a function of the angle φ between $\boldsymbol{T}$ and the armchair orientation [see Eq. (2.13)]. In
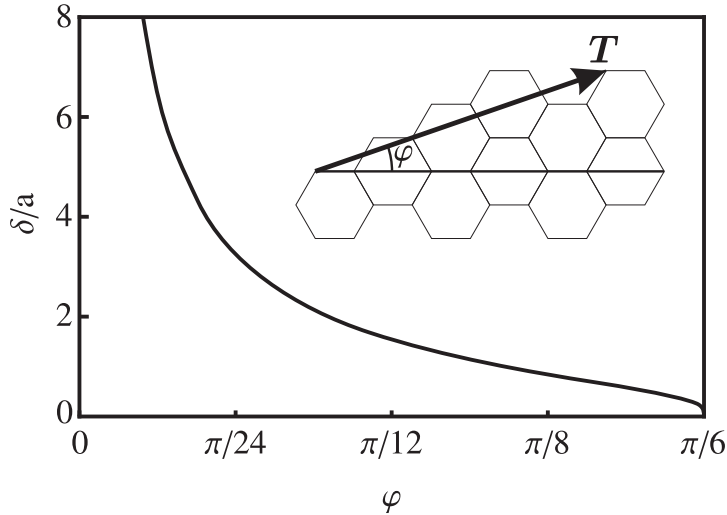
Figure 2.2: Dependence on the orientation φ of the distance δ from the boundary within which the zigzag-type boundary condition breaks down. The curve is calculated from formula (2.24) valid in the limit $|\boldsymbol{T}| \gg a$ of large periods. The boundary condition becomes precise upon approaching the zigzag orientation $\varphi = \pi/6$.

the case $n > m$ when sublattice B has more modes than conditions, the largest decay length δ follows upon interchanging n and m.

As seen from Fig. 2.2, the resulting distance δ within which the zigzag-type boundary condition breaks down is zero for the zigzag orientation ($\varphi = \pi/6$) and tends to infinity as the orientation of the boundary approaches the armchair orientation ($\varphi = 0$). (For finite periods the divergence is cut off at $\delta \sim |\boldsymbol{T}| \gg a$.) The increase of δ near the armchair orientation is rather slow: For $\varphi \gtrsim 0.1$ the zigzag-type boundary condition remains precise on the scale of a few unit cells away from the boundary.

Although the presented derivation is only valid for periodic boundaries and low energies, such that the wavelength is much larger than the length $|\boldsymbol{T}|$ of the boundary period, we argue that these conditions may be relaxed. Indeed, since the boundary condition is local, it cannot depend on the structure of the boundary far away, hence the periodicity of the boundary cannot influence the boundary condition. It can also not depend on the wavelength once the wavelength is larger than the typical size of a boundary feature (rather than the length of the period). Since for most boundaries both δ and the scale of the boundary roughness are of the order of several unit cells, we conclude that the zigzag boundary condition is in general a good approximation.

2.3.5   Density of edge states near a zigzag-like boundary

A zigzag boundary is known to support a band of dispersionless states [26], which are localized within several unit cells near the boundary. We calculate the 1D density of these edge states near an arbitrary zigzag-like boundary. Again assuming that the sublattice A has more boundary modes than conditions ($n < m$), for each k there are $N_A(k) - N_A$ linearly independent states (2.18), satisfying the boundary condition. For $k \neq 0$ the number of boundary modes is equal to $N_A = n - (m - n)/3$, so that for each k there are

$$N_{\text{states}} = N_A(k) - n = (m - n)/3 \tag{2.25}$$

edge states. The number of the edge states for the case when $n > m$ again follows upon interchanging n and m. The density ρ of edge states per unit length is given by

$$\rho = \frac{N_{\text{states}}}{|\boldsymbol{T}|} = \frac{|m - n|}{3a\sqrt{n^2 + nm + m^2}} = \frac{2}{3a}|\sin\varphi|. \tag{2.26}$$

The density of edge states is maximal $\rho = 1/3a$ for a perfect zigzag edge and it decreases continuously when the boundary orientation φ approaches the armchair one. Eq. (2.26) explains the numerical data of Ref. [26], providing an analytical formula for the density of edge states.

2.4   Staggered boundary potential

The electron-hole symmetry (2.12), which restricts the boundary condition to being either of zigzag-type or of armchair-type, is broken by an electrostatic potential. Here we consider, motivated by Ref. [18], the effect of a staggered potential at the zigzag boundary. We show that the effect of this potential is to change the boundary condition in a continuous way from $\Psi = \pm\tau_z \otimes \sigma_z\Psi$ to $\Psi = \pm\tau_z \otimes (\boldsymbol{\sigma} \cdot [\hat{\boldsymbol{z}} \times \boldsymbol{n}_B])\Psi$. The first boundary condition is of zigzag-type, while the second boundary condition is produced by an infinitely large mass term at the boundary [23].

The staggered potential consists of a potential $V_A = +\mu$, $V_B = -\mu$ on the A-sites and B-sites in a total of $2N$ rows closest to the zigzag edge parallel to the y-axis (see Fig. 2.3). Since this potential does not mix the valleys, the boundary condition near a zigzag edge with staggered potential has the form

$$\Psi = -\tau_z \otimes (\sigma_z \cos\theta + \sigma_y \sin\theta)\Psi, \tag{2.27}$$

in accord with the general boundary condition (2.10). For $\theta = 0, \pi$ we have the zigzag boundary condition and for $\theta = \pm\pi/2$ we have the infinite-mass boundary condition.

To calculate the angle θ we substitute Eq. (2.20) into the tight-binding equation (2.11) (including the staggered potential at the left-hand side) and search for a solution in the limit $\varepsilon = 0$. The boundary condition is precise for the zigzag orientation, so we may set $\alpha_p = \alpha'_p = 0$. It is sufficient to consider a single valley, so we also set $\Psi_3 = \Psi_4 = 0$. The remaining nonzero components are $\Psi_1 e^{i\boldsymbol{K}\cdot\boldsymbol{r}} \equiv \psi_A(i)e^{iKy}$

and $\Psi_2 e^{i\boldsymbol{K}\cdot\boldsymbol{r}} \equiv \psi_B(i)e^{iKy}$, where i in the argument of $\psi_{A,B}$ numbers the unit cell away from the edge and we have used that $\boldsymbol{K}$ points in the y-direction. The resulting difference equations are

$$-\mu\psi_A(i) = t[\psi_B(i) - \psi_B(i-1)], \; i = 1, 2, \dots N, \tag{2.28a}$$

$$\mu\psi_B(i) = t[\psi_A(i) - \psi_A(i+1)], \; i = 0, 1, 2, \dots N-1, \tag{2.28b}$$

$$\psi_A(0) = 0. \tag{2.28c}$$

For the Ψ_1, Ψ_2 components of the Dirac spinor Ψ the boundary condition (2.27) is equivalent to

$$\psi_A(N)/\psi_B(N) = -\tan(\theta/2). \tag{2.29}$$

Substituting the solution of Eq. (2.28) into Eq. (2.29) gives

$$\cos\theta = \frac{1 + \sinh(\kappa)\sinh(\kappa + 2N\mu/t)}{\cosh(\kappa)\cosh(\kappa + 2N\mu/t)}, \tag{2.30}$$

with $\sinh\kappa = \mu/2t$. Eq. (2.30) is exact for $N \gg 1$, but it is accurate within 2% for any N. The dependence of the parameter θ of the boundary condition on the staggered potential strength μ is shown in Fig. 2.4 for various values of N. The boundary condition is closest to the infinite mass for $\mu/t \sim 1/N$, while the regimes $\mu/t \ll 1/N$ or $\mu/t \gg 1$ correspond to a zigzag boundary condition.
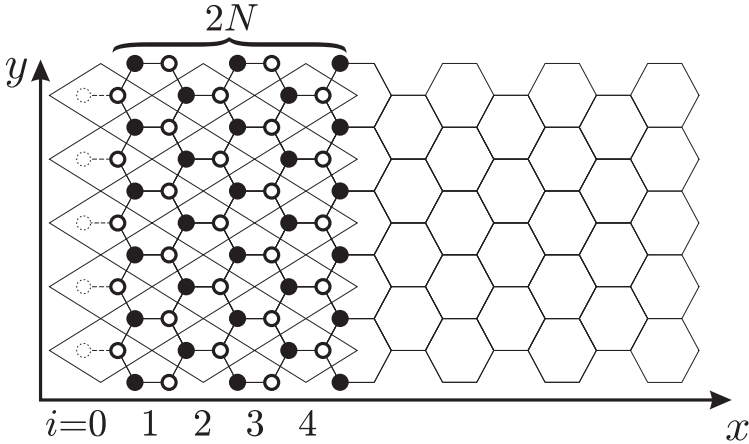
Figure 2.3: Zigzag boundary with $V = +\mu$ on the A-sites (filled dots) and $V = -\mu$ on the B-sites (empty dots). The staggered potential extends over $2N$ rows of atoms nearest to the zigzag edge. The integer i counts the number of unit cells away from the edge.
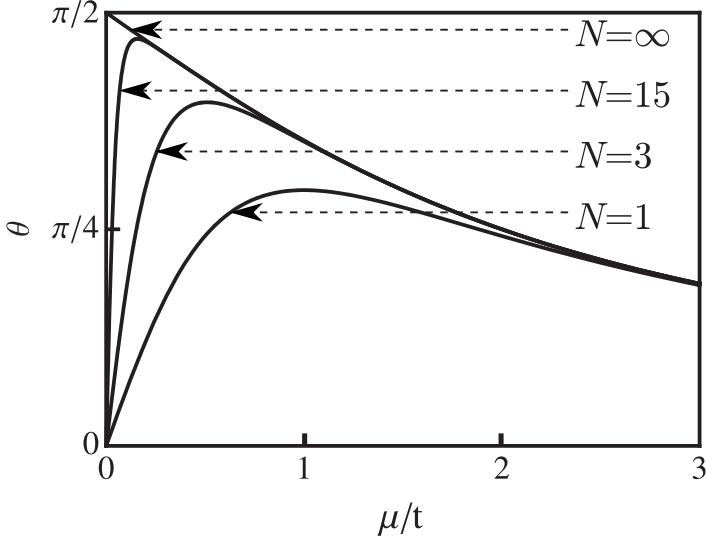
Figure 2.4: Plot of the parameter θ in the boundary condition (2.27) at a zigzag edge with the staggered potential of Fig. 2.3. The curves are calculated from Eq. (2.30). The values $\theta = 0$ and $\theta = \pi/2$ correspond, respectively, to the zigzag and infinite-mass boundary conditions.

2.5 Dispersion relation of a nanoribbon

A graphene nanoribbon is a carbon monolayer confined to a long and narrow strip. The energy spectrum $\varepsilon_n(k)$ of the n-th transverse mode is a function of the wave number k along the strip. This dispersion relation is nonlinear because of the confinement, which also may open up a gap in the spectrum around zero energy. We calculate the dependence of the dispersion relation on the boundary conditions at the two edges $x = 0$ and $x = W$ of the nanoribbon (taken along the y-axis).

In this section we consider the most general boundary condition (2.10), constrained only by time-reversal symmetry. We do not require that the boundary is purely a termination of the lattice, but allow for arbitrary local electric fields and strained bonds. The conclusion of Sec. 2.3, that the boundary condition is either zigzag-like or armchair-like, does not apply therefore to the analysis given in this section.

The general solution of the Dirac equation (2.1) in the nanoribbon has the form $\Psi(x, y) = \Psi_{n,k}(x)e^{iky}$. We impose the general boundary condition (2.10),

$$\Psi(0, y) = (\boldsymbol{\nu}_1 \cdot \boldsymbol{\tau}) \otimes (\boldsymbol{n}_1 \cdot \boldsymbol{\sigma})\Psi(0, y), \tag{2.31a}$$

$$\Psi(W, y) = (\boldsymbol{\nu}_2 \cdot \boldsymbol{\tau}) \otimes (\boldsymbol{n}_2 \cdot \boldsymbol{\sigma})\Psi(W, y), \tag{2.31b}$$

with three-dimensional unit vectors $\boldsymbol{\nu}_i$, $\boldsymbol{n}_i$, restricted by $\boldsymbol{n}_i \cdot \hat{\boldsymbol{x}} = 0$ ($i = 1, 2$). (There is no restriction on the $\boldsymbol{\nu}_i$.) Valley isotropy of the Dirac Hamiltonian (2.2) implies that

the spectrum does not depend on $\boldsymbol{\nu}_1$ and $\boldsymbol{\nu}_2$ separately but only on the angle γ between them. The spectrum depends, therefore, on three parameters: The angle γ and the angles θ_1, θ_2 between the z-axis and the vectors $\boldsymbol{n}_1$, $\boldsymbol{n}_2$.

The Dirac equation $H\Psi = \varepsilon\Psi$ has two plane wave solutions $\Psi \propto \exp(iky + iqx)$ for a given ε and k, corresponding to the two (real or imaginary) transverse wave numbers q that solve $(\hbar v)^2 (k^2 + q^2) = \varepsilon^2$. Each of these two plane waves has a twofold valley degeneracy, so there are four independent solutions in total. Since the wavefunction in a ribbon is a linear combination of these four waves, and since each of the Eqs. (2.31a,2.31b) has a two-dimensional kernel, these equations provide four linearly independent equations to determine four unknowns. The condition that Eq. (2.31) has nonzero solutions gives an implicit equation for the dispersion relation of the nanoribbon:

$$\cos\theta_1 \cos\theta_2 (\cos\omega - \cos^2\Omega) + \cos\omega \sin\theta_1 \sin\theta_2 \sin^2\Omega$$
$$- \sin\Omega[\sin\Omega\cos\gamma + \sin\omega\sin(\theta_1 - \theta_2)] = 0, \quad (2.32)$$

where $\omega^2 = 4W^2[(\varepsilon/\hbar v)^2 - k^2]$ and $\cos\Omega = \hbar vk/\varepsilon$.

For $\theta_1 = \theta_2 = 0$ and $\gamma = \pi$ Eq. (5.2) reproduces the transcendental equation of Ref. [21] for the dispersion relation of a zigzag ribbon. In the case $\theta_1 = \theta_2 = \pi/2$ of an armchair-like nanoribbon, Eq. (5.2) simplifies to

$$\cos\omega = \cos\gamma. \tag{2.33}$$

This is the only case when the transverse wave function $\Psi_{n,k}(x)$ is independent of the longitudinal wave number k. In Fig. 2.5 we plot the dispersion relations for several different boundary conditions.

The low energy modes of a nanoribbon with $|\varepsilon| < \hbar v|k|$ [see panels a-d of Fig. 2.5] have imaginary transverse momentum since $q^2 = (\varepsilon/\hbar v)^2 - k^2 < 0$. If $|q|$ becomes larger than the ribbon width W, the corresponding wave function becomes localized at the edges of the nanoribbon and decays in the bulk. The dispersion relation (2.32) for such an edge state simplifies to $\varepsilon = \hbar v|k|\sin\theta_1$ for the state localized near $x = 0$ and $\varepsilon = -\hbar v|k|\sin\theta_2$ for the state localized near $x = W$. These dispersive edge states with velocity $v\sin\theta$ generalize the known [26] dispersionless edge states at a zigzag boundary (with $\sin\theta = 0$).

Inspection of the dispersion relation (2.32) gives the following condition for the presence of a gap in the spectrum of the Dirac equation with arbitrary boundary condition: Either the valleys should be mixed ($\gamma \neq 0, \pi$) or the edge states at opposite boundaries should have energies of opposite sign ($\sin\theta_1 \sin\theta_2 > 0$ for $\gamma = \pi$ or $\sin\theta_1 \sin\theta_2 < 0$ for $\gamma = 0$).

As an example, we calculate the band gap for the staggered potential boundary condition of Sec. 2.4. We assume that the opposite zigzag edges have the same staggered potential, so that the boundary condition is

$$\Psi(0, y) = +\tau_z \otimes (\sigma_z \cos\theta + \sigma_y \sin\theta)\Psi(0, y), \tag{2.34a}$$
$$\Psi(W, y) = -\tau_z \otimes (\sigma_z \cos\theta + \sigma_y \sin\theta)\Psi(W, y). \tag{2.34b}$$
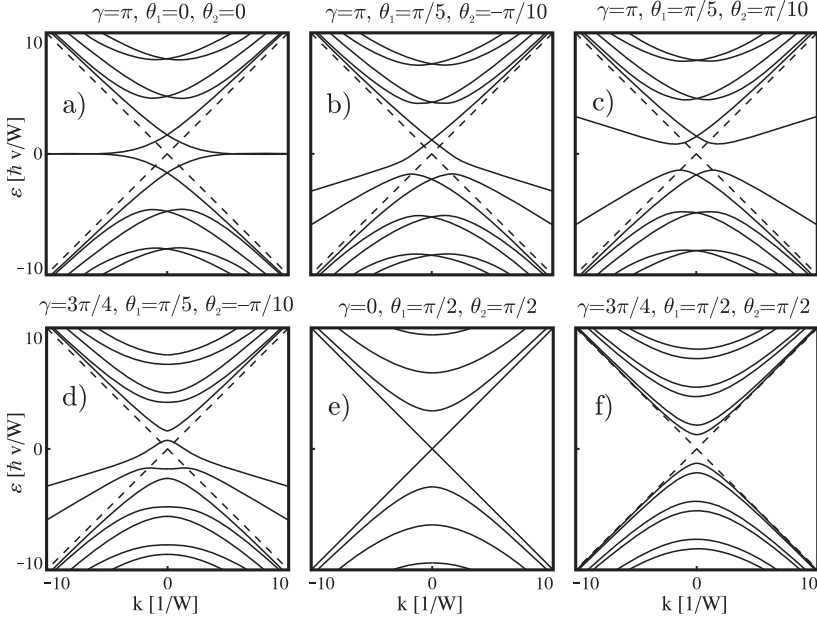
Figure 2.5: Dispersion relation of nanoribbons with different boundary conditions. The large-wave number asymptotes $|\varepsilon| = \hbar v|k|$ of bulk states are shown by dashed lines. Modes that do not approach these asymptotes are edge states with dispersion $|\varepsilon| = \hbar v|k \sin\theta_i|$. The zigzag ribbon with $\gamma = \pi$ and $\theta_1 = \theta_2 = 0$ (a) exhibits dispersionless edge states at zero energy [26]. If θ_1 or θ_2 are nonzero (b, c) the edge states acquire linear dispersion and if $\sin\theta_1 \sin\theta_2 > 0$ (c) a band gap opens. If γ is unequal to 0 or π (d) the valleys are mixed which makes all the level crossings avoided and opens a band gap. Armchair-like ribbons with $\theta_1 = \theta_2 = \pi/2$ (e, f) are the only ribbons having no edge states.

The dependence of θ on the parameters μ, N of the staggered potential is given by Eq. (2.30). This boundary condition corresponds to $\gamma = \pi$, $\theta_1 = \theta_2 = \theta$, so that it has a gap for any nonzero θ. As shown in Fig. 2.6, $\Delta(\theta)$ increases monotonically with θ from the zigzag limit $\Delta(0) = 0$ to the infinite-mass limit $\Delta(\pi/2) = \pi\hbar v/W$.

2.6 Band gap of a terminated honeycomb lattice

In this section we return to the case of a boundary formed purely by termination of the lattice. A nanoribbon with zigzag boundary condition has zero band gap according to the Dirac equation (Fig. 2.5a). According to the tight-binding equations there is a nonzero gap Δ, which however vanishes exponentially with increasing width W of the nanoribbon. We estimate the decay rate of $\Delta(W)$ as follows.
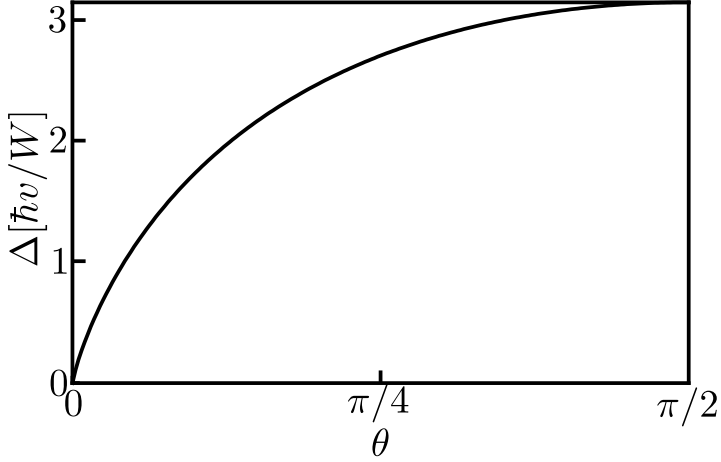
Figure 2.6: Dependence of the band gap Δ on the parameter θ in the staggered potential boundary condition (2.34).

The low energy states in a zigzag-type nanoribbon are the hybridized zero energy edge states at the opposite boundaries. The energy ε of such states may be estimated from the overlap between the edge states localized at the opposite edges,

$$\varepsilon = \pm(\hbar v/W)\exp(-W/l_{\text{decay}}). \tag{2.35}$$

In a perfect zigzag ribbon there are edge states with $l_{\text{decay}} = 0$ (and $\varepsilon = 0$), so that there is no band gap. For a ribbon with a more complicated edge shape the decay length of an edge state is limited by δ, the length within which the boundary condition breaks down (see Sec. 2.3.D). This length scale provides the analytical estimate of the band gap in a zigzag-like ribbon:

$$\Delta \sim \frac{\hbar v}{W}e^{-W/\delta}, \tag{2.36}$$

with δ given by Eqs. (2.23) and (2.24).

The band gap of an armchair-like ribbon is

$$\Delta = (\hbar v/W)\arccos(\cos\gamma) \tag{2.37}$$

[see Eq. (2.33) and panels e,f of Fig. 2.5]. Adding another row of atoms increases the nanoribbon width by one half of a unit cell and increases γ by $\boldsymbol{K} \cdot \boldsymbol{R}_3 = 4\pi/3$, so the product ΔW in such a ribbon is an oscillatory function of W with a period of 1.5 unit cells.

To test these analytical estimates, we have calculated $\Delta(W)$ numerically for various orientations and configurations of boundaries. As seen from Fig. 2.7, in ribbons with a non-armchair boundary the gap decays exponentially $\propto \exp[-f(\varphi)W/a]$ as a function

of W. Nanoribbons with the same orientation φ but different period $|\boldsymbol{T}|$ have the same decay rate f. As seen in Fig. 2.8, the decay rate obtained numerically agrees well with the analytical estimate $f = a/\delta$ following from Eq. (2.36) (with δ given as a function of φ in Fig. 2.2). The numerical results of Fig. 2.7 are consistent with earlier studies of the orientation dependence of the band gap in nanoribbons [22], but the exponential decrease of the gap for non-armchair ribbons was not noticed in those studies.
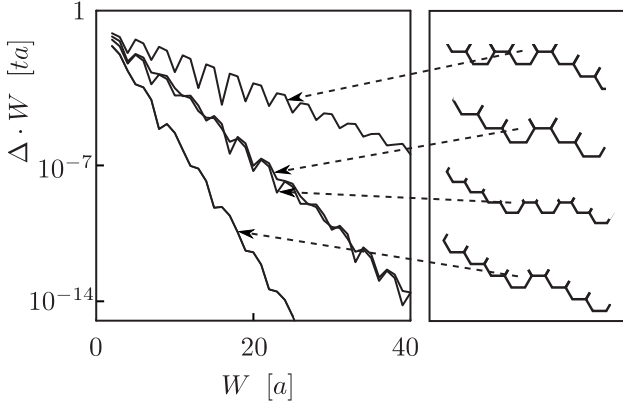
Figure 2.7: Dependence of the band gap Δ of zigzag-like nanoribbons on the width W. The curves in the left panel are calculated numerically from the tight-binding equations. The right panel shows the structure of the boundary, repeated periodically along both edges.
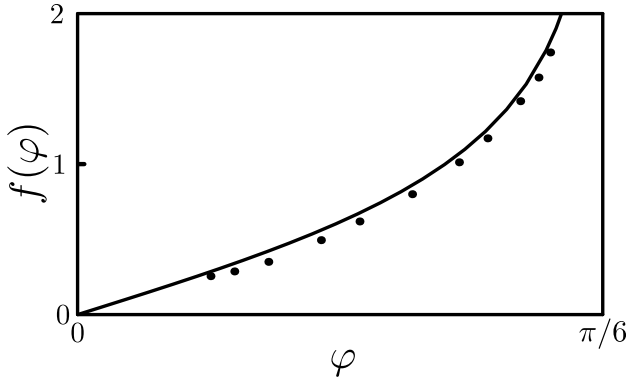
Figure 2.8: Dependence of the gap decay rate on the orientation φ of the boundary (defined in the inset of Fig. 2.2). The dots are the fits to numerical results of the tight-binding equations, the solid curve is the analytical estimate (2.36).

For completeness we show in Fig. 2.9 our numerical results for the band gap in an

armchair-like nanoribbon ($\varphi = 0$). We see that the gap oscillates with a period of 1.5 unit cells, in agreement with Eq. (2.37).
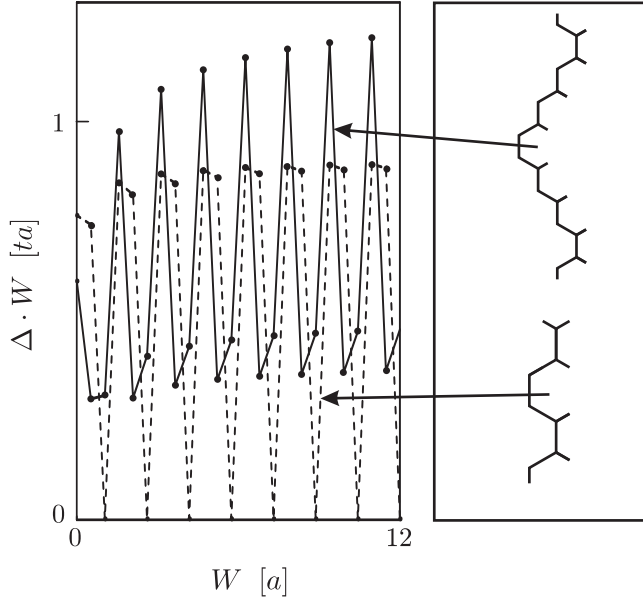
Figure 2.9: Dependence of the band gap Δ on the width W for an armchair ribbon (dashed line) and for a ribbon with a boundary of the same orientation but with a larger period (solid line). The curves are calculated numerically from the tight-binding equations.

2.7   Conclusion

In summary, we have demonstrated that the zigzag-type boundary condition $\Psi = \pm\tau_z \otimes \sigma_z \Psi$ applies generically to a terminated honeycomb lattice. The boundary condition switches from the plus-sign to the minus-sign at the angles $\varphi = 0 \pmod{\pi/3}$, when the boundary is parallel to $1/3$ of all the carbon-carbon bonds (see Fig. 2.10).

The distance δ from the edge within which the boundary condition breaks down is minimal ($= 0$) at the zigzag orientation $\varphi = \pi/6 \pmod{\pi/3}$ and maximal at the armchair orientation. This length scale governs the band gap $\Delta \approx (\hbar v / W) \exp(-W/\delta)$ in a nanoribbon of width W. We have tested our analytical results for Δ with the numerical solution of the tight-binding equations and find good agreement.

While the lattice termination by itself can only produce zigzag or armchair-type boundary conditions, other types of boundary conditions can be reached by breaking the electron-hole symmetry of the tight-binding equations. We have considered the effect

of a staggered potential at a zigzag boundary (produced for example by edge magnetization [18]), and have calculated the corresponding boundary condition. It interpolates smoothly between the zigzag and infinite-mass boundary conditions, opening up a gap in the spectrum that depends on the strength and range of the staggered potential.

We have calculated the dispersion relation for arbitrary boundary conditions and found that the edge states which are dispersionless at a zigzag edge acquire a dispersion for more general boundary conditions. Such propagating edge states exist, for example, near a zigzag edge with staggered potential.

Our discovery that the zigzag boundary condition is generic explains the findings of several computer simulations [26, 28, 29] in which behavior characteristic of a zigzag edge was observed at non-zigzag orientations. It also implies that the mechanism of gap opening at a zigzag edge of Ref. [18] (production of a staggered potential by magnetization) applies generically to any $\varphi \neq 0$. This may explain why the band gap measurements of Ref. [25] produced results that did not depend on the crystallographic orientation of the nanoribbon.
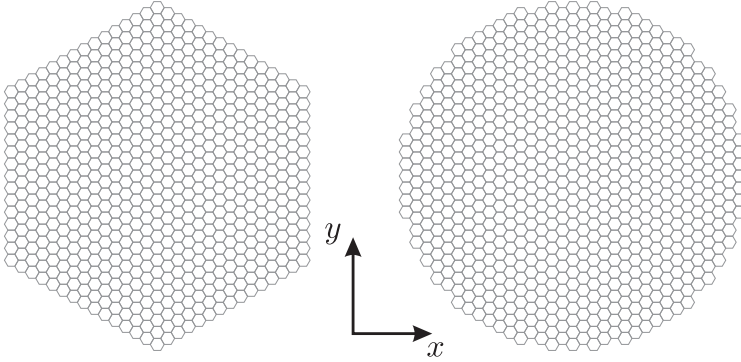
Figure 2.10: These two graphene flakes (or quantum dots) both have the same zigzag-type boundary condition: $\Psi = \pm \tau_z \otimes \sigma_z \Psi$. The sign switches between $+$ and $-$ when the tangent to the boundary has an angle with the x-axis which is a multiple of $60°$.

2.A Derivation of the general boundary condition

We first show that the anticommutation relation (2.7) follows from the current conservation requirement (2.6). The current operator in the basis of eigenvectors of M has the block form

$$\boldsymbol{n}_B \cdot \boldsymbol{J} = \begin{pmatrix} X & Y \\ Y^\dagger & Z \end{pmatrix}, \quad M = \begin{pmatrix} 1 & 0 \\ 0 & -1 \end{pmatrix}. \tag{2.38}$$

The Hermitian subblock X acts in the two-dimensional subspace of eigenvectors of M with eigenvalue 1. To ensure that $\langle \Psi | \boldsymbol{n}_B \cdot \boldsymbol{J} | \Psi \rangle = 0$ for any Ψ in this subspace it

is necessary and sufficient that $X = 0$. The identity $(\mathbf{n}_B \cdot \mathbf{J})^2 = 1$ is equivalent to $YY^\dagger = 1$ and $Z = 0$, hence $\{M, \mathbf{n}_B \cdot \mathbf{J}\} = 0$.

We now show that the most general 4×4 matrix M that satisfies Eqs. (2.5) and (2.7) has the 4-parameter form (2.8). Using only the Hermiticity of M, we have the 16-parameter representation

$$M = \sum_{i,j=0}^{3} (\tau_i \otimes \sigma_j) c_{ij}, \tag{2.39}$$

with real coefficients c_{ij}. Anticommutation with the current operator brings this down to the 8-parameter form

$$M = \sum_{i=0}^{3} \tau_i \otimes (\mathbf{n}_i \cdot \boldsymbol{\sigma}), \tag{2.40}$$

where the $\mathbf{n}_i$'s are three-dimensional vectors orthogonal to n_B. The absence of off-diagonal terms in M^2 requires that the vectors $\mathbf{n}_1$, $\mathbf{n}_2$, $\mathbf{n}_3$ are multiples of a unit vector $\tilde{\mathbf{n}}$ which is orthogonal to $\mathbf{n}_0$. The matrix M may now be rewritten as

$$M = \tau_0 \otimes (\mathbf{n}_0 \cdot \boldsymbol{\sigma}) + (\tilde{\mathbf{\nu}} \cdot \boldsymbol{\tau}) \otimes (\tilde{\mathbf{n}} \cdot \boldsymbol{\sigma}). \tag{2.41}$$

The equality $M^2 = 1$ further demands $n_0^2 + \tilde{\nu}^2 = 1$, leading to the 4-parameter representation (2.8) after redefinition of the vectors.

2.B   Derivation of the boundary modes

We derive the characteristic equation (2.17) from the tight-binding equation (2.11) and the definitions of the boundary modes (2.14) and (2.15). In the low energy limit $\varepsilon/t \ll a/|\mathbf{T}|$ we may set $\varepsilon \to 0$ in Eq. (2.11), so it splits into two decoupled sets of equations for the wave function on sublattices A and B:

$$\psi_B(\mathbf{r}) + \psi_B(\mathbf{r} - \mathbf{R}_1) + \psi_B(\mathbf{r} - \mathbf{R}_2) = 0, \tag{2.42a}$$

$$\psi_A(\mathbf{r}) + \psi_A(\mathbf{r} + \mathbf{R}_1) + \psi_A(\mathbf{r} + \mathbf{R}_2) = 0. \tag{2.42b}$$

Substituting $\mathbf{R}_1$ by $\mathbf{R}_2 + \mathbf{R}_3$ in these equations and using the definition (2.15) of λ we express $\psi(\mathbf{r} + \mathbf{R}_2)$ through $\psi(\mathbf{r})$,

$$\psi_B(\mathbf{r} + \mathbf{R}_2) = -(1 + \lambda)^{-1} \psi_B(\mathbf{r}), \tag{2.43a}$$

$$\psi_A(\mathbf{r} + \mathbf{R}_2) = -(1 + \lambda) \psi_A(\mathbf{r}). \tag{2.43b}$$

Eqs. (2.15) and (2.43) together allow to find the boundary mode with a given value of λ on the whole lattice:

$$\psi_B(\mathbf{r} + p\mathbf{R}_2 + q\mathbf{R}_3) = \lambda^q (-1 - \lambda)^{-p} \psi_B(\mathbf{r}), \tag{2.44a}$$

$$\psi_A(\mathbf{r} + p\mathbf{R}_2 + q\mathbf{R}_3) = \lambda^q (-1 - \lambda)^{p} \psi_A(\mathbf{r}), \tag{2.44b}$$
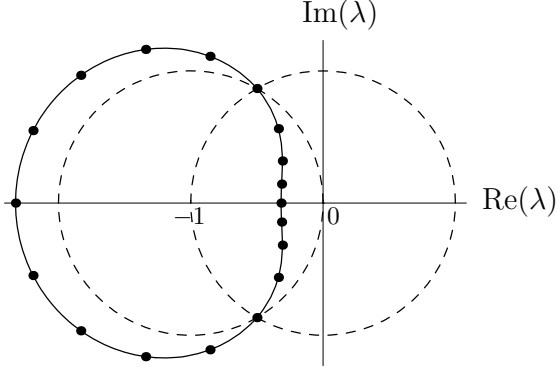
Figure 2.11: Plot of the solutions of the characteristic equations (2.45, 2.46) for $n = 5$, $m = 11$, and $k = 0$. The dots are the roots, the solid curve is the contour described by Eq. (2.45), and the dashed circles are unit circles with centers at 0 and -1.

with p and q arbitrary integers. Substituting $\psi(\boldsymbol{r} + \boldsymbol{T})$ into Eq. (2.14) from Eq. (2.44) and using $\boldsymbol{T} = (n + m)\boldsymbol{R}_2 + n\boldsymbol{R}_3$ we arrive at the characteristic equation (2.17).

We now find the roots of the Eq. (2.17) for a given k. It is sufficient to analyze the equation for sublattice A only since the calculation for sublattice B is the same after interchanging n and m. The analysis of Eq. (2.17a) simplifies in polar coordinates,

$$|1 + \lambda|^{m+n} = |\lambda|^n \tag{2.45}$$

$$(m + n)\arg(-1 - \lambda) - k - n\arg(\lambda) = 2\pi l, \tag{2.46}$$

with $l = 0, \pm 1, \pm 2 \dots$. The curve defined by Eq. (2.45) is a contour on the complex plane around the point $\lambda = -1$ which crosses points $\lambda_{\pm} = -1/2 \pm i\sqrt{3}/2$ (see Fig. 2.11). The left-hand side of Eq. (2.46) is a monotonic function of the position on this contour. If it increases by $2\pi\Delta l$ on the interval between two roots of the equation, then there are $\Delta l - 1$ roots inside this interval. For $k = 0$ both λ_- and λ_+ are roots of the characteristic equation. So in this case the number N_A of roots lying inside the unit circle can be calculated from the increment of the left-hand side of Eq. (2.46) between λ_- and $\lambda+$:

$$N_A = \frac{1}{2\pi}\left[(n + m)\frac{2\pi}{3} + n\frac{2\pi}{3}\right] - 1 = n - \frac{n - m}{3} - 1. \tag{2.47}$$

Similarly, on sublattice B, we have (upon interchanging n and m),

$$N_B = m - \frac{m - n}{3} - 1. \tag{2.48}$$

The same method can be applied to calculate λ_n. Since there are $n - 1$ roots on the contour defined by Eq. (2.45) between λ_n and λ_n^*, the increment of the left-hand side of Eq. (2.46) between λ_n^* and λ_n must be equal to $2\pi(n - 1) \approx 2\pi n$ (for $|\boldsymbol{T}| \gg a$), which immediately leads to Eq. (2.24) for λ_n.

Chapter 3

Detection of valley polarization in graphene by a superconducting contact

3.1 Introduction

The quantized Hall conductance in graphene exhibits the half-integer quantization $G_H = (n + \frac{1}{2})(4e^2/h)$ characteristic of massless Dirac fermions [30, 31]. The lowest plateau at $2e^2/h$ extends to zero carrier density because there is no gap between conduction and valence bands, and it has only a twofold spin degeneracy because it lacks the valley degeneracy of the higher plateaus. The valley degeneracy of the lowest Landau level is removed at the edge of the carbon monolayer, where the current-carrying states at the Fermi level are located. Depending on the crystallographic orientation of the edge, the edge states may lie fully within a single valley, or they may be a linear combination of states from both valleys [32, 33]. The type of valley polarization remains hidden in the Hall conductance, which is insensitive to edge properties.

Here we propose a method to detect the valley polarization of quantum Hall edge states, using a superconducting contact as a probe. In the past, experimental [34–37] and theoretical [38–42] studies of the quantum Hall effect with superconducting contacts have been carried out in the context of semiconductor two-dimensional electron gases. The valley degree of freedom has not appeared in that context. In graphene, the existence of two valleys related by time-reversal symmetry plays a key role in the process of Andreev reflection at the normal-superconducting (NS) interface [43]. A nonzero subgap current through the NS interface requires the conversion of an electron approaching in one valley into a hole leaving in the other valley. This is suppressed if the edge states at the Fermi level lie exclusively in a single valley, creating a sensitivity of the conductance of the NS interface to the valley polarization.

Allowing for a general type of valley polarization, we calculate that the two-terminal conductance G_{NS} (measured between the superconductor and a normal-metal contact) is given by

$$G_{NS} = \frac{2e^2}{h}(1 - \cos\Theta), \tag{3.1}$$
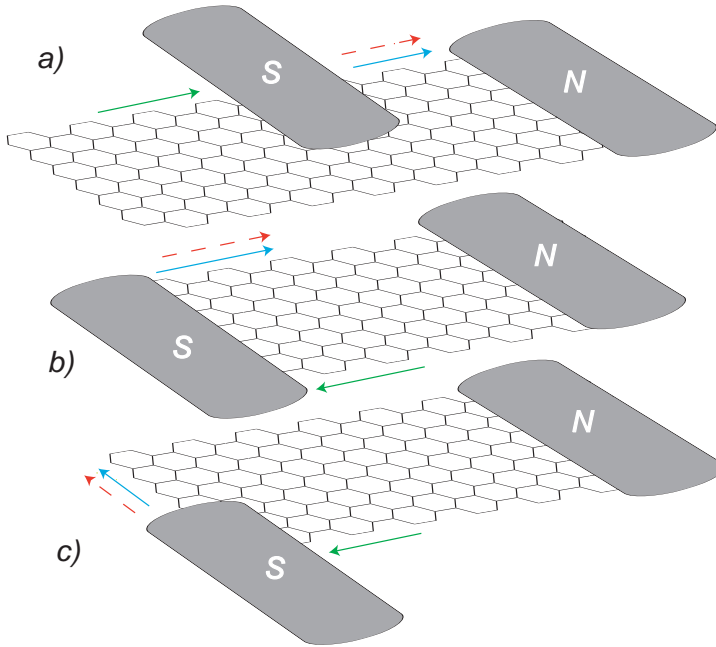
Figure 3.1: Three diagrams of a graphene sheet contacted by one normal-metal (N) and one superconducting (S) electrode. Edge states approaching and leaving the superconductor are indicated by arrows. The solid line represents an electron state (green: isospin ν_1; blue: isospin ν_2), and the dashed line represents a hole state (red: isospin $-\nu_2$).

when the Hall conductance $G_H = 2e^2/h$ is on the lowest plateau. [1] Here $\cos \Theta = \nu_1 \cdot \nu_2$ is the cosine of the angle between the valley isospins ν_1, ν_2 of the states along the two graphene edges connected by the superconductor (see Fig. 3.1). If the superconductor covers a single edge (Fig. 3.1a), then $\Theta = 0 \Rightarrow G_{NS} = 0$ — no current can enter into the superconductor without intervalley relaxation. If the superconductor connects different edges (Figs. 3.1b,c) then G_{NS} can vary from 0 to $4e^2/h$ — depending on the relative orientation of the valley isospins along the two edges.

---

[1]The edge channels responsible for Eq. (3.1) were not considered in an earlier study of G_{NS} in a magnetic field by Ref. [44].

3.2 Dispersion of the edge states

We start our analysis from the Dirac-Bogoliubov-De Gennes (DBdG) equation [43]

$$\begin{pmatrix} H - \mu & \Delta \\ \Delta^* & \mu - THT^{-1} \end{pmatrix} \Psi = \varepsilon \Psi, \tag{3.2}$$

with H the Dirac Hamiltonian, Δ the superconducting pair potential, and T the time reversal operator. The excitation energy ε is measured relative to the Fermi energy μ. Each of the four blocks in Eq. (3.2) represents a 4×4 matrix, acting on 2 sublattice and 2 valley degrees of freedom. The wave function $\Psi = (\Psi_e, \Psi_h)$ contains a pair of 4-dimensional vectors Ψ_e and Ψ_h that represent, respectively, electron and hole excitations.

The pair potential Δ is isotropic in both the sublattice and valley degrees of freedom. It is convenient to choose a "valley isotropic" basis such that the Hamiltonian H is isotropic in the valley degree of freedom, [2]

$$\begin{aligned} H &= v \begin{pmatrix} (\boldsymbol{p} + e\boldsymbol{A}) \cdot \boldsymbol{\sigma} & 0 \\ 0 & (\boldsymbol{p} + e\boldsymbol{A}) \cdot \boldsymbol{\sigma} \end{pmatrix} \\ &= v\tau_0 \otimes (\boldsymbol{p} + e\boldsymbol{A}) \cdot \boldsymbol{\sigma}, \end{aligned} \tag{3.3}$$

with v the Fermi velocity, $\boldsymbol{p} = (\hbar/i)(\partial/\partial x, \partial/\partial y)$ the canonical momentum operator in the x-y plane of the graphene layer and $\boldsymbol{A}$ the vector potential corresponding to a perpendicular magnetic field B. The Pauli matrices σ_i and τ_i act on the sublattice and valley degree of freedom, respectively (with σ_0 and τ_0 representing the 2×2 unit matrix). The time reversal operator in the valley isotropic basis reads

$$T = \begin{pmatrix} 0 & i\sigma_y \\ -i\sigma_y & 0 \end{pmatrix} C = -(\tau_y \otimes \sigma_y)C, \tag{3.4}$$

with C the operator of complex conjugation. For later use we note that the particle current operator $\boldsymbol{J} = (\boldsymbol{J}_e, \boldsymbol{J}_h)$ has electron and hole components

$$\boldsymbol{J} = v(\tau_0 \otimes \boldsymbol{\sigma}, -\tau_0 \otimes \boldsymbol{\sigma}). \tag{3.5}$$

Substitution of Eqs. (3.3) and (3.4) into Eq. (3.2) gives the DBdG equation in the valley isotropic form

$$\begin{pmatrix} H_+ - \mu & \Delta \\ \Delta^* & \mu - H_- \end{pmatrix} \Psi = \varepsilon \Psi, \tag{3.6}$$

$$H_\pm = v\tau_0 \otimes (\boldsymbol{p} \pm e\boldsymbol{A}) \cdot \boldsymbol{\sigma}. \tag{3.7}$$

We seek a solution in the normal region (where $\Delta \equiv 0$), at energies below the excitation gap Δ_0 in the superconductor. Electron and hole excitations cannot propagate into the

---

[2]The operators (3.3) and (3.4) in the valley isotropic basis are related to their counterparts in Ref. [43] by the unitary transformation $H \to UHU^\dagger$, $T \to UTU^\dagger$, with $U = \frac{1}{2}(\tau_0 + \tau_z) \otimes \sigma_0 + \frac{1}{2}(\tau_0 - \tau_z) \otimes \sigma_x$. Since Δ is a scalar, it remains unchanged by this transformation.

superconductor at subgap energies, and the magnetic field confines them in the normal region to within a magnetic length $l_m = \sqrt{\hbar/eB}$ of the edge. We consider separately the edge states along the insulating edge of the graphene layer and along the interface with the superconductor.

The edges are assumed to be smooth on the scale of l_m ($\approx 25\,\text{nm}$ at $B = 1\,\text{T}$), so that they may be treated locally as a straight line with a homogeneous boundary condition. The magnetic field should be less than the critical field of the superconductor. (Ref. [37] used Nb, with a critical field of 2.6 T, to maintain superconductivity in the quantum Hall effect regime.)

The edge states at the insulating and superconducting boundaries are different because of the different boundary conditions. Using only the condition of particle current conservation, these have the general form [19]

$$\Psi = M\Psi, \tag{3.8}$$

with M a unitary and Hermitian matrix that anticommutes with the particle current operator:

$$M = M^\dagger, \quad M^2 = 1, \quad M(\boldsymbol{n} \cdot \boldsymbol{J}) + (\boldsymbol{n} \cdot \boldsymbol{J})M = 0. \tag{3.9}$$

The unit vector $\boldsymbol{n}$ lies in the x-y plane, perpendicular to the boundary and pointing outward.

At the NS interface the matrix M is given by [45]

$$M = \begin{pmatrix} 0 & M_{\text{NS}} \\ M_{\text{NS}}^\dagger & 0 \end{pmatrix}, \quad M_{\text{NS}} = \tau_0 \otimes e^{i\phi + i\beta \boldsymbol{n} \cdot \boldsymbol{\sigma}}, \tag{3.10}$$

with $\beta = \arccos(\varepsilon/\Delta_0) \in (0, \pi)$ determined by the order parameter $\Delta = \Delta_0 e^{i\phi}$ in the superconductor.

The insulating (I) edge does not mix electrons and holes, so M is block-diagonal with electron block M_I and hole block $TM_\text{I}T^{-1}$. The boundary condition is determined by confinement on the scale of the lattice constant $a \ll l_m$, so it should preserve time-reversal symmetry. This implies that M_I should commute with T. The most general matrix that also satisfies Eq. (3.9) is given by [3]

$$M = \begin{pmatrix} M_\text{I} & 0 \\ 0 & M_\text{I} \end{pmatrix}, \quad M_\text{I} = (\boldsymbol{v} \cdot \boldsymbol{\tau}) \otimes (\boldsymbol{n}_\perp \cdot \boldsymbol{\sigma}), \tag{3.11}$$

parameterized by a pair of three-dimensional unit vectors $\boldsymbol{v}$ and $\boldsymbol{n}_\perp$. The vector $\boldsymbol{n}_\perp$ should be orthogonal to $\boldsymbol{n}$ but $\boldsymbol{v}$ is not so constrained. Three common types of confinement are the zigzag edge, with $\boldsymbol{v} = \pm\hat{\boldsymbol{z}}$, $\boldsymbol{n}_\perp = \hat{\boldsymbol{z}}$; the armchair edge, with $\boldsymbol{v} \cdot \hat{\boldsymbol{z}} = 0$, $\boldsymbol{n}_\perp \cdot \hat{\boldsymbol{z}} = 0$; and infinite mass confinement, with $\boldsymbol{v} = \hat{\boldsymbol{z}}$, $\boldsymbol{n}_\perp \cdot \hat{\boldsymbol{z}} = 0$.

To determine the edge states we consider a local coordinate system such that the boundary is along the y-axis (so $\boldsymbol{n} = -\hat{\boldsymbol{x}}$), and we choose a local gauge such that

---

[3]Without the restriction to time-reversal symmetry the most general form of M_I is $M_\text{I} = \tau_0 \otimes ((\boldsymbol{n}_\perp \times \boldsymbol{n}) \cdot \boldsymbol{\sigma}) \cos\alpha + (\boldsymbol{v} \cdot \boldsymbol{\tau}) \otimes (\boldsymbol{n}_\perp \cdot \boldsymbol{\sigma}) \sin\alpha$. This four-parameter family of boundary conditions is more general than the three-parameter family of Ref. [19].
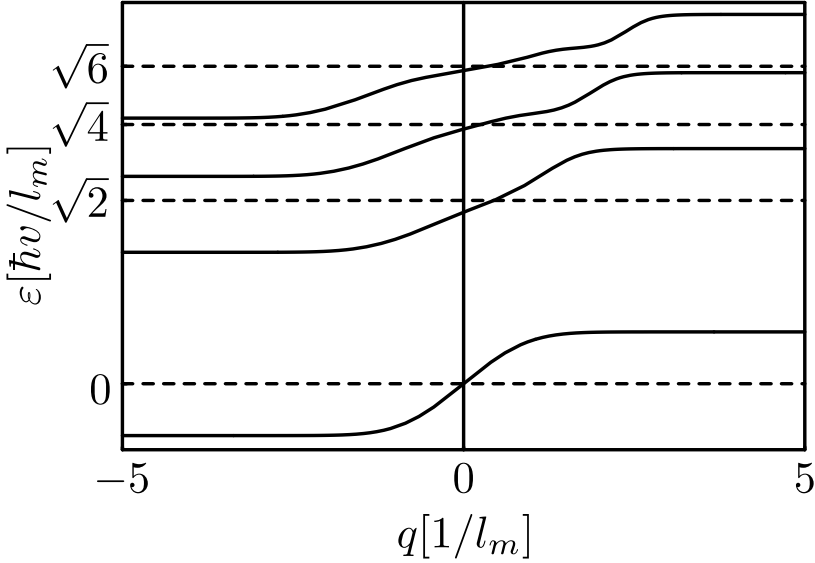
Figure 3.2:   Dispersion relation of edge states in graphene along the normal-superconducting interface, calculated from Eq. (3.15) for $|\varepsilon| \ll \Delta_0$. The dotted lines are for $\mu = 0$, the solid lines for $\mu = 0.4\,\hbar v / l_m$.

$\boldsymbol{A} = Bx\hat{\boldsymbol{y}}$. The wave number q along the boundary is then a good quantum number. In order to simplify the notation we measure energies in units of $\hbar v / l_m$ and lengths in units of l_m. (Units will be reinstated in the final results.) Eigenstates of Eq. (3.6) that decay for $x \to \infty$ have the form

$$\Psi(x, y) = e^{iqy} \begin{pmatrix} C_e \otimes \Phi_e(x + q) \\ C_h \otimes \Phi_h(x - q) \end{pmatrix}, \tag{3.12}$$

$$\Phi_e(\xi) = e^{-\frac{1}{2}\xi^2} \begin{pmatrix} -i(\mu + \varepsilon)H_{(\mu+\varepsilon)^2/2-1}(\xi) \\ H_{(\mu+\varepsilon)^2/2}(\xi) \end{pmatrix}, \tag{3.13}$$

$$\Phi_h(\xi) = e^{-\frac{1}{2}\xi^2} \begin{pmatrix} H_{(\mu-\varepsilon)^2/2}(\xi) \\ -i(\mu - \varepsilon)H_{(\mu-\varepsilon)^2/2-1}(\xi) \end{pmatrix}, \tag{3.14}$$

in the region $x > 0$ (where $\Delta \equiv 0$). The function $H_\alpha(x)$ is the Hermite function. The two-component spinors C_e and C_h determine the valley isospin of the electron and hole components, respectively.

The dispersion relation between energy ε and momentum q follows by substitution of the state (3.12) into the boundary condition (3.8). At the NS interface we take Eq.
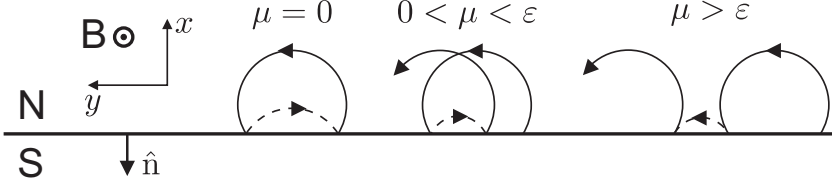
Figure 3.3: Cyclotron orbits of Andreev reflected electrons and holes.

(3.10) for the boundary condition and obtain

$$f_{\mu+\varepsilon}(q) - f_{\mu-\varepsilon}(-q) = \frac{\varepsilon[f_{\mu+\varepsilon}(q)f_{\mu-\varepsilon}(-q) + 1]}{\sqrt{\Delta_0^2 - \varepsilon^2}},$$

$$f_\alpha(q) = \frac{H_{\alpha^2/2}(q)}{\alpha H_{\alpha^2/2-1}(q)}. \tag{3.15}$$

The solutions $\varepsilon_n(q)$, numbered by a mode index $n = 0, \pm 1, \pm 2, \ldots$, are plotted in Fig. 3.2. Notice that the dispersion relation has the inversion symmetry $\varepsilon(q) = -\varepsilon(-q)$. Each mode has a twofold valley degeneracy, because the boundary condition (3.10) is isotropic in the valley isospin $\boldsymbol{v}$. The two degenerate eigenstates (labeled $\pm$) have $C_e^\pm = c_e|\pm\boldsymbol{v}\rangle$, $C_h^\pm = c_h|\pm\boldsymbol{v}\rangle$, with $|\pm\boldsymbol{v}\rangle$ eigenstates of $\boldsymbol{v}\cdot\boldsymbol{\tau}$. [4]

The expectation value $v_n = \hbar^{-1}d\varepsilon_n/dq$ of the velocity along the boundary in the n-th mode is determined by the derivative of the dispersion relation. We see from Fig. 3.2 that the edge states all propagate in the same direction, dictated by the sign of B and μ. The velocity vanishes for $|q| \to \infty$, as the NS edge states evolve into the usual dispersionless Landau levels deep in the normal region. For $q \to -\infty$ the Landau levels contain electron excitations at energy $\varepsilon_n = \sqrt{2}(\hbar v/l_m)\,\mathrm{sign}\,(n)\sqrt{|n|} - \mu$, while for $q \to \infty$ they contain hole excitations with $\varepsilon_n = \sqrt{2}(\hbar v/l_m)\,\mathrm{sign}\,(n)\sqrt{|n|} + \mu$. For $\mu = 0$ the NS edge states have zero velocity at any q for $|\varepsilon| \ll \Delta_0$. As illustrated in Fig. 3.3, the localization of the edge states as $\mu \to 0$ happens because for $|\varepsilon| > |\mu|$ the electron and hole excitations move in opposite directions along the boundary, while for $|\varepsilon| < |\mu|$ they move in the same direction.

Turning now to the insulating edge, we take the boundary condition (3.11). For an edge along the y-axis we have $\boldsymbol{n}_\perp = (0, \sin\theta, \cos\theta)$. The valley degeneracy is broken in general, with different dispersion relations for the two eigenstates $|\pm\boldsymbol{v}\rangle$ of $\boldsymbol{v}\cdot\boldsymbol{\tau}$. The dispersion relations for electrons and holes are related by $\varepsilon_h^\pm(q) = -\varepsilon_e^\mp(-q)$. For sufficiently small μ there is one electron and one hole state at the Fermi level, of opposite isospins. (Note that electrons and holes from the *same* valley have *opposite* isospins.) We fix the sign of $\boldsymbol{v}$ such that $|+\boldsymbol{v}\rangle$ is the electron eigenstate and $|-\boldsymbol{v}\rangle$ the hole eigenstate. We find that $\varepsilon_e^+(q)$ is determined by the equation

$$f_{\mu+\varepsilon}(q) = \tan(\theta/2), \tag{3.16}$$

---

[4]The coefficients $c_{e,h}$ are given by $c_e/c_h = (\mu - \varepsilon)H_{(\mu-\varepsilon)^2/2-1}(-q)/(iH_{(\mu+\varepsilon)^2/2}(q)\cos\beta + i(\mu+\varepsilon)H_{(\varepsilon+\mu)^2/2-1}(q)\sin\beta)$.
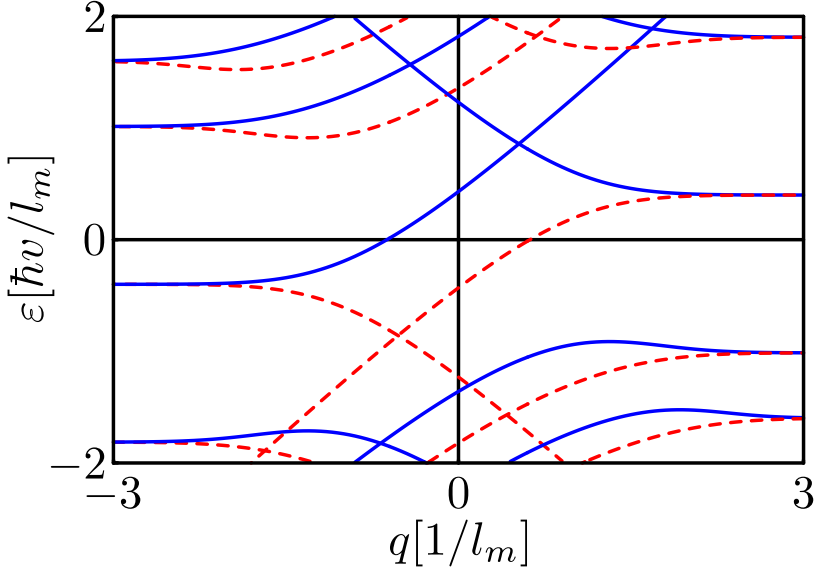
Figure 3.4: Dispersion relation of states along the insulating edge, calculated from Eqs. (3.16) and (3.17) for $\mu = 0.4\,\hbar v/l_m$ and $\theta = \pi/2$. The solid lines are the electron states (blue ε_e^+, red ε_e^-), the dashed lines are the hole states (blue ε_h^+, red ε_h^-).

while $\varepsilon_e^-(q)$ is determined by

$$f_{\mu+\varepsilon}(q) = -\cotan(\theta/2). \tag{3.17}$$

The dispersion relations plotted in Fig. 3.4 are for the case $\theta = \pi/2$ of an armchair edge. The case $\theta = 0$ of a zigzag edge contains additional dispersionless states away from the Fermi level [32], but these play no role in the electrical conduction.

To determine the conductance G_{NS} we need to calculate the transmission matrix t of the edge states at the Fermi level. Edge states approach the superconductor along the insulating edge I_1 (with parameters ν_1, θ_1), then propagate along the NS interface, and finally return along the insulating edge I_2 (with parameters ν_2, θ_2). At sufficiently small μ each insulating edge I_p supports only two propagating modes, one electron mode $\propto |+\nu_p\rangle$ and one hole mode $\propto |-\nu_p\rangle$. The NS interface also supports two propagating modes at small μ, of mixed electron-hole character and valley degenerate. The conductance is given by [46]

$$G_{\mathrm{NS}} = \frac{2e^2}{h}(1 - T_{ee} + T_{he}) = \frac{4e^2}{h}T_{he}, \tag{3.18}$$

with $T_{ee} = |t_{++}|^2$ the probability that an electron incident along I_1 returns along I_2 as an electron and $T_{he} = |t_{-+}|^2$ the probability that the electron returns as a hole. Because

electrons and holes cannot enter into the superconductor, these two probabilities must add up to unity — hence the second equality in Eq. (3.18). (The factor of two accounts for the spin degeneracy.)

3.3   Calculation of the conductance

Since the unidirectional motion of the edge states prevents reflections, the transmission matrix t from I_1 to I_2 is the product of the transmission matrices t_1 from I_1 to NS and t_2 from NS to I_2. Each of the matrices t_p is a 2×2 unitary matrix, diagonal in the basis $|\pm \nu_p\rangle$:

$$t_p = e^{i\phi_p}|+\nu_p\rangle\langle+\nu_p| + e^{i\phi'_p}|-\nu_p\rangle\langle-\nu_p|. \tag{3.19}$$

The phase shifts ϕ_p, ϕ'_p need not be determined. Using $|\langle\nu_1|\pm\nu_2\rangle|^2 = \frac{1}{2}(1 \pm \nu_1 \cdot \nu_2)$, we obtain from $t = t_2 t_1$ the required transmission probabilities

$$T_{he} = 1 - T_{ee} = \tfrac{1}{2}(1 - \nu_1 \cdot \nu_2). \tag{3.20}$$

Substitution into Eq. (3.18) gives our central result (3.1).

Referring to Fig. 3.1, we see that $G_{NS} = 0$ in the case (a) of a superconducting contact to a single edge ($\nu_1 = \nu_2$) — regardless of whether the edge is zigzag or armchair. In the case (c) of a contact between a zigzag and an armchair edge we have $\nu_1 \cdot \nu_2 = 0 \Rightarrow G_{NS} = 2e^2/h$. The case (b) of a contact between two opposite edges has $\nu_1 = -\nu_2 \Rightarrow G_{NS} = 4e^2/h$ if both edges are zigzag; the same holds if both edges are armchair separated by a multiple of three hexagons (as in the figure); if the number of hexagons separating the two armchair edges is not a multiple of three, then $\nu_1 \cdot \nu_2 = 1/2 \Rightarrow G_{NS} = e^2/h$.

Intervalley relaxation at a rate Γ tends to equalize the populations of the two degenerate modes propagating along the NS interface. This becomes appreciable if $\Gamma L/v_0 \gtrsim 1$, with L the length of the NS interface and $v_0 = \hbar^{-1}d\varepsilon_0/dq \simeq \min(v/2, \sqrt{2}\,\mu l_m/\hbar)$ the velocity along the interface. The density matrix $\rho = \rho_0(1 - e^{-\Gamma L/v_0}) + \rho_1 e^{-\Gamma L/v_0}$ then contains a valley isotropic part $\rho_0 \propto \tau_0$ with $T_{ee} = T_{eh} = 1/2$ and a nonequilibrium part $\rho_0 \propto |\nu_1\rangle\langle\nu_1|$ with T_{ee}, T_{eh} given by Eq. (3.20). The conductance then takes the form

$$G_{NS} = \frac{2e^2}{h}\left(1 - e^{-\Gamma L/v_0}\cos\Theta\right). \tag{3.21}$$

A nonzero conductance when the supercurrent covers a single edge ($\Theta = 0$) is thus a direct measure of the intervalley relaxation.

3.4   Conclusion

In conclusion, we have shown that the valley structure of quantum Hall edge states in graphene, which remains hidden in the Hall conductance, can be extracted from the current that flows through a superconducting contact. Since such contacts have now been

fabricated succesfully [47, 48], we expect that this method to detect valley polarization can be tested in the near future.

Chapter 4

Theory of the valley-valve effect in graphene nanoribbons

4.1 Introduction

The massless conduction electrons in a two-dimensional carbon lattice respond differently to an electric field than ordinary massive electrons do. Because the magnitude v of the velocity of a massless particle is independent of its energy, a massless electron moving along the field lines cannot be backscattered — since that would require $v = 0$ at the turning point. The absence of backscattering was discovered in carbon nanotubes [49], where it is responsible for the high conductivity in the presence of disorder.

A graphene nanoribbon is essentially a carbon nanotube that is cut open along the axis and flattened. One distinguishes armchair and zigzag nanotubes, depending on whether the cut runs parallel or perpendicular to the carbon-carbon bonds. The edges of the nanoribbon fundamentally modify the ability of an electric field to backscatter electrons. As discovered in computer simulations by Wakabayashi and Aoki [50], a potential step in a zigzag nanoribbon blocks the current when it crosses the Fermi level, forming a *p-n* junction (= a junction of states in conduction and valence band). The current blocking was interpreted in Ref. [51] by analogy with the spin-valve effect in ferromagnetic junctions [52]. In this analogy the valley polarization in a zigzag nanoribbon plays the role of the spin polarization in a ferromagnet — hence the name "valley-valve" effect.

It is the purpose of this chapter to present a theory for this unusual phenomenon. A theory is urgently needed, because the analogy between spin valve and valley valve fails dramatically to explain the computer simulations of Fig. 4.1: The current blocking by the *p-n* junction turns out to depend on the parity of the number N of atom rows in the ribbon. The current is blocked when N is even (zigzag configuration), while it is not blocked when N is odd (anti-zigzag configuration, see Fig. 4.2). This even-odd difference (first noticed in connection with the quantum Hall effect [53]) is puzzling since zigzag and anti-zigzag nanoribbons are indistinguishable at the level of the Dirac
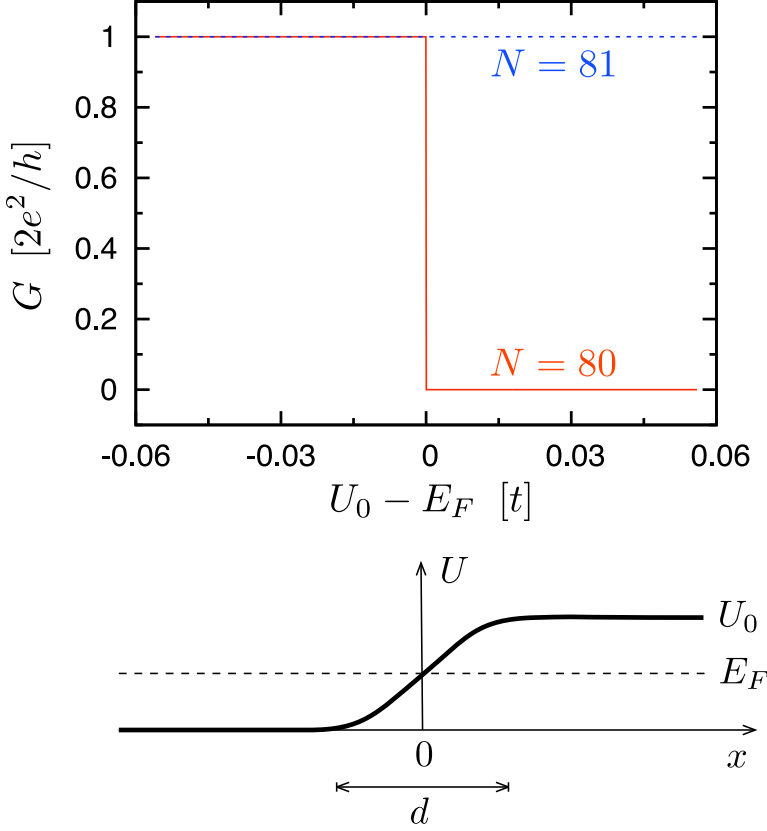
Figure 4.1: Conductance G of a zigzag nanoribbon containing a potential step $U = \frac{1}{2}U_0[1 + \tanh(2x/d)]$. The red and blue curves are obtained by computer simulation of the tight-binding model of graphene, with parameters $d = 10\,a$, $E_F = 0.056\,t$, where a is the lattice constant and t is the nearest-neighbor hopping energy. Upon varying U_0 the conductance switches abruptly to zero when the Fermi level E_F is crossed and a *p-n* junction is formed (red solid curve; the deviation from an ideally quantized step function is $\lesssim 10^{-7}$). This "valley-valve" effect occurs only for an even number N of carbon atom rows (zigzag configuration). When N is odd (anti-zigzag configuration), the conductance remains fixed at $2e^2/h$ (blue dotted curve, again quantized within 10^{-7}).

equation[1] [21], which is the wave equation that governs the low-energy dynamics in graphene.

---

[1]The dependence of boundary conditions on the number N of atoms across the ribbon is a key distinction between zigzag and armchair edges. The boundary condition of the Dirac equation for an armchair nanoribbon depends on N (modulo 3), but there is no N-dependence for a zigzag nanoribbon.
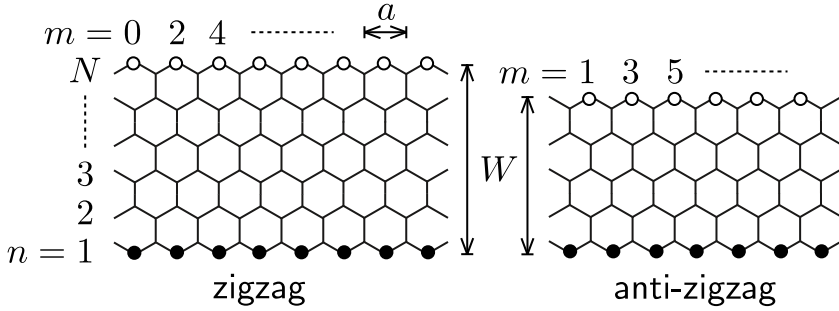
Figure 4.2: Nanoribbons in the zigzag configuration (left panel, N even) and in the anti-zigzag configuration (right panel, N odd). In both cases the atoms at opposite edges belong to different sublattices (indicated by black and white dots).

4.2   Breakdown of the Dirac equation at a potential step

The applicability of the Dirac equation rests on the assumption that a smooth potential step causes no intervalley scattering. As we now show, it is this assumption which fails in the *p-n* junction, breaking the analogy between spin valve and valley valve. In the spin valve, a spin-up electron incident on a ferromagnetic junction which only transmits spin-down is simply reflected as spin-up. The current blocking can therefore be understood without invoking spin-flip scattering. In the valley valve, however, an electron in valley K incident on a *p-n* junction which only transmits valley K' cannot be reflected in valley K. Both transmission and reflection require a switch of the valley from K to K' (see Fig. 4.3). We conclude that *a p-n junction in a zigzag nanoribbon is an intrinsic source of intervalley scattering*. It does not matter how smooth the potential step might be, since the incoming and outgoing states are from different valleys, the scattering must switch valleys to preserve the current.

   As we have illustrated in Fig. 4.3, the source of intervalley scattering is a pair of localized edge states at the *p-n* interface. It is well-known that the lowest mode in a zigzag nanoribbon is confined near the edges [26]. The transverse extension $\xi(\varepsilon) \sim W/\ln|\varepsilon W/\hbar v|$ of an edge state depends on the kinetic energy $\varepsilon = E_F - U$. We define the *p-n* interface as the line where $E_F - U(x, y) = 0$. This line intersects the two edges at the points $\boldsymbol{r}_\pm = (x_\pm, y_\pm)$, with $y_+ = (\frac{3}{2}N - 1)a/\sqrt{3} \equiv W$ and $y_- = 0$ the y-coordinates of the row of atoms at the upper and lower edge, respectively. (Note that $\boldsymbol{r}_\pm$ is well-defined also for a smooth interface.) Upon approaching the *p-n* interface, ε decreases from E_F to 0 hence ξ decreases from $\xi(E_F) \equiv \xi_0$ to a minimal value of order of the lattice constant a. An electron incident on the *p-n* junction in valley K is therefore attracted to a pair of localized edge states centered at $\boldsymbol{r}_\pm$. Their wave vector k spans the interval of order $1/a$ between the valleys K and K' — thereby allowing for the intervalley scattering needed to repel the electron into valley K'.
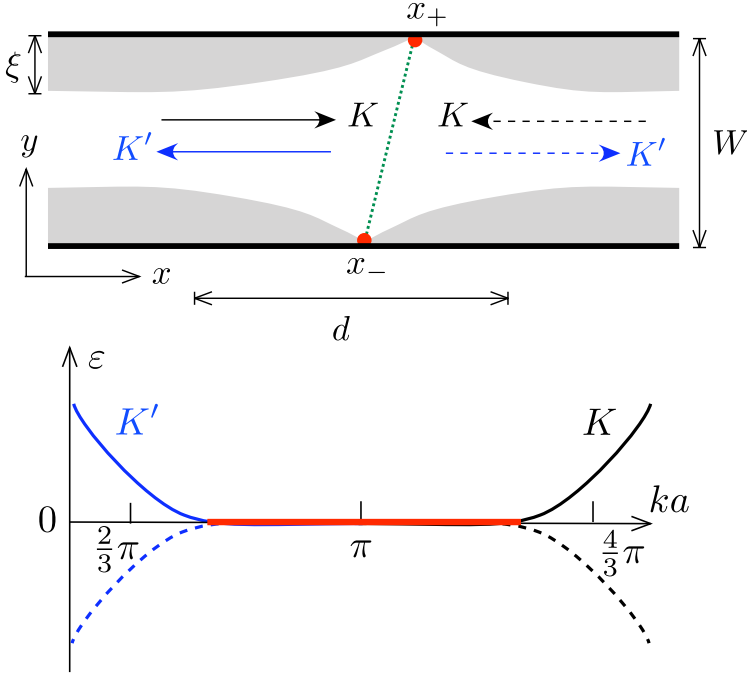
Figure 4.3: Top panel: Zigzag nanoribbon containing a *p-n* interface from x_- to x_+ (dotted line). The spatial extension of edge states in the lowest mode is indicated by the grey areas. Incoming edge states are in valley K, while outgoing edge states are in valley K'. The arrows indicate the direction of propagation, in the conduction band (solid) and valence band (dashed). The corresponding dispersion relations are plotted in the lower panel. The localized (dispersionless) edge state, responsible for the intervalley scattering, is indicated in red.

4.3   Scattering theory beyond the Dirac equation

Now that we have identified the mechanism for intervalley scattering, we need to calculate the coupling of the propagating edge states to the pair of localized edge states, in order to determine whether an incident electron is transmitted or reflected at the *p-n* interface. For this purpose we have developed a scattering theory based directly on the tight-binding Hamiltonian,

$$H_0 = t \sum_{\text{neighbors}} |n, m\rangle\langle n', m'|, \tag{4.1}$$

thereby going beyond the Dirac equation. The calculation is outlined below, but we first present the result — which is remarkably simple: The transmission probability T [and hence the conductance $G = (2e^2/h)T$] is determined by the lateral displacement

$\Delta = x_+ - x_-$ of the localized states, according to

$$T = \tfrac{1}{2} - \tfrac{1}{2}\cos(N\pi + 2\pi\Delta/3a), \tag{4.2}$$

for $W \gg \Delta$. This is the central result of this chapter.

We have derived Eq. (4.2) by projecting the tight-binding Hamiltonian onto the pair of (nearly degenerate) lowest modes, and then solving a scattering problem in k-space. As illustrated in Fig. 4.3 (lower panel), incoming and outgoing states have wave vectors near $k_{\mathrm{in}} \approx 4\pi/3a$ and $k_{\mathrm{out}} \approx 2\pi/3a$, respectively. The unitary transformation of an incoming state into an outgoing state is governed by the 2×2 transfer matrix M in the linear relation

$$\Psi(k) = M(k, k')\Psi(k'). \tag{4.3}$$

Here we have introduced the two-component wave function $\Psi(k) = (\psi_k^+, \psi_k^-)$ in k-space. (For later use we also introduce the Pauli matrices σ_i acting on the $\pm$ degree of freedom of the nearly degenerate lowest modes, with σ_0 the 2×2 unit matrix.) Once we know M, the scattering matrix $S = \Omega_{\mathrm{out}}M(k_{\mathrm{out}}, k_{\mathrm{in}})\Omega_{\mathrm{in}}^\dagger$ follows by a change of basis such that $\Omega_X \Psi(k_X)$ (with X labeling "in" or "out") has the first component in the conduction band (left end of the nanoribbon) and the second component in the valence band (right end of the nanoribbon).

An analytical calculation is possible for $W \gg \xi_0$, when we can, following Ref. [26], approximate the lowest modes $\psi_k^\pm = 2^{-1/2}(\psi_k^A \pm \psi_k^B)$ by

$$\psi_k^A(m, n) = C(k)e^{imka/2}[-2\cos(ka/2)]^{n-1}\pi_{n+m+1}, \tag{4.4}$$

$$\psi_k^B(m, n) = C(k)e^{imka/2}[-2\cos(ka/2)]^{N-n}\pi_{n+m}, \tag{4.5}$$

with $C(k) = \sqrt{-1 - 2\cos ka}$ a normalization factor. We have defined $\pi_p = 1$ if p even and $\pi_p = 0$ if p odd. The integer n labels the row of atoms in the y-direction and m labels the column of atoms in the x-direction (see Fig. 4.2). This approximation is accurate in the whole range $(2\pi/3a, 4\pi/3a)$ of k, except within an interval of order $1/W$ from the end points. The wave functions ψ_k^A, ψ_k^B are edge states, extended either along the lower edge (on the A sublattice, indicated by black dots in Fig. 4.2) or along the upper edge (on the B sublattice, white dots).

The nearest-neigbor tight-binding Hamiltonian (4.1) is diagonal in the basis of the modes $\psi_k^\pm$, with matrix elements

$$\langle k, \pm|H_0|k', \pm\rangle = \pm\varepsilon(k)a^{-1}\delta(k - k'), \tag{4.6}$$

$$\varepsilon(k) = 2tC(k)^2[-2\cos(ka/2)]^N. \tag{4.7}$$

Since $\varepsilon(\pi/a - \delta k) = (-1)^N\varepsilon(\pi/a + \delta k)$, the parity of N determines whether or not $\psi_k^\pm$ switches between conduction and valence band as k crosses the point π/a. This band switch is at the origin of the parity dependence of the valley-valve effect, since it introduces a parity dependence of the matrices $\Omega_{\mathrm{in}} = \sigma_0$, $\Omega_{\mathrm{out}} = \sigma_1^N$ that transform the transfer matrix into the scattering matrix.

We model the *p-n* interface by a linear potential profile,

$$U_{nm} = U_x m/2 + U_y(n - N/2), \tag{4.8}$$

tilted by an angle $\theta = \arctan(\frac{2}{3}\sqrt{3}\,U_y/U_x)$. Upon projection onto the two-component space spanned by $\Psi(k)$, the Hamiltonian $H = H_0 + U$ becomes an integral kernel $H(k, k')$ with a 2×2 matrix structure:

$$H(k, k') = \varepsilon(k)a^{-1}\delta(k - k')\sigma_3 + iU_x a^{-2}\frac{d}{dk}\delta(k - k')\sigma_0$$
$$+ \tfrac{1}{2}Na^{-1}U_y\delta(k - k')\sigma_1. \tag{4.9}$$

The integral equation

$$a \int_{2\pi/3a}^{4\pi/3a} dk'\, H(k, k')\Psi(k') = E\Psi(k) \tag{4.10}$$

amounts to a system of two first order differential equations:

$$\left(\varepsilon(k)\sigma_3 + iU_x a^{-1}\sigma_0\frac{d}{dk} + \frac{1}{2}NU_y\sigma_1\right)\Psi(k) = E\Psi(k). \tag{4.11}$$

This system gives directly an expression for the transfer matrix,

$$M(k, k') = \exp\left[i(k' - k)aE/U_x\right] T \exp\left[i\int_{k'}^{k} dq\,\Omega(q)\right], \tag{4.12}$$

$$\Omega(q) = \frac{\varepsilon(q)a}{U_x}\sigma_3 + \frac{\Delta}{2}\sigma_1. \tag{4.13}$$

The scalar phase factor $\exp[i(k' - k)aE/U_x]$ has no effect on the transmission probability, so we will omit it in what follows. The symbol T orders the operators in the exponent with respect to the variable q (from $q = k$ at the left to $q = k'$ at the right). The scattering matrix follows from

$$S = \sigma_1^N M(k_{\text{out}}, k_{\text{in}}). \tag{4.14}$$

We may evaluate Eq. (4.12) analytically if $W \gg \Delta$, because then the integration interval can be separated into subintervals in which the contribution of one of the terms can be neglected. The calculation is described in App. 4.A. The result is

$$M(k_{\text{out}}, k_{\text{in}}) = e^{i\alpha\sigma_3}\exp[-i(\pi\Delta/3a)\sigma_1]e^{i\alpha'\sigma_3}, \tag{4.15}$$

with a phase shift $\alpha = (-1)^N\alpha'$ that need not be determined. Substitution into Eq. (4.14) yields the result (4.2) for the transmission probability $T = |S_{12}|^2$.

The regime $\Delta \gtrsim W$ can be analyzed by a numerical evaluation of the integral (4.12). The result, shown in Fig. 4.5 (solid curve), is that the conductance oscillations are damped for $\Delta \gtrsim W$.
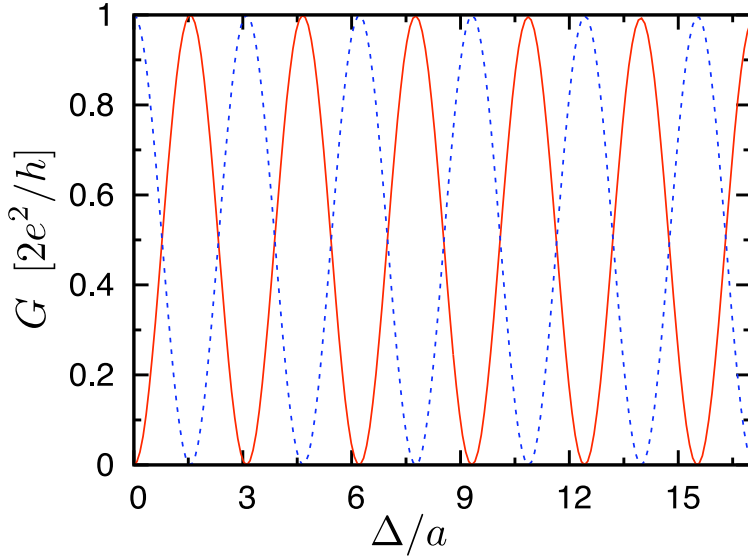
Figure 4.4:   Conductance for a tilted *p-n* interface, with potential $U = \frac{1}{2}U_0\{1 + \tanh[2(x - y\tan\theta)/d]\}$, at fixed $U_0 = 2E_F$ as a function of the relative displacement $\Delta \equiv x_+ - x_- = W\tan\theta$ of the intersection of the interface with the edges of the nanoribbon. The parameters are the same as in Fig. 4.1, which corresponds to $\Delta = 0$. The data from this computer simulation is described by the analytical result (4.2).

4.4   Comparison with computer simulations

The current blocking ($T = 0$) obtained in the computer simulations of Refs. [50, 51] is the special case N even, $\Delta = 0$, corresponding to a zigzag configuration with potential U independent of y. In the anti-zigzag configuration (N odd) we have instead $T = 1$, in accord with the simulations of Fig. 4.1. More generally, we can tilt the interface so that $\Delta \neq 0$. The simulations for a tilted *p-n* interface shown in Fig. 4.4 are well described by the analytical result (4.2), for $\Delta \ll W \simeq 70\,a$. Note in particular the sum rule $G(N) + G(N + 1) \approx e^2/h$, first observed in the computer simulations of Ref. [53].

For larger Δ/W a phase shift appears and a reduction of the amplitude of the oscillations, with $G \simeq 0$ for $\Delta \gtrsim W$. We compare the conductance calculated by numerical evaluation of the integral (4.12) with the data from the computer simulations and find good agreement, see Fig. 4.5.

4.5   Extensions of the theory

The theory presented so far can be extended in several ways.

We have assumed that the width W of the nanoribbon is sufficiently narrow that there
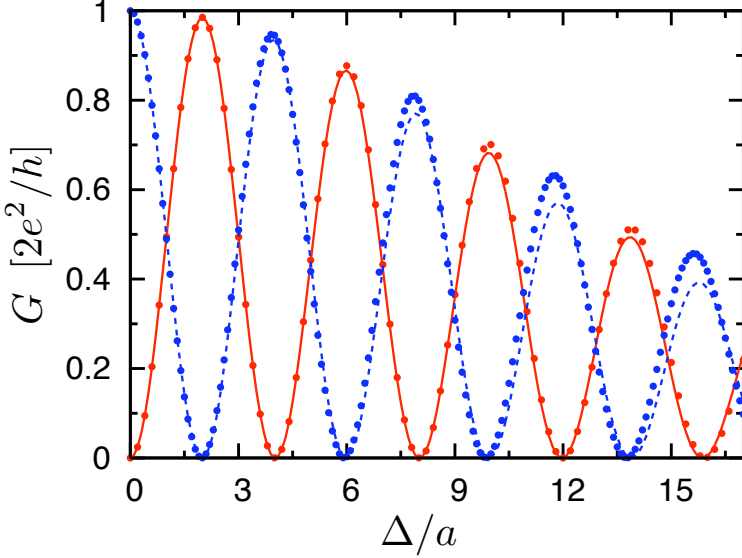
Figure 4.5: Comparison between results of computer simulations (dots) and numerical evaluation of Eq. (4.12). The parameters are $N = 20$ (solid line) and $N = 21$ (dashed line), $U_0 = 2E_F = 0.0058\,t$ and $d \equiv E_F/U_x = 100\,a$.

is only a single propagating mode at the Fermi level, which requires $W < 4a\tau/E_F$ [51]. The assumption can be relaxed in the case of a smooth p-n interface, because higher modes have an exponentially small transmission probability if the Fermi wavelength $\lambda_F \simeq W \ll d$ [54].

Next-nearest-neighbor hopping was not included in the theory, and one might be concerned that it could modify our result substantially because the edge states are then no longer dispersionless [55]. We have found that this is actually not a relevant perturbation: Next-nearest-neigbor hopping (with hopping energy t') adds a term $2t'(2 + \cos ka)a^{-1}\delta(k - k')\sigma_0$ to the projected Hamiltonian (4.9). This is an irrelevant perturbation because its only effect is to multiply the transfer matrix (4.12) by a scalar phase factor.

As a check, we have repeated the computer simulations with the inclusion of next-nearest-neighbor hopping[2] in the tight-binding model (for the realistic ratio $t'/t = 0.1$). As shown in Fig. 4.6, the result (4.2) still applies for $\Delta \ll W$.

Eq. (4.2) was derived for a linear potential profile U, but the derivation can be extended to include a smoothly varying potential landscape δU (smooth on the scale of the

---

[2]Next-nearest-neigbor hopping gives both a displacement and a finite width to the energy interval $2t' < \varepsilon < 3t'$ in which conduction and valence bands coincide [with $\varepsilon(2\pi/3a) = 3t' = \varepsilon(4\pi/3a)$ and $\varepsilon(\pi/a) = 2t'$]. To form a p-n junction, the Fermi level should lie above this interval in the n-region and below this interval in the p-region. Eq. (4.2) then still holds, with $\Delta = x_+ - x_-$ calculated from the lateral displacement of the points $\boldsymbol{r}_\pm$ on the boundary at which $U - E_F = 3t'$.
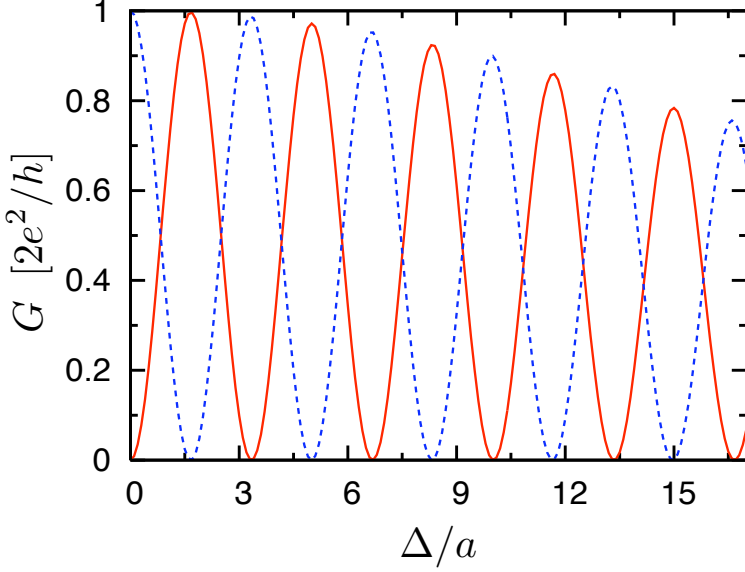
Figure 4.6: The conductance of a tilted *p-n* interface with next-nearest neighbor hopping included ($t'/t = 0.1$). The parameters of the ribbon are $E_F = 0.19\,t$, $U_0 = 0.16\,t$, and $d = 100\,a$. The number of atoms across the ribbon is $N = 40$ (solid line) and $N = 41$ (dashed line).

lattice constant). Electrostatic disorder therefore affects the conductance only through the lateral displacement Δ of the points on the boundary at which $U + \delta U - E_F = 0$.

Edge disorder cannot be accounted for in this simple way, but in view of the small lateral extension of the localized edge state we might not need a well-defined zigzag edge over long distances in order for Eq. (4.2) to apply.

4.6   Conclusion

In conclusion, we have presented a theory for the current blocking by a *p-n* junction in a zigzag nanoribbon. The dependence on the parity of the number N of atoms across the ribbon, not noticed in earlier computer simulations [50, 51], is explained in terms of the parity of the lowest mode under a switch of sublattice: Incident and transmitted modes have opposite parity for N even, leading to complete reflection ($G = 0$), while they have the same parity for N odd, leading to complete transmission ($G = 2e^2/h$). A variation of the electrostatic potential in the direction transverse to the ribbon can invert the parity dependence of the conductance, while preserving the sum rule $G(N) + G(N + 1) \approx 2e^2/h$.

This switching behavior may have device applications, if the structure of the edges

can be controlled (which is not the case in presently available samples). Even if such control is not forthcoming, the mechanism for current blocking proposed here can be operative in an uncontrolled way in disordered nanoribbons, producing highly resistive *p-n* interfaces at random positions along the ribbon. Conduction through the resulting series of weakly coupled regions would show an activated temperature dependence as a result of the Coulomb blockade [56], as observed experimentally [24, 25].

4.A Evaluation of the transfer matrix

To evaluate the transfer matrix $M(k_{\text{out}}, k_{\text{in}})$ in the regime $W \gg \Delta$ we use the fact that the energy $\varepsilon(k)$ of the lowest modes decays exponentially $\sim \exp(-Na\delta k)$ away from the integration limits $k_{\text{in}}, k_{\text{out}}$ [see Eq. (4.7)]. We separate the integration in the momentum-ordered exponent (4.12) into three intervals:

$$M(k_{\text{out}}, k_{\text{in}}) = T \exp\left[i \int_{k_2}^{k_{\text{out}}} \Omega(q)dq\right]$$

$$T \exp\left[i \int_{k_1}^{k_2} \Omega(q)dq\right] T \exp\left[i \int_{k_{\text{in}}}^{k_1} \Omega(q)dq\right]. \quad (4.16)$$

We choose $k_{\text{in}} - k_1 = k_2 - k_{\text{out}} \gtrsim 1/W$, such that $|\varepsilon(k_1)| = |\varepsilon(k_2)| \lesssim U_x$. Then the contribution of the term $\sigma_1 \Delta/2$ in $\Omega(q)$ to the integrals over the first and the third intervals is of order $\Delta/W \ll 1$, so that this term may be neglected. The contribution of the term $\sigma_3 \varepsilon(q)a/U_x$ to the integral over the second interval is of order $a/W \ll 1$ so it can also be neglected. The three integrals can now be evaluated analytically, with the result:

$$M(k_{\text{out}}, k_{\text{in}}) = e^{i\alpha\sigma_3} \exp\left[i(k_2 - k_1)\frac{\Delta}{2}\sigma_1\right] e^{i\alpha'\sigma_3}. \quad (4.17)$$

This is equivalent to Eq. (4.15) since $k_2 - k_1 = -2\pi/3a + O(1/W)$.

Chapter 5

Robustness of edge states in graphene quantum dots

5.1 Introduction

The experimental discovery of graphene [3, 57], a monolayer of carbon atoms, has opened room for new electronic 'devices (for reviews, see Refs. [58–60]). A peculiarity of finite graphene sheets is the existence of electronic states localized at the boundary, so-called *edge states*.

A crystallographically clean zigzag edge was theoretically predicted to sustain zero-energy edge states [26, 61, 62]. Later, it was shown [63] that any generic graphene boundary not breaking electron-hole subband (sublattice) symmetry also supports these zero energy edge states. Similar states exist at zigzag edges of graphene bilayers [64, 65], and in other multilayered graphene systems [66]. Experimentally, these states were observed in STM experiments near monatomic steps on a graphite surface [67–69].

The presence of large number of localized states is important for the predicted edge magnetism in graphene nanoribbons [62, 70], a topic that has recently seen renewed interest in the context of graphene spintronics [18, 71–74]. Apart from edge magnetism, interacting edge states may also result in other correlated ground states [75–77].

Edge states also play a role in confined geometries, when the edge to area ratio is large enough so that the electronic properties of the boundary may become dominant. One example for such a geometry are graphene quantum dots that have been under intense experimental study recently [78–83], with quantum dot sizes in the range from a few tens of nanometers to micrometers. Another example are antidot arrays that have been subject of several theoretical studies [84–87] and have also been realized experimentally [88–91].

Different edges have been observed in graphite [67–69, 92] and graphene [93–96]. In particular, the existence of boundaries with a long-range crystalline order in exfoliated graphene has been questioned [97]. In addition, the existence of unsaturated dangling bonds at edges makes them reactive, and it is unclear how they are passivated [98–101]. Hence, it is likely that graphene edges are perturbed and that the presence of edge
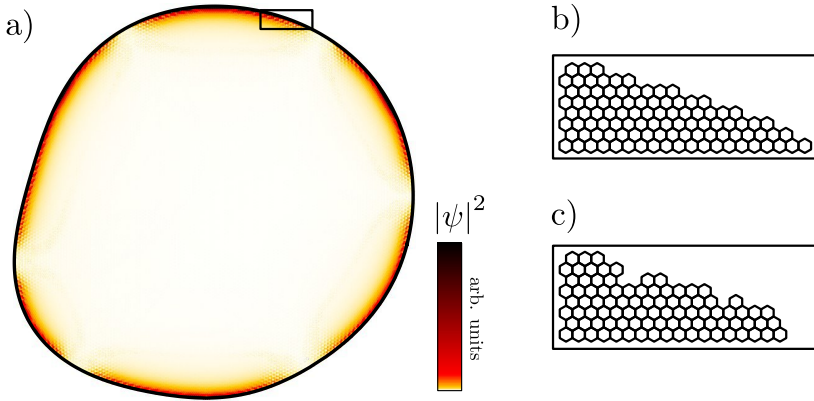
Figure 5.1: A graphene quantum dot. The excess density of states due to edge states is shown in a color plot, as calculated for a quantum dot with a smooth boundary and no particle-hole symmetry breaking perturbations (a). In general, edge states are present both near a smooth boundary (b) and a boundary with short range disorder (c). In order to avoid the oscillatory pattern on the lattice scale, for every unit cell we only plot the atom with the largest occupation probability.

distortions has to be taken into account.

The aim this chapter is to show that edge states can be expected in realistic disordered quantum dots. We also analyse the particular properties of edge states such as their number and compressibility. We start the analysis in Section 5.2 by using the theory of Ref. [63] for a relation between the number of edge states per unit length of a smooth boundary (see Fig. 5.1b) and the angle the boundary makes with respect to the crystallographic axis. We extend the earlier results by calculating the correction to the edge states number coming from the edge roughness (Fig. 5.1c). Having the total number of edge states and their momentum distribution we apply perturbation theory to see how confinement energy and particle-hole symmetry breaking terms in the Hamiltonian shift the edge states from zero energy. Confinement energy spreads a delta function-like peak in the density of states into a hyperbolic one. In contrast, particle-hole symmetry breaking terms spread the edge states nearly homogeneously over a band of finite width. For realistic dot sizes around tens of nanometers we find the latter to be more important.

In Section 5.3 we perform numerical simulations on quantum dots of experimentally relevant sizes. These numerical calculations confirm our analytic results. We also study the magnetic field dependence of edge states in quantum dots. Whereas magnetic field spectroscopy of energy levels has up to now mainly been a useful tool to probe bulk states in graphene quantum dots [81, 82, 102], we show how to employ this technique also to identify edge states. In addition, we study the level statistics of edge states.

Finally in Section 5.4, we calculate an upper bound on the magnetic moment of a

graphene dot due to edge state polarization. We also give an upper bound on the relative weight of the edge states with respect to the bulk states. By knowing the magnitude of additional compressibility due to the edge states we estimate parameters of an antidot lattice in which edge states would be visible in SET experiments.

We conclude in Section 5.5.

5.2 Analytical calculation of the edge states density

5.2.1 Number of edge states

The density of edge states per unit length was calculated for a smooth edge in Ref. [63]

$$\frac{dN}{dl} = \frac{2}{3a} |\sin \phi|, \tag{5.1}$$

with $-\pi/6 < \phi < \pi/6$ the angle boundary makes with a nearest armchair direction, and a the lattice constant. This expression is valid on the scales larger than the boundary roughness scale and another scale $\delta(\phi)$ dependent on boundary structure. For most boundary orientations, except the ones very close to armchair direction $\delta(\phi) \sim a$. Approximating the dot shape by a circle, and integrating Eq. 5.1 along the whole perimeter of the dot, we get

$$N = \int_0^L \frac{dN}{dl} dL = \frac{4 - 2\sqrt{3}}{\pi} \times \frac{L}{a}, \tag{5.2}$$

with L circumference of the dot and a the lattice constant. This density of states is the difference between total density of waves evanescent away from the boundary and the number of conditions the wave function must satisfy on the selected sublattice (see Ref. [63] for a more detailed description). If a small fraction α of random outermost atoms of the smooth edge oriented at angle ϕ with armchair direction is etched, the number of conditions for the wave function on the minority sublattice increases by

$$\delta N = 2\alpha \sin \phi. \tag{5.3}$$

This leads to the reduction of the number of the edge states near an edge with atomic scale disorder:

$$N' = N(1 - 2\alpha). \tag{5.4}$$

Note that Eq. (5.4) only gives the local density of low energy edge states. It should not be confused with Lieb's theorem [13], which connects the number of states with exactly zero energy with the difference in the number of sublattice sites in a bipartitte sublattice. Lieb's theorem was applied to graphene in Refs. [84, 86, 103], and for a disordered quantum dot geometry it predicts [86] number of zero-energy modes $\sim \sqrt{L}$. Our analysis shows that there will be $\sim L$ low energy edge states, although most of them do not lie at exactly zero energy. Hence, there is no contradiction with Lieb's theorem.

5.2.2 Edge state dispersion

There are two different mechanisms which give finite energy to otherwise zero energy edge states: the overlap between edge states on different sublattices, and terms breaking sublattice symmetry at the edge. The dispersion resulting from these perturbations can be calculated by applying degenerate perturbation theory, acting on the wave functions ψ_n, belonging exclusively to A or B sublattice. The long wavelength part of these wave functions is defined by the conformal invariance of Dirac equation, so they can be approximated as plane waves belonging to one of the six facets of the dot with well-defined boundary condition, extended along the facet and decaying into the bulk. These wave functions have longitudinal momenta

$$k_n \sim \frac{n}{R} \tag{5.5}$$

approximately equally spaced due to phase space arguments.

We first estimate the energy dispersion due to edge state overlap, or in other words by finite size effects. Particle-hole symmetry prevents coupling between states on the same sublattice, so the dispersion of edge states in a finite system can be calculated from the matrix element between the edge states on different sublattices. These states are separated from each other by a distance of an order of the dot radius R and their decay length away from the boundary is proportional to difference k between their momentum and the momentum of the nearest Dirac point (Dirac momentum), so the energy is

$$E(k) \sim \frac{v_{\text{F}}}{R} e^{-kR}, \tag{5.6}$$

where v_{F} is the Fermi velocity and we set $\hbar = 1$. We note that Eq. 5.6 is very similar to the energy of edge states in zigzag nanoribbons [104]. Substituting the value of momentum of the edge states from Eq. (5.5) into Eq. (5.6) we calculate the density of edge states per unit energy

$$\rho(E) \equiv \left| \frac{dn}{dE} \right| \sim \frac{1}{E} \tag{5.7}$$

The atoms passivating the edge perturb the π-orbitals of carbon atoms to which they are bound. This interaction breaks the effective electron-hole symmetry of graphene around the Dirac point. Next-nearest neighbor hopping is breaking this symmetry at the edges as well [55, 105], and it was shown to be equivalent to the edge potential [106]. The dispersion of the edge states near a zigzag edge due to these two perturbations is

$$E = (\Delta\epsilon - t')[2\cos(K) + 1], \quad 2\pi/3 < K < 4\pi/3, \tag{5.8}$$

where K is the full momentum of the edge state, $\Delta\epsilon$ is the average strength of the edge potential and t' the next-nearest neighbor hopping strength. Despite it is not straightforward to generalize this equation to an arbitrary orientation of the edge, the general effect of the electron-hole symmetry breaking terms is to smear the zero energy peak in the density of states into a band between energies of approximately 0 and $E_0 \equiv \Delta\epsilon - t'$

for the most localized states, while the more extended states are near the Dirac energy. The one dimensional van Hove singularity in the density of states at $E = E_0$ will be smeared out, due to the presence of a minimum decay length of the edge states when the orientation of the boundary is not exactly zigzag [63].

The energy due to finite size of the dot given by Eq. (5.6) is at best of an order of $E \sim v_F/R \approx ta/R$. It is less than tens of millivolts for dots above 10nm size. On the other hand the energy due to the edge potentials and next-nearest neighbor hopping (Eq. (5.8)) is likely to be around hundreds of millivolts. Accordingly in realistic dots with edge potentials and next-nearest neighbor hopping term edge states occupy the band between the Dirac point and E_0 with approximately constant density

$$\rho_{\text{edge}} = c(1 - 2\alpha) \frac{R}{a|E_0|}, \tag{5.9}$$

with $c = 8 - 4\sqrt{3} \approx 1$.

5.3   Numerical results

In order to confirm the analytical results of the previous sections we have performed numerical simulations of the energy spectrum of graphene quantum dots with sizes relevant for experiments. In the following we present results for a quantum dot with the shape of a deformed circle[1] (c.f. Fig.5.1), characterized by an average radius R. Although we focus on a particular quantum dot here, we have found through numerical studies that the characteristic features of our results are independent from the details of the dot shape.

The numerical simulations are based on a tight-binding model of graphene with Hamiltonian

$$H = -\sum_{i,j} t_{ij} c_i^\dagger c_j + h.c. \tag{5.10}$$

where the hopping $t_{ij} = t$ for nearest neighbors and $t_{ij} = t'$ for next-nearest neighbors [60]. The effects of a magnetic field are incorporated through the Peierls phase [107] as

$$t_{ij} \rightarrow t_{ij} \times \exp\left(\frac{ie}{\hbar} \int_{\mathbf{x}_i}^{\mathbf{x}_j} d\mathbf{s}\, \mathbf{A}(\mathbf{x})\right), \tag{5.11}$$

where $\mathbf{x}_i$ and $\mathbf{x}_j$ are the positions of atom i and j, respectively, and $\mathbf{A}(\mathbf{x})$ is the magnetic vector potential.

The quantum dots are constructed by "cutting" the desired shape out of the hexagonal graphene grid. For a shape that is smooth on the length scale of the lattice constant as considered here, this results in edges with a locally well-defined orientation (*smooth*

---

[1]The dot has the shape of a deformed disk, with a radius $R(\theta)$ depending on the angle of direction θ. The numerical calculations presented in the text use $R(\theta) = R + 0.2R\sin(\theta) + 0.05R\sin(2\theta) - 0.025R\sin(3\theta) + 0.02R\sin(4\theta) - 0.01R\sin(5\theta)$.

edges, see Fig. 5.1(b)). In order to account for edge disorder on the lattice scale (*rough edges*, see Fig. 5.1(c)), we adopt the disorder model introduced in Ref. [108]: Starting from the smooth edge, atoms at the boundary are removed randomly with probability p, with dangling bonds removed after each pass. This procedure is repeated N_{sweep} times.

The energy spectrum of the dot tight-binding Hamiltonian is calculated numerically using standard direct eigenvalue algorithms [109] and matrix bandwidth reduction techniques [110] if a large part of the spectrum is needed. In contrast, if only a few eigenvalues and -vectors are sought, we apply an iterative technique [111] in shift-and-invert mode.[2]

5.3.1 Systems with electron-hole symmetry

We first focus on the electron-hole symmetric case, i.e. $t' = 0$ and the absence of potentials. Fig. 5.2(a) shows the number of states $N(E)$ per energy interval ΔE for dots with smooth and rough edges. We can clearly identify the edge states close to $E = 0$ and the linearly increasing bulk density of states. Approximating the circumference of the dot as $L \approx 2\pi R$, Eq. (5.2) predicts $N \approx 170$ edge states for a quantum dot with a smooth edge, which is in very good agreement with $N = 169 \pm 6$ edge states obtained from the numerical simulation by summing over the three central bins, where the number of states differs noticeably from the linear bulk density of states. The number of edge states N' in the dot with atomic scale disorder can be estimated from Eq. (5.3) by approximating $\alpha \approx pN_{sweep}$ yielding $N' \approx 0.5N$ for the disorder parameters used in the simulation ($N_{sweep} = 5$, $p = 0.05$), again in good agreement with the numerical simulations.

In order to examine the behavior of the edge state density of states in more detailed close to $E = 0$, we estimate the density of states numerically as

$$\rho((E_{i+1} + E_i)/2) = \frac{1}{E_{i+1} - E_i} \, , \tag{5.12}$$

where E_i is the energy of the i-th state in the dot. Fig. 5.2(b) shows the numerically computed $\rho(E)$ for quantum dots with smooth and rough edges. As predicted in Eq. (5.7), we find a $1/E$-dependence close to $E = 0$; quite remarkably, we find an excellent agreement with this scaling for more than ten orders of magnitude. The clustering of data points at $\rho(E) = 10^{16}t^{-1}$ is due to the finite precision in the numerical calculations. It should be noted that we found this remarkable agreement with theoretical predictions without averaging over an energy window or different dot shapes, implying that the spectrum of edge states is highly non-random even in a quantum dot with random shape. We come back to this point in Sec. 5.3.4.

5.3.2 Broken electron-hole symmetry

Next we focus on perturbations breaking the electron-hole symmetry. For this we consider a finite next-nearest neighbor hopping t' uniformly within the quantum dot, as well

---

[2]For the solution of the sparse linear system arising in the shift-and-invert problem, we apply the MUMPS package, Ref. [112].
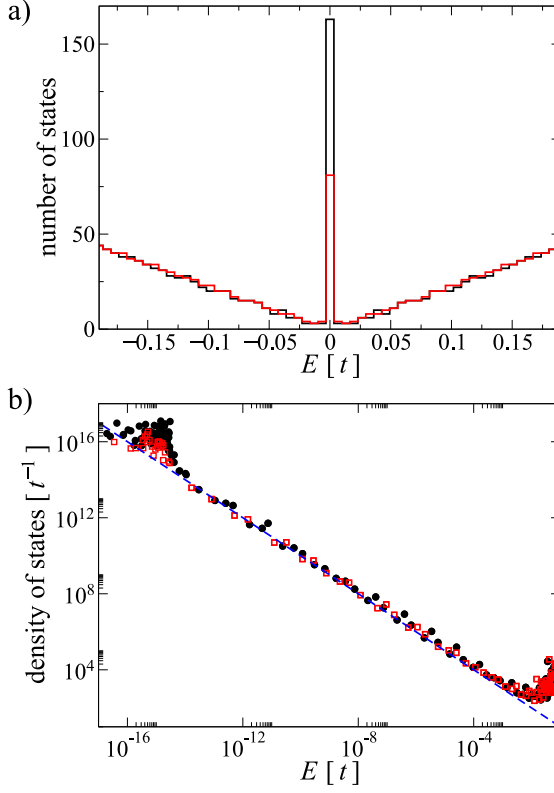
Figure 5.2: Electronic states in a graphene quantum dot close to the Dirac point. The graphene quantum dot has the shape of a deformed circle (see Fig. 5.1) with $R = 160a \approx 40\,\text{nm}$, and we consider both smooth and rough edges as shown in Fig. 5.1(b) and (c) respectively. The parameters for the edge disorder are $N_{\text{sweep}} = 5$ and $p = 0.05$ (see the main text for a discussion of the edge disorder model). (a) Number of states per energy interval ΔE for a quantum dot with smooth (black lines) and rough edges (red lines), with $\Delta E = 0.4t/61$. (b) Density of states estimated numerically from Eq. (5.12) for a quantum dot with smooth (black symbols) and rough edges (red symbols). For comparison, the blue dashed line shows a $1/E$-dependence.

as a random potential at the quantum dot edge, where an energy U_0 is assigned to edge atoms with probability p_{edge}.

Fig. 5.3(a) shows the number of states per energy window ΔE for finite t', but in the absence of an edge potential. In order to identify the edge states properly, we compare the numerical data including the edge states to the number of bulk states estimated [60]
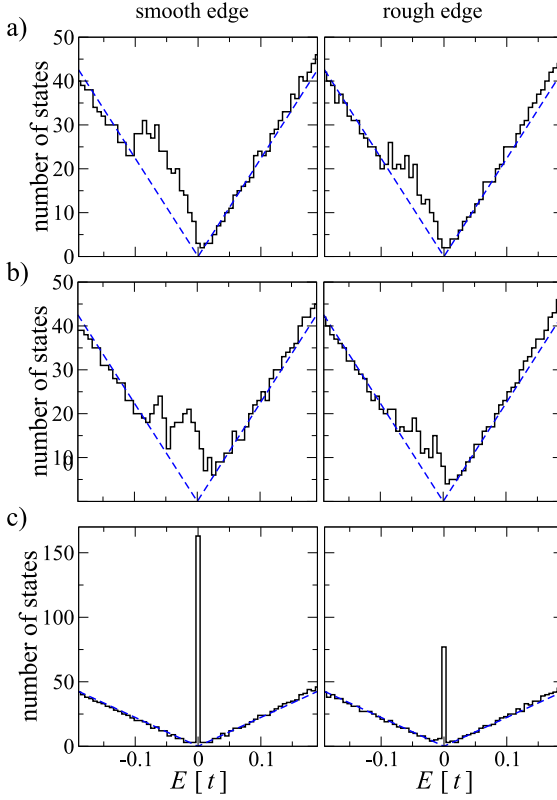
Figure 5.3: Number of states (black lines) per energy interval ΔE for a graphene quantum dot with smooth (left panels) and rough (right panels) edges. We show results for situations with broken electron-hole symmetry: (a) finite next-nearest neighbor hopping and no edge potential ($t' = 0.1t$ and $U_0 = 0$) and (b,c) finite next-nearest neighbor hopping including an edge potential ($t' = 0.1t$, with (b) $p_{\text{edge}} = 0.25$ and $U_0 = 0.2t$, and (c) $p_{\text{edge}} = 1$ and $U_0 = 0.1t$). The remaining parameters are as in Fig. 5.2. The blue dashed lines show the number of bulk states N_{bulk} estimated from the linear density of states of the Dirac dispersion Eq. (5.13).

from the linear Dirac density of states,

$$N_{\text{bulk}}(E) = \frac{2\,|E|\,R^2}{v_{\text{F}}^2} \tag{5.13}$$

approximating the area of the quantum dot as $A = \pi R^2$. The excess edge state density of states can be clearly identified, both in the case of smooth and rough edges. The bulk density of states close to $E = 0$ is unaffected by a finite t', the effect of electron-hole asymmetry on the bulk states only shows for energies $|E| > 0.1t$. The central edge state

peak observed for $t' = 0$ (c.f. Fig.5.2) is broadened and shifted towards the hole side, but the total number of edge states remains unchanged from the $t' = 0$ case. The excess density due to the edge states is approximately constant in the energy range between $t' = -0.1t$ and 0, in accordance with the prediction from Eq. (5.9). As before, atomic scale edge disorder only results in a reduction of the total number of edge states.

The presence of an additional edge potential changes the energy range of the edge states. In Fig. 5.3(b) we show results for an average edge potential $\Delta\epsilon = 0.05t$. Correspondingly, the majority of the edge states occupies uniformly an energy window between $\Delta\epsilon - t' = -0.05t$ and 0. A few states can still be found beyond this energy window, as the randomness of the edge potential has been neglected in the arguments of Section 5.2.2. Instead, if the edge potential is uniform, the dispersion of the edge state due to next-nearest neighbor hopping can be cancelled exactly by $\Delta\epsilon = -t'$, as shown in Fig. 5.3(c). This particular example strikingly shows the equivalence of next-nearest neighbor hopping and an edge potential, as predicted in Ref. [106].

The narrowing of the energy band width occupied by the edge state due to an edge potential may also be a possible explanation (amongst others [113]) for the fact that STM measurements on zigzag graphene edges found a peak in the density of states only a few tens of meV below the Dirac point [67, 69], far less than expected from estimated values of the next-nearest neighbor hopping [60].

5.3.3   Broken time-reversal symmetry: Finite magnetic field

We now consider the effects of a finite magnetic field on the edge state energies. The evolution of edge states in a magnetic field has been studied theoretically for special geometries and a particle-hole symmetric spectrum [114, 115]. Recently, the magnetic field dependence of the energy levels in a graphene quantum dot has been also been subject to an experimental investigation [81]. However, in the theoretical calculations used to interpret these experiments the graphene edge states were excluded artificially. As we show below, the presence of edge states results in a much richer magnetic field dependence of energy levels in a graphene dot, in particular when particle-hole symmetry is broken.

In Fig. 5.4 we show the numerically calculated magnetic field dependence of the energy levels in a graphene quantum dot close to the Dirac point, for finite t' and edge potential. In order to distinguish between edge and bulk states, we also plot the participation ratio [116, 117]:

$$p = \frac{\left(\sum_i |\psi(i)|^2 \right)^2}{N \sum_i |\psi(i)|^4} \tag{5.14}$$

where the index i runs over atomic sites and N denotes the total number of atoms in the dot. The participation ratio p can be interpreted as the fraction of atoms occupied by an electron for a given energy level. Thus, $p \sim 1$ for extended states ($p \approx 0.3 - 0.4$ in quantum dots) and $p \ll 1$ for localized edge states ($p \approx 10^{-4} - 10^{-2}$).

Instead of a uniform flow of energy levels towards the $n =$ Landau level as calculated in Ref. [81], we observe that the most strongly localized states only show a very weak
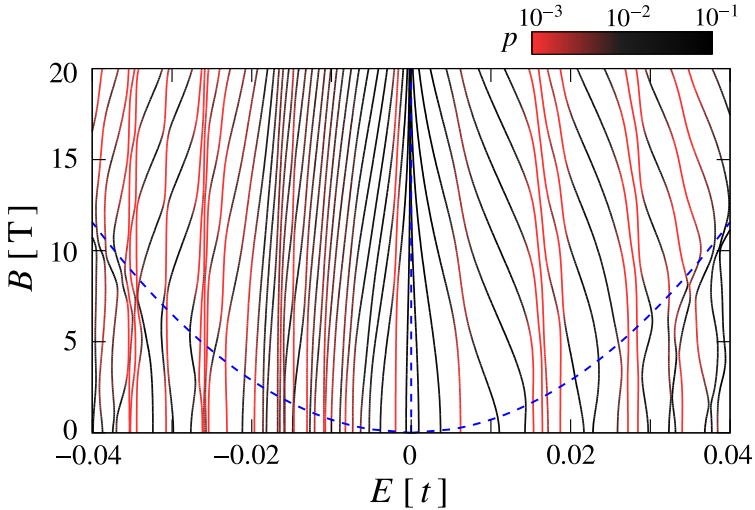
Figure 5.4: Magnetic field dependence of the energy levels (black lines) in a desymmetrized quantum dot with $R = 100a$ (deformed circle as shown in Fig. 5.1). The participation ratio p of the states is color-encoded, with the most strongly localized states in red. The blue dashed lines indicate the energy of the $n = 0, \pm 1$ Landau levels of graphene. The calculations includes finite next-nearest neighbor hopping $t' = 0.1t$ and a random edge potential with $p_{\mathrm{edge}} = 0.25$ and $U_0 = 0.2t$.

magnetic field dependence (apart from avoided crossings), leading to a far richer energy spectrum. Note that this effect is most prominent on the hole side of the spectrum where the majority of the edge states reside, as can be simply seen by comparing the number of states for $E > 0$ and $E < 0$. This weak magnetic field dependence of the localized edge states can be understood from the fact that bulk states start to be affected by the magnetic field when the cyclotron radius becomes comparable to the dot size, whereas edge state energies are expected to only change significantly when the cyclotron radius becomes comparable to the edge state *decay length* which is much smaller than the dot dimensions.

Note that this type of behavior is similar to the magnetic field dependence of the low-energy spectrum of graphene in the presence of lattice vacancies [118]. In fact, such vacancies can be considered as internal edges and also carry a localized state.

Hence, energy levels insenstitive to magnetic field are characteristic for localized (edge) states. In the light of this observation, it would be very interesting to see if experiments can identify such states, which would be a strong indication for the presence of such states.

5.3.4   Level statistics of edge states

The bulk states of chaotic graphene quantum dots confined by lattice termination have been shown to follow the level statistics of the Gaussian orthogonal ensemble (GOE), as expected for a system with time-reversal symmetry [119, 120] (scattering at the quantum dot boundary mixes the K and K'-valley). The edge states however are tied to the boundary of the quantum dot only, and should not necessarily follow the same level statistics as the extended states. Instead, being localized states they are rather expected to follow Poisson statistics, as has also been noted in Ref. [119], but not been demonstrated explicitly.

To check these expectations we have studied the level spacing distribution of edge states in quantum dots. For this purpose we have identified edge states using the participation ratio and worked with the edge state spectrum alone. This spectrum has been unfolded [121] using the average density of states and scaled to an average level spacing of unity. The distribution $P(S)$ of the nearest-neighbor level spacings S in the unfolded spectrum is then normalized such that $\int P(S)dS = 1$ and $\int SP(S)dS = 1$.

Fig. 5.5 shows the level spacing distributions for the electron-hole symmetric case ($t' = 0$) and for broken electron-hole symmetry ($t' = 0.1t$). Surprisingly, the edge states follow the GOE statistics if $t' = 0$. Only if a finite t' is included, they exhibit a statistics close to Poisson. These classifications are additionally corroborated by the integrated level spacing distributions shown in the inset of Fig. 5.5.

This striking difference in level statistics can be explained by the different nature of the wave functions: The graphene Hamiltonian exhibits a chiral symmetry for $t' = 0$ that results in an equal occupation probability of sublattice A and B for every individual wave function [21]. Since the edge wave function at a certain type of zigzag edge is nonzero only on one sublattice, every eigenstate for $t' = 0$ must also occupy another part of the boundary of the opposite kind, as illustrated in Fig. 5.6. This leads to an artificial long-range coupling between edge states and thus to level repulsion, resulting finally in GOE statistics. If this chiral symmetry is broken, for example by next-nearest neighbor hopping,[3] edge state wave functions may be localized at a single edge only (Fig. 5.6(a)). Whereas edge states localized at the same part of the boundary still may feel level repulsion, parts that are further away may only interact via hybridization with bulk states which typically happens for edges states decaying further into the bulk, as seen in Fig. 5.6(b). For the type of quantum dots under consideration (Fig. 5.1), this results in six approximately independent series of energy levels, and hence an approximate Poisson statistics.

A finite next-nearest neighbor hopping t' (or another chiral symmetry breaking term) thus does not only change properties of the edge states quantitatively, but leads to a striking, qualitatively different level statistics.

---

[3]In Ref. [119] the chiral symmetry was broken by a mass term.
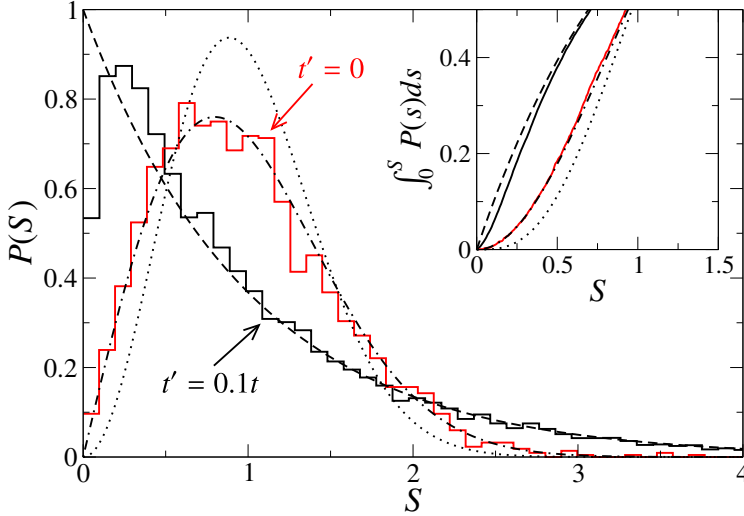
Figure 5.5: Level spacing distributions for quantum dots with smooth edges for $t' = 0$ (solid red curve) and $t' = 0.1t$ (solid black curve), together with the theoretical predictions for Poisson statistics (dashed line), the Gaussian orthogonal ensemble (dash-dotted line), and the Gaussian unitary ensemble (dotted line). The inset shows details the integrated level spacing distribution for small level spacings S (same line colors and -types as the main plot). The level distribution statistics has been obtained by averaging individual level distributions from 100 quantum dots similar to the type shown in Fig. 5.1, with average radius $R = 160a$. A state has been identified as an edge state, if its participation ratio $p_i < 0.05$ (the result is insensitive to the change of this value). For $t' = 0$ we have also omitted all states with an energy smaller than the numerical precision.

5.4 Discussion and physical implications

5.4.1 Formation of magnetic moments at the edges

An extensively discussed topic in the graphene literature is the formation of localized moments at boundaries [18, 71, 73, 75–77, 122, 123]. The previous analysis allows us to set approximate bounds on the maximum magnetic moment in a graphene quantum dot.

The interaction energy between two electrons of opposite spin in a boundary state of area $k_i^{-1} \times R \approx a \times R$ is:

$$E_{ee} \approx \frac{e^2}{R} \log \left(\frac{R}{a} \right) \tag{5.15}$$

where e is the electronic charge. States with energies $|\epsilon_i - E_F| \lesssim E_{ee}^i$ will be spin polarized. Since the density of edge states is nearly constant and given by Eq. (5.9), the
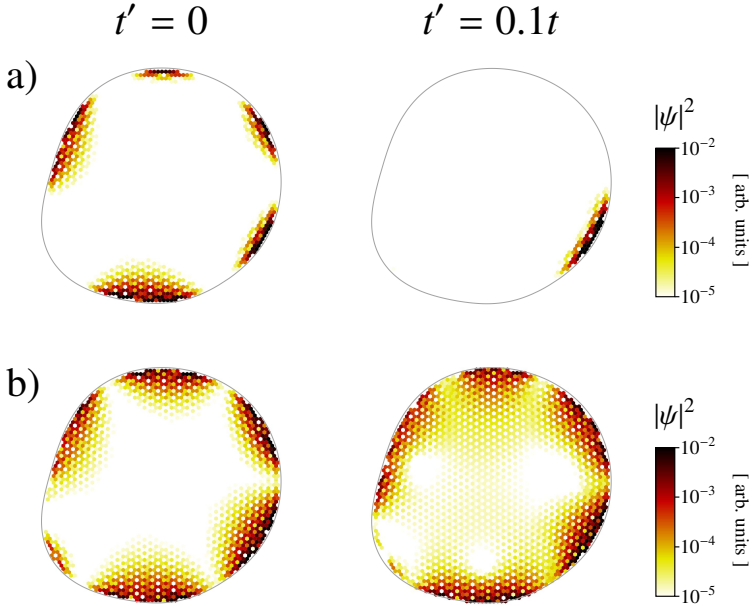
Figure 5.6: Color plot of wave function density in a graphene quantum dot (shape as described in Fig. 5.1) for the e-h symmetric case ($t' = 0$, left column) and for broken e-h symmetry ($t' = 0.1t$, right column) on the examples of a mode that is (a) strongly decaying and (b) slowly decaying into the bulk. Note that for presentation purposes we have chosen a rather small dot ($R = 30a$), but the behavior does not change qualitatively for larger dots. Just like in Fig. 5.1 we only plot in each unit cell the atom with the largest occupation probability.

position of the Fermi level is not relevant. Using the density of states given in Eq. (5.9), we obtain for the number of spins in a quantum dot:

$$N_{\text{spins}} \approx E_{ee} \rho_{\text{edge}} = c(1 - 2\alpha) \frac{e^2}{a E_0} \log\left(\frac{R}{a}\right) \sim 20(1 - 2\alpha) \log\left(\frac{R}{a}\right), \qquad (5.16)$$

where for last estimate we took $E_0 = 0.3$ eV. The maximal number of polarized spins depends only logarithmically on the size of the dot.

In general, the states at the edge of a quantum dot will belong to one of the two sublattices with equal probability. States localized at different sublattices interact antiferromagnetically [124]. If we neglect this interaction, we expect a maximum magnetic moment comparable with N_{spins}. When the antiferromagnetic interaction contributes to the formation of the total magnetic moment, its value will be proportional to the number of uncompensated sites at the edges, which will scale as $\sqrt{N_{\text{spins}}}$.

5.4.2   Fraction of edge states

Our results suggests that edge and bulk states can coexist in a range of energy of order E_0 near the Dirac point. From Eqs. (5.9) and (5.13), the average ratio between edge and bulk states in this energy range is

$$\frac{N_{edge}}{N_{bulk}} \approx c(1 - 2\alpha) \frac{v_{\mathrm{F}}^2}{E_0^2 a R} \tag{5.17}$$

This gives, for a diameter of 100nm and $E_0 = 0.3$eV an upper bound of $N_{edge}/N_{bulk} \lesssim 1/2$.

5.4.3   Detection in antidot lattices

A conclusive way of detecting the existence of edge states can be the measurement of their contribution to the electronic compressibility. It is hard to detect the edge states in a single quantum dot because the ground state properties are dominated by the charging energy. Also, the contribution of edge states to the density of states in most large-scale samples will be negligible compared to the bulk contribution. However it is possible to circumvent both problems in antidot lattices. The Coulomb energy does not play a role in this case due to absence of confinement. On the other hand, the existence of multiple antidots allows us to reach a large edge-area ratio. To estimate whether it is possible to detect edge states, we use the value of minimal compressibility (or the minimal density of states) of bulk graphene, measured in Ref. [125]:

$$\frac{\partial \mu}{\partial n} = 3 \times 10^{-10} \mathrm{meVcm}^2 \tag{5.18}$$

and we assume that the width of the band of edge states is around $E_0 \approx 0.3$ eV.

We consider an antidot lattice with antidot size L of the same order of magnitude as the antidot spacing. Using the analysis in the previous section, the density of states per unit area associated to the edge states is:

$$N_{area}^{-1}(E) \approx E_0 a L \tag{5.19}$$

Comparing this expression with eq. 5.18, and using $E_0 \approx 0.3$ eV, we find that the contribution from the edge states is comparable to the bulk inverse compressibility for $L \lesssim 1\mu$m. Hence, the additional density of states near the edge will be visible in compressibility measurements using a single electron transistor (SET) since the size of the SET tip is around 100 nanometers [125]. Our results may be the reason of p-doping observed in antidot lattices experimentally [126, 127].

5.5   Conclusions

We have analyzed generic properties of the electronic spectrum in graphene quantum dots. We find that some of the electronic states will be localized at the edges and form

a narrow band. The density of states in this band is $\propto 1/E$ in graphene dot without electron-hole symmetry breaking perturbations. In presence of such perturbations, the density of the edge states is approximately constant and scales as R/aE_0, where R is the dot radius, a is the lattice constant, and E_0 is an energy scale which describes the edge potentials and next-nearest neighbor hopping.

If chiral symmetry is present, the edge states experience strong level repulsion and are described by the Gaussian orthogonal ensemble. Chiral symmetry breaking terms (such as next-nearest neighbor hopping) however lift this spurious level repulsion leading to the Poissonian statistics expected for localized states. In contrast, extended states will be described by the orthogonal or unitary ensembles, depending on the strength of the intervalley scattering at the boundaries [119, 128].

Having an analytical model for the edge states allows us to estimate the maximum spin polarization due to the presence of edge states. We predict that the additional density of states due to edge states will be visible in SET experiments. Effect of edge states on transport in quantum dots and more detailed investigation of interaction effects remains a direction for further research.

Part II

Majorana edge states in topological superconductors

Chapter 6

Topological quantum computation away from the ground state with Majorana fermions

6.1 Introduction

Topological quantum computation is manipulation of the wave function within a degenerate many-body ground state of many nonabelian anyons. Interchanging the anyons applies a unitary transformation to the ground state wave function. The simplest of the nonabelian anyons useful for topological quantum computation are Majorana fermions. These are expected to exist in 5/2 fractional quantum Hall effect [5] and in certain exotic superconductors [6, 129–131]. In 5/2 fractional quantum Hall effect the Majorana fermions are charge e/4 quasiholes, and in superconductors Majorana fermions are zero energy single particle states either trapped in vortex cores or other inhomogeneities [129, 132–134].

Superconducting implementations of Majorana fermions potentially allow for a larger bulk gap of a few Kelvin as compared with 500 mK for fractional quantum Hall effect. One significant difference between the superconductors and the fractional quantum Hall effect is that Majorana fermions in superconductors appear where the superconducting gap in excitation spectrum closes. This means that Majorana fermions would not be isolated from other excitations by the bulk gap, but coexisting with a lot of bound fermionic states with level spacing of the order of the minigap Δ^2/E_F, where $\Delta \sim 1$ K is the superconducting gap and E_F the fermi energy [135]. If $E_F \sim 1$ eV, minigap is at least a thousand times smaller than the bulk gap, so coupling between Majorana states and excited states is unavoidable with existing experimental methods. Already detection of Majorana fermions becomes problematic in this regime and requires ballistic samples and spatial resolution of density of states on the scale of Fermi wave length [136]. This is why there is research aimed at increasing the minigap [137].

We adopt a different strategy and show that coupling to excited states does not remove the topological protection as long as different Majorana fermions stay decoupled. The topological protection persists because coupling to excited states has to preserve the global fermion parity. Using only the conservation of the global fermion parity and

the fact that different Majorana fermions are well separated we identify new Majorana operators, which are protected even if the original Majorana fermions coexist with many excited states. We also check that the braiding rules for the new Majorana operators are the same as for original ones.

6.2　Fermion parity protection

We start from a brief introduction to Majorana fermions, for more information see e.g. Ref. [8]. A single Majorana fermion is described by a fermionic annihilation operator γ which is equal to the creation operator

$$\gamma = \gamma^\dagger. \tag{6.1}$$

Due to this defining property of Majorana fermions they are also called "real fermions" or "particles equal to their own antiparticles". Substituting Eq. 6.1 into the fermion anticommutation relation we get

$$\{\gamma, \gamma^\dagger\} = 2\gamma^2 = 2\gamma^\dagger\gamma = 1. \tag{6.2}$$

The last equality is a manifestation of the fact that a single Majorana fermion is pinned to the fermi level and accordingly is always half-filled. Additionally it is not possible to add a perturbation to the Hamiltonian, which would move a single Majorana level away from fermi level, at least two Majorana fermions are required. The only possible coupling term between two Majorana fermions has the form

$$H_\gamma = i\varepsilon\gamma_1\gamma_2. \tag{6.3}$$

The perturbation H_γ hybridizes two Majorana states into a single complex fermion state at energy ε and with creation and annihilation operators

$$a_{12}^\dagger = \frac{\gamma_1 + i\gamma_2}{\sqrt{2}}, \quad a_{12} = \frac{\gamma_1 - i\gamma_2}{\sqrt{2}}. \tag{6.4}$$

If Majorana fermions are well separated, the coupling between them decays exponentially with the distance between them [6, 136]. Additionally if the superconductor is grounded, the charging energy also vanishes, leaving the Majorana fermions completely decoupled [138]. In the limit when coupling between Majorana fermions ε is negligibly small, H_γ has two zero energy eigenstates which differ by fermion parity

$$(1 - 2a_{12}^\dagger a_{12}) = 2i\gamma_1\gamma_2. \tag{6.5}$$

If the system has N decoupled Majorana fermions, the ground state has $2^{N/2}$ degeneracy and it is spanned by fermionic operators with the form (6.4). Braiding Majorana fermions performs unitary rotations in the ground state space and makes the basis for topological quantum computation.

To understand how coupling with excited states gives nontrivial evolution to the wave function of Majorana fermions we begin from a simple example. We consider a toy model containing only two Majorana fermions γ_1 and γ_2 and a complex fermion a bound in the same vortex as γ_1. At $t = 0$ we turn on the coupling between γ_1 and a with Hamiltonian

$$H_{a1} = i\varepsilon(a + a^\dagger)\gamma_1. \tag{6.6}$$

At $t = \pi\hbar/\varepsilon$ we turn off H_{a1} and give finite energy to the fermion by a term $\varepsilon a^\dagger a$. We denote by $|0\rangle$ the state where two Majorana fermions share no fermion, so an eigenstate of $2i\gamma_1\gamma_2$ with eigenvalue 1, and by $|1\rangle$ the eigenstate of $2i\gamma_1\gamma_2$ with eigenvalue -1. If the system begins from a state $|0\rangle$, then it evolves into an excited state $a^\dagger|1\rangle$, so the Majorana qubit flips. This seems to destroy the topological protection, however there is one interesting detail: since there are two degenerate ground states $|0\rangle$ and $|1\rangle$, there are also two degenerate excited states: $a^\dagger|0\rangle$ and $a^\dagger|1\rangle$. So while $|0\rangle$ changes into $a^\dagger|1\rangle$, $|1\rangle$ changes into $a^\dagger|0\rangle$. The two end states differ by total fermion parity, which is the actual topologically protected quantity. In the following we identify the degrees of freedom which are protected by nonlocality of Majorana fermions and do not rely on the system staying in the ground state.

We consider a system with N vortices or other defects trapping Majorana fermions with operators γ_i, where i is the number of the vortex. Additionally every vortex has a set of m_i excited complex fermion states with creation operators a_{ij}, with $j \leq m_i$ the number of the excited state. We first consider the excitation spectrum of the system when the vortices are not moving and show that it is possible to define new Majorana operators which are protected by fermion parity conservation even when there are additional fermions in the vortex cores. Parity of all the Majorana fermions is given by $(2i)^{n/2}\prod_{i=1}^{N}\gamma_i$, so the total fermion parity of N vortices, which is a fundamentally preserved quantity, is then equal to

$$P = (2i)^{n/2}\prod_{i=1}^{N}\gamma_i \times \prod_{i=1}^{N}\prod_{j=1}^{m_i}[1 - 2a_{ij}^\dagger a_{ij}] = (2i)^{n/2}\prod_{i=1}^{N}\prod_{j=1}^{m_i}[1 - 2a_{ij}^\dagger a_{ij}]\gamma_i. \tag{6.7}$$

This form of parity operator suggests to introduce new Majorana operators according to

$$\Gamma_i = \prod_{j=1}^{m_i}[1 - 2a_{ij}^\dagger a_{ij}]\gamma_i. \tag{6.8}$$

It is easy to verify that Γ_i satisfy the fermionic anticommutation relations and the Majorana reality condition (6.1). The total fermion parity written in terms of Γ_i mimics the fermion parity without excited states in the vortices

$$P = (2i)^{n/2}\prod_{i=1}^{N}\Gamma_i, \tag{6.9}$$

so the operators $(2i)^{1/2}\Gamma_i$ can be identified as *the local part of the fermion parity operator* belonging to a single vortex. We now show that the operators Γ_i are protected from

local perturbations. Let the evolution of system be described by evolution operator

$$U = U_1 \otimes U_2 \otimes \cdots \otimes U_n, \tag{6.10}$$

with U_i evolution operators in i-th vortex. The system evolution must necessarily preserve the full fermion parity

$$P = U^\dagger P U, \tag{6.11}$$

and hence

$$(2i)^{n/2} \prod_{i=1}^{N} \Gamma_i = (2i)^{n/2} \prod_{i=1}^{N} U_i^\dagger \times \prod_{i=1}^{N} \Gamma_i \times \prod_{i=1}^{N} U_i = (2i)^{n/2} \prod_{i=1}^{N} U_i^\dagger \Gamma_i U_i. \tag{6.12}$$

This equation should hold for any set of allowed U_i. Taking $U_i = \mathbf{1}$ for all $i \neq j$ we come to

$$U_j^\dagger \Gamma_j U_j = \Gamma_j, \tag{6.13}$$

for any U_j. In other words, the new Majorana operators Γ_j are indeed not changed by any possible local perturbations.

We now need to show that the protected Majorana operators Γ_i follow the same braiding rules [139] as the original ones. The abelian part of braiding, namely the Berry phase [140, 141], is not protected from inelastic scattering in vortices, so it will be completely washed out. The non-abelian part of the braiding rules is completely described by the action of the elementary exchange of two neighboring vortices T on the Majorana operators. As shown in Ref. [139], exchanging Majorana fermions γ_i and γ_j is described by $\gamma_i \to \gamma_j$, $\gamma_j \to -\gamma_i$. The fermion parity operators $(1 - 2a_{ij}^\dagger a_{ij})$ have trivial exchange statistics as any number operators. Applying these rules to exchange of two vortices containing excited states gives

$$\Gamma_i = \prod_{k=1}^{m_i} [1 - 2a_{ik}^\dagger a_{ik}] \gamma_i \to \prod_{k=1}^{m_j} [1 - 2a_{jk}^\dagger a_{jk}] \gamma_j = \Gamma_j, \tag{6.14a}$$

$$\Gamma_j = \prod_{k=1}^{m_j} [1 - 2a_{jk}^\dagger a_{jk}] \gamma_j \to \prod_{k=1}^{m_i} [1 - 2a_{ik}^\dagger a_{ik}] (-\gamma_i) = -\Gamma_i. \tag{6.14b}$$

This finishes the proof that braiding rules are the same for Γ_i.

6.3 Discussion

Our proof of protection of Majorana fermions and their braiding properties from conservation of fermion parity only relies on particle statistics of Majorana and complex fermions. Consequently it fully applies to the Moore-Read state of 5/2 fractional quantum Hall effect, p-wave superfluids of cold atoms [142], or any other implementation

of Majorana fermions. Part of this proof can be reproduced using topological considerations in the following manner. If a perturbation is added to the Hamiltonian and additional excitations are created in a vortex, the fusion outcome of all these excitations cannot change unless these excitations are braided or interchanged with those from other vortices. So if a system is prepared in a certain state, then excitations are created in vortices, braiding is performed and finally the excitations are removed, the result has to be the same as if there were no excitations. Our proof using parity conservation, however, allows additionally to identify which part of the Hilbert space stays protected when excitations are present. Since removing the low energy excitations does not seem feasible, this identification is very important. It allows a more detailed analysis of particular implementations of the quantum computation with Majorana fermions. For example we conclude that implementation of the phase gate using charging energy, as described in Ref. [143], does not suffer from temperature being larger than the minigap since it relies on fermion parity, not on the wave function structure.

Since all the existing readout schemes of a Majorana qubit [9, 130, 144–146] are measuring the full fermion parity of two vortices, and not just the parity of the fermion shared by two Majorana fermions, all these methods also work if Majorana fermions coexist with excited states. The signal strength however is reduced significantly when the temperature is comparable with the minigap due to dephasing of the internal degrees of freedom of vortices. Using interferometry of Josephson vortices [143], which do not trap low energy excitations allows to avoid this problem.

In conclusion, we have shown that topological quantum computation with Majorana fermions is not sensitive to presence of additional localized states coexisting with Majorana fermions in superconducting vortices. This significantly relaxes the requirements on the temperature needed to achieve topological protection of Majorana fermions.

Chapter 7

Splitting of a Cooper pair by a pair of Majorana bound states

7.1 Introduction

Majorana bound states are coherent superpositions of electron and hole excitations of zero energy, trapped in the middle of the superconducting energy gap by a nonuniformity in the pair potential. Two Majorana bound states nonlocally encode a single qubit (see Fig. 7.1, top panel). If the bound states are widely separated, the qubit is robust against local sources of decoherence and provides a building block for topological quantum computation [8, 132].

While Majorana bound states have not yet been demonstrated experimentally, there is now a variety of candidate systems. In an s-wave superconductor, zero-point motion prevents the formation of bound states at zero energy. Early proposals for Majorana bound states therefore considered p-wave superconductors [6, 139], with Sr_2RuO_4 as a candidate material [147], or p-wave superfluids formed by fermionic cold atoms [148]. More recently, it was discovered [130, 149, 150] that Majorana bound states can be induced by s-wave superconductivity in a metal with a Dirac spectrum (such as graphene or the boundary of a topological insulator). Several tunneling experiments have been proposed [151–153] to search for the Majorana bound states predicted to occur in these systems.

Here we show that crossed Andreev reflection [154–156] by a pair of Majorana bound states is a direct probe of the nonlocality. *Crossed* Andreev reflection is the nonlocal conversion of an electron excitation into a hole excitation, each in a separate lead. *Local* Andreev reflection, in contrast, converts an electron into a hole in the same lead. Equivalently, local Andreev reflection injects a Cooper pair in a single lead, while crossed Andreev reflection splits a Cooper pair over two leads. We have found that at sufficiently low excitation energies, *local Andreev reflection by a pair of Majorana bound states is fully suppressed in favor of crossed Andreev reflection.*

The suppression is not a property of the leads dispersion relation (as in Refs. [157,
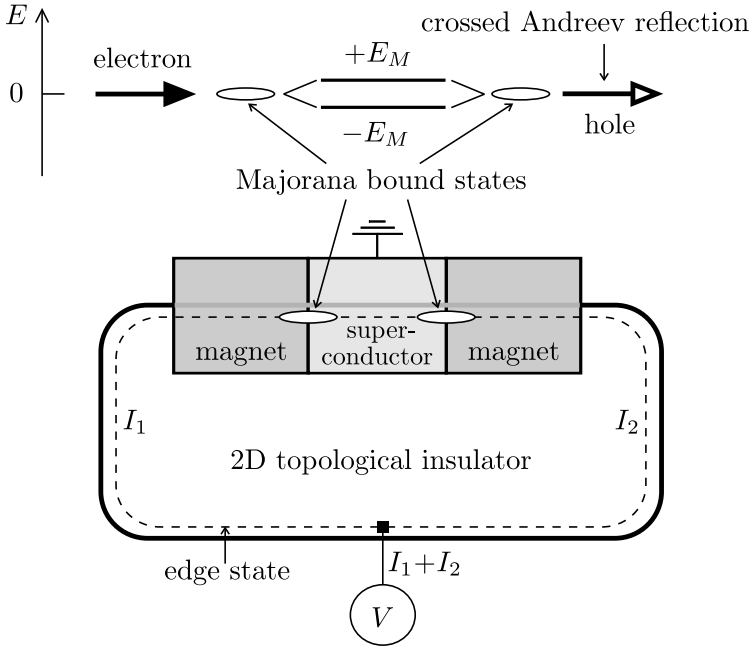
Figure 7.1: Top panel: Energy diagram of two Majorana bound states (levels at zero energy), which split into a pair of levels at $\pm E_M$ upon coupling. Whether the upper level is excited or not determines the states $|1\rangle$ and $|0\rangle$ of a qubit. Crossed Andreev reflection probes the nonlocality of this Majorana qubit. Lower panel: Detection of crossed Andreev reflection by correlating the currents I_1 and I_2 that flow into a superconductor via two Majorana bound states.

158]), but directly probes the Majorana character of the Hamiltonian [8]:

$$H_M = iE_M\gamma_1\gamma_2, \tag{7.1}$$

of the pair of weakly coupled bound states (labeled 1 and 2). The γ_i's are Majorana operators, defined by $\gamma_i = \gamma_i^\dagger$, $\gamma_i\gamma_j + \gamma_j\gamma_i = 2\delta_{ij}$. The coupling energy E_M splits the two zero-energy levels into a doublet at $\pm E_M$. The suppression of local Andreev reflection happens when the width Γ_M of the levels in the doublet (which is finite because of leakage into the leads) and the excitation energy E are both $\ll E_M$. (The relative magnitude of Γ_M and E does not matter.)

Our theoretical analysis is particularly timely in view of recent advances in the experimental realization of topological insulators in two-dimensional (2D) HgTe quantum wells [159, 160] and 3D BiSb crystals [161]. Topological insulators are characterized by an inverted band gap, which produces metallic states at the interface with vacuum or any material with a normal (noninverted) band gap [162–164]. The metallic states are

2D surface states if the insulator is 3D, while if the insulator is 2D the metallic states are 1D edge states.

These recent experiments [159–161] used nonsuperconducting electrodes. A superconducting proximity effect between Nb and BiSb was reported in earlier work [165], so that we expect a search for the predicted [130] Majorana bound states to be carried out in the near future. Anticipating these developments, we will identify observable consequences of the suppression of local Andreev reflection, by calculating the shot noise in a 2D topological insulator with a superconducting electrode (Fig. 7.1, lower panel). A similar calculation can be done for the 3D case, and indeed our conclusions are quite general — as we will now demonstrate by showing that the Majorana Hamiltonian (7.1) directly implies the suppression of local Andreev reflection.

7.2   Calculation of noise correlators

For this purpose write the unitary scattering matrix $S(E)$ in a model-independent form,

$$S(E) = 1 + 2\pi i W^\dagger (H_M - E - i\pi W W^\dagger)^{-1} W, \qquad (7.2)$$

with W the matrix that describes the coupling of the scatterer (Hamiltonian H_M) to the leads. In our case, we have

$$W = \begin{pmatrix} w_1 & 0 & w_1^* & 0 \\ 0 & w_2 & 0 & w_2^* \end{pmatrix}, \quad H_M = \begin{pmatrix} 0 & iE_M \\ -iE_M & 0 \end{pmatrix}. \qquad (7.3)$$

The expression for H_M is Eq. (7.1) in the basis $\{\Phi_1, \Phi_2\}$ of the two Majorana bound states, while W is the coupling matrix in the basis $\{\Phi_{e,1}, \Phi_{e,2}, \Phi_{h,1}, \Phi_{h,2}\}$ of propagating electron and hole modes in leads 1 and 2. We have assumed that lead 1 is coupled only to bound state 1 and lead 2 only to bound state 2, and we have also assumed that the energy dependence of the coupling amplitudes w_i can be neglected. (In the exact calculation given later on for a specific model, neither assumption will be made.) Without loss of generality we can choose the w_i's to be purely real numbers by adjusting the phases of the basis states in the leads.

Substitution of Eq. (7.3) into Eq. (7.2) gives the electron and hole blocks of the scattering matrix,

$$S \equiv \begin{pmatrix} s^{ee} & s^{eh} \\ s^{he} & s^{hh} \end{pmatrix} = \begin{pmatrix} 1+A & A \\ A & 1+A \end{pmatrix}, \qquad (7.4)$$

which turn out to depend on a single 2×2 matrix A with elements

$$A = Z^{-1} \begin{pmatrix} i\Gamma_1(E + i\Gamma_2) & -E_M\sqrt{\Gamma_1\Gamma_2} \\ E_M\sqrt{\Gamma_1\Gamma_2} & i\Gamma_2(E + i\Gamma_1) \end{pmatrix}. \qquad (7.5)$$

We have abbreviated

$$Z = E_M^2 - (E + i\Gamma_1)(E + i\Gamma_2), \quad \Gamma_i = 2\pi w_i^2. \qquad (7.6)$$

(The width Γ_M introduced earlier equals $\Gamma_1 + \Gamma_2$.) Unitarity of S is guaranteed by the identity

$$A + A^\dagger + 2AA^\dagger = 0. \tag{7.7}$$

In the limit of low excitation energies and weak coupling to the leads, this simplifies to

$$A \approx \frac{\sqrt{\Gamma_1 \Gamma_2}}{E_M} \begin{pmatrix} 0 & -1 \\ 1 & 0 \end{pmatrix}, \quad \text{for } E, \Gamma_i \ll E_M. \tag{7.8}$$

The scattering matrix $s^{he} = A$ that describes Andreev reflection of an electron into a hole has therefore only off-diagonal elements in this limit, so only *crossed* Andreev reflection remains. More specifically, an electron incident in lead 1 is transferred to the other lead 2 either as an electron or as a hole, with equal probabilities $p = \Gamma_1 \Gamma_2 / E_M^2$. The probability for local Andreev reflection is smaller than the probability p for crossed Andreev reflection by a factor $(\Gamma_1 / \Gamma_2)(E^2/E_M^2 + \Gamma_2^2/E_M^2) \ll 1$.

Because the probabilities to transfer to the other lead as an electron or as a hole are the same, crossed Andreev reflection cannot be detected in the time averaged current $\bar{I}_i$ in lead i, but requires measurement of the current fluctuations $\delta I_i(t) = I_i(t) - \bar{I}_i$. We consider the case that both leads are biased equally at voltage V, while the superconductor is grounded. At low temperatures $T \ll eV/k_B$ the current fluctuations are dominated by shot noise. In the regime $p \ll 1$ of interest, this noise consists of independent current pulses with Poisson statistics [166]. The Fano factor (ratio of noise power and mean current) measures the charge transferred in a current pulse.

The total (zero frequency) noise power $P = \sum_{ij} P_{ij}$, with

$$P_{ij} = \int_{-\infty}^{\infty} dt \, \overline{\delta I_i(0) \delta I_j(t)}, \tag{7.9}$$

has Fano factor $F = P/e\bar{I}$ (with $\bar{I} = \sum_i \bar{I}_i$) equal to 2 rather than equal to 1 because the superconductor can only absorb electrons in pairs [167]. As we will now show, the suppression of local Andreev reflection by the pair of Majorana bound states produces a characteristic signature in the individual noise correlators P_{ij}.

The general expressions for $\bar{I}_i$ and P_{ij} in terms of the scattering matrix elements are [168]:

$$\bar{I}_i = \frac{e}{h} \int_0^{eV} dE \left(1 - R_{ii}^{ee} + R_{ii}^{hh}\right), \tag{7.10}$$

$$P_{ij} = \frac{e^2}{h} \int_0^{eV} dE \, P_{ij}(E), \tag{7.11}$$

with the definitions

$$P_{ij}(E) = \delta_{ij} R_{ii}^{ee} + \delta_{ij} R_{ii}^{hh} - R_{ij}^{ee} R_{ji}^{ee} - R_{ij}^{hh} R_{ji}^{hh}$$
$$+ R_{ij}^{eh} R_{ji}^{he} + R_{ij}^{he} R_{ji}^{eh}, \tag{7.12}$$

$$R_{ij}^{xy}(E) = \sum_k s_{ik}^{xe}(E)[s_{jk}^{ye}(E)]^*, \quad x, y \in \{e, h\}. \tag{7.13}$$

Substitution of the special form (7.4) of S for the pair of Majorana bound states, results in

$$\bar{I}_i = \frac{2e}{h} \int_0^{eV} dE \, (AA^\dagger)_{ii}, \tag{7.14}$$

$$P_{ij} = e \bar{I}_i \delta_{ij} + \frac{2e^2}{h} \int_0^{eV} dE \left[\, |A_{ij} + (AA^\dagger)_{ij}|^2 - |(AA^\dagger)_{ij}|^2 \, \right], \tag{7.15}$$

where we have used the identity (7.7).

We now take the low energy and weak coupling limit, where A becomes the off-diagonal matrix (7.8). Then we obtain the remarkably simple result

$$P_{ij} = e \bar{I}_1 = e \bar{I}_2 = \frac{e \bar{I}}{2}, \ \ \text{for} \ \ eV, \Gamma_i \ll E_M. \tag{7.16}$$

The total noise power $P \equiv \sum_{ij} P_{ij} = 2e \bar{I}$ has Fano factor two, as it should be for transfer of Cooper pairs into a superconductor [167], but the noise power of the separate leads has unit Fano factor: $F_i \equiv P_{ii}/e \bar{I}_i = 1$. Because local Andreev reflection is suppressed, the current pulses in a single lead transfer charge e rather than $2e$ into the superconductor. The positive cross-correlation of the current pulses in the two leads ensures that the total transferred charge is $2e$. This "splitting" of a Cooper pair is a highly characteristic signature of a Majorana qubit, reminiscent of the h/e (instead of $h/2e$) flux periodicity of the Josephson effect [132, 133, 169].

Notice that for any stochastic process the cross-correlator is bounded by the auto-correlator,

$$|P_{12}| \leq \tfrac{1}{2}(P_{11} + P_{22}). \tag{7.17}$$

The positive cross-correlation (7.16) is therefore maximally large. This is a special property of the low energy, weak coupling limit. There is no inconsistency with the conclusion of Bolech and Demler [152], that the currents into two Majorana bound states fluctuate independently, because that conclusion applies to the regime $eV \gg E_M$. The duration $\hbar/eV$ of the current pulses is then shorter than the time $\hbar/E_M$ needed to transfer charge between the bound states, so no cross-correlations can develop. In this high-voltage regime the two Majorana bound states behave as independent Andreev resonances, for which the noise correlators are known [170],

$$P_{ii} = e \bar{I}_i, \ \ P_{12} = 0, \ \ \text{for} \ \ eV \gg E_M, \Gamma_i. \tag{7.18}$$

While the Fano factors of the individual leads $F_i = 1$ remain the same, the total noise power $P \equiv \sum_{ij} P_{ij} = e \bar{I}$ has Fano factor $F = 1$ rather than $F = 2$ when the cross-correlator P_{12} vanishes in the high-voltage regime.

As a specific model that can be solved exactly and is experimentally relevant, we consider a 2D topological insulator contacted at the edge by one superconducting electrode in between a pair of magnets (Fig. 7.1, bottom panel). As discoverd by Fu and Kane [130], a Majorana bound state appears at the intersection of the interface between

a magnet and a superconductor with the edge of the insulator. The four-component wave function $\Psi = (\Psi_{e\uparrow}, \Psi_{e\downarrow}, \Psi_{h\uparrow}, \Psi_{h\downarrow})$ of the edge state satisfies [130]:

$$\begin{pmatrix} \boldsymbol{m} \cdot \boldsymbol{\sigma} + vp\sigma_z - E_F & \Delta \\ \Delta^* & \boldsymbol{m} \cdot \boldsymbol{\sigma} - vp\sigma_z + E_F \end{pmatrix} \Psi = E\Psi. \qquad (7.19)$$

Here $p = -i\hbar\partial/\partial x$ is the momentum operator, E_F the Fermi energy, v the Fermi velocity, Δ the superconducting pair potential, $\boldsymbol{m}$ the magnetization vector, and $\boldsymbol{\sigma} = (\sigma_x, \sigma_y, \sigma_z)$ the vector of Pauli matrices (acting in the space of right and left movers $\uparrow, \downarrow$).

We set $\Delta(x) = 0$ everywhere except $\Delta = \Delta_0$ for $0 < x < l_0$. We also set $\boldsymbol{m}(x) = 0$ everywhere except $\boldsymbol{m} = (m_0, 0, 0)$ for $-l_1 < x < 0$ and $\boldsymbol{m} = (m_0 \cos\phi, m_0 \sin\phi, 0)$ for $l_0 < x < l_0 + l_2$. We assume that $|m_0| > |E_F|$, so that the Fermi level lies in a gap in the magnets as well as in the superconductor. The decay length in the superconductor is the coherence length $\xi_0 = \hbar v/\Delta_0$, while the decay length in the magnets is given by $\lambda_0 = \hbar v(m_0^2 - E_F^2)^{-1/2}$. For $\lambda_0 \lesssim \xi_0$ the only bound state at the magnet–superconductor interface is the zero-energy Majorana state.

We have calculated the scattering states for this model by matching the Ψ's at the opposite sides of the four interfaces $x = -l_1, 0, l_0, l_0 + l_2$. The resulting scattering matrix is then substituted in the general expressions (7.10–7.13) to obtain the zero-temperature, zero-frequency noise correlators as a function of the applied voltage V. Representative results are shown in Fig. 7.2 (data points). At low voltages we confirm the unit Fano factor and maximal cross-correlation of Eq. (7.16), obtained from the model-independent scattering matrix (7.2). Also the crossover to the conventional high-voltage regime (7.18) of independent resonances is clearly visible.

For a quantitative comparison of the two calculations we need the splitting and broadening of the Majorana bound states in the tunneling regime $l_1, l_2 \gg \lambda_0, l_0 \gg \xi_0$. We find

$$E_M = e^{-l_0/\xi_0} \cos\left[\frac{\phi}{2} + \frac{E_F l_0}{\hbar v} + \arctan\left(\frac{E_F \lambda_0}{\hbar v}\right)\right] \frac{2\hbar v}{\xi_0 + \lambda_0}, \qquad (7.20)$$

$$\Gamma_i = e^{-2l_i/\lambda_0}(1 - E_F^2/m_0^2) \frac{2\hbar v}{\xi_0 + \lambda_0}. \qquad (7.21)$$

Notice that the level splitting can be controlled by varying the angle ϕ between the magnetizations at the two sides of the superconductor.[1] In Fig. 7.2 we use these parameters to compare the model-independent calculation based on the scattering matrix (7.2) (curves) with the results from the model Hamiltonian (7.19) (data points), and find excellent agreement.

The setup sketched in Fig. 7.1 might be realized in a HgTe quantum well [159, 160]. The relevant parameters for this material are as follows. The gap in the bulk insulator is of the order of 20 meV and the magnetic gap can be as large as 3 meV at

---

[1]With respect to the level splitting, the angle ϕ between the magnetizations plays the same role as the superconducting phase difference in the Josephson junction of Ref. [133]. One can indeed derive an exact duality relation for the Hamiltonian (7.19) under the interchange $(m_x, m_y, m_z) \leftrightarrow (\text{Re}\,\Delta, \text{Im}\,\Delta, E_F)$
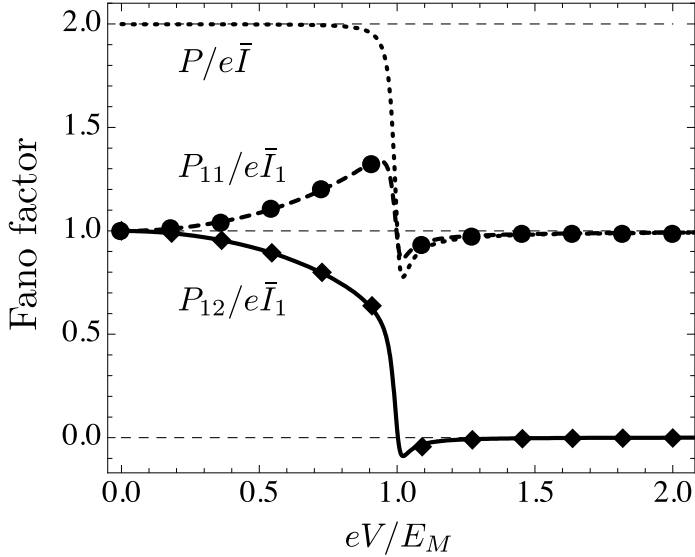
Figure 7.2: Data points: Auto-correlator P_{11} (circles) and cross-correlator P_{12} (diamonds) of the current fluctuations for the model Hamiltonian (7.19). The parameters chosen are $E_F = 0$, $\phi = 0$, $m_0/\Delta_0 = 1$, $l_0 = 2.3\,\xi_0$, $l_1 = l_2 = 3\,\xi_0$. The correlators are normalized by $e\bar{I}_1$, to demonstrate the low- and high-voltage limits (7.16) and (7.18). The dashed and solid curves result from the model-independent scattering matrix (7.2), with the parameters given by Eqs. (7.20) and (7.21). The dotted curve is the corresponding result for the total noise power $P = \sum_{ij} P_{ij}$, normalized by $e\bar{I} = e\sum_i \bar{I}_i$.

a magnetic field of 1 T. The smallest energy scale is therefore the gap induced by the superconductor, estimated [133] at $\Delta_0 = 0.1$ meV. With $\hbar v = 0.36$ meV $\cdot$ μm this gives a superconducting coherence length of $\xi_0 = 3.6\,\mu$m, comparable to the magnetic penetration length λ_0 at a field of 0.03 T. For the calculation in Fig. 7.2 we took $\xi_0 = \lambda_0$ and then took the length l_0 of the superconducting contact equal to $2.3\,\xi_0 \simeq 8\,\mu$m, and the lengths l_1, l_2 of the magnets both equal to $3\,\xi_0 \simeq 11\,\mu$m. The level splitting is then $E_M = 0.1\,\Delta_0 = 10\,\mu$eV $\cong 100$ mK. At a temperature of the order of 10 mK we would then have a sufficiently broad range of voltages where $k_B T < eV < E_M$.

7.3 Conclusion

In conclusion, we have demonstrated the suppression of local Andreev reflection by a pair of Majorana bound states at low excitation energies. The remaining crossed Andreev reflection amounts to the splitting of a Cooper pair over the two spatially separated halves of the Majorana qubit. This nonlocal scattering process has a characteristic signature in the maximal positive cross-correlation ($P_{12} = P_{11} = P_{22}$) of the current

fluctuations. The splitting of a Cooper pair by the Majorana qubit produces a pair of excitations in the two leads that are maximally entangled in the momentum (rather than the spin) degree of freedom, and might be used as "flying qubits" in quantum information processing.

Chapter 8

Electrically detected interferometry of Majorana fermions in a topological insulator

8.1 Introduction

There is growing experimental evidence [171–173] that the 5/2 fractional quantum Hall effect (FQHE) is described by the Moore-Read state [5]. This state has received much interest in the context of quantum computation [8], because its quasiparticle excitations are Majorana bound states. A qubit can be stored nonlocally in a pair of widely separated Majorana bound states, so that no local source of decoherence can affect it [132]. The state of the qubit can be read out and changed in a fault-tolerant way by edge state interferometry [174–176]. This "measurement based topological quantum computation" [177] combines static quasiparticles within the Hall bar to store the qubits, with mobile quasiparticles at the edge of the Hall bar to perform logical operations by means of interferometric measurements.

The electronic correlations in the Moore-Read state involve a pairing of spin-polarized fermions, equivalent to a superconducting pairing with $p_x + ip_y$ orbital symmetry [6, 139, 178]. Such an exotic pairing might occur naturally in the Sr_2RuO_4 superconductor [147], or it might be produced artificially in p-wave superfluids formed by fermionic cold atoms [148]. Recently, Fu and Kane [130] showed how a conventional s-wave superconductor might produce Majorana bound states, if brought in proximity to a topological insulator. This class of insulators has metallic surface states with massless quasiparticles, as has been demonstrated in Bi_xSb_{1-x} alloys [161] and Bi_2Se_3 single crystals [179, 180]. The latter material is particularly promising for applications because it remains a topological insulator at room temperature. The 5/2 FQHE, in contrast, persists only at temperatures well below 1 K [171–173].

While induced superconductivity in a topological insulator seems an attractive alternative to the FQHE for the purpose of quantum computation, one crucial difference creates a major obstacle: Quasiparticle excitations in the Moore-Read state have charge $\pm e/4$ (generated by changing the filling fraction of the half-filled Landau level), but in a superconductor the excitations have charge zero (the charge is screened by the supercon-
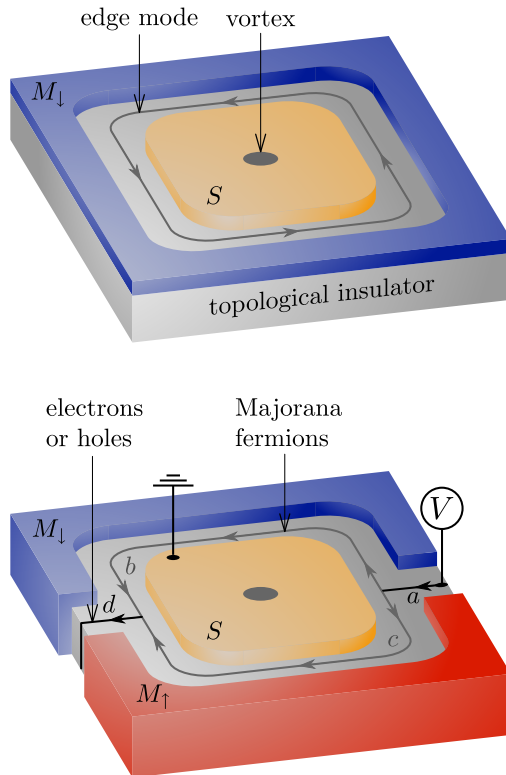
Figure 8.1: Three-dimensional topological insulator in proximity to ferromagnets with opposite polarization ($M_\uparrow$ and $M_\downarrow$) and to a superconductor (S). The top panel shows a single chiral Majorana mode along the edge between superconductor and ferromagnet. This mode is charge neutral, so it cannot be detected electrically. The Mach-Zehnder interferometer in the bottom panel converts a charged current along the domain wall into a neutral current along the superconductor (and vice versa). This allows for electrical detection of the parity of the number of enclosed vortices, as explained in the text.

ducting condensate). All known schemes [174–176] for edge state interferometry rely on electrical detection, and this seems impossible if the edge states carry no electrical current. It is the purpose of this work to propose a way around this obstacle, by showing how a pair of neutral Majorana fermions can be converted phase coherently and with unit probability into a charged Dirac fermion.

We first give a qualitative description of the mechanism of electrically detected Majorana interferometry, and then present a quantitative theory. Our key idea is to combine

edge channels of opposite chiralities in a single interferometer, by means of a magnetic domain wall. The appearance of counterpropagating edge channels in a single superconducting domain is a special feature of a topological insulator in proximity to a ferromagnet, where the propagation direction is determined by the way time reversal symmetry is broken outside of the condensate (hence by the polarization of the ferromagnets) — rather than being determined by the order parameter of the condensate (as in a $p_x \pm i p_y$ superconductor or FQHE droplet).

Refering to the lower panel of Fig. 8.1, we see that electrons or holes (with Dirac fermion operators $c_a^\dagger$ and c_a) propagate along the domain wall a until they reach the superconductor, where they are split into a pair of Majorana fermions γ_b and γ_c of opposite chirality:

$$c_a^\dagger \to \gamma_b + i\gamma_c, \quad c_a \to \gamma_b - i\gamma_c. \tag{8.1}$$

(Here we have used that $\gamma = \gamma^\dagger$, which is the defining property of a Majorana fermion.)

The Dirac-to-Majorana fermion conversion expressed by Eq. (8.1) relies on the fact that the electron or hole mode at the domain wall couples to *a pair* of Majorana modes, so that the full information encoded by the complex fermion c_a is encoded by two real fermions γ_b and γ_c. This is the essential distinction from the process of electron tunneling into a Majorana bound state [151–153, 181], which couples to *a single* Majorana fermion and can therefore not transfer the full information.

Upon leaving the superconductor the Majorana fermions recombine into an electron $c_d^\dagger$ or hole c_d depending on the number n_v of superconducting vortices enclosed by the two arms of the interferometer,

$$\gamma_b + (-1)^{n_v} i\gamma_c \to c_d^\dagger, \quad \gamma_b - (-1)^{n_v} i\gamma_c \to c_d. \tag{8.2}$$

For n_v an even integer, no charge is transfered to the superconductor, while for n_v odd a charge $\pm 2e$ is absorbed by the superconducting condensate. The conductance G, measured by application of a voltage between a point on the domain wall and the superconductor, becomes equal (in the zero-temperature, zero-voltage limit) to $G = 0$ for $n_v =$ even and $G = 2e^2/h$ for $n_v =$ odd.

8.2 Scattering matrix approach

Proceeding now to a theoretical description, we recall that the surface of a three-dimensional topological insulator, in the presence of a magnetization $M(r)$ and superconducting order parameter $\Delta(r)$, is described by the following Hamiltonian [130]:

$$H = \begin{pmatrix} M \cdot \sigma + v_F p \cdot \sigma - E_F & \Delta \\ \Delta^* & M \cdot \sigma - v_F p \cdot \sigma + E_F \end{pmatrix}. \tag{8.3}$$

Here $p = (p_x, p_y, 0)$ is the momentum on the surface, $\sigma = (\sigma_x, \sigma_y, \sigma_z)$ is the vector of Pauli matrices, v_F is the Fermi velocity, and E_F the Fermi energy. The two magnetizations $M_\uparrow$ and $M_\downarrow$ in Fig. 8.1 correspond to $M = (0, 0, M_0)$ and $M = (0, 0, -M_0)$,

respectively. Particle-hole symmetry is expressed by the anticommutation $H\,\Xi = -\Xi H$ of the Hamiltonian with the operator

$$\Xi = \begin{pmatrix} 0 & i\sigma_y\mathcal{C} \\ -i\sigma_y\mathcal{C} & 0 \end{pmatrix}, \tag{8.4}$$

with $\mathcal{C}$ the operator of complex conjuation.

There is a single chiral Majorana mode with amplitude ψ (group velocity v_m) at a boundary between a region with a superconducting gap and a region with a magnetic gap [130]. At a domain wall between two regions with opposite signs of M_z there are two chiral Dirac fermion modes, an electron mode with amplitude ϕ^e and a hole mode with amplitude ϕ^h. The scattering matrix $S_{\text{in}}(\varepsilon)$ describes scattering at excitation energy ε from electron and hole modes (along edge a) to two Majorana modes (along edges b and c in Fig. 8.1), according to

$$\begin{pmatrix} \psi_b \\ \psi_c \end{pmatrix} = S_{\text{in}} \begin{pmatrix} \phi_a^e \\ \phi_a^h \end{pmatrix}. \tag{8.5}$$

Particle-hole symmetry for the scattering matrix is expressed by

$$S_{\text{in}}(\varepsilon) = S_{\text{in}}^*(-\varepsilon) \begin{pmatrix} 0 & 1 \\ 1 & 0 \end{pmatrix}. \tag{8.6}$$

At small excitation energies $|\varepsilon| \ll |M_z|, |\Delta|$ the ε-dependence of S_{in} may be neglected. (The excitation energy is limited by the largest of voltage V and temperature T.) Then Eq. (8.6) together with unitarity ($S_{\text{in}}^{-1} = S_{\text{in}}^{\dagger}$) fully determine the scattering matrix,

$$S_{\text{in}} = \frac{1}{\sqrt{2}} \begin{pmatrix} 1 & 1 \\ \pm i & \mp i \end{pmatrix} \begin{pmatrix} e^{i\alpha} & 0 \\ 0 & e^{-i\alpha} \end{pmatrix}, \tag{8.7}$$

up to a phase difference α between electron and hole (which will drop out of the conductance and need not be further specified). The sign ambiguity (matrix elements $+i, -i$ or $-i, +i$) likewise does not affect the conductance.

The scattering matrix S_{out} for the conversion from Majorana modes to electron and hole modes can be obtained from S_{in} by time reversal,

$$S_{\text{out}}(\boldsymbol{M}) = S_{\text{in}}^T(-\boldsymbol{M}) = \frac{1}{\sqrt{2}} \begin{pmatrix} e^{i\alpha'} & 0 \\ 0 & e^{-i\alpha'} \end{pmatrix} \begin{pmatrix} 1 & \pm i \\ 1 & \mp i \end{pmatrix}. \tag{8.8}$$

The phase shift α' may be different from α, because of the sign change of $\boldsymbol{M}$ upon time reversal, but it will also drop out of the conductance.

The full scattering matrix S of the Mach-Zehnder interferometer in Fig. 8.1 is given by the matrix product

$$S \equiv \begin{pmatrix} S_{ee} & S_{eh} \\ S_{he} & S_{hh} \end{pmatrix} = S_{\text{out}} \begin{pmatrix} e^{i\beta_b} & 0 \\ 0 & e^{i\beta_c} \end{pmatrix} S_{\text{in}}, \tag{8.9}$$
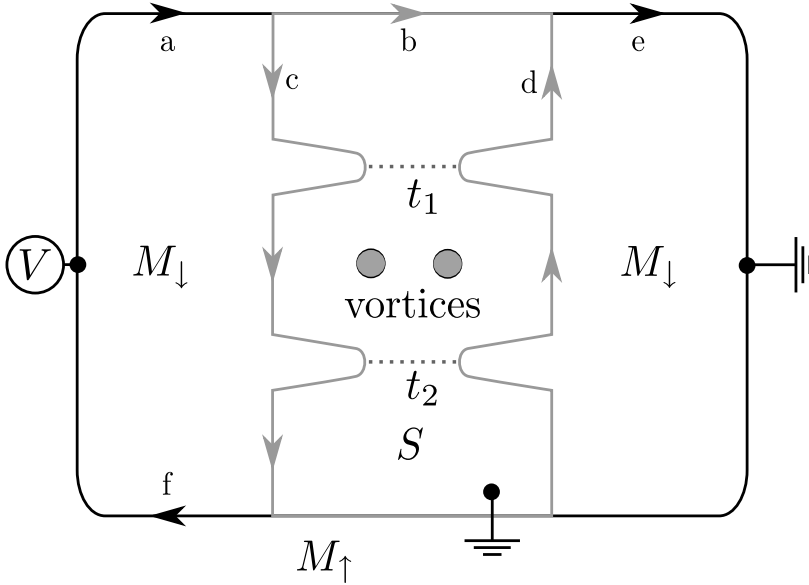
Figure 8.2: Fabry-Perot interferometer, allowing to measure the state of a qubit encoded in a pair of vortices. Black lines represent electron or hole modes at domain walls, gray lines represent Majorana modes at magnet-superconductor interface.

where β_b and β_c are the phase shifts accumulated by the Majorana modes along edge b and c, respectively. The relative phase

$$\beta_b - \beta_c = \varepsilon \delta L/\hbar v_m + \pi + n_v \pi \tag{8.10}$$

consists of three terms: A dynamical phase (proportional to the length difference $\delta L = L_b - L_c$ of the two arms of the interferometer), a Berry phase of π from the rotation of the spin-1/2, and an additional phase shift of π per enclosed vortex.

The differential conductance follows from

$$G(V) = \frac{2e^2}{h}|S_{he}(eV)|^2 = \frac{2e^2}{h}\sin^2\left(\frac{n_v\pi}{2} + \frac{eV\delta L}{2\hbar v_m}\right). \tag{8.11}$$

As announced in the introduction, the linear response conductance $G(0)$ vanishes if the number of vortices is even, while it has the maximal value of $2e^2/h$ if the number is odd. A finite temperature T will obscure the even-odd effect if $k_B T \gtrsim \hbar v_m/\delta L$. By reducing δL, the thermal smearing can be eliminated — leaving the requirement $k_B T \ll |M_z|, |\Delta|$ as the limiting factor.

8.3   Fabry-Perot interferometer

The Mach-Zehnder interferometer can distinguish between an even and an odd number n_v of enclosed *vortices*. The next step towards measurement based topological quantum computation is to distinguish between an even and an odd number n_f of enclosed *fermions*. If n_v is odd, the parity of n_f is undefined, but if n_v is even, the parity of n_f is a topologically protected quantity that determines the state of a qubit [8]. To electrically read out the state of a qubit encoded in a pair of charge-neutral vortices, we combine the Fabry-Perot interferometer of the FQHE [175, 176] with our Dirac-Majorana converter.

The geometry is shown in Fig. 8.2. Electrons are injected in the upper left arm a of the interferometer (biased at a voltage V) and the current I is measured in the upper right arm e (which is grounded). The electron at a is split into a pair of Majorana fermions ψ_b and ψ_c, according to the scattering matrix S_{in}. A pair of constrictions allows tunneling from ψ_c to ψ_d, with amplitude t_{dc}. Finally, the Majorana fermions ψ_d and ψ_b are recombined into an electron or hole at e, according to the scattering matrix S_{out}. The resulting net current $I = (e^2/h)V(|T_{ee}|^2 - |T_{he}|^2)$ (electron current minus hole current) is obtained from the transfer matrix

$$T = S_{\text{out}} \begin{pmatrix} e^{i\beta_b} & 0 \\ 0 & t_{dc} \end{pmatrix} S_{\text{in}} \Rightarrow I = \frac{e^2}{h} V \operatorname{Re}\left(e^{-i\beta_b} t_{dc}\right). \qquad (8.12)$$

Notice that the current is proportional to the tunnel *amplitude*, rather than to the tunnel probability. In the low-voltage limit, to which we will restrict ourselves in what follows, the phase shift β_b vanishes and t_{dc} is real (because of electron-hole symmetry) — so I directly measures the tunnel amplitude.

In general, two types of tunnel processes across a constriction contribute to t_{dc}: A Majorana fermion at the edge of the superconductor can tunnel through the superconducting gap to the opposite edge of the constriction either directly as a fermion or indirectly via vortex tunneling [182]. Fermion tunneling typically dominates over vortex tunneling, although quantum phase slips (and the associated vortex tunneling) might become appreciable in constrictions with a small capacitance [183] or in superconductors with a short coherence length [184]. Only vortex tunneling is sensitive to the fermion parity n_f, through the phase factor $(-1)^{n_f}$ acquired by a vortex that encircles n_f fermions. Because of this sensitivity, vortex tunneling is potentially distinguishable on the background of more frequent fermion tunneling events.

The contribution to t_{dc} from fermion tunneling is simply $t_{f,1} + (-1)^{n_v} t_{f,2}$, to lowest order in the fermion tunnel amplitudes $t_{f,1}$ and $t_{f,2}$ at the first and second constriction. There is no dependence on n_f, so we need not consider it further.

To calculate the contribution to t_{dc} from vortex tunneling, we apply the vortex tunnel Hamiltonian [182] $H_i = v_i \sigma_i \sigma_i'$, where $i = 1, 2$ labels the two constrictions and v_i is the tunnel coupling. The operators σ_i and σ_i' create a vortex at the left and right end of constriction i, respectively. The lowest order contribution to t_{dc} is of second order in the tunnel Hamiltonian, because two vortices need to tunnel in order to transfer a single Majorana fermion. The calculation of t_{dc} will be presented elsewhere, but the n_v and n_f dependence can be obtained without any calculation, as follows.

Three terms can contribute to second order in H_i, depending on whether both vortices tunnel at constriction number 1 (amplitude t_1^2), both at constriction number 2 (amplitude t_2^2), or one at constriction number 1 and the other at constriction number 2 (amplitude $2t_1t_2$). The resulting expression for t_{dc} is

$$t_{dc} = t_1^2 + t_2^2 + (-1)^{n_f} 2t_1t_2, \quad \text{if } n_v \text{ is even.} \tag{8.13}$$

We see that if the two constrictions are (nearly) identical, so $t_1 \approx t_2 \equiv t$, the tunnel amplitude t_{dc} and hence the current I_{vortex} due to vortex tunneling vanish if the fermion parity is odd, while $I_{\text{vortex}} = (e^2/h)V \times 4t^2$ if the fermion parity is even.[1]

8.4   Conclusion

In summary, we have proposed a method to convert a charged Dirac fermion into a pair of neutral Majorana fermions, encoding the charge degree of freedom in the relative phase of the two Majorana's. The conversion can be realized on the surface of a topological insulator at a junction between a magnetic domain wall (supporting a chiral charged mode) and two magnet-superconductor interfaces (each supporting a Majorana mode). We found that at low voltages the Dirac-Majorana conversion is geometry independent and fully determined by the electron-hole symmetry. It allows for the electrical read-out of a qubit encoded nonlocally in a pair of vortices, providing a building block for measurement based topological quantum computation.

Much experimental progress is needed to be able to perform Majorana interferometry in any system, and the topological insulators considered here are no exception. Induced superconductivity with critical temperature $T_c > 4\,\text{K}$ has been demonstrated in BiSb [165]. It is likely that the same could be achieved in Bi_2Se_3 (the most promising realization of a three-dimensional topological insulator [179, 180]). The even-odd vortex number effect of Eq. (8.11) would then be measurable at temperatures T well below T_c — if the arms of the interferometer can be balanced to eliminate thermal smearing ($\delta L < \hbar v_m / k_B T$). This would be the first experimental mile stone, reachable with current technology. The even-odd fermion number effect of Eq. (8.13) requires coherent vortex tunneling, which is a more long-term experimental challenge [183, 184].

---

[1]Eq. (8.13) assumes that the number n_v of bulk vortices in between the two constrictions is even, so that n_f is well-defined. When n_v is odd, a vortex tunneling at constriction number 2 exchanges a fermion with the bulk vortices [139]. If both vortices tunnel at constriction number 2, the two fermion exchanges compensate with a phase factor of -1, but if one vortex tunnels at constriction 1 and the other at constriction 2, then the single fermion exchange prevents the transfer of a Majorana fermion across the superconductor. The resulting expression for t_{dc} therefore contains only two terms, $t_{dc} = t_1^2 - t_2^2$, if n_v is odd.

Chapter 9

Domain wall in a chiral *p*-wave superconductor: a pathway for electrical current

9.1 Introduction

Chiral edge states are gapless excitations at the boundary of a two-dimensional system that can propagate in only a single direction. They appear prominently in the quantum Hall effect [185, 186]: The absence of backscattering in a chiral edge state explains the robustness of the quantization of the Hall conductance against disorder. Analogous phenomena in a superconductor with broken time reversal symmetry are known as the spin quantum Hall effect [6, 7, 187] and the thermal quantum Hall effect [188, 189], in reference to the transport of spin and heat along chiral edge states.

Unlike the original (electrical) quantum Hall effect, both these superconducting analogues have eluded observation, which is understandable since it is so much more difficult to measure spin and heat transport than electrical transport. Proposals to detect chiral edge states in a superconductor through their equilibrium magnetization are hindered by screening currents in the bulk, which cancel the magnetic field (Meissner effect) [190–193].

Here we show that the boundary between domains of opposite chirality ($p_x \pm i p_y$) in a chiral *p*-wave superconductor forms a one-way channel for electrical charge, in much the same way as edge states in the quantum Hall effect. This is not an immediate consequence of chirality: Since the charge of excitations in a superconductor is only conserved modulo the Cooper pair charge of $2e$, the absence of backscattering in a superconducting chiral edge state does not imply conservation of the electrical current. Indeed, one chiral edge state within a single domain has zero conductance due to electron-hole symmetry. We calculate the conductance of the domain wall, measured between a pair of metal contacts at the two ends (see Fig. 9.1), and find that it is nonzero, regardless of the separation of the contacts.

Our analysis is generally applicable to so-called class-D topological superconduc-
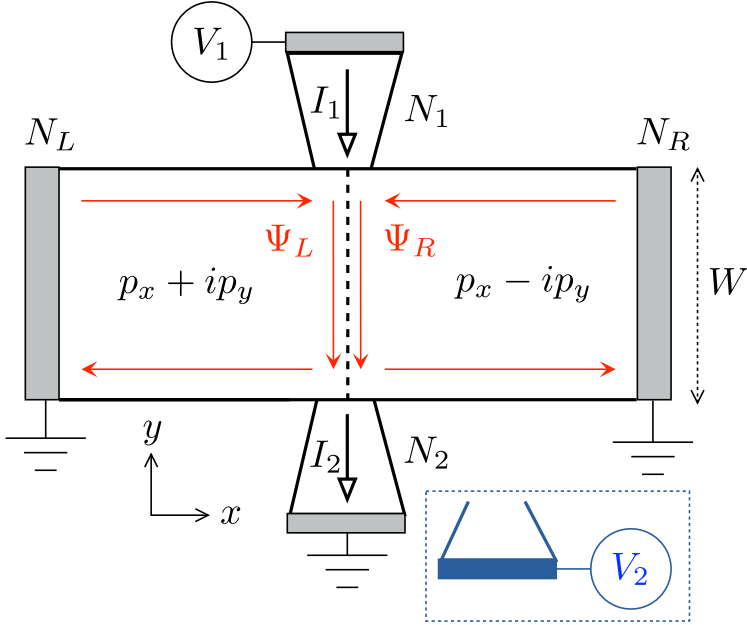
Figure 9.1: Superconducting strip divided by a domain wall (dashed line, length W) into domains with $p_x \pm i p_y$ symmetry. The edge states Ψ_L, Ψ_R of opposite chirality in the two domains are indicated by red arrows. These unpaired Majorana modes can carry heat current between contacts N_L and N_R, but no electrical current. A normal metal electrode N_1 at voltage V_1 injects charge into the domain wall, which is detected as an electrical current I_2 at the other end N_2. In an alternative measurement configuration (indicated in blue), contact N_2 measures a voltage V_2 without drawing a current.

tors [12, 194], characterized by the presence of electron-hole symmetry and the absence of both time-reversal and spin-rotation symmetry. It can be applied to the various realizations of chiral *p*-wave superconductors proposed in the literature (strontium ruthenate [193], superfluids of fermionic cold atoms [148, 195], and ferromagnet-superconductor heterostructures [131, 196]).

9.2   Calculation of transport properties

We start from the Bogoliubov-De Gennes equation,

$$
\begin{pmatrix} H_0 - E_F & \Delta \\ \Delta^\dagger & -H_0^* + E_F \end{pmatrix} \begin{pmatrix} u \\ v \end{pmatrix} = E \begin{pmatrix} u \\ v \end{pmatrix}, \tag{9.1}
$$

for coupled electron and hole excitations $u(\boldsymbol{r}), v(\boldsymbol{r})$ at energy E above the Fermi level E_F. The single-particle Hamiltonian is $H_0 = (\boldsymbol{p} + e\boldsymbol{A})^2/2m + U$, with $\boldsymbol{p} = -i\hbar\partial/\partial\boldsymbol{r}$

the momentum, $A(r)$ the vector potential, and $U(r)$ the electrostatic potential. The dynamics is two-dimensional, so $r = (x, y)$, $p = (p_x, p_y)$. The pair potential Δ has the spin-polarized-triplet p-wave form [140]:

$$\Delta = (2p_F)^{-1}(\eta \cdot p + p \cdot \eta),\tag{9.2}$$

in terms of a two-component order parameter $\eta = (\eta_x, \eta_y)$. The two chiralities $p_x \pm i p_y$ correspond to $\eta_\pm = \Delta_0 e^{i\phi}(1, \pm i)$, with Δ_0 the excitation gap and ϕ the superconducting phase. Since $\Delta^\dagger = -\Delta^*$, a solution (u, v) of Eq. (9.1) at energy E is related to another solution (v^*, u^*) at energy $-E$ (electron-hole symmetry). A domain wall along $x = 0$, with a phase difference ϕ between the domains, has order parameter [197, 198]

$$\eta_x(x) = \Delta_0[e^{-i\phi/2} \cos \chi(x) + e^{i\phi/2} \sin \chi(x)],\tag{9.3a}$$

$$\eta_y(x) = i\Delta_0[e^{-i\phi/2} \cos \chi(x) - e^{i\phi/2} \sin \chi(x)],\tag{9.3b}$$

The function $\chi(x)$ increases from 0 to $\pi/2$ over a coherence length $\xi_0 = \hbar v_F/\Delta_0$ around $x = 0$.

At energies E below Δ_0 the excitations are nondegenerate chiral edge states Ψ_L and Ψ_R circulating in opposite directions in the two domains [190, 199–201]. (See Fig. 9.1.) At the domain wall the two states mix, so that an excitation entering the domain wall in the state Ψ_L^{in} or Ψ_R^{in} can exit in either of the two states Ψ_L^{out} and Ψ_R^{out}. We first analyze this edge state scattering problem between contacts N_L and N_R, and then introduce the contacts N_1 and N_2 to the domain wall.

The edge state excitations have creation operators $\gamma^\dagger(E) = (\gamma_L^\dagger(E), \gamma_R^\dagger(E))$, which satisfy the electron-hole symmetry relation

$$\gamma(E) = \gamma^\dagger(-E).\tag{9.4}$$

At zero energy one has $\gamma = \gamma^\dagger$, so these are Majorana fermions [140]. The unitary scattering matrix $S(E)$ relates incoming and outgoing operators, $\gamma^{\text{out}}(E) = S(E)\gamma^{\text{in}}(E)$. Electron-hole symmetry for both γ^{in} and γ^{out} requires $S(E)\gamma^{\text{in}}(E) = \gamma^{\text{in}}(E)S^\dagger(-E)$, hence $S(E) = S^*(-E)$. The zero-energy scattering matrix $S(0) \equiv S_{dw}$ of the domain wall is therefore a real unitary, or orthogonal, matrix. We may parametrize it by

$$S_{dw} = \begin{pmatrix} \cos \psi & \sin \psi \\ (-1)^{p+1} \sin \psi & (-1)^p \cos \psi \end{pmatrix} = \sigma_z^p e^{i\psi\sigma_y},\tag{9.5}$$

in terms of a mixing angle ψ and a parity index $p \in \{0, 1\}$.

The mixing angle $\psi = k_y W$ is determined by the phase accumulated by the pair of chiral Majorana modes, as they propagate with wave number $\pm k_y$ along the domain wall of length W. The dispersion relation $E(k_y)$ of the Majorana modes was calculated in Ref. [200], for a step function order parameter at $x = 0$, including also the effect of a tunnel barrier $U = U_0\delta(x)$ (tunnel probability D, zero magnetic field). By equating $E(k_y) = 0$ and solving for k_y we obtain the mixing angle

$$\psi = k_F W \sqrt{D} \cos(\phi/2).\tag{9.6}$$

The mixing angle can in principle be measured through thermal transport between contacts N_L and N_R, since the heat current through the domain wall is $\propto \sin^2 \psi$. In what follows we consider instead a purely electrical measurement of transport along the domain wall, that (as we shall see) is independent of the degree of mixing of the Majorana modes.

The measurement that we propose consists of the injection of electrons from contact N_1 at voltage V_1 (relative to the superconductor) and the detection at contact N_2. We consider two detection schemes: In the first scheme contact N_2 is kept at the same potential as the superconductor and measures a current I_2, leading to the nonlocal conductance $G_{12} = I_2/V_1$. In the second scheme contact N_2 is a voltage probe drawing no net current and measuring a voltage V_2. The ratio $R_{12} = V_2/I_1$, with I_1 the current entering the superconductor through contact N_1, is the nonlocal resistance. The two nonlocal quantities are related by $R_{12} = G_{12}/G_1 G_2$, with $G_i = |I_i/V_i|$ the contact conductance of electrode N_i (measured with the other contact grounded).

We take the zero-temperature and zero-voltage limit, so that we can use the zero-energy scattering matrix to calculate the various conductances. The scattering problem at contact N_1 involves, in addition to the Majorana operators $\boldsymbol{\gamma} = (\gamma_L, \gamma_R)$, the electron and hole annihilation operators a_n and b_n in mode $n = 1, 2, \dots N$. These are related by $b_n(E) = a_n^\dagger(-E)$. The even and odd combinations $\gamma_n^\pm$, defined by

$$\begin{pmatrix} \gamma_n^+ \\ \gamma_n^- \end{pmatrix} = u \begin{pmatrix} a_n \\ b_n \end{pmatrix}, \quad u = \sqrt{\frac{1}{2}} \begin{pmatrix} 1 & 1 \\ -i & i \end{pmatrix}, \tag{9.7}$$

satisfy the same electron-hole symmetry relation (9.4) as γ_L, γ_R, and therefore represent Majorana fermions at $E = 0$. We denote $\boldsymbol{\gamma}_n = (\gamma_n^+, \gamma_n^-)$ and collect these operators in the vector $\boldsymbol{\Gamma} = (\boldsymbol{\gamma}_1, \boldsymbol{\gamma}_2, \dots \boldsymbol{\gamma}_N)$. The scattering matrix S_1 of contact N_1 relates incoming and outgoing operators,

$$\begin{pmatrix} \boldsymbol{\gamma} \\ \boldsymbol{\Gamma} \end{pmatrix}_{\text{out}} = S_1 \begin{pmatrix} \boldsymbol{\gamma} \\ \boldsymbol{\Gamma} \end{pmatrix}_{\text{in}}, \quad S_1 = \begin{pmatrix} r_1 & t_1 \\ t_1' & r_1' \end{pmatrix}. \tag{9.8}$$

Electron-hole symmetry implies that S_1 is $(2N + 2) \times (2N + 2)$ orthogonal matrix at zero energy. Similarly, the zero-energy scattering matrix S_2 of contact N_2 is a $(2N' + 2) \times (2N' + 2)$ orthogonal matrix. (The number of modes is N, N' in contacts N_1, N_2 respectively.)

The $2N' \times 2N$ transmission matrix

$$t_{21} = t_2' S_{dw} t_1 = t_2' \sigma_z^p e^{i\psi\sigma_y} t_1 \tag{9.9}$$

from contact N_1 to N_2 is the product of the $2 \times 2N$ submatrix t_1 of S_1 (transmission from N_1 to the domain wall), the 2×2 scattering matrix S_{dw} (transmission along the domain wall), and the $2N' \times 2$ submatrix t_2' of S_2 (transmission from the domain wall to N_2).

The total transmission probability T_{ee}, summed over all modes, of an electron at

contact N_1 to an electron at contact N_2 is given by

$$T_{ee} = \tfrac{1}{4}\mathrm{Tr}\, U^\dagger t_{21}^\dagger U(1 + \Sigma_z)U^\dagger t_{21}U(1 + \Sigma_z) \tag{9.10}$$

$$= \tfrac{1}{4}\mathrm{Tr}\, t_{21}^\dagger(1 - \Sigma_y)t_{21}(1 - \Sigma_y), \tag{9.11}$$

where we have defined the direct sums $U = u \oplus u \cdots \oplus u$, $\Sigma_i = \sigma_i \oplus \sigma_i \cdots \oplus \sigma_i$ and we have used that $u\sigma_z u^\dagger = -\sigma_y$. Similarly, the total electron-to-hole transmission probability T_{he} reads

$$T_{he} = \tfrac{1}{4}\mathrm{Tr}\, t_{21}^\dagger(1 + \Sigma_y)t_{21}(1 - \Sigma_y). \tag{9.12}$$

Since $I_2 = (e^2/h)V_1(T_{ee} - T_{he})$, the nonlocal conductance takes the form

$$G_{12} = (e^2/h)\tfrac{1}{2}\mathrm{Tr}\, t_{21}^T \Sigma_y t_{21} \Sigma_y. \tag{9.13}$$

We have used that $t_{21}^\dagger = t_{21}^T$ and $\mathrm{Tr}\, t_{21}^T \Sigma_y t_{21} = 0$ (being the trace of an antisymmetric matrix). The nonlocal resistance can be written in a similar form upon division by the contact conductances,

$$R_{12} = \frac{G_{12}}{G_1 G_2}, \quad G_i = (e^2/h)\tfrac{1}{2}\mathrm{Tr}\,(1 - \Sigma_y r_i'^T \Sigma_y r_i'). \tag{9.14}$$

We will henceforth set e^2/h to unity in most equations.

Substitution of Eq. (9.9) into Eq. (9.13) gives the conductance

$$G_{12} = \tfrac{1}{2}\mathrm{Tr}\, T_1 S_{dw}^T T_2 S_{dw}, \tag{9.15}$$

in terms of the 2×2 matrices $T_1 = t_1 \Sigma_y t_1^T$, $T_2 = t_2'^T \Sigma_y t_2'$. We now use the identity

$$\mathrm{Tr}\, A_1 A_2 = \tfrac{1}{2}\left(\mathrm{Tr}\, A_1 \sigma_y\right)\left(\mathrm{Tr}\, A_2 \sigma_y\right), \tag{9.16}$$

valid for any pair of 2×2 antisymmetric matrices A_1, A_2. Taking $A_1 = T_1$, $A_2 = S_{dw}^T T_2 S_{dw}$ we arrive at

$$G_{12} = (-1)^p \alpha_1 \alpha_2, \quad \alpha_i = \tfrac{1}{2}\mathrm{Tr}\, T_i \sigma_y, \tag{9.17a}$$

$$R_{12} = (-1)^p \beta_1 \beta_2, \quad \beta_i = \alpha_i/G_i, \tag{9.17b}$$

since $\mathrm{Tr}\, S_{dw}^T T_2 S_{dw} \sigma_y = (-1)^p \mathrm{Tr}\, T_2 \sigma_y$ in view of Eq. (9.5).

Eq. (9.17) expresses the nonlocal conductance and resistance in terms of the scattering matrices S_1, S_2 of the two contacts N_1, N_2. The scattering matrix S_{dw} of the domain wall enters only through the parity index p, and not through the mixing angle ψ. That the transferred charge depends only on a parity index is a generic feature of a single-mode scattering problem with class D symmetry [144, 145, 202–204]. Quite generally, p counts the number (modulo 2) of zero-energy bound states, which in our case would be trapped in vortices in the domain wall.

A measurement of the domain wall conductance would have several characteristic features: Most prominently, the conductance is zero unless both contacts N_1 and N_2 are at the domain wall; if at least one contact is moved away from the domain wall, the conductance vanishes because a single Majorana edge mode cannot carry an electrical current at the Fermi level.[1] This feature would distinguish chiral p-wave superconductors (symmetry class D) from chiral d-wave superconductors (symmetry class C), where the Majorana edge modes come in pairs and can carry a current. The chirality itself can be detected by interchanging the injecting and detecting contacts: only one choice can give a nonzero conductance. While vortices trapped in the domain wall can change the sign of the conductance (through the parity index p), other properties of the domain wall have no effect on G_{12}. In particular, there is no dependence on the length W.

To illustrate these features in a model calculation, we consider the case of two single-mode contacts ($N = N' = 1$) coupled to the domain wall through a disordered interface. We model the effect of disorder using random contact scattering matrices S_1 and S_2, drawn independently with a uniform distribution from the ensemble of 4×4 orthogonal matrices. In the context of random-matrix theory [121], uniformly distributed ensembles of unitary matrices are called "circular", so our ensemble could be called the "circular real ensemble" (CRE) — to distinguish it from the usual circular unitary ensemble (CUE) of complex unitary matrices.[2]

Using the expression for the uniform measure on the orthogonal group [204] (see also App. 9.A), we obtain the distributions of the parameters α_i and β_i characterizing contact N_i:

$$P(\alpha) = 1 - |\alpha|, \quad P(\beta) = (1 + |\beta|)^{-2}, \quad |\alpha|, |\beta| \leq 1. \quad (9.18)$$

The distribution of the nonlocal conductance $G_{12} = (-1)^p \alpha_1 \alpha_2$, plotted in Fig. 9.2, then follows from

$$P(G_{12}) = \int_{-1}^{1} d\alpha_1 \int_{-1}^{1} d\alpha_2 \, \delta(G_{12} - \alpha_1 \alpha_2) P(\alpha_1) P(\alpha_2)$$
$$= 4|G_{12}| - 4 - 2(1 + |G_{12}|) \ln |G_{12}|, \quad |G_{12}| < 1. \quad (9.19)$$

(There is no dependence on the parity index p because P is symmetric around zero.) The distribution of the nonlocal resistance $R_{12} = (-1)^p \beta_1 \beta_2$ follows similarly and as we can see in Fig. 9.2 it lies close to $P(G_{12})$.

The difference between the two quantities G_{12} and R_{12} becomes important if the contacts between the metal and the superconductor contain a tunnel barrier. A tunnel barrier suppresses G_{12} but has no effect on R_{12}. More precisely (for more details see App. 9.B), any series resistance in the single-mode contacts N_1 and N_2 which does not

---

[1]That the nonlocal conductance vanishes if one of the two contacts couples only to a single domain, can be seen directly from Eq. (9.17): If, say, contact 1 couples only to the right domain, then only the $2, 2$ element of T_1 can be nonzero, but since this matrix is antisymmetric the $2, 2$ element must also vanish and T_1 must be zero identically. This implies $\alpha_1 = 0$, hence $G_{12} = 0$.

[2]The name "circular orthogonal ensemble" (COE) might be more appropriate for the ensemble of uniformly distributed orthogonal matrices, but this name is already in use for the ensemble of unitary symmetric matrices.
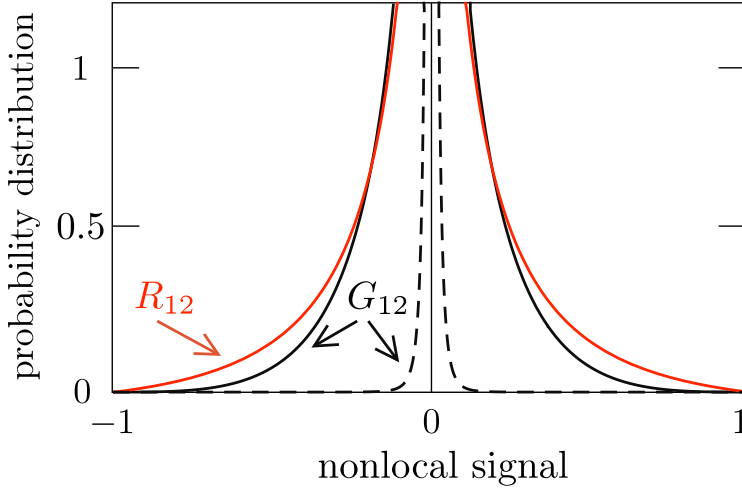
Figure 9.2: Solid curves: probability distributions of the nonlocal conductance G_{12} (in units of e^2/h) and nonlocal resistance R_{12} (in units of h/e^2). These are results for a random distribution of the 4×4 orthogonal scattering matrices S_1 and S_2. The dashed curve shows the narrowing effect on $P(G_{12})$ of a tunnel barrier in both contacts (tunnel probability $\tau = 0.1$). In contrast, $P(R_{12})$ is not affected by a tunnel barrier.

couple electrons and holes drops out of the nonlocal resistance R_{12}. This remarkable fact is again a consequence of the product rule (9.16), which allows to factor a series conductance into a product of conductances. A tunnel barrier in contact i then appears as a multiplicative factor in α_i and G_i, and thus drops out of the ratio $\beta_i = \alpha_i/G_i$ determining R_{12}.

To demonstrate the effect of a tunnel barrier (tunnel probability τ), we have calculated the distribution of α using the Poisson kernel of the CRE [205], with the result

$$P(\alpha, \tau) = \frac{\tau^2}{[\tau + (1-\tau)|\alpha|]^3} - \frac{\tau^2|\alpha|}{[\tau + (1-\tau)\alpha^2]^2}. \tag{9.20}$$

The distribution of β remains given by Eq. (9.18), independent of τ. The dashed curves in Fig. 9.2 show how the resulting distribution of the nonlocal conductance becomes narrowly peaked around zero for small τ, in contrast to the distribution of the nonlocal resistance.

9.3   Discussion

Among the various candidate systems for chiral p-wave superconductivity, the recent proposal [131] based on the proximity effect in a semiconducting two-dimensional electron gas seems particularly promising for our purpose. Split-gate quantum point con-

tacts (fabricated with well-established technology) could serve as single-mode injector and detector of electrical current. The chirality of the superconducting domains is determined by the polarity of an insulating magnetic substrate, so the location of the domain wall could be manipulated magnetically. The appearance of a nonlocal signal between the two point contacts would detect the domain wall and the disappearance upon interchange of injector and detector would demonstrate the chirality.

As a direction for further research, we note that domains of opposite chirality are formed spontaneously in disordered samples. Since, as we have shown here, domain walls may carry electric current, a network of domain walls contributes to the conductivity and may well play a role in the anomalous (parity violating) current-voltage characteristic reported recently [206].

9.A   Averages over the circular real ensemble

To calculate the distributions (9.18) of the parameters α_i and β_i we need the probability distribution of the 4×4 scattering matrix S_i of contact $i = 1, 2$ in the CRE. We may either work in the basis of electron and hole states, as in Ref. [204], or in the basis of Majorana states. Here we give a derivation of Eq. (9.18) using the latter basis (which is the basis we used in the main text).

A 4×4 orthogonal scattering matrix has the polar decomposition

$$S = \begin{pmatrix} e^{i\phi_1\sigma_y} & 0 \\ 0 & e^{i\phi_2\sigma_y} \end{pmatrix} \begin{pmatrix} S & C \\ (-1)^{p+1}C & (-1)^p S \end{pmatrix} \begin{pmatrix} e^{i\phi_3\sigma_y} & 0 \\ 0 & e^{i\phi_4\sigma_y} \end{pmatrix}, \qquad (9.21)$$

$$C = \begin{pmatrix} \cos\psi_1 & 0 \\ 0 & \cos\psi_2 \end{pmatrix}, \quad S = \begin{pmatrix} \sin\psi_1 & 0 \\ 0 & \sin\psi_2 \end{pmatrix}, \qquad (9.22)$$

in terms of six real angles. We need the uniform measure on the orthogonal group, which defines the probability distribution in the circular real ensemble (CRE). This calculation proceeds along the same lines as in Ref. [204] (where a different parametrization, in the electron-hole basis, was used). The result is that the angles $\phi_1, \phi_2, \phi_3, \phi_4$ are uniformly distributed in $(0, 2\pi)$, while the angles ψ_1, ψ_2 have the distribution

$$P(\psi_1, \psi_2) = \tfrac{1}{4}|\cos^2\psi_1 - \cos^2\psi_2|, \quad 0 < \psi_1, \psi_2 < \pi. \qquad (9.23)$$

We can now obtain the joint distribution $P(\alpha_i, G_i)$ of the injection (or detection) efficiency α_i and the (dimensionless) contact conductance G_i of contact i. (We drop the label i for ease of notation.) By definition,

$$\alpha = \tfrac{1}{2}\mathrm{Tr}\, t\sigma_y t^T \sigma_y = \cos\psi_1 \cos\psi_2, \qquad (9.24)$$

$$G = 1 - \tfrac{1}{2}\mathrm{Tr}\, r\sigma_y r^T \sigma_y = 1 - \sin\psi_1 \sin\psi_2. \qquad (9.25)$$

Notice the trigonometric inequality

$$0 \le |\alpha| \le G \le 2 - |\alpha|. \qquad (9.26)$$
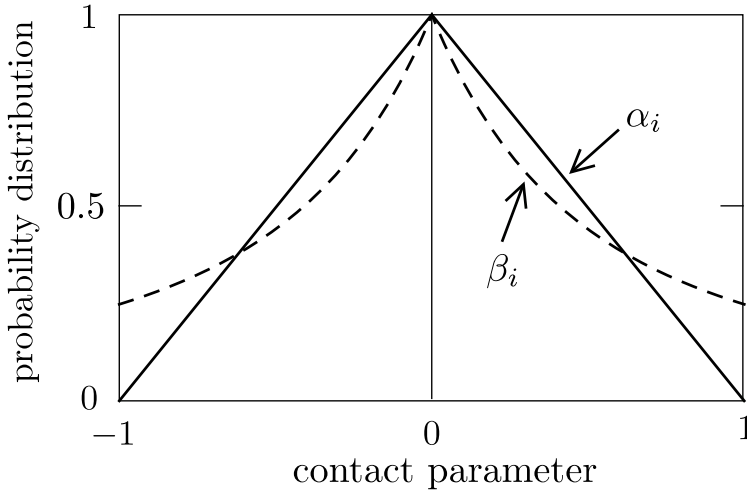
Figure 9.3: Probability distributions of the parameters α_i and $\beta_i = \alpha_i / G_i$ that characterize a single-mode contact in the CRE, given by Eqs. (9.28) and (9.30). The distribution (9.29) of $G_i - 1$ is the same as that of α_i, but these two quantities are not independent because of the inequality (9.26).

By averaging over the CRE we find, remarkably enough, that the joint distribution of α and G is uniform when constrained by this inequality,

$$P(\alpha, G) = \int_0^\pi d\psi_1 \int_0^\pi d\psi_2 \, P(\psi_1, \psi_2)$$
$$\times \, \delta(\alpha - \cos\psi_1 \cos\psi_2)\delta(G - 1 + \sin\psi_1 \sin\psi_2)$$
$$= \begin{cases} 1/2 & \text{if } 0 \leq |\alpha| \leq G \leq 2 - |\alpha|, \\ 0 & \text{elsewise.} \end{cases} \tag{9.27}$$

The marginal distributions of α, G, and $\beta = \alpha/G$ now follow by integration over $P(\alpha, G)$,

$$P(\alpha) = 1 - |\alpha|, \quad |\alpha| < 1, \tag{9.28}$$

$$P_G(G) = 1 - |G - 1|, \quad 0 < G < 2, \tag{9.29}$$

$$P(\beta) = (1 + |\beta|)^{-2}, \quad |\beta| < 1, \tag{9.30}$$

in accord with Eq. (9.18). We have plotted these distributions in Fig. 9.3.

9.B   Proof that the tunnel resistance drops out of the nonlocal resistance

According to Eq. (9.17), the nonlocal conductance G_{12} is determined by the product of the injection efficiency α_1 of contact N_1 and the detection efficiency α_2 of contact N_2. A tunnel barrier between the metal electrode and the superconductor suppresses the injection/detection efficiencies and thereby suppresses the nonlocal conductance.

The nonlocal resistance R_{12} is determined by the ratio α_i / G_i of the injection/detection efficiency and the contact conductance G_i. Since both α_i and G_i are suppressed by a tunnel barrier, one might hope that R_{12} would remain of order e^2 / h. In this Appendix we investigate the effect of a tunnel barrier on the nonlocal resistance, and demonstrate that it drops out identically for a single-mode contact between the normal metal and the superconductor.

The key identity that we will use to prove this cancellation, is the product rule (9.16) and two corollaries:

$$\tfrac{1}{2}\mathrm{Tr}\left(\prod_i M_i\right)\sigma_y\left(\prod_i M_i\right)^T\sigma_y = \prod_i\left(\tfrac{1}{2}\mathrm{Tr}\,M_i\sigma_y M_i^T\sigma_y\right), \tag{9.31a}$$

$$\tfrac{1}{2}\mathrm{Tr}\,(M\sigma_y M^T\sigma_y)^{-1} = \left[\tfrac{1}{2}\mathrm{Tr}\,M\sigma_y M^T\sigma_y\right]^{-1}, \tag{9.31b}$$

valid for arbitrary 2×2 matrices M_i.

Considering any one of the two contacts, we assume that its scattering matrix S_0 is modified by a tunnel barrier with scattering matrix δS. Transmission and reflection submatrices are defined as in Eq. (9.8),

$$S_0 = \begin{pmatrix} r_0 & t_0 \\ t_0' & r_0' \end{pmatrix}, \quad \delta S = \begin{pmatrix} \delta r & \delta t \\ \delta t' & \delta r' \end{pmatrix}. \tag{9.32}$$

For a single-mode contact, each submatrix has dimension 2×2. Both S_0 and δS are real orthogonal matrices at zero energy (in the basis of Majorana fermions). The tunnel barrier does not couple electrons and holes, which means that the submatrices of δS must commute with σ_y,

$$[\sigma_y, \delta r] = [\sigma_y, \delta r'] = [\sigma_y, \delta t] = [\sigma_y, \delta t'] = 0. \tag{9.33}$$

The submatrices of S_0 are not so constrained.

The total scattering matrix S of the contact is constructed from S_0 and δS, according to the composition rule for scattering matrices. The transmission and reflection submatrices of S take the form

$$t = t_0(1 - \delta r r_0')^{-1}\delta t, \tag{9.34a}$$

$$t' = \delta t'(1 - r_0'\delta r)^{-1}t_0', \tag{9.34b}$$

$$r' = \delta r' + \delta t' r_0'(1 - \delta r r_0')^{-1}\delta t, \tag{9.34c}$$

$$r = r_0 + t_0\delta r(1 - r_0'\delta r)^{-1}t_0'. \tag{9.34d}$$

The injection efficiency α and detection efficiency α' are defined by

$$\alpha = \tfrac{1}{2}\mathrm{Tr}\, t\sigma_y t^T \sigma_y, \quad \alpha' = \tfrac{1}{2}\mathrm{Tr}\, t'\sigma_y t'^T \sigma_y. \qquad (9.35)$$

Using the identities (9.31a) and (9.31b) we can factor these quantities,

$$\alpha = \alpha_0 \delta\alpha/X, \quad \alpha' = \alpha_0' \delta\alpha'/X, \qquad (9.36)$$

into the product of the injection/detection efficiencies α_0, α_0' without the tunnel barrier and terms containing the effect of the tunnel barrier:

$$\alpha_0 = \tfrac{1}{2}\mathrm{Tr}\, t_0\sigma_y t_0^T \sigma_y, \quad \alpha_0' = \tfrac{1}{2}\mathrm{Tr}\, t_0'\sigma_y t_0'^T \sigma_y, \qquad (9.37a)$$

$$\delta\alpha = \tfrac{1}{2}\mathrm{Tr}\, \delta t\sigma_y \delta t^T \sigma_y, \quad \delta\alpha' = \tfrac{1}{2}\mathrm{Tr}\, \delta t'\sigma_y \delta t'^T \sigma_y, \qquad (9.37b)$$

$$X = \tfrac{1}{2}\mathrm{Tr}\, (1 - \delta r r_0')\sigma_y (1 - \delta r r_0')^T \sigma_y. \qquad (9.37c)$$

Since δt and $\delta t'$ commute with σ_y, the terms $\delta\alpha, \delta\alpha'$ simplify to

$$\delta\alpha = \delta\alpha' = \tfrac{1}{2}\mathrm{Tr}\, \delta t \delta t^T, \qquad (9.38)$$

where we have used the orthogonality condition, $\delta S^T \delta S = \delta S \delta S^T = 1$, to equate the traces of $\delta t \delta t^T$ and $\delta t' \delta t'^T$. The term X can similarly be reduced to

$$X = 1 + (1 - \delta\alpha)(1 - G_0) - \mathrm{Tr}\, \delta r r_0', \qquad (9.39)$$

where G_0 is the contact conductance (in units of e^2/h) in the absence of the tunnel barrier:

$$G_0 = \tfrac{1}{2}\mathrm{Tr}\, (1 - r_0'\sigma_y r_0'^T \sigma_y). \qquad (9.40)$$

We now turn to the contact conductances G_i, in order to show that the effect of the tunnel barrier is contained in the same factor $\delta\alpha/X$ (which will then cancel out of the ratio $\beta_i = \alpha_i/G_i$). Considering again a single contact, and dropping the index i for ease of notation, we start from the definition of the contact conductance (in units of e^2/h):

$$G = \tfrac{1}{2}\mathrm{Tr}\, (1 - r'\sigma_y r'^T \sigma_y). \qquad (9.41)$$

We substitute Eq. (9.34c), and try to factor out the terms containing the transmission and reflection matrices of the tunnel barrier.

It is helpful to first combine the two terms in Eq. (9.34c) into a single term, using the orthogonality of δS:

$$r' = -(\delta t'^T)^{-1}\delta r^T \delta t + \delta t' r_0'(1 - \delta r r_0')^{-1}\delta t$$
$$= (\delta t'^T)^{-1}(r_0' - \delta r^T)(1 - \delta r r_0')^{-1}\delta t. \qquad (9.42)$$

We now substitute Eq. (9.42) into Eq. (9.13) and use the identities (9.31) to factor the trace,

$$G = 1 - X^{-1}\tfrac{1}{2}\mathrm{Tr}\, (r_0' - \delta r^T)\sigma_y (r_0'^T - \delta r)\sigma_y$$
$$= 1 - X^{-1}(2 - \delta\alpha - G_0 - \mathrm{Tr}\, \delta r r_0'), \qquad (9.43)$$

where we also used the commutation relations (9.33). The remaining trace of $\delta r r'_0$ can be eliminated with the help of Eq. (9.39), and so we finally arrive at the desired result:

$$G = G_0 \delta\alpha / X. \tag{9.44}$$

Chapter 10

Quantized conductance at the Majorana phase transition in a disordered superconducting wire

10.1 Introduction

It has been predicted theoretically [207, 208] that the *s*-wave proximity effect of a superconducting substrate can drive a spin-polarized and spin-orbit coupled semiconductor nanowire into a topological phase [6, 132, 209], with a Majorana fermion trapped at each end of the wire. There exists now a variety of proposals [143, 210, 211] for topological quantum computing in nanowires that hope to benefit from the long coherence time expected for Majorana fermions. A superconducting proximity effect in InAs wires (which have the required strong spin-orbit coupling) has already been demonstrated in zero magnetic field [212], and now the experimental challenge is to drive the system through the Majorana phase transition in a parallel field.

Proposals to detect the topological phase have focused on the detection of the Majorana bound states at the end points of the wire, through their effect on the current-voltage characteristic [203, 213] or the AC Josephson effect [133, 200]. These signatures of the topological phase would stand out in a clean single-mode wire, but the multiple modes and potential fluctuations in a realistic system are expected to produce a chain of coupled Majorana's [214, 215], which would form a band of low-lying excitations that would be difficult to distinguish from ordinary fermionic bound states [216].

Here we propose an altogether different detection strategy: Rather than trying to detect the Majorana bound states inside the topological phase, we propose to detect the phase transition itself. A topological phase transition is characterized by a change in the topological quantum number Q. The value of $Q = (-1)^m$ is determined by the parity of the number m of Majorana bound states at each end of the wire, with $Q = -1$ in the topological phase [217, 218].

In accord with earlier work [219], we relate the topological quantum number to the determinant of the matrix r of quasiparticle reflection amplitudes, which crosses zero at

the phase transition. This immediately implies a unit transmission eigenvalue at the transition. Disorder may shift the position of the transition but it cannot affect the unit height of the transmission peak. We propose experiments to measure the transmission peak in both thermal and electrical transport properties, and support our analytical predictions by computer simulations.

10.2 Topological charge

We consider a two-terminal transport geometry, consisting of a disordered superconducting wire of length L, connected by clean normal-metal leads to reservoirs in thermal equilibrium (temperature τ_0). The leads support $2N$ right-moving modes and $2N$ left-moving modes at the Fermi level, with mode amplitudes ψ_+ and ψ_-, respectively. The spin degree of freedom is included in the number N, while the factor of two counts the electron and hole degree of freedom.

The $4N \times 4N$ unitary scattering matrix S relates incoming and outgoing mode amplitudes,

$$\begin{pmatrix} \psi_{-,\mathrm{L}} \\ \psi_{+,\mathrm{R}} \end{pmatrix} = S \begin{pmatrix} \psi_{+,\mathrm{L}} \\ \psi_{-,\mathrm{R}} \end{pmatrix}, \quad S = \begin{pmatrix} r & t' \\ t & r' \end{pmatrix}, \tag{10.1}$$

where the labels L and R distinguish modes in the left and right lead. The four blocks of S define the $2N \times 2N$ reflection matrices r, r' and transmission matrices t, t'.

Time-reversal symmetry and spin-rotation symmetry are broken in the superconductor, but electron-hole symmetry remains. At the Fermi energy electron-hole symmetry implies that if (u, v) is an electron-hole eigenstate, then also (v^*, u^*). Using this symmetry we can choose a basis such that all modes have purely real amplitudes. In this so-called Majorana basis S is a real orthogonal matrix, $S^{\mathrm{t}} = S^{\dagger} = S^{-1}$. (The superscript t indicates the transpose of a matrix.) More specifically, since $\det S = 1$ the scattering matrix is an element of the special orthogonal group $\mathrm{SO}(4N)$. This is symmetry class D [220–225].[1]

The scattering matrix in class D has the polar decomposition

$$S = \begin{pmatrix} O_1 & 0 \\ 0 & O_2 \end{pmatrix} \begin{pmatrix} \tanh \Lambda & (\cosh \Lambda)^{-1} \\ (\cosh \Lambda)^{-1} & -\tanh \Lambda \end{pmatrix} \begin{pmatrix} O_3 & 0 \\ 0 & O_4 \end{pmatrix}, \tag{10.2}$$

in terms of four orthogonal matrices $O_p \in \mathrm{SO}(2N)$ and a diagonal real matrix Λ with diagonal elements $\lambda_n \in (-\infty, \infty)$. The absolute value $|\lambda_n|$ is called a Lyapunov exponent, related to the transmission eigenvalue $T_n \in [0, 1]$ by $T_n = 1/\cosh^2 \lambda_n$. We identify

$$Q = \operatorname{sign} Q, \quad Q = \operatorname{Det} r = \operatorname{Det} r' = \prod_{n=1}^{2N} \tanh \lambda_n. \tag{10.3}$$

---

[1]There exist, in addition to class D, four more symmetry classes with a topological phase transition in a wire geometry. The quantized conductance at the transition point appears generically. This is a manifestation of the "super-universality" of Ref. [224].

This relation expresses the fact that reflection from a Majorana bound state contributes a scattering phase shift of π, so a phase factor of -1. The sign of $\prod_n \tanh \lambda_n$ thus equals the parity of the number m of Majorana bound states at one end of the wire (see App. 10.A). (It makes no difference which end, and indeed r and r' give the same Q.)

To put this expression for Q into context, we first note that it may be written equivalently as $Q = \text{Det}\, O_1 O_3$ if we restrict the λ_n's to non-negative values and allow Det O_p to equal either $+1$ or -1. The sign of Q then corresponds to the topological classification of a class-D network model derived by Merz and Chalker [219]. We also note that Q can be written equivalently in terms of the Pfaffian of $\ln M M^\dagger$ (with M the transfer matrix in a suitable basis), as described in App. 10.A. A Pfaffian relation for the topological quantum number Q_{clean} in class D has been derived by Kitaev [132] for a clean, translationally invariant system. We will verify later on that Q and Q_{clean} agree for a clean system.

10.3 Transport properties at the phase transition

An immediate consequence of Eq. (10.3) is that at the topological phase transition one of the λ_n's vanishes [219, 223, 224], so the corresponding transmission eigenvalue $T_n = 1$ at the transition point. The sign change of Q ensures that T_n fully reaches its maximal value of unity, it cannot stop short of it without introducing a discontinuity in Q. Generically there will be only a single unit transmission eigenvalue at the transition, the others being exponentially suppressed by the superconducting gap. The thermal conductance $G_{\text{th}} = G_0 \sum_n T_n$ of the wire will then show a peak of quantized height $G_0 = \pi^2 k_B^2 \tau_0 / 6h$ at the transition.

Our claim of a quantized conductance at the transition point is consistent with earlier work [221–225] on class D ensembles. There a broad distribution of the conductance was found in the large-L limit, but the key difference is that we are considering a single disordered sample of finite length, and the value of the control parameter at which the conductance is quantized is sample specific. We will now demonstrate how the peak of quantized conductance arises, first for a simple analytically solvable model, then for a more complete microscopic Hamiltonian that we solve numerically.

The analytically solvable model is the effective low-energy Hamiltonian of a class-D superconductor with a random gap, which for a single mode in the Majorana basis has the form

$$H = -i\hbar v_F \sigma_z \partial/\partial x + \Delta(x)\sigma_y. \tag{10.4}$$

We have assumed, for simplicity, that right-movers and left-movers have the same velocity v_F, but otherwise this is the generic form to linear order in momentum, constrained by the electron-hole symmetry requirement $H = -H^*$. An eigenstate Ψ of H at energy zero satisfies

$$\Psi(x) = \exp\left(-\frac{1}{\hbar v_F}\sigma_x \int_0^x \Delta(x')dx'\right)\Psi(0). \tag{10.5}$$

By substituting $\Psi(0) = (1, r)$, $\Psi(L) = (t, 0)$ we obtain the reflection amplitude

$$r = \tanh(L\bar{\Delta}/\hbar v_F), \quad \bar{\Delta} = L^{-1} \int_0^L \Delta(x) dx. \tag{10.6}$$

In this simple model, a change of sign of the spatially averaged gap $\bar{\Delta}$ is the signature of a topological phase transition.[2]

If $\bar{\Delta}$ is varied by some external control parameter, the thermal conductance $G_{th} = G_0 \cosh^{-2}(L\bar{\Delta}/\hbar v_F)$ has a peak at the transition point $\bar{\Delta} = 0$, of height G_0 and width $\hbar v_F/L$ (Thouless energy). The $1/\cosh^2$ line shape is the same as for a thermally broadened tunneling resonance, but the quantized peak height (irrespective of any asymmetry in the coupling to the left and right lead) is highly distinctive.

For a more realistic microscopic description of the quantized conductance peak, we have performed a numerical simulation of the model [207, 208] of a semiconductor nanowire on a superconducting substrate. The Bogoliubov-De Gennes Hamiltonian

$$H = \begin{pmatrix} H_R - E_F & \Delta \\ \Delta^* & E_F - \sigma_y H_R^* \sigma_y \end{pmatrix} \tag{10.7}$$

couples electron and hole excitations near the Fermi energy E_F through an s-wave superconducting order parameter Δ. Electron-hole symmetry is expressed by

$$\sigma_y \tau_y H^* \sigma_y \tau_y = -H, \tag{10.8}$$

where the Pauli matrices σ_y and τ_y act, respectively, on the spin and the electron-hole degree of freedom. The excitations are confined to a wire of width W and length L in the $x - y$ plane of the semiconductor surface inversion layer, where their dynamics is governed by the Rashba Hamiltonian

$$H_R = \frac{p^2}{2m_{eff}} + U(r) + \frac{\alpha_{so}}{\hbar}(\sigma_x p_y - \sigma_y p_x) + \tfrac{1}{2} g_{eff} \mu_B B \sigma_x. \tag{10.9}$$

The spin is coupled to the momentum $p = -i\hbar \partial/\partial r$ by the Rashba effect, and polarized through the Zeeman effect by a magnetic field B parallel to the wire (in the x-direction). Characteristic length and energy scales are $l_{so} = \hbar^2/m_{eff}\alpha_{so}$ and $E_{so} = m_{eff}\alpha_{so}^2/\hbar^2$. Typical values in InAs are $l_{so} = 100$ nm, $E_{so} = 0.1$ meV, $g_{eff}\mu_B = 2$ meV/T.

We have solved the scattering problem numerically [226] by discretizing the Hamiltonian (10.7) on a square lattice (lattice constant a), with a short-range electrostatic disorder potential $U(x, y)$ that varies randomly from site to site, distributed uniformly in the interval $(-U_0, U_0)$. (Equivalent results are obtained for long-range disorder, as shown in App. 10.B.) The disordered superconducting wire (S) is connected at the two ends to clean metal leads (N$_1$, N$_2$), obtained by setting $U \equiv 0$, $\Delta \equiv 0$ for $x < 0$, $x > L$.

---

[2]We need an even number of modes to calculate Q without any sign ambiguity, so the single disordered mode described by the Hamiltonian (10.4) is supplemented by a second clean mode in a topologically trivial phase (uniform $\Delta_0 > 0$). The sign of Q is then completely determined by the sign of r in Eq. (10.6).
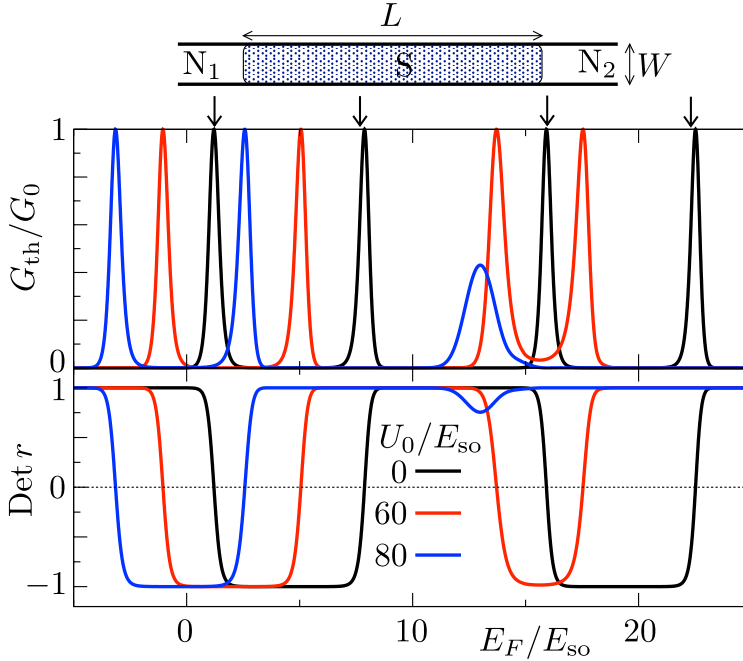
Figure 10.1: Thermal conductance and determinant of reflection matrix of a disordered multimode superconducting wire as a function of Fermi energy. The curves are calculated numerically from the Hamiltonian (10.7)–(10.9) on a square lattice (lattice constant $a = l_{\mathrm{so}}/20$), for parameter values $W = l_{\mathrm{so}}$, $L = 10 l_{\mathrm{so}}$, $\Delta = 10 E_{\mathrm{so}}$, $g_{\mathrm{eff}} \mu_B B = 21 E_{\mathrm{so}}$, and three different disorder strengths U_0. The arrows indicate the expected position of the topological phase transition in an infinite clean wire ($U_0 = 0$, $L \to \infty$), calculated from Eq. (10.10). Disorder reduces the topologically nontrivial interval (where $\mathrm{Det}\, r < 0$), and may even remove it completely, but the conductance quantization remains unaffected as long as the phase transition persists.

Results for the thermal conductance and topological quantum number are shown in Fig. 10.1, as a function of the Fermi energy (corresponding to a variation in gate voltage). For the parameters listed in the caption the number N of modes in the normal leads increases from 1 to 2 at $E_F/E_{\mathrm{so}} \approx 10$ and from 2 to 3 at $E_F/E_{\mathrm{so}} \approx 15$. We emphasize that Fig. 10.1 shows raw data, without any averaging over disorder.

For a clean system ($U_0 = 0$, black curves) the results are entirely as expected: A topologically nontrivial phase (with $\mathrm{Det}\, r < 0$) may appear for odd N while there is no topological phase for N even [134, 227, 228]. The topological quantum number of an infinitely long clean wire (when the component p_x of momentum along the wire is a good quantum number) can be calculated from the Hamiltonian $H(p_x)$ using Kitaev's

Pfaffian formula [132, 227],

$$Q_{\text{clean}} = \text{sign}\left(\text{Pf}\left[\sigma_y \tau_y H(0)\right]\text{Pf}\left[\sigma_y \tau_y H(\pi/a)\right]\right). \tag{10.10}$$

(The multiplication by $\sigma_y \tau_y$ ensures that the Pfaffian is calculated of an antisymmetric matrix.) The arrows in Fig. 10.1 indicate where Q_{clean} changes sign, in good agreement with the sign change of Q calculated from Eq. (10.3). (The agreement is not exact because L is finite.)

Upon adding disorder Q_{clean} can no longer be used (because p_x is no longer conserved), and we rely on a sign change of Q to locate the topological phase transition. Fig. 10.1 shows that disorder moves the peaks closer together, until they merge and the topological phase disappears for sufficiently strong disorder. We have also observed the inverse process, a disorder-induced splitting of a peak and the appearance of a topological phase, in a different parameter regime than shown in Fig. 10.1. Our key point is that, as long as the phase transition persists, disorder has no effect on the height of the conductance peak, which remains precisely quantized — without any finite-size effects.

Since electrical conduction is somewhat easier to measure than thermal conduction, we now discuss two alternative signatures of the topological phase transition which are purely electrical. An electrical current I_1 is injected into the superconducting wire from the normal metal contact N_1, which is at a voltage V_1 relative to the grounded superconductor. An electrical current I_2 is transmitted as quasiparticles into the grounded contact N_2, the difference $I_1 - I_2$ being drained to ground as Cooper pairs via the superconductor. The nonlocal conductance $G = \bar{I}_2/V_1$ is determined by the time averaged current $\bar{I}_2$, while the correlator of the time dependent fluctuations δI_2 determines the shot noise power $P = \int_{-\infty}^{\infty} dt \, \langle \delta I_2(0) \delta I_2(t) \rangle$ (in the regime $k_B \tau_0 \ll eV_1$ where thermal noise can be neglected).

These two electrical transport properties are given in terms of the $N \times N$ transmission matrices t_{ee} and t_{he} (from electron to electron and from electron to hole) by the expressions [168]

$$G = (e^2/h)\,\text{Tr}\,T_-, \quad P = (e^3 V_1/h)\,\text{Tr}\left(T_+ - T_-^2\right), \tag{10.11}$$

$$T_\pm = t_{ee}^\dagger t_{ee} \pm t_{he}^\dagger t_{he}. \tag{10.12}$$

Electron-hole symmetry relates $t_{ee} = t_{hh}^*$ and $t_{he} = t_{eh}^*$. This directly implies that $\text{Tr}\,T_+ = \frac{1}{2}\text{Tr}\,tt^\dagger = \frac{1}{2}\sum_n T_n$. If in addition we assume that at most one of the T_n's is nonzero we find that T_- vanishes (see App. 10.C). We conclude that G remains zero across the topological phase transition, while P/V_1 peaks at the quantized value $e^3/2h$. This is the second signature of the phase transition.[3]

The third signature is in the electrical conductance. Since $G = 0$ for a single open transmission channel, we add (topologically trivial) open channels by means of a parallel normal metal conductor in a ring geometry. A magnetic flux Φ through the ring produces Aharonov-Bohm oscillations with a periodicity $\Delta\Phi = h/e^*$. The effective charge

---

[3]We do not plot the quantized shot noise peak in a separate figure, because our numerical simulation shows that P in units of $e^3 V_1/2h$ is indistinguishable on the scale of Fig. 10.1 from G_{th} in units of G_0.
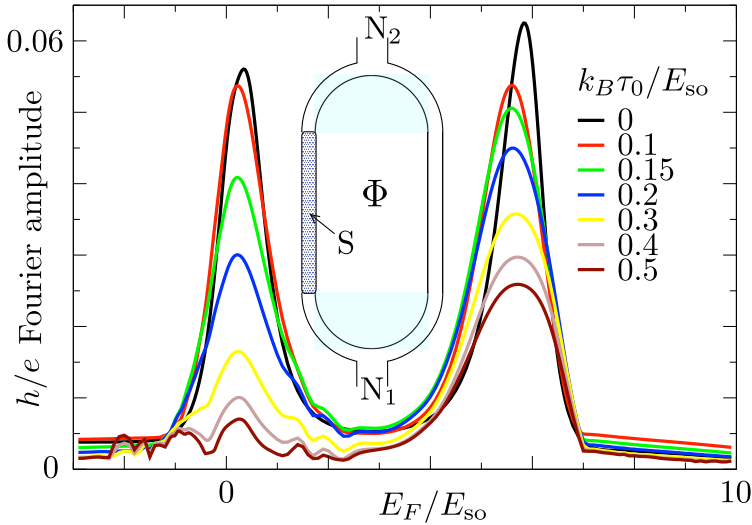
Figure 10.2: Fourier amplitude with flux periodicity h/e of the magnetoconductance oscillations, calculated numerically from the Hamiltonian (10.7)–(10.9) for a single disorder strength $U_0 = 50\,E_{\rm so}$ and seven different temperatures τ_0. The inset shows the Aharonov-Bohm ring geometry. The parameters of the superconducting segment of the ring (S) are the same as in Fig. 10.1, with $N = 1$ in this range of Fermi energies. The normal part of the ring has $N = 8$ propagating modes to avoid localization by the disorder (which has the same strength throughout the ring).

$e^* = e$ if electrons or holes can be transmitted individually through the superconducting arm of the ring, while $e^* = 2e$ if only Cooper pairs can be transmitted [229, 230]. We thus expect a period doubling from $h/2e$ to h/e of the magnetoconductance oscillations at the phase transition, which is indeed observed in the computer simulations (Fig. 10.2). To show the relative robustness of the effect to thermal averaging, we repeated the calculation at several different temperatures τ_0. For $E_{\rm so} \simeq 0.1\,{\rm meV}$ the characteristic peak at the phase transition remains visible for temperatures in the readily accessible range of 100–500 mK.

10.4   Conclusion

In conclusion, our analytical considerations and numerical simulations of a model Hamiltonian [207, 208] of a disordered InAs wire on a superconducting substrate show three signatures of the transition into the topological phase (Figs. 10.1 and 10.2): A quantized thermal conductance and electrical shot noise, and a period doubling of the magnetoconductance oscillations. These unique signatures of the Majorana phase transition provide alternatives to the detection of Majorana bound states [133, 200, 203, 213, 214, 216],

which are fundamentally insensitive to the obscuring effects of disorder in a multimode wire.

10.A Derivation of the scattering formula for the topological quantum number

10.A.1 Pfaffian form of the topological quantum number

The topological quantum number Q of a disordered wire is given in Eq. (10.3) as the sign of the determinant of the reflection matrix. That is the form which is most convenient for computations. In order to derive this relationship and also to compare it with results in the literature for translationally invariant systems [132], it is convenient to rewrite it in terms of the transfer matrix M. It then takes the form of a Pfaffian, rather than a determinantal, relation.

The $4N \times 4N$ transfer matrix M relates the mode amplitudes to the right (R) and to the left (L) of the disordered wire,

$$\begin{pmatrix} \psi_{+,R} \\ \psi_{-,R} \end{pmatrix} = M \begin{pmatrix} \psi_{+,L} \\ \psi_{-,L} \end{pmatrix}, \quad M = \begin{pmatrix} m_{++} & m_{+-} \\ m_{-+} & m_{--} \end{pmatrix}. \tag{10.13}$$

The condition of particle current conservation is $\sigma_z M^\dagger \sigma_z = M^{-1}$, where the Pauli matrix σ_z acts on the block structure indicated in Eq. (10.13). In the Majorana basis of real mode amplitudes M is a real matrix, hence

$$\sigma_z M^t \sigma_z = M^{-1}. \tag{10.14}$$

The transfer matrix has the polar decomposition

$$M = \begin{pmatrix} O_2 & 0 \\ 0 & O_4^t \end{pmatrix} \begin{pmatrix} \cosh \Lambda & -\sinh \Lambda \\ -\sinh \Lambda & \cosh \Lambda \end{pmatrix} \begin{pmatrix} O_3 & 0 \\ 0 & O_1^t \end{pmatrix}$$
$$= \begin{pmatrix} O_2 & 0 \\ 0 & O_4^t \end{pmatrix} \exp(-\Lambda \sigma_x) \begin{pmatrix} O_3 & 0 \\ 0 & O_1^t \end{pmatrix}, \tag{10.15}$$

where the matrices $O_p \in \mathrm{SO}(2N)$ and $\Lambda = \mathrm{diag}\,(\lambda_1, \lambda_2 \ldots, \lambda_{2N})$ are the same as in the polar decomposition (10.2) for the scattering matrix. One readily checks that Eq. (10.14) is satisfied.

The polar decomposition (10.15) allows us to compute

$$\sigma_z \ln(M M^\dagger) = \Omega \begin{pmatrix} 0 & -2\Lambda \\ 2\Lambda & 0 \end{pmatrix} \Omega^t, \quad \Omega = \begin{pmatrix} O_2 & 0 \\ 0 & O_4^t \end{pmatrix}. \tag{10.16}$$

This is an antisymmetric matrix, so it has a Pfaffian,

$$\mathrm{Pf}\left(\sigma_z \ln M M^\dagger\right) = \prod_{n=1}^{2N} 2\lambda_n. \tag{10.17}$$

We have used the identity

$$\text{Pf } BAB^{\text{t}} = \text{Det } B \text{ Pf } A, \tag{10.18}$$

with $\text{Det } \Omega = 1$.

We conclude that the topological quantum number (10.3) can equivalently be written as

$$Q = \text{sign} \left[\text{Pf} \left(\sigma_z \ln M M^{\dagger} \right) \right]. \tag{10.19}$$

10.A.2   How to count Majorana bound states

To determine the topological quantum number of the disordered superconducting wire we seek the number of Majorana bound states. Particle-hole symmetry ensures that any bound state at zero energy is a Majorana fermion (since the creation and annihilation operators are related by $\gamma^{\dagger}(E) = \gamma(-E)$ and therefore are identical at $E = 0$). However, we cannot directly search for zero-energy eigenstates: Even if the Majorana fermions are maximally separated by the entire length L of the wire they will still have a nonzero tunnel coupling which splits their energies apart, away from zero.

The issue here is how to distinguish strongly coupled from weakly coupled Majorana fermions. Any ordinary fermionic excitation, with distinct creation and annihilation operators $a^{\dagger} \neq a$, can be described by a pair of *strongly coupled* Majorana fermion operators $\gamma_1 = a + a^{\dagger}$, $\gamma_2 = i(a - a^{\dagger})$. In contrast, the Majorana bound states at opposite ends of the wire are *weakly coupled* Majorana fermions.

Our geometry of a disordered wire connected at the ends to metal contacts allows for a natural distinction of weak versus strong coupling: We call a pair of Majorana bound states "strongly coupled" if they are more strongly coupled to each other than to one of the ends of the wire. Conversely, weakly coupled Majorana bound states are more strongly coupled to one end of the wire than to any other Majorana. The topological quantum number counts only weakly coupled Majorana's.

This distinction between weak and strong coupling can be made operational by means of the thought experiment illustrated in Fig. 10.3: We close the wire into a ring by connecting the two ends through a superconductor which is in a topologically trivial phase (with a uniform positive gap Δ_0). Destructive interference in the two arms of the ring can eliminate the tunnel splitting between a pair of Majorana bound states and produce two-fold degenerate zero-energy eigenstates, if the coupling between the two Majorana's through each arm of the ring is of comparable strength.

So we vary Δ_0 (allowing also for mode mixing at the junction between the two arms of the ring) and find that a number m of two-fold degenerate states appear at zero energy. This means that the disordered wire contains m pairs of Majorana's which are more strongly coupled to the ends of the wire than to each other (otherwise the couplings through the two arms of the ring could not have been equalized by varying Δ_0). The number m thus counts the number of weakly coupled Majorana bound states, which gives the topological quantum number $Q = (-1)^m$.
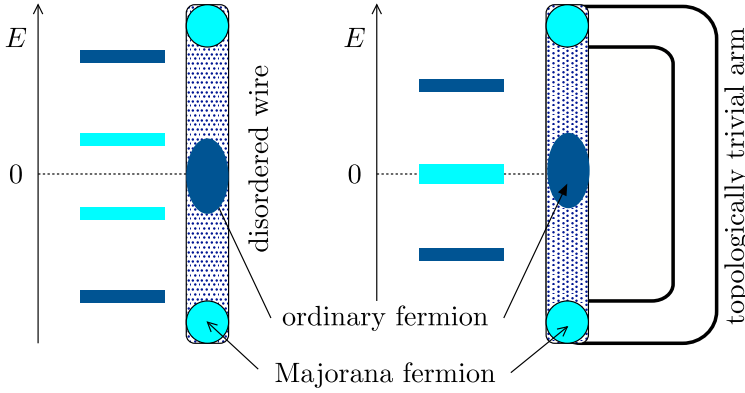
Figure 10.3: Procedure to count weakly coupled Majorana bound states in a disordered superconducting wire. Majorana fermions at the two ends of the wire (light blue) are weakly coupled, so their energy is not exactly zero and we need a way to distinguish them from an ordinary fermionic excitation (dark blue). To that end we close the wire into a ring through a topologically trivial superconductor and ask whether destructive interference of the tunnel splitting in the two arms of the ring can produce a pair of two-fold degenerate zero-energy states.

10.A.3   Topological quantum number of a disordered wire

Now that we have an operational definition of the topological quantum number of a finite system, our next step is to relate this to the scattering parameters λ_n in Eq. (10.3). For this purpose it is easiest to work with the transfer matrix, rather than the scattering matrix. An eigenstate Ψ of the ring must be single-valued as we go around the ring, so in terms of the transfer matrices M and M_0 of the two arms of the ring we have the condition $M_0 M \Psi = \Psi$. This leads to the determinantal condition

$$\mathrm{Det}\,(1 - M_0 M) = 0. \tag{10.20}$$

We choose to work in a basis where the orthogonal matrices O_p in Eq. (10.15) are equal to the unit matrix. Each of the $n = 1, 2, \ldots 2N$ eigenchannels of the disordered wire can then be treated separately, with 2×2 transfer matrices $M_n = \exp(-\sigma_x \lambda_n)$ at zero energy. The topologically trivial arm of the ring (of length L_0 and coherence length $\xi_0 = \hbar v_F / \Delta_0 > 0$, without any disorder) has transfer matrix $M_0 = \exp(-\sigma_x L_0/\xi_0)$. The condition for an eigenstate at zero energy reads

$$\mathrm{Det}\,(1 - e^{-\sigma_x L_0/\xi_0} e^{-\sigma_x \lambda_n}) = 0, \tag{10.21}$$

which has a twofold degenerate solution if the ratio L_0/ξ_0 is tuned to the value $-\lambda_n$. This is the pair of weakly coupled Majorana bound states in the n-th eigenchannel that we are searching for. Because $\xi_0 > 0$, by definition in a topologically trivial phase, the pair exists only if $\lambda_n < 0$.

We conclude that the number of pairs m of weakly coupled Majorana bound states equals the number of negative λ_n's, hence

$$Q = (-1)^m = \operatorname{sign}\left(\prod_{n=1}^{2N} \lambda_n\right),$$ (10.22)

as announced in Eq. (10.3).

10.B   Numerical simulations for long-range disorder

Fig. 10.1 in the main text demonstrates that the quantized thermal conductance at the Majorana phase transition is insensitive to short-range disorder (correlation length ξ of the order of the lattice constant a). Here we show that long-range disorder similarly has no effect on the quantization. (The stability of Majorana bound states against short-range and long-range disorder was investigated in Ref. [227].)

As before, we solve the scattering problem numerically by discretizing the Hamiltonian (10.7) on a square lattice (with a total number of N_{tot} lattice points in the disordered region). The disorder is modeled as a superposition of impurities with a Gaussian profile,

$$U(\boldsymbol{r}) = \sum_{i=1}^{N_{\text{imp}}} U_i \exp\left[-\frac{(\boldsymbol{r} - \boldsymbol{r}_i)^2}{2\xi^2}\right],$$ (10.23)

where N_{imp} is the number of impurities. (We fixed the impurity concentration $n_{\text{imp}} = N_{\text{imp}}/N_{\text{tot}}$ at 5%.) The strength U_i of an individual impurity is randomly distributed in the interval $(-U_0, U_0)$, and the impurity positions $\boldsymbol{r}_i$ are chosen randomly from the N_{tot} lattice points.

The results of the calculation are shown in Fig. 10.4, for different values of the correlation length ξ. In all cases, we observe as before that the thermal conductance remains quantized as long as the topological phase persists. For sufficiently strong disorder, the merging of two peaks signals the disappearance of the topological phase and a breakdown of the conductance quantization.

10.C   Electrical conductance and shot noise at the topological phase transition

The expression (10.11) for the nonlocal electrical conductance and shot noise of the superconducting wire can be evaluated further if there is only a single open transmission channel. The $2N \times 2N$ transmission matrix

$$t = \begin{pmatrix} t_{ee} & t_{eh} \\ t_{he} & t_{hh} \end{pmatrix}$$ (10.24)
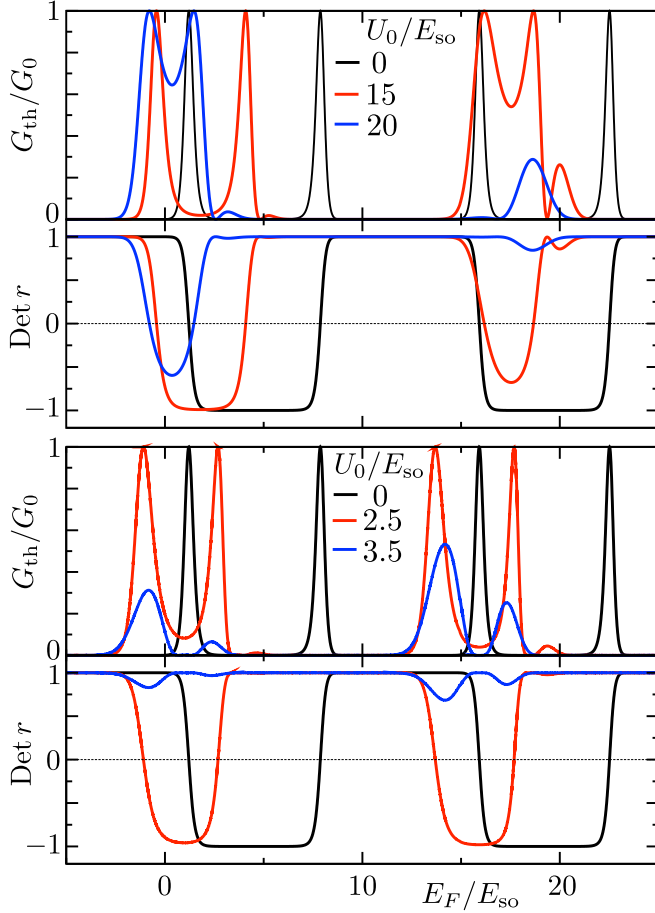
Figure 10.4: Same as Fig. 10.1, for an impurity potential with correlation length $\xi = 2\,a$ (upper panel) and $\xi = 10\,a$ (lower panel.

is then of rank 1, which means that the $N \times N$ submatrices $t_{ee}, t_{hh}, t_{he}, t_{eh}$ have the dyadic form

$$t_{ee} = |u_{\mathrm{R}}\rangle\langle u_{\mathrm{L}}|, \quad t_{hh} = |v_{\mathrm{R}}\rangle\langle v_{\mathrm{L}}|,$$
$$t_{he} = |v_{\mathrm{R}}\rangle\langle u_{\mathrm{L}}|, \quad t_{eh} = |u_{\mathrm{R}}\rangle\langle v_{\mathrm{L}}|. \tag{10.25}$$

The matrix $T_{\pm}$ then becomes

$$T_{\pm} = |u_{\mathrm{L}}\rangle\langle u_{\mathrm{L}}|\big(\langle u_{\mathrm{R}}|u_{\mathrm{R}}\rangle \pm \langle v_{\mathrm{R}}|v_{\mathrm{R}}\rangle\big). \tag{10.26}$$

Electron-hole symmetry requires $|v_{\mathrm{R}}\rangle = |u_{\mathrm{R}}^*\rangle$, hence $T_- = 0$, $T_+ = \frac{1}{2}\mathrm{Tr}\,tt^\dagger$, and thus $G = 0$, $P = (e^3 V_1/2h)\,\mathrm{Tr}\,tt^\dagger$.

Chapter 11

Theory of non-Abelian Fabry-Perot interferometry in topological insulators

11.1 Introduction

One of the most promising tools in topological quantum computing [8, 9] is non-Abelian edge state interferometry [174–176]. Its main idea is that moving a fractional excitation (anyon) existing at an edge of a topological medium around localized anyons in the bulk allows to extract information about the state of the latter. The theory of edge state interferometry was initially developed for Ising anyons in the 5/2 fractional quantum Hall (FQH) state and p-wave superconductors [174–176, 182], building on earlier work on FQH systems [5, 6, 231, 232]. Recent experiments [173], which provide evidence for non-Abelian braiding statistics in the 5/2 FQH state (see the detailed discussion in Ref. [233]) are using this method, and it is generally considered the most promising way to measure the state of topological qubits.

   We present a theory of non-Abelian edge state interferometry of the Majorana modes existing at the surface of a 3D topological insulator brought in contact with an s-wave superconductor and a ferromagnetic insulator [130]. The main difference of an interferometry setup in this system, as compared with 5/2 FQH interferometer, is the need for an additional "Dirac to Majorana converter" [144, 145]. This element is required because unlike in the FQH effect the edge excitations near a superconductor carry no charge and thus allow no electric readout. This converter initially transforms the charged excitations injected from a current source into superpositions of two neutral excitations existing at different edges of the superconductor. Later another converter recombines a pair of neutral excitations exiting the interferometer into a charged particle, either an electron or a hole, that can be measured as a current pulse. The difference between the two systems is summarized in Fig. 11.1. The "Dirac to Majorana converter" is not available in chiral p-wave superconductors, since the chirality of the neutral edge modes is then set by time-reversal symmetry breaking in the condensate, and not by the external region of the system (magnet). Such a limitation combined with the absence of charged modes makes electric readout of interferometry experiment much less viable in a chiral p-wave

superconductor.

The description of the "Dirac to Majorana converter" using single particle formalism was done in Refs. [144, 145]. The qualitative description of the non-Abelian Fabry-Perot interferometer was presented in Ref. [145]. In this chapter we use conformal field theory (CFT) to describe and analyze the non-Abelian excitations following Ref. [182].

An important difference between the systems is the following: In the 5/2 FQH effect the charge density and accordingly charge current of anyons may be defined locally, since anyons have charge $e/4$ or $e/2$ in this system. Excitation of charge e^* has an energy cost of e^*V for being created in the system. This energy cost provides a natural cutoff for the current, whereas in the superconducting systems due to the absence of charge in the edge excitations the only cutoff is set by the finite temperature. The neutrality of the edge excitations does not only mean that a finite voltage does not provide a cutoff for the conductance, but also results in a different temperature scaling exponent of the conductance. In the topological insulator setup the conductance diverges at low temperatures as $\Gamma \sim T^{-7/4}$, while in the FQH setup it goes as $\Gamma \sim T^{-3/2}$.

The experimental requirements for a realization of edge state interferometry in topological insulators were discussed in Refs. [144] and [145]. An additional requirement for non-Abelian interferometry is the need for a sufficiently high amplitude of the vortex tunneling, $\lambda_\sigma \sim \exp(-\sqrt{E_C/E_J})$, with E_J the Josephson energy and E_C the charging energy. It is non-negligible only if the superconducting islands in the system have small capacitive energy E_C [183].

The outline of this chapter is as follows: In Sec. 11.2 we introduce the effective model that we use to describe the fermions that propagate along magnetic domain walls and the superconducting-magnet domain walls. In particular we introduce the representation of these fermions in terms of Majorana fields, which we use later. In Sec. 11.3 we review the linear response formula that we use to calculate the non-local conductance, the experimentally relevant quantity that we are interested in. In Sec. 11.4 we give a detailed account of the perturbative calculation of the conductance, and we consider the most interesting case of vortex tunneling in Sec. 11.5. In Sec. 11.6 we show how the proposed setup can be used to measure the fermion parity (and hence the topological charge) of the Majorana qubit that is stored in a pair of bulk vortices. Our conclusions are to be found in Sec. 11.7. We provide a detailed description of the formalism that we use to describe the peculiar vortex field in the appendices.

11.2 Chiral fermions

11.2.1 Domain wall fermions

It is known that there exists a single chiral fermion mode on each mass domain wall in the 2D Dirac equation. This mode is localized near the domain wall but is allowed to propagate along the domain wall in only one direction (hence the name chiral). This is most easily seen using an index theorem that relates the difference in a topological number ($\tilde{N}_3$ in the language of Ref. [234]) between the two domains and the difference
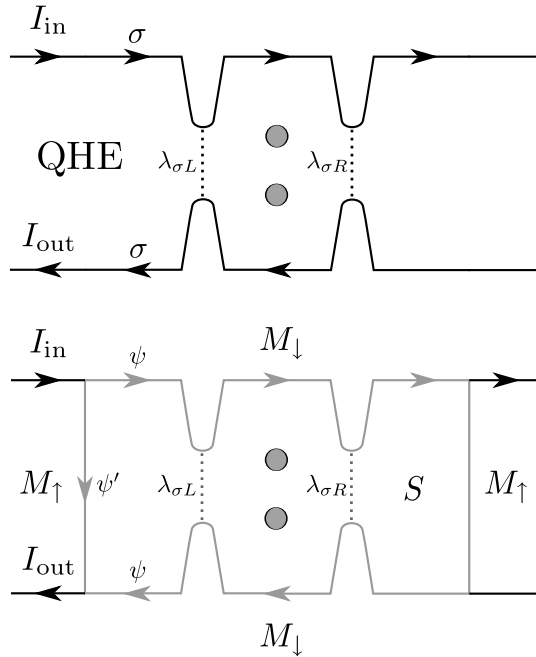
Figure 11.1: Edge state Fabry-Perot interferometer in the 5/2 FQH system (top panel) and in a topological insulator/s-wave superconductor heterostructure (bottom panel). The charge is transferred locally at the tunneling point in FQH effect, and is only well-defined in the ferromagnetic domain walls (i.e. the leads) in the topological insulator setup. Regions labeled S, $M_\uparrow$, and $M_\downarrow$ denote parts of topological insulator in proximity of a superconductor and of ferromagnetic insulators with different polarizations. Grey circles in the middle of the central island are Majorana bound states forming a Majorana qubit, which can be measured by the interferometer.

in the number of right- and left-moving states that live in the domain wall [234]. In the ferromagnetic domain wall that we are interested in the change in $\tilde{N}_3$ across the domain wall is ± 1. If the domain wall is also abrupt enough then only one chiral fermion exists in the domain wall.

A similar argument can be made using the Dirac-Bogoliubov-de Gennes (BdG) equation with gaps generated by the superconducting order parameter Δ. In the case that we consider (s-wave pairing) $\tilde{N}_3$ is zero if the gap is dominated by the superconducting gap $|\Delta|$ and non-zero (± 1) when the gap is of ferromagnetic character. Because of the double counting of states in the BdG equation this implies that $\frac{1}{2}$ of a chiral fermion state exists on a superconducting-magnetic domain wall. This is exactly the number of degrees of freedom that is encoded in a *chiral Majorana fermion* field.

Alternatively one can argue for the existence of these states by solving the BdG

equation explicitly for certain simple domain wall profiles or use $\boldsymbol{k} \cdot \boldsymbol{p}$ theory [144]. We now proceed to a theoretical description of these states. In particular we will see that it is fruitful to describe both kinds of domain walls in terms of Majorana fields.

11.2.2   Theoretical description

In the leads (ferromagnetic domain walls), where the superconducting order parameter vanishes, the system consists of a single normal edge state which propagates in only one direction, i.e. a single chiral charged mode. This can be described by a complex fermionic field $\hat{\Psi}(x)$ with Hamiltonian

$$H(t) = \frac{1}{2\pi} \int dx : \hat{\Psi}^\dagger(x)[vp_x - \mu(x,t)]\hat{\Psi}(x): . \tag{11.1}$$

Here : : denotes normal ordering. We use units such that $\hbar = 1$ unless specified otherwise. The kinetic energy operator vp_x is defined as

$$vp_x = i\frac{\overleftarrow{\partial}_x v(x) - v(x)\overrightarrow{\partial}_x}{2} \rightarrow -i\sqrt{v(x)}\overrightarrow{\partial}_x\sqrt{v(x)}, \tag{11.2}$$

where we have introduced the spatially varying velocity $v(x)$ in a symmetric way such that vp_x is a Hermitean operator. The stationary (energy E) solution to the time-dependent Schrödinger equation corresponding to Eq. (11.1) for zero chemical potential $\mu = 0$ is

$$\Psi_E(x,t) = \sqrt{\frac{v(0)}{v(x)}} \exp\left(iE\left[\int_0^x \frac{dx'}{v(x')} - t\right]\right)\Psi_E(0,0). \tag{11.3}$$

This implies that

$$\langle\hat{\Psi}(x,t)\hat{\Psi}^\dagger(0,0)\rangle = \frac{[v(x)v(0)]^{-1/2}}{a + i\left[t - \int_0^x dx'/v(x')\right]}, \tag{11.4}$$

where a is a short time cutoff which should be taken to zero. If the velocity v is constant the result simplifies to

$$v\langle\hat{\Psi}(x,t)\hat{\Psi}^\dagger(0,0)\rangle = \frac{1}{a + i(t - x/v)} \equiv \frac{1}{a + iu}. \tag{11.5}$$

The normalization in Eq. (11.1) is chosen to yield this result without any extra normalization factors. Note that it implies (in the limit $a \rightarrow 0^+$) that the anti-commutation relation for the field is $\{\hat{\Psi}(x), \hat{\Psi}^\dagger(x')\} = 2\pi\delta(x - x')$.

An important consequence of the chiral nature of the excitations is that the correlation functions only depend on the difference of the *Lorentz time* $u = t - x/v$. According to Eq. (11.4) the same is true also for a spatially varying velocity with the proper interpretation of the length difference. Because of this property we will mostly work with a

spatially homogeneous velocity that we will set to unity ($v = 1$) in the following calculations. It is also useful to go from the Hamiltonian to the corresponding Lagrangian

$$L = \frac{1}{2\pi} \int dx : \hat{\Psi}^\dagger(x)[i\, \partial_t - vp_x + \mu(x,t)]\hat{\Psi}(x):, \tag{11.6}$$

since the coupling to the gauge field is most transparent in this formalism.

11.2.3   Majorana fermion representation

We can decompose $\hat{\Psi}(x)$ into independent Majorana fields $\psi(x) = \psi^\dagger(x)$ and $\psi'^\dagger(x) = \psi'(x)$ as

$$\hat{\Psi}(x,t) = \frac{e^{iA(x,t)}}{\sqrt{2}}[\psi(x,t) + i\,\psi'(x,t)]. \tag{11.7}$$

The anti-commutation relations of the Majorana fields are

$$\{\psi(x), \psi(x')\} = \{\psi'(x), \psi'(x')\} = 2\pi\delta(x - x'), \quad \{\psi(x), \psi'(x')\} = 0. \tag{11.8}$$

In terms of ψ and ψ' the Lagrangian becomes

$$L = \frac{1}{4\pi} \int dx\Big[:\psi(x)(i\,\partial_t - vp_x)\psi(x): + :\psi'(x)(i\,\partial_t - vp_x)\psi'(x):\Big]$$

$$+ \frac{ie}{2\pi} \int dx\, F(x,t)v(x)\psi'(x)\psi(x), \tag{11.9}$$

where $F(x,t)$ depends on the phase $A(x,t)$, i.e. it is gauge dependent:

$$- eF(x,t) = \frac{\mu(x,t)}{v(x)} - \frac{1}{v(x)}\partial_t A(x,t) - \partial_x A(x,t). \tag{11.10}$$

Note that this means that a time-independent spatially varying chemical potential can be gauged away up to possible boundary terms.

   One of the most interesting features of the system that we consider is that the two Majorana fields that appear in this action can becomes spatially separated when a superconducting region is sandwiched in between the two magnetic regions in a magnetic domain wall as discussed previously. Thus the action in Eq. (11.9) can be used to describe the setup in Fig. 11.2, in which the two Majorana fields ψ and ψ' are spatially separated inside of the interferometer. It is important to remember that the coordinate systems of the two fields are different in this representation.

   From the Lagrangian and the coupling to the gauge field we now identify the charge current operator as

$$\hat{J}(x) = \frac{-ev(x)}{2\pi} : \hat{\Psi}^\dagger(x)\hat{\Psi}(x) := \frac{ie}{2\pi}v(x)\psi'(x)\psi(x). \tag{11.11}$$

This form of the current operator in terms of the Majorana fields is very important for the following calculations. It is only well-defined if the two Majorana modes are at
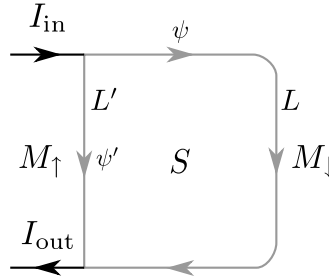
Figure 11.2: Free fermion propagation setup. The two Majorana modes ψ and ψ' are spatially separated by the superconducting region. Thus the effective propagation length from in to out can be different for the two modes, i.e. $L' \neq L$.

the same position in space, hence there is no coupling to the electric field inside of the interferometer where the two Majorana wires are spatially separated. This is also an important difference between the FQH setup where local charge current operators can be defined at the tunneling point contacts. This simplifies the calculation because the local charge transfer is directly related to the measurements done far away. In our system we don't have this luxury and must consider the leads explicitly.

11.3   Linear response formalism for the conductance

If we write the Lagrangian in Eq. (11.9) as $L = L_0 - H'(t)$, where the term on the last line is

$$H'(t) = -\int dx \, \hat{J}(x,t) F(x,t), \tag{11.12}$$

we are in the position to use the standard linear response Kubo formula [235], to calculate the conductance tensor Γ. Following Ref. [236] we introduce an AC chemical potential localized in the source lead, which we take to have coordinates $x < 0$. We choose a constant gauge $A(x,t) = A$ so that $F(x,t) = -\Theta(-x)\cos(\Omega t)e^{-\delta|t|}V/v(x)$.[1] The conductance Γ is defined as the magnitude of the in-phase current divided by the applied voltage difference V. Following the usual steps, with the current operator in Eq. (11.11) and assuming that the two Majorana modes are independent, we obtain the formula

$$\Gamma = \frac{e^2}{\pi h} \lim_{\Omega,\delta\to 0^+} \int_0^\infty dt' \int_0^\infty dt \, \mathrm{Im}[G_{ji}^> G_{j'i'}^>] \cos(\Omega t) e^{-\delta t}. \tag{11.13}$$

---

[1] Other gauges are also commonly used. Another choice, used e.g. in Refs. [237] and [238], is to use a source that is localized in the region of space where the potential is changing.

Here we have reintroduced the correct units of conductance e^2/h. We have also used the fact that in a chiral system the response in the region $x > 0$ to a spatially uniform extended source $x \leq 0$ at a particular time $t' = 0$ is equivalent to the response to a point source at $x = 0$ that is on for $t' \geq 0$. The important quantities to calculate are the Green's functions

$$G_{ji}^{>} \equiv \langle \psi(y,t)\psi(0,t') \rangle \equiv \langle \psi_j \psi_i \rangle, \tag{11.14a}$$

$$G_{j'i'}^{>} \equiv \langle \psi'(y',t)\psi'(0',t') \rangle \equiv \langle \psi'_{j'} \psi'_{i'} \rangle. \tag{11.14b}$$

Here the indexes i and j are shorthands for the coordinates of the source $(0,t')$ and current measurement (y,t). Similarly for the primed coordinate system, which is typically not the same in the setups that we consider as discussed previously.

Because the correlation functions only depends on $t - t'$ it is possible to perform the integral over $t + t'$ in Eq. (11.13) explicitly, the resulting expression is

$$\Gamma = -\frac{e^2}{\pi h} \int_0^{\infty} dt \, \mathrm{Im}[G_{ji}^{>} G_{j'i'}^{>}] t, \tag{11.15}$$

where it is understood that the source term is taken at $t' = 0$. Here we have also used the fact that the correct limit is to take $\delta \to 0^+$ first and then $\Omega \to 0$. Because we are interested in the finite temperature result the cut-off provided by the thermal length is enough to render the expression convergent. This is the master formula that we will use to calculate the conductance in the following.

If both Majorana modes propagates freely (the setup is sketched in Fig. 11.2) we can use the finite temperature propagator

$$G_{j'i'}^{>} = \frac{1}{z_{j'i'}} \equiv \frac{\pi T}{\sin \pi T[a + i u_{j'i'}]} \underset{a \to 0^+}{=} \pi \delta(u_{j'i'}) - i \mathscr{P} \frac{\pi T}{\sinh(\pi T u_{j'i'})}, \tag{11.16}$$

where $u_{j'i'} = t - L'$. The Green's function of the other edge $G_{ji}^{>}$ is given by the same expression with L (the effective length of propagation) instead of L'. Substituting the expressions for the Green's functions into Eq. (11.15) we obtain

$$\Gamma = \frac{e^2}{h} \frac{\pi T(L - L')}{\sinh[\pi T(L - L')]}, \tag{11.17}$$

in the limit $a \to 0^+$. This formula agrees with the linear response limit of the the result obtained with the scattering formalism in Ref. [144], and shows how the path difference enters in the finite temperature case.

To obtain the response in the source lead we take the limit $L' \to L$ with the result that

$$\Gamma = \frac{e^2}{h}. \tag{11.18}$$

This is the expected (and correct) result for a system with one propagating channel. If $L' \neq L$ we also obtain Eq. (11.18) as long as $T|L - L'| \ll 1$, in the zero temperature

limit the result is thus independent of the path length difference. The Eq. (11.18) agrees with the limit $V \to 0$ of the previous results [144, 145], which were based on the scattering formalism.

This calculation explicitly demonstrates how the "Dirac to Majorana converter" operates. The most intuitive way to understand it is to study the current operator in Eq. (11.11). In the usual (Dirac) picture it corresponds to the creation of an electron-hole pair. It can also be interpreted as the creation of a pair of Majorana excitations in the normal wire. When these excitations approach the superconductor they become spatially separated, as demonstrated in Fig. 11.2, but they can only be measured by simultaneously annihilating them in the drain lead.

In the following two sections we will keep one of the Majorana wires as a "reference Majorana" that propagates freely along one edge. The other "active Majorana" will have to tunnel through the bulk to go to the drain and contribute to the current. Tunneling can take place either as a fermion (Sec. 11.4) or as a pair of vortices (Sec. 11.5).

11.4 Perturbative formulation

In tunneling problems we want to calculate the Green's function $G_{ji}^{>} = \langle \psi_j \psi_i \rangle$, where ψ_i and ψ_j live on different edges of the sample, in the presence of a perturbation δH that couples the two edges. Assuming that the system is in a known state at time t_0, we may express the expectation value in the interaction picture as

$$G_{ji}^{>} = \langle U(t_0, t) \psi_j(t) U(t, 0) \psi_i(0) U(0, t_0) \rangle. \tag{11.19}$$

Here $U(t, t')$ is the time evolution operator in the interaction picture. For $t \geq t'$ it is given by the familiar time-ordered exponential $U(t, t') = \mathcal{T} \exp[-i \int_{t'}^{t} ds \delta H(s)]$.

In the following we will assume that the average at $t = t_0$ is a thermal one at temperature T. A perturbative expansion is obtained by expanding the time-ordered and anti-time-ordered exponentials in this expression in powers of δH. This procedure is equivalent to the Schwinger-Keldysh formalism, which in addition provides a scheme to keep track of whether one is propagating forward or backward in time. We will also assume that the perturbation was turned on in the infinite past, i.e. we set $t_0 = -\infty$.

As a warm-up for the vortex tunneling calculation we will now consider the simpler case of fermion tunneling, described by a tunneling term $H_\psi(t_1) = i \lambda_\psi \psi_2 \psi_1 / (2\pi)$ as in Ref. [182]. Here ψ_1 (ψ_2) is located at the tunneling point at the upper (lower) edge. The system and the coordinate convention we use are sketched in Fig. 11.3. The leading contribution to conductance comes at first order in the tunneling amplitude λ_ψ. After a straightforward expansion and collection of terms we obtain

$$G_{ji}^{>} = \frac{\lambda_\psi}{2\pi} \int_{-\infty}^{t} dt_1 \{\psi_j, \psi_2\} \langle \psi_1 \psi_i \rangle - \frac{\lambda_\psi}{2\pi} \int_{-\infty}^{0} dt_1 \{\psi_i, \psi_1\} \langle \psi_j \psi_2 \rangle + \mathcal{O}(\lambda_\psi^2). \tag{11.20}$$

Here we have used the fact that the two groups of fermions on different edges, i.e (ψ_j, ψ_2) and (ψ_i, ψ_1), are independent. It is straightforward to evaluate this expression

using Eq. (11.16) together with $\{\psi_i, \psi_1\} = 2\pi\delta(u_{1i})$, and $\{\psi_j, \psi_2\} = 2\pi\delta(u_{2j})$, where $u_{1i} = t_1 - L_{\text{top}}$ and $u_{2j} = t_1 - t + L_{\text{bottom}}$. Because of the geometry of the problem the second term on the right hand side of Eq. (11.20) vanishes due to causality (the Lorentz time arguments never coincide). The Green's function $G_{ji}^>$ to leading order in tunneling strength is therefore

$$G_{ji}^> = \lambda_\psi \frac{\pi T}{\sin \pi T[a + i(t - L)]}, \tag{11.21}$$

where $L = L_{\text{top}} + L_{\text{bottom}}$ is the effective propagation length of the Majorana fermion. Using the result of Sec. 11.3 we then find that the conductance of this setup is

$$\Gamma = \lambda_\psi \frac{e^2}{h}, \tag{11.22}$$

at $T = 0$. Once again this result agrees with the zero frequency, zero voltage limit of the results obtained with the scattering method in previous work [144, 145].
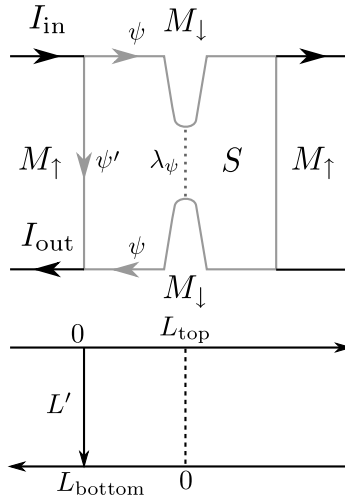
Figure 11.3: Top panel: fermion tunneling setup. The coordinate conventions used in Sec. 11.4 are shown in the bottom panel.

11.5   Vortex tunneling

The main focus of this chapter is to study how the tunneling of a pair of vortices can effectively transfer a fermion, and hence give a contribution to the conductance. Schematically the vortex tunneling term can be written as

$$\mathcal{H}_\sigma = \lambda_\sigma \sigma_b(x)\sigma_t(x'), \tag{11.23}$$

where the index t (b) denotes the top (bottom) edge. As it stands this term is not well-defined without more information about the two spin fields σ, this is discussed in great detail in Ref. [182]. We provide a detailed description of the formalism that we use to deal with this issue in the appendixes.

11.5.1 Coordinate conventions

To have a well-defined prescription for the commutation relation of fields on different edges we will treat the two edges as spatially separated parts of the same edge. This reasoning has been employed in a number of works studying tunneling in the FQH effect, see for example Refs. [239] and [240]. This approach leaves a gauge ambiguity: should we choose the bottom edge to have spatial coordinates smaller or larger than that of the top edge? The correct choice is fixed by noting that the current operator at the source should commute with the vortex tunneling term at equal times because of the locality and gauge invariance. A similar argument can be made considering the current operator at the measurement position before the information about the tunneling event has had time to reach it. Since we want the vortex tunneling event to commute with fermions on the reference edge at all times we are forced to use the coordinate convention shown in Fig. 11.4 in which the spatial coordinates on bottom edge are always larger than those on top edge.[2] The vortex tunneling then corresponds to changing the phase of the superconducting order parameter by $\pm 2\pi$ to the right of the tunneling point in the figure.
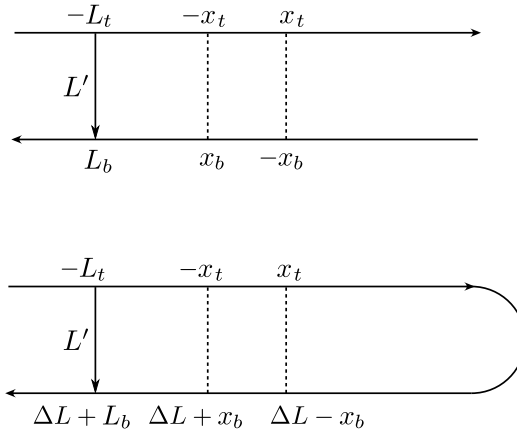
Figure 11.4: Top panel: independent coordinate system for the two edges. Bottom panel: coordinate system in which the two edges are treated as spatially separated parts of the same edge. This allows us to correctly capture the commutation relations of the fields on different edges in the relevant limit $\Delta L \to \infty$.

---

[2]Other gauges choices are possible, but are more cumbersome to use in the calculation.

In addition it is convenient to introduce an even more compact notation. We denote $\psi_t(0, -L_t) \equiv \psi_i$, $\psi_b(t, \Delta L + L_b) \equiv \psi_j$, $\sigma_t(t_1, -x_t) \equiv \sigma_1$, $\sigma_b(t_1, \Delta L + x_b) \equiv \sigma_2$, $\sigma_t(t_2, x_t) \equiv \sigma_3$, $\sigma_b(t_2, \Delta L - x_b) \equiv \sigma_4$. The two tunneling terms in the Hamiltonian are then written as $\lambda_\sigma T_{12}$ and $\lambda_\sigma T_{34}$. The modification needed to allow for different tunneling amplitudes $\lambda_{\sigma L}$ and $\lambda_{\sigma R}$ at the left and right tunneling points (see Fig. 11.1) is straightforward. The "Lorentz times" u for right-movers are $u \equiv t - x$. We use additional short-hand notations $u_{\alpha\beta} \equiv u_\alpha - u_\beta$ and $s_{\alpha\beta} \equiv \text{sign}(u_\alpha - u_\beta)$. The Lorentz times of the six operators used in the calculation are

$$
\begin{aligned}
u_i &= L_t \\
u_1 &= t_1 + x_t \\
u_3 &= t_2 - x_t \\
u_j &= t - L_b - \Delta L \\
u_2 &= t_1 - x_b - \Delta L \\
u_4 &= t_2 + x_b - \Delta L.
\end{aligned}
\tag{11.24}
$$

Taking the limit of large spatial separation $\Delta L \to +\infty$ we see that $s_{ij} = 1$. Accordingly, in this limit also $s_{kl} = 1$ for any $k \in \{i, 1, 3\}$ and $l \in \{j, 2, 4\}$.

In the following perturbative treatment we will assume that $t_2 \geq t_1$. This means that to calculate the full Green's function $G^>_{ji}$ we should sum over the four processes for which the first and the second vortex tunneling events happen at the right or the left tunneling point. The amplitudes of the two processes in which vortex tunneling events occur at different points are related by changing $x_t \to -x_t$ and $x_b \to -x_b$. Likewise the amplitudes of the processes in which both evens occur at the same tunneling point can be obtained from the amplitude of the process with vortex tunneling at different points by setting $x_t = x_b = 0$ and setting $L_t \to L_t \pm x_t$ and $L_b \to L_b \pm x_b$.

11.5.2 Perturbative calculation of $G^>$

In the appendices we demonstrate how one can evaluate the averages of the contributions to the integrands generated in the perturbative expansion of $G^>_{ji}$. The technically simplest way of performing the calculation is to use the commutation relation between fermions and tunneling terms [see Eq. (11.69)]

$$
T_{12}\psi_3 = s_{13}s_{23}\psi_3 T_{12},
\tag{11.25}
$$

to transform the correlation functions into one of the two forms in Eq. (11.70). The limit of large spatial separation $\Delta L \to \infty$ can then be taken using Eq. (11.71). Finally we use the functional form of the correlation function of a ψ and two σ's that is fixed by conformal invariance [241]:

$$
\langle \sigma_1 \sigma_3 \psi_i \rangle = \frac{z_{13}^{3/8}}{\sqrt{2} z_{1i}^{1/2} z_{3i}^{1/2}}.
\tag{11.26}
$$

The result of this calculation is the same as the limit $\Delta L \to \infty$ of the full six-point function that can also be calculated using bosonization and a doubling trick, see App. 11.A.

The first non-vanishing contribution to the fermion propagator $G^>$ comes at second order in the vortex tunneling term. It is then convenient to divide the intermediate time integrals into different regions. We will use the following labeling conventions: (a) $t_1 < t_2 < 0$, (b) $t_1 < 0 < t_2 < t$, and (c) $0 < t_1 < t_2 < t$. We now calculate the contribution to the integrand from each region separately.

Let us first consider the interval $t_1 < t_2 < 0$. By straightforward expansion, and using the exchange algebra we obtain the integrand in this region

$$
\begin{aligned}
I_{(a)} &= \langle \psi_j \psi_i T_{34} T_{12} \rangle + \langle T_{12} T_{34} \psi_j \psi_i \rangle \\
&\quad - \langle T_{34} \psi_j \psi_i T_{12} \rangle - \langle T_{12} \psi_j \psi_i T_{34} \rangle \\
&= s_{i1} s_{i2} (s_{i3} s_{i4} - s_{3j} s_{4j}) \langle \psi_j T_{34} T_{12} \psi_i \rangle \\
&\quad - s_{1j} s_{2j} (s_{i3} s_{i4} - s_{3j} s_{4j}) \langle \psi_j T_{12} T_{34} \psi_i \rangle.
\end{aligned}
\tag{11.27}
$$

The minus signs are generated when the two tunneling terms are on different Keldysh branches, i.e. when one comes from evolving forward in time and one backwards. We can simplify this expression further by noting that because of the geometry we always have $s_{i3} = s_{i1} = 1$ in this region. Thus

$$
I_{(a)} \equiv I^> = (1 + s_{j4})(\langle \psi_j T_{34} T_{12} \psi_i \rangle + s_{j2} \langle \psi_j T_{12} T_{34} \psi_i \rangle).
\tag{11.28}
$$

Let us now consider the interval $t_1 < 0 < t_2 < t$. We denote the contribution to the integrand in this region by $I_{(b)}$. Expanding we get

$$
\begin{aligned}
I_{(b)} &= \langle T_{12} T_{34} \psi_j \psi_i \rangle + \langle \psi_j T_{34} \psi_i T_{12} \rangle \\
&\quad - \langle T_{12} \psi_j T_{34} \psi_i \rangle - \langle T_{34} \psi_j \psi_i T_{12} \rangle = \ldots = I^>.
\end{aligned}
\tag{11.29}
$$

To see that we get the same expression as in region (a) we have used the fact that $s_{i1} = 1$ in this region. Performing the same calculation as in regions (a) and (b) for the interval $0 < t_1 < t_2 < t$ we find that also in this region

$$
I_{(c)} = I^>,
\tag{11.30}
$$

and hence we can use $I^>$ throughout all regions. Using cluster decomposition (i.e. taking the limit of spatial separation) and the explicit correlation functions we get the expression for the integrand. Putting back the integrals and the strength of the tunneling term we obtain the leading term in the perturbative expansion of the Green's function

$$
\begin{aligned}
G^> = \frac{\lambda_\sigma^2}{2^{3/2}} \int_{-\infty}^t dt_1 \int_{t_1}^t dt_2 \frac{(1 + s_{j4})}{(|z_{j2}||z_{j4}|)^{1/2}(z_{3i} z_{1i})^{1/2}} \\
[(1 + s_{j2}) \operatorname{Re}(z_{31}^{3/8} z_{42}^{3/8}) - (1 - s_{j2}) \operatorname{Im}(z_{31}^{3/8} z_{42}^{3/8})].
\end{aligned}
\tag{11.31}
$$

Note that this expression is a short form that includes a sum of many terms, it is valid for real times only and the analytic structure of the the Green's function is not apparent. It

is useful to shift the time-coordinates $t_j = t - L_b - x_b - s_j$ for $j = 1, 2$. The resulting expression is

$$G^> = \frac{\lambda_\sigma^2}{\sqrt{2}} \int_0^\infty ds_1 \int_0^{s_1} ds_2 \frac{1}{(|z_{j2}||z_{j4}|)^{1/2}(z_{3i}z_{1i})^{1/2}}$$
$$[(1 + s_{j2}) \operatorname{Re}(z_{31}^{3/8} z_{42}^{3/8}) - (1 - s_{j2}) \operatorname{Im}(z_{31}^{3/8} z_{42}^{3/8})], \quad (11.32)$$

where

$$
\begin{aligned}
u_{j2} &= 2x_b + s_1 \\
u_{j4} &= s_2 \\
u_{1i} &= \tilde{t} + x_t - x_b - s_1 \\
u_{3i} &= \tilde{t} - x_t - x_b - s_2 \\
u_{31} &= s_1 - s_2 - 2x_t \\
u_{42} &= s_1 - s_2 + 2x_b \\
\tilde{t} &= t - L_t - L_b.
\end{aligned}
\qquad (11.33)
$$

Note that the dependence on the parameters t, L_t, and L_b only enters in the combination $\tilde{t}$. The analytic structure is much more transparent in this equation. For tunneling at the same point, i.e. $x_t = x_b = 0$, we always have $s_{j2} = 1$ and the result simplifies to

$$G^>_{x_b = x_t = 0} = \lambda_\sigma^2 \sqrt{2} \cos\left(\frac{3\pi}{8}\right) \int_0^\infty ds_1 \int_0^{s_1} ds_2 \frac{|z_{31}|^{3/4}}{(|z_{j2}||z_{j4}|)^{1/2}(z_{3i}z_{1i})^{1/2}}. \quad (11.34)$$

From this expression we see that $\operatorname{Re}[G^>] \neq 0$ only for times such that $t \geq L_t + L_b$. Since $\operatorname{Re}[G^>]$ is proportional to the retarded Green function G^R, this is a reflection of the causality of the theory: information has to have time to propagate through the system for G^R to be non-zero.

The Green's function $G^>$ has a singular part that is given by

$$G^> \sim \lambda_\sigma^2 T^{-3/4}[-i \log|\xi| + \pi \Theta(\xi)], \quad (11.35)$$

with $\Theta(x)$ the Heaviside step function and

$$\xi = T(t - L_t - L_b - x_t - x_b) \ll 1. \quad (11.36)$$

11.5.3 Conductance

Substituting the propagator in Eq. (11.16) for the reference edge into the expression for conductance in Eq. (11.15) we obtain

$$\frac{\Gamma}{e^2/h} = -L' \operatorname{Im}[G^>]_{t=L'} + \int_0^\infty dt \, \mathcal{P} \frac{Tt}{\sinh(\pi T u_{j'i'})} \operatorname{Re}[G^>]. \quad (11.37)$$

Together with Eq. (11.32) this expression provides a closed expression determining the contribution from each process to the conductance, which may be directly evaluated numerically. Since $G^>$ only has a logarithmic divergence, the short distance cutoff a may be directly set to zero in this expression. By substituting the singular part of $G^>$ into Eq. (11.37) one can see that the conductance contribution is a continuous function of all the parameters of the problem. It may be written as

$$\Gamma_{LR} = \frac{e^2}{h} \frac{\lambda_\sigma^2 F[x_t T, x_b T, (L_t + L_b)T, L'T]}{T^{7/4}}, \tag{11.38}$$

with F a universal continuous function. In the low temperature limit, when all of the arguments of F are small, the contributions to conductance from vortex tunneling at different points Γ_{LL}, Γ_{RR}, Γ_{LR}, and Γ_{RL} are all equal to each other and to

$$\Gamma_0 = \frac{e^2}{h} \frac{\lambda_\sigma^2 F(0,0,0,0)}{T^{7/4}}, \tag{11.39}$$

with $F(0,0,0,0) \approx 1.5$. In the other limit, when either $|x_t + x_b|T \gg 1$ or $|L_t + L_b - L'|T \gg 1$ the function F is exponentially small, or in other words conductance is suppressed due to thermal averaging. We have evaluated the conductance of a single point contact due to vortex tunneling numerically with the result shown in Fig. 11.5. At low temperatures $\Gamma \times T^{7/4} \to$ constant as expected, and at high temperatures $\Gamma \sim \exp(-T|L' - L_t - L_b|)$.
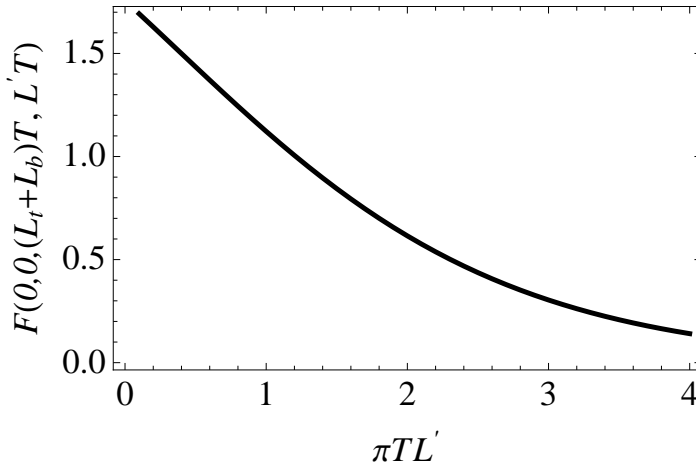
Figure 11.5: Normalized conductance $F[0, 0, (L_t + L_b)T, L'T] \equiv (h/e^2)\Gamma T^{7/4}/\lambda_\sigma^2$ of a single quantum point contact due to vortex tunneling as a function of temperature. The parameters of the setup are $L_t = L_b = L'$.

The scaling exponent of conductance $-7/4$ is different from $-3/2$, the exponent of tunneling conductance in the 5/2 FQH effect. This naturally follows from the very

different mechanisms of conduction in the two systems: current is carried by charged modes in 5/2 FQH system, while "Dirac to Majorana converter" forms current in topological insulators. This difference is reflected in the existence of a charge operator for each edge in the quantum Hall setup that allows the definition of a current operator that measures the current that flows between the two edges [231]. This current operator is defined locally at the tunneling point contact and can be used directly in the perturbative calculation of the current. In the FQH setup the leading contribution therefore involves a four-point function of the σ's. In the topological insulator setup the processes that contribute to the current correlations have to transfer a ψ between the two edges, which means that the six-point function of four σ's and two ψ's gives the leading contribution. Bare vortex tunneling given by the four-point function of σ's does not transfer Majorana fermions and is therefore irrelevant for the current in the topological insulator setup.

11.6 Quasiclassical approach and fermion parity measurement

The most interesting application of the interferometer setup with vortex tunneling is that it allows for the detection of the fermion parity of the superconducting island between the two point contacts [174–176]. This is possible because vortices acquire a phase of π when they are moved around an odd number of fermions [139]. In the simplest case, when there are only two bulk vortices in the central region, as shown in Fig. 11.1, the interferometric signal reads out the state of the qubit formed by the bulk vortices.

Without loss of generality we consider the case of two bulk vortices that are situated in between the left and the right tunneling regions. From the point of view of the electronic excitations the bulk vortices can be described by two localized Majorana bound states [130], with corresponding operators γ_a and γ_b. To describe the action of the vortex tunneling term on these excitations we include, following Ref. [242], an extra term $\hat{P}_{ab} = i\gamma_a\gamma_b$ in the left tunneling operator. This operator captures the property that upon changing the phase of the order parameter in the superconductor by $\pm 2\pi$ the Majorana modes localized in the vortex cores gains a minus sign.

In the absence of bulk-edge coupling the fermion parity of the vortex pair is a good quantum number that does not change with time. In that case the extra term that is added to the left tunneling term $\hat{P}_{ab}$ measures the fermion parity of the qubit defined by γ_a and γ_b. This means that we can replace $\hat{P}_{ab} \to (-1)^{n_f}$, where n_f is the number of fermions in the two vortices. In the second order calculation this factor enters only in the contributions where one vortex tunnels at the left tunneling point and one at the right, so the total conductance is equal to

$$\Gamma = \Gamma_{LL} + \Gamma_{RR} + (-1)^{n_f} (\Gamma_{LR} + \Gamma_{RL}). \tag{11.40}$$

The expressions for the Γ's were calculated in the previous section. The effect of bulk-edge coupling is presumably similar to the case of the 5/2 FQH effect that has been studied in great detail recently [242–245].

The phenomenological picture of the non-Abelian interferometry, as introduced in Ref. [145], can be summarized in the following way. First an incoming electron is split into two Majorana fermions when it approaches the superconductor. Next one of these Majorana fermions is further split into two edge vortices, or σ excitations. The edge vortices tunnel at either of the two point contacts, and recombine into a Majorana fermion again. Finally two Majorana fermions combine into electron or a hole as they leave the superconductor. At zero voltage any dynamic phases are prohibited by electron-hole symmetry, so the outgoing current may be written as

$$I = \frac{e^2}{h} V \left[\tilde{\lambda}_{\sigma L}^2 + \tilde{\lambda}_{\sigma R}^2 + 2(-1)^{n_f} \tilde{\lambda}_{\sigma L} \tilde{\lambda}_{\sigma R} \right], \qquad (11.41)$$

where $\tilde{\lambda}_{\sigma a}$ (with $a = L, R$) is an effective vortex tunneling amplitude (here we allow for different vortex tunneling amplitudes at the left and right tunneling points).

Comparing Eqs. (11.39)-(11.40) with Eq. (11.41) we see that at low temperatures the effective vortex tunneling amplitude is equal to

$$\tilde{\lambda}_{\sigma a} = \lambda_{\sigma a} T^{-7/8} \sqrt{F(0,0,0,0)}. \qquad (11.42)$$

Once this identification is done, the quasiclassical picture is directly applicable given that $1/T$ is much larger than the characteristic length of the system and the second order perturbation theory still holds ($\tilde{\lambda}_{\sigma a} \ll 1$).

11.7 Conclusions

In this chapter we have introduced a theory for a non-Abelian interferometer on the surface state of a 3D topological insulator brought in proximity to an s-wave superconductor. This theory uses CFT to describe the vortex field following Ref. [182], and is an extension of the earlier qualitative discussion in Ref. [145]. In particular we showed that if the temperature is low and tunneling is sufficiently weak, it is possible to introduce an effective tunneling amplitude of vortices according to Eq. (11.42). This justifies the simple quasiclassical description of vortex tunneling used in Ref. [145].

Because the vortex tunneling term is a relevant operator, the perturbative treatment is only valid at high enough temperatures. This statement is reflected in the divergence of conductance $\Gamma \sim T^{-7/4}$. The scaling exponent $-7/4$ is different from the tunneling conductance scaling exponent $-3/2$ of the 5/2 FQH setup in the linear response regime due to the different structure of current operators in the two systems.

11.A Vortex tunneling term

In this appendix we show how one can calculate the amplitude for transferring a fermion between the two edges in terms of two vortex tunneling events using bosonization with the help of a doubling trick. This is an old technique that goes back to the seventies

[246], which is now textbook material [241, 247]. In the appendices we use the condensed coordinate conventions introduced in Sec. 11.5.1, but we'll keep the gauge choice implied by the sign of s_{ij} unspecified.

11.A.1   Non-chiral extension of the system

The logic of the procedure can be motivated as follows (see also the construction in Ref. [242]). We are interested in the tunneling of a chiral Majorana fermion between two edges of a sample (cf. Fig. 11.4). Because of the fermion doubling feature it is convenient to enlarge the system by adding an additional counter-propagating chiral Majorana fermion. These two copies can then be described as the continuum limit of a lattice model of local Majorana fermions (described by lattice operators $\gamma_l^\dagger = \gamma_l$) that are allowed to hop to their nearest neighbors:

$$H = -t \sum_{l=1}^{2N} i\gamma_l\gamma_{l+1}. \tag{11.43}$$

The fermion parity operator is then $\hat{P} \equiv \prod_{l=1}^{2N} e^{i\pi/4}\gamma_l$. This system is known to map onto the (quantum) Ising chain in a transverse field at criticality (see e.g. Ref. [247]), which is also equivalent to the classical 2D Ising model at its critical point. In the Ising model there are spin and disorder fields that are non-local in terms of the lattice fermions. It is easy to write down explicit expressions for the spin and disorder operators in terms of a string of Majorana fermions on the lattice, for example

$$\sigma_{2i+1}\sigma_{2j+1} = \prod_{l=2i+1}^{2j} e^{i\pi/4}\gamma_l, \tag{11.44a}$$

$$\mu_{2i}\mu_{2j} = \prod_{l=2i}^{2j-1} e^{i\pi/4}\gamma_l, \tag{11.44b}$$

$$\sigma_{2i+1}\mu_{2j} = e^{-i\pi/4} \prod_{l=2i+1}^{2j-1} e^{i\pi/4}\gamma_l. \tag{11.44c}$$

It is clear from these expressions that a $\sigma\mu$ term changes the fermion parity of the system whereas $\sigma\sigma$ and $\mu\mu$ do not.

Now we are not interested in the lattice theory itself but rather the low-energy theory which is obtained in the continuum limit of the lattice model. This limit is known to map onto the Ising CFT. This is a thoroughly studied system and we can hence rely on results from the large literature on this topic.

In particular, on the lattice we know that a vortex tunneling term has to be of the form $\sigma_1\sigma_2$ or $\mu_1\mu_2$, otherwise the fermion parity is changed. Furthermore, from the

operator product expansion of the Ising CFT [241, 248]:

$$\sigma_1\sigma_2 \quad \sim \quad \frac{1}{(z_{12}\bar{z}_{12})^{1/8}} + \frac{1}{2}(z_{12}\bar{z}_{12})^{3/8}i\psi_2\bar{\psi}_2, \tag{11.45a}$$

$$\mu_1\mu_2 \quad \sim \quad \frac{1}{(z_{12}\bar{z}_{12})^{1/8}} - \frac{1}{2}(z_{12}\bar{z}_{12})^{3/8}i\psi_2\bar{\psi}_2, \tag{11.45b}$$

we see that a pair of σ's (or a pair of μ's) can change the parity of right-movers. Since our tunneling term is not allowed to do this we take the tunneling term in the non-chiral system to be $\tilde{T}_{12} \propto \sigma_1\sigma_2 + \mu_1\mu_2$. Clearly the parity-changing term is canceled with this choice. Another way of putting this is to say that this combination enforces the tunneling term to be in the identity channel.

It is known that two *independent* copies of the Ising model can be bosonized using Abelian bosonization [241, 246]. It is then a straightforward calculation (using for example the explicit expressions in the appendix of Ref. [248]) to show that the doubled tunneling term can be bosonized as

$$\widetilde{T}_{12}\widetilde{T}'_{12} = \cos\Big(\frac{\phi_1 - \phi_2}{2}\Big)\cos\Big(\frac{\bar{\phi}_1 - \bar{\phi}_2}{2}\Big). \tag{11.46}$$

It is important to note that the primed system is an *independent* copy of the system in this expression, and that it is introduced as a trick to allow for a simple calculation of various correlation functions.

11.A.2   From non-chiral back to chiral

Since we are only interested in the right-moving part of the tunneling term we would like to get rid of the left-moving part in the last equation. Because of the factorization of the right- and left-moving parts we are allowed to use

$$T_{12}T'_{12} = \cos\Big(\frac{\phi_1 - \phi_2}{2}\Big), \tag{11.47}$$

as the doubled tunneling term in the chiral system. Here the cosines are to be understood as shorthands for $\cos(a - b) = (e^{ia}e^{-ib} + e^{-ia}e^{ib})/2$. The exponentials in these expressions are actually dimensionful vertex operators, see e.g. Ref. [249] for a detailed discussion. With this representation together with the bosonized representation of the Majorana fermion in the unprimed system

$$\psi_i = \sqrt{2}\cos(\phi_i), \tag{11.48}$$

and the standard bosonization formula (which holds if $\sum_{i=1}^{N}\alpha_i = 0$, otherwise the expectation value vanishes)

$$\langle e^{i\alpha_1\phi_1}e^{i\alpha_2\phi_2}\cdots e^{i\alpha_N\phi_N}\rangle = \prod_{1\leq i<j\leq N} z_{ij}^{\alpha_i\alpha_j}, \tag{11.49}$$

with

$$z_{ij} = \frac{\sin[\pi T (a + i u_{ij})]}{\pi T}, \tag{11.50}$$

we can in principle calculate any correlation function using the bosonization formalism. In particular we can calculate the full six-point function including two ψ's and two tunneling terms. This will be done in the next subsection, but let us first check that the representation reproduces known results for the 2-, 3- and 4-point functions.

Let us first consider the vortex 2-point function. This is calculated via

$$\langle T_{12} \rangle^2 = \langle T_{12} T_{12}' \rangle = \frac{1}{z_{12}^{1/4}}. \tag{11.51}$$

Taking the square root we obtain the correct result for a field with dimension $\frac{1}{16}$

$$\langle T_{12} \rangle = \frac{1}{z_{12}^{1/8}}. \tag{11.52}$$

Similarly the fermion two-point function is $\langle \psi_i \psi_j \rangle = z_{ij}^{-1}$. The vortex 4-point function can be computed from

$$\langle T_{12} T_{34} \rangle^2 = \frac{1}{2} \Big[\Big(\frac{z_{13} z_{24}}{z_{12} z_{23} z_{34} z_{14}} \Big)^{1/4} + \Big(\frac{z_{14} z_{23}}{z_{13} z_{24} z_{12} z_{34}} \Big)^{1/4} \Big]. \tag{11.53}$$

Taking the square root of this expression we get the known correlation function of four σ's for which σ_1 and σ_2 fuse to the identity [250–252]. Now we use the conventions from the main part of the chapter and take the limit $\Delta L \to \infty$. In this case only one of the terms in Eq. (11.53) survives and

$$\langle T_{12} T_{34} \rangle \underset{\Delta L \to \infty}{=} \frac{1}{\sqrt{2}} \Big(\frac{z_{14} z_{23}}{z_{13} z_{24} z_{12} z_{34}} \Big)^{1/8}. \tag{11.54}$$

We also have

$$\langle \psi_i T_{12} \rangle = 0, \tag{11.55}$$

which is consistent with the notion that the tunneling of a vortex cannot create a fermion (or equivalently change the fermion parity). It is also straightforward to show that

$$\langle \psi_i \psi_j T_{12} \rangle \underset{\Delta L \to \infty}{=} 0, \tag{11.56}$$

which means that a single vortex tunneling event is not enough to be able to transfer a fermion between the two edges.

11.A.3   The six-point function

To calculate the contribution from a tunneling of two vortices we need the six-point function of two ψ's and four σ's. This correlation function is a special case of the more

general one that was first calculated in Ref. [253] with a similar method. To calculate the six-point function we use

$$
\langle \psi_i \psi_j T_{12} T_{34} \rangle \langle T'_{12} T'_{34} \rangle = 2 \Big\langle \cos(\phi_i) \cos(\phi_j) \cos\Big(\frac{\phi_1 - \phi_2}{2}\Big) \cos\Big(\frac{\phi_3 - \phi_4}{2}\Big) \Big\rangle.
$$

$$
= \frac{1}{4 z_{ij} (z_{12} z_{34})^{1/4}} \times \Big\{ \Big[\Big(\frac{z_{i1} z_{i3} z_{j2} z_{j4}}{z_{i2} z_{i4} z_{j1} z_{j3}}\Big)^{1/2} + (i \leftrightarrow j) \Big] \Big(\frac{z_{13} z_{24}}{z_{14} z_{23}}\Big)^{1/4}
$$

$$
+ \Big[\Big(\frac{z_{i1} z_{i4} z_{j2} z_{j3}}{z_{i2} z_{i3} z_{j1} z_{j4}}\Big)^{1/2} + (i \leftrightarrow j) \Big] \Big(\frac{z_{14} z_{23}}{z_{13} z_{24}}\Big)^{1/4} \Big\}. \quad (11.57)
$$

Dividing this with the square root of Eq. (11.53) the result agrees with that of Ref. [253]. We now take the limit of spatial separation $\Delta L \to \infty$, the only one term that remains is

$$
\langle \psi_i \psi_j T_{12} T_{34} \rangle \langle T'_{12} T'_{34} \rangle \underset{\Delta L \to \infty}{=} \frac{(z_{13} z_{24})^{1/4}}{4 (z_{i1} z_{i3} z_{j2} z_{j4})^{1/2}} \times \frac{(z_{i2} z_{i4} z_{j1} z_{j3})^{1/2}}{z_{ij} (z_{12} z_{34} z_{14} z_{23})^{1/4}}. \quad (11.58)
$$

Combining this with Eq. (11.54) we find

$$
\langle \psi_i \psi_j T_{12} T_{34} \rangle = \frac{(z_{13} z_{24})^{3/8}}{2^{3/2} (z_{i1} z_{i3} z_{j2} z_{j4})^{1/2}} \times \frac{(z_{i2} z_{i4} z_{j1} z_{j3})^{1/2}}{z_{ij} (z_{14} z_{23})^{1/2}}, \quad (11.59)
$$

To get this result we have removed the phases associated with $z_{12}^{-1/8}$ and $z_{34}^{-1/8}$. These phases are canceled when one makes sure that the tunneling term is described by a Hermitean term in the Hamiltonian. This is exactly the phase of $\langle T_{12} \rangle$ in Eq. (11.52).

Other orderings of the fermions and the tunneling terms are obtained by exchanging the indexes, for example

$$
\langle \psi_i T_{12} \psi_j T_{34} \rangle = \frac{(z_{13} z_{24})^{3/8}}{2^{3/2} (z_{i1} z_{i3} z_{2j} z_{j4})^{1/2}} \times \frac{(z_{i2} z_{i4} z_{1j} z_{j3})^{1/2}}{z_{ij} (z_{14} z_{23})^{1/2}}. \quad (11.60)
$$

The indexes on the z's should have the same order as they appear in in the original expression. This prescription was used in e.g. Ref. [243] and is equivalent to the Keldysh formalism for chiral bosons which is reviewed in e.g. Refs. [254] and [240]. In the limit of spatial separation the last term gives a phase factor that depends on the order of the tunneling terms and the fermions according to

$$
e^{i \alpha_p} = -i s_{ij} \begin{cases} 1, & p = ij1234, \ 1234ij, \ 12ij34 \\ -1, & p = i1234j \\ i s_{ij}, & p = i12j34, \ 12i34j. \end{cases} \quad (11.61)
$$

11.B   Exchange algebra

An alternative formalism is provided by the exchange algebra of Ref. [255]. In this formalism the action of the spin field is described by two types of operators a and b

and their conjugates. a creates an excitation with dimension $\frac{1}{16}$ when acting on the vacuum, which is denoted by the shorthand $a|0\rangle = |\frac{1}{16}\rangle$. The conjugate $a^\dagger$ interpolates in the opposite direction: $a^\dagger|\frac{1}{16}\rangle = |0\rangle$. Similarly b and $b^\dagger$ interpolates between states of dimensions $\frac{1}{16}$ and $\frac{1}{2}$ according to $b|\frac{1}{16}\rangle = |\frac{1}{2}\rangle$ and $b^\dagger|\frac{1}{2}\rangle = |\frac{1}{16}\rangle$. The exchange algebra is described by the following relations

$$\begin{pmatrix} a_1 a_2^\dagger \\ b_1^\dagger b_2 \end{pmatrix} = \frac{e^{is_{12}\frac{\pi}{8}}}{\sqrt{2}} \begin{pmatrix} 1 & e^{-is_{12}\frac{\pi}{2}} \\ e^{-is_{12}\frac{\pi}{2}} & 1 \end{pmatrix} \begin{pmatrix} a_2 a_1^\dagger \\ b_2^\dagger b_1 \end{pmatrix}, \tag{11.62}$$

$$a_1^\dagger a_2 = e^{-is_{12}\frac{\pi}{8}} a_2^\dagger a_1, \tag{11.63a}$$

$$b_1 b_2^\dagger = e^{-is_{12}\frac{\pi}{8}} b_2 b_1^\dagger, \tag{11.63b}$$

$$b_1 a_2 = e^{-is_{12}\frac{\pi}{8}} e^{is_{12}\frac{\pi}{2}} b_2 a_1, \tag{11.63c}$$

$$a_1^\dagger b_2^\dagger = e^{-is_{12}\frac{\pi}{8}} e^{is_{12}\frac{\pi}{2}} a_2^\dagger b_1^\dagger. \tag{11.63d}$$

The tunneling operator, e.g. T_{12}, consists of a product of two σ's in the identity channel, which we denote $[\sigma_1 \sigma_2]_I$. When acting on states with dimension 0 or $\frac{1}{2}$ this implies that we are allowed to use the representations

$$[\sigma_1 \sigma_2]_I \rightarrow \begin{cases} a_1^\dagger a_2, & |0\rangle \rightarrow |0\rangle \\ b_1 b_2^\dagger, & |\frac{1}{2}\rangle \rightarrow |\frac{1}{2}\rangle \end{cases}. \tag{11.64}$$

Another important point is that the tunneling term should be represented by a Hermitean term in the Hamiltonian. This can be achieved by explicitly adding the Hermitean conjugate in the definition of the tunneling term:

$$T_{12} \propto [\sigma_1 \sigma_2 + \sigma_2 \sigma_1]_I = \begin{cases} (1 + e^{-is_{12}\frac{\pi}{8}})[\sigma_2 \sigma_1]_I \\ (1 + e^{is_{12}\frac{\pi}{8}})[\sigma_1 \sigma_2]_I \end{cases}. \tag{11.65}$$

In the last step we used Eqs. (11.64) and (11.63). By adjusting the amplitude to conform with the result of the previous section [see discussion below Eq. (11.59)] we define

$$T_{12} = e^{-is_{12}\frac{\pi}{16}} [\sigma_2 \sigma_1]_I = e^{is_{12}\frac{\pi}{16}} [\sigma_1 \sigma_2]_I, \tag{11.66}$$

which is Hermitean.

Similarly we can represent the fermion field in terms of a's and b's with coinciding arguments[3]

$$\psi_1 \propto \begin{cases} b_1 a_1, & |0\rangle \rightarrow |\frac{1}{2}\rangle \\ a_1^\dagger b_1^\dagger, & |\frac{1}{2}\rangle \rightarrow |0\rangle \end{cases}. \tag{11.67}$$

---

[3]The correct expression is obtained in the properly scaled limit of coinciding coordinates. For example, to go from $|\frac{1}{2}\rangle \rightarrow |0\rangle$ we may use $\psi(u) = \lim_{\delta \rightarrow 0^+} C\delta^{-3/8} a^\dagger(u+\delta)b^\dagger(u)$. Here C is a constant that can be determined by fixing the normalization, but this is not necessary to derive the commutation relations.

Using Eqs. (11.67) and (11.64) together with the exchange algebra of Eqs. (11.62) and (11.63) it is straightforward to show that in all cases we have the following commutation relations

$$[\sigma_1\sigma_2]_I \psi_3 = s_{13}s_{23}\psi_3[\sigma_1\sigma_2]_I, \tag{11.68}$$

which immediately implies the commutation relation between a tunneling term and a fermion is

$$T_{12}\psi_3 = s_{13}s_{23}\psi_3 T_{12}. \tag{11.69}$$

With this very important relation we can always transform the correlation functions that we want to calculate (see Sec. 11.5.2) into one of two different forms:

$$\langle \psi_j T_{12} T_{34} \psi_i \rangle, \tag{11.70a}$$

$$\langle \psi_j T_{34} T_{12} \psi_i \rangle. \tag{11.70b}$$

Using the exchange algebra we can cluster decompose the last two expressions, in the limit of spatial separation we are left with

$$\langle \psi_j T_{12} T_{34} \psi_i \rangle \underset{\Delta L \to \infty}{=} \frac{e^{-is_{12}\frac{\pi}{2}}}{\sqrt{2}} \langle \psi_j b_2 a_4 \rangle \langle a_1^\dagger b_3^\dagger \psi_i \rangle, \tag{11.71a}$$

$$\langle \psi_j T_{34} T_{12} \psi_i \rangle \underset{\Delta L \to \infty}{=} \frac{e^{-is_{12}\frac{\pi}{2}}}{\sqrt{2}} \langle \psi_j b_4 a_2 \rangle \langle a_3^\dagger b_1^\dagger \psi_i \rangle. \tag{11.71b}$$

We have checked that the result of the formalism in this appendix gives identical results to those of the formalism in App. 11.A. Although the exchange algebra is derived at $T = 0$ it also holds at finite temperatures.

Chapter 12

Probing Majorana edge states with a flux qubit

12.1   Introduction

Chiral Majorana fermion edge states were originally predicted to exist in the 5/2 fractional quantum Hall plateau [5]. These edge states support not only neutral fermionic excitations but also more exotic edge vortices. A single edge vortex corresponds to a π phase shift to all fermions situated to one side of it [182, 242, 244]. Two edge vortices may either fuse into an edge fermion or annihilate each other, with the outcome depending on the preceding evolution of the system. In other words, the edge theory (together with the corresponding bulk theory) possesses non-Abelian statistics [6, 9, 129, 139]. This unusual physics and its potential applications to topological quantum computation are the reasons why the Majorana edge states have attracted much attention recently [8, 174–176, 240, 256].

Similar non-Abelian anyons and their corresponding edge states appear in superconducting systems as well. Initially it was discovered that p-wave superconductors support non-Abelian anyons in the bulk and chiral Majorana edge states [6, 234]. Later it was shown that depositing a conventional s-wave superconductor on the surface of a topological insulator while breaking time-reversal symmetry provides an alternative route to realize these non-Abelian states [130, 144, 145]. Alternative proposals include substituting the topological insulator by a two-dimensional electron gas with spin-orbit coupling [131, 228, 257] or by a half-metal [258, 259]. The realizations of Majorana edge states using s-wave superconductors have the following advantages: first, they rely on combining simple, well-studied ingredients. Second, the materials do not have to be extremely pure unlike samples needed to support the fractional quantum Hall edge states. Finally, the superconducting implementations of Majorana fermions may feature a larger bulk excitation gap and may therefore be operated at higher temperatures.

The downside of the superconducting implementations of Majorana edge states is the lack of means to manipulate edge vortices [144, 145]. Different from the 5/2 fractional quantum Hall state, the edge vortices are not coupled to charge and thus cannot be controlled by applying voltages [260]. Therefore, the standard proposal to probe the

edge vortices in superconducting systems is to inject fermion excitations into the edge, to let them split into edge vortices, and finally to conclude about the behavior of the edge vortices from the detection of the fermion excitations after the subsequent fusion of edge vortices [144, 145, 260, 261].

In this chapter, we propose a more direct way to manipulate and measure edge vortices using a flux qubit consisting of a superconducting ring interrupted by a Josephson junction [143, 262]. Our main idea is based on the following observations: first, an edge vortex is created when a superconducting vortex crosses the edge. Second, the motion of the superconducting vortices can be fully controlled by a flux qubit, since by applying a flux bias to the qubit one can tune the energy cost for a vortex being present in the superconducting ring [262]. In this way, attaching a flux qubit to a system supporting Majorana edge states allows to directly create, control, and measure edge vortices without relying on splitting and fusing fermionic excitations.

We note that our proposal is not necessarily advantageous for the purposes of topological quantum computing since quantum computing with Majorana fermions may even be realized without ever using edge states [143, 210, 211]. Instead the aim of our investigation is to develop a better tool for probing the fractional excitations of the edge theory.

The chapter is organized as follows. In Sec. 12.2, we discuss a schematic setup of a system where a pair of chiral Majorana fermion edge modes couple to a flux qubit as a probe of the edge states and briefly list our main findings. In Sec. 12.3, we review the connection between the one-dimensional critical transverse-field Ising model and Majorana fermion modes. We identify the vortex tunneling operators between two edge states as the disorder fields of the Ising model, and subsequently derive an effective Hamiltonian for the flux qubit coupled to Majorana modes. In Sec. 12.4, we provide the necessary formalism for evaluating the expectation values for the flux qubit state and qubit susceptibilities. In Sec. 12.5 and Sec. 12.6, we compute the qubit expectation values and the two-point qubit correlation functions in the presence of the edge state coupling, and use these results to derive the qubit susceptibility. In Sec. 12.7, we analyze higher order corrections to correlation functions of the qubit state. We summarize our results in Sec. 12.8. Additionally, we include some mathematical details in two Appendices.

12.2   Setup of the system

In this work, we consider the following setup: a strip of s-wave superconductor is deposited on the surface of either a three-dimensional topological insulator or a semiconductor with strong spin-orbit coupling and broken time-reversal symmetry (or any other superconducting setup supporting Majorana edge states). As depicted in Fig. 12.1, a pair of counter-propagating Majorana fermion edge modes appears at the two opposite edges of the superconductor [144, 145]. To avoid mixing between counter-propagating edge states, the width of the superconductor should be much larger than the superconducting coherence length $\hbar v_F / \Delta$. Here and in the following, v_F denotes the Fermi velocity of the topological insulator (semiconductor) and Δ the proximity-induced superconduct-

ing pair-potential. In order to avoid mixing of the two counter-propagating edge modes at the ends of the sample, we require either the length of the superconducting strip to be longer than the dephasing length or metallic leads to be attached to the ends of the sample.

A flux qubit, consisting of a superconducting ring with a small inductance interrupted by a Josephson junction, is attached to the heterostructure supporting the Majorana edge modes, as shown in Fig. 12.1. By applying an external flux, the two classical states of the superconducting ring corresponding to the phase difference of 0 and 2π across the junction can be tuned to be almost degenerate [262]. In this regime, the flux qubit can be viewed as a quantum two-level system with an energy difference ε (which we choose to be positive) between the states $|0\rangle$ and $|2\pi\rangle$ and a tunneling amplitude δ between them. The transition between the two qubit states is equivalent to the process of a vortex tunneling through the Josephson junction in or out of the superconducting ring. For convenience, we will refer to the Hilbert space spanned by the qubit states $|0\rangle$ and $|2\pi\rangle$ as a spin-1/2 system. For example, we are going to call the Pauli matrices $\sigma^{x,y,z}$ acting on the qubit states the qubit spin.

A vortex tunneling through the weak link in the superconductor from one edge to the other is a phase slip of 2π of the superconducting phase difference at the tunneling point. Due to this event, all fermions to one side of the weak link gain a phase of π. As will be shown below, the vortex tunneling operator can be identified with the operator of the disorder field of a one-dimensional critical Ising model onto which the Majorana edge modes can be mapped.

Since vortex tunneling events couple the qubit spin to the Majorana edge modes, we expect various observables of the qubit to carry signatures of this coupling. The main theory parameter that we are after is the scaling dimension $\Delta_\mu = 1/8$ of the edge vortex operator (disorder field). Our main results apply to the regime when vortex tunneling is weak $\varepsilon \gg \delta$.

We find that the reduction of the spin expectation value in the z-direction due to the vortex tunneling acquires a nontrivial scaling exponent

$$1 - \langle \sigma^z \rangle \propto \frac{\delta^2}{\varepsilon^{2-2\Delta_\mu}} = \frac{\delta^2}{\varepsilon^{7/4}}. \tag{12.1}$$

Similarly, the spin expectation value along the x-direction is proportional to $\varepsilon^{2\Delta_\mu - 1} = \varepsilon^{-3/4}$ thereby probing the scaling dimension of the disorder field.

Besides the static measurements of spin expectation values, the frequency-dependent susceptibilities, that characterize the response of the polarization of the qubit spin, also provide information about the Majorana edge states. Experimentally they can be determined by measuring the response of the qubit when an oscillating magnetic field is coupled to the qubit that changes either the energy difference ε or the tunneling amplitude δ. The frequency dependence of the susceptibilities exhibits a non-Lorentzian resonant response around the frequency $\omega \approx \varepsilon$ (here and in the following, we set $\hbar = 1$). It is modified by the coupling to the Majorana edge states and shows the scaling behavior

$$|\chi(\omega)| \propto \frac{1}{|\omega - \varepsilon|^{1-2\Delta_\mu}} = \frac{1}{|\omega - \varepsilon|^{3/4}}, \tag{12.2}$$
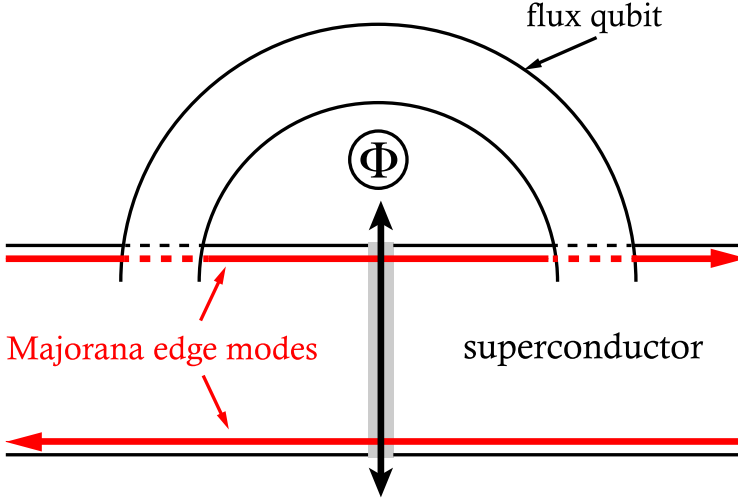
Figure 12.1: Schematic setup of the Majorana fermion edge modes coupled to a flux qubit. A pair of counter-propagating edge modes appears at two opposite edges of a topological superconductor. A flux qubit, that consists of a superconducting ring and a Josephson junction, shown as a gray rectangle, is attached to the superconductor in such a way that it does not interrupt the edge states flow. As indicated by the arrow across the weak link, vortices can tunnel in and out of the superconducting ring through the Josephson junction.

as long as $\varepsilon \gg |\omega - \varepsilon|$, and the distance $|\omega - \varepsilon|$ from the resonance is larger than the width of the resonance. The phase change of susceptibility at the resonance $\delta\phi = 3\pi/4$ is different from the π phase change for a usual oscillator. The origin of the extra $\pi/4$ phase shift is the Abelian part of the statistical angle of the vortex excitations [8].

12.3   Edge states and coupling to the qubit

12.3.1   Coupling of the flux qubit to the edge states

The flux qubit has two low energy states, corresponding to a phase difference $\phi = 0$ or $\phi = 2\pi$ across the Josephson junction at $x = x_0$. The Hamiltonian of the qubit is given by

$$H_Q = -\frac{\varepsilon}{2}\sigma^z - \frac{\delta}{2}e^{i\alpha}\sigma^+ - \frac{\delta}{2}e^{-i\alpha}\sigma^-. \tag{12.3}$$

The energy difference ε can be tuned by applying an external flux to the qubit while the tunneling amplitude $\delta > 0$ can be manipulated by changing the Josephson coupling of the junction [262]. The tunneling phase α is proportional to the charge induced on the sides of the junction and its fluctuations are the main source of qubit decoherence. For

simplicity we neglect the charge noise so that we can assume that α is static and set it to zero without loss of generality. The qubit Hamiltonian now reads

$$H_Q = -\frac{\varepsilon}{2}\sigma^z - \frac{\delta}{2}\sigma^x. \tag{12.4}$$

When there is no phase difference across the Josephson junction ($\phi = 0$), the Hamiltonian of the chiral Majorana modes appearing at the edges of the superconductor, as shown in Fig. 12.1, reads

$$H_{\text{MF}} = \frac{iv_M}{2} \int \frac{dx}{2\pi} [\psi_d(x)\partial_x\psi_d(x) - \psi_u(x)\partial_x\psi_u(x)], \tag{12.5}$$

where v_M is the velocity of the Majorana modes, and $\psi_u(x)$ and $\psi_d(x)$ are the Majorana fermion fields at the upper and lower edges of the superconductor in Fig. 12.1. The sign difference between the terms containing ψ_u and ψ_d is due to the fact that the modes are counter-propagating. The Majorana fermion fields obey the anti-commutation relations

$$\{\psi_u(x), \psi_u(x')\} = \{\psi_d(x), \psi_d(x')\} = 2\pi\delta(x - x'),$$
$$\{\psi_u(x), \psi_d(x')\} = 0. \tag{12.6}$$

A vortex tunneling through the weak link at $x = x_0$ advances the phase of each Cooper pair in the region $x \leq x_0$ by 2π. For Majorana fermions, just like any other fermions, this results in phase shift of π. The effect of this phase shift is a gauge transformation

$$H_{\text{MF}} \mapsto PH_{\text{MF}}P, \tag{12.7}$$

where the parity operator P is given by

$$P = \exp\left[i\pi \int_{-\infty}^{x_0} dx\, \rho_e(x)\right], \tag{12.8}$$

with the fermion density $\rho_e(x) = [\pi\delta(x) + i\psi_u(x)\psi_d(x)]/2\pi$. The relation between the phase slip and the parity operator was discussed and used in previous work focusing on the 5/2 fractional quantum Hall state [242, 244, 256].

Combining the Hamiltonian of the Majorana edge states (12.5, 12.7) with the qubit Hamiltonian (12.4), we get the full Hamiltonian of the coupled system in the basis of $|0\rangle$ and $|2\pi\rangle$:

$$\mathcal{H} = \begin{pmatrix} H_{\text{MF}} & 0 \\ 0 & PH_{\text{MF}}P \end{pmatrix} + H_Q. \tag{12.9}$$

The first part of Hamiltonian represents the chiral Majorana edge states coupled to the phase slip of the superconductor while the second part is the bare flux qubit Hamiltonian.

Because the parity operator (12.8) is highly nonlocal if expressed in terms of Majorana fermions, it is desirable to map the Majorana modes on a system where the vortex tunneling event becomes a local operator. To this end, we establish the equivalence of the chiral Majorana edge modes with the long wavelength limit of the one-dimensional transverse-field Ising model at its critical point [246, 263].

12.3.2   Mapping on the critical Ising model

The lattice Hamiltonian of the Ising model at the critical point is given by [246, 263]:

$$H_I = -J \sum_n (s_n^x s_{n+1}^x + s_n^z), \tag{12.10}$$

where s_n^α are the spin-1/2 operators at site n. With the Jordan-Wigner transformation,

$$
\begin{aligned}
s_n^+ &= c_n \exp(i\pi \sum_{j<n} c_j^\dagger c_j), \\
s_n^- &= c_n^\dagger \exp(i\pi \sum_{j<n} c_j^\dagger c_j), \quad s_n^z = 1 - 2c_n^\dagger c_n,
\end{aligned}
\tag{12.11}
$$

the Ising model (12.10) can be cast in terms of fermions as

$$H_I = J \sum_n [(c_n - c_n^\dagger)(c_{n+1} + c_{n+1}^\dagger) + c_n^\dagger c_n - c_n c_n^\dagger]. \tag{12.12}$$

Here $s_i^\pm \equiv (s_i^x \pm i s_i^y)/2$ obey the usual onsite spin commutation relations while the fermions operators $c_i^\dagger$ and c_i obey canonical anti-commutation relations.

For each fermion, we introduce a pair of Majorana operators $\psi_n = \psi_n^\dagger$ and $\bar\psi_n = \bar\psi_n^\dagger$ such that

$$c_n = \frac{e^{-i\pi/4}}{2}(\psi_n + i\bar\psi_n). \tag{12.13}$$

The Majorana fermions satisfy the Clifford algebra

$$\{\psi_m, \psi_n\} = \{\bar\psi_m, \bar\psi_n\} = 2\delta_{mn}, \qquad \{\psi_m, \bar\psi_n\} = 0. \tag{12.14}$$

In terms of the Majorana operators, the Hamiltonian (12.12) assumes the form

$$H_I = -\frac{iJ}{2} \sum_n (\psi_n \psi_{n+1} - \bar\psi_n \bar\psi_{n+1} + \psi_n \bar\psi_{n+1} - \bar\psi_n \psi_{n+1} - 2\psi_n \bar\psi_n). \tag{12.15}$$

In the long wavelength limit, the Hamiltonian (12.15) reduces to (12.5) with the identification of the continuum Majorana operators

$$\psi_u(x) \mapsto \sqrt{\frac{\pi}{a}}\psi_n, \quad \psi_d(x) \mapsto \sqrt{\frac{\pi}{a}}\bar\psi_n, \quad x \mapsto na \tag{12.16}$$

and the velocity $v_M \mapsto 2Ja$. To complete the mapping, the bandwidth of the Ising model should be related to the cutoff energy Λ of the linear dispersion of the Majorana edge states, $\Lambda \mapsto J$. Thereby, a pair of counter-propagating Majorana edge states, $\psi_u(x)$ and $\psi_d(x)$, can be mapped on the low energy sector of the one-dimensional transverse-field Ising model at its critical point.

For the parity operator (12.8), we obtain a representation in terms of the Ising model with the following procedure: we first discretize $\int^{x_0} dx\, \rho_e(x)$ using the mapping (12.16) and identify $x_0 \equiv n_0 a$ as a lattice point on the Ising model. Thereafter, we obtain an expression for the vortex tunneling operator P in terms of the Ising model

$$P \mapsto \exp\left(i\pi \sum_{j \leq n_0} c_j^\dagger c_j\right) = \prod_{j \leq n_0} s_j^z \equiv \mu_{n_0+1/2}^x, \tag{12.17}$$

by using Eq. (12.13) and the Jordan-Wigner transformation (12.11). Here, μ^x is the disorder field of the Ising model, i.e., the dual field of the spin field [246, 263–265]. The Ising Hamiltonian has a form identical to Eq. (12.10) when expressed through μ operators,

$$H_I = -J \sum_n (\mu_{n-1/2}^x \mu_{n+1/2}^x + \mu_{n+1/2}^z), \tag{12.18}$$

with $\mu_{n+1/2}^z = s_n^z s_{n+1}^z$.[1] We see that the parity operator is indeed a local operator in the dual description of the Ising model. After mapping on the Ising model Eq. (12.7) becomes (here and in the following, we use the shortcut notation $\mu = \mu^x$)

$$P H_{\mathrm{MF}} P \mapsto \mu_{n_0+1/2}\, H_I\, \mu_{n_0+1/2}, \tag{12.19}$$

and the full Hamiltonian of Majorana edge states and the flux qubit (12.9) maps onto

$$\mathcal{H} \mapsto \mathcal{H}_I = \begin{pmatrix} H_I & 0 \\ 0 & \mu_{n_0+1/2}\, H_I\, \mu_{n_0+1/2} \end{pmatrix} + H_Q. \tag{12.20}$$

Finally, an additional unitary transformation

$$\mathcal{H}_I \mapsto V \mathcal{H}_I V^\dagger, \tag{12.21}$$

$$V = V^\dagger = \begin{pmatrix} 1 & 0 \\ 0 & \mu_{n_0+1/2} \end{pmatrix}, \tag{12.22}$$

yields

$$\mathcal{H}_I = H_I - \frac{\varepsilon}{2}\tau^z - \frac{\delta}{2}\tau^x \mu_{n_0+1/2}. \tag{12.23}$$

Here, τ^i are the Pauli matrices acting in the Hilbert space spanned by the states $|0\rangle$ and $\mu_{n_0+1/2}|2\pi\rangle$. The operators of the qubit spin can be expressed through $\tau^{x,y,z}$ as

$$\sigma^z = \tau^z, \quad \sigma^x = \tau^x \mu_{n_0+1/2}, \quad \sigma^y = \tau^y \mu_{n_0+1/2}. \tag{12.24}$$

We use the Hamiltonian in the form of Eq. (12.23) and the qubit spin operators (12.24) in the rest of the chapter.

---

[1] In the present work, the Jordan-Wigner transformation (12.11) is introduced for the Ising spin fields s^x. If the transformation is introduced for the disorder field, as in Refs. [241] and [248], one should interchange the Ising spin field and the disorder field in our discussion.

The way of identifying *two* edge Majorana states with a *complete* transverse field Ising model presented above is different from the one commonly used in preceding research. Usually, the *chiral part* of the Ising model is identified with a *single* Majorana edge [182, 260]. The advantages of our method are the possibility to write a complete Hamiltonian of the problem and simplified book-keeping, while its drawback is the need for the right-moving edge and the left-moving edge to have the same geometries. Overall the differences are not important and both methods can be used interchangeably.

12.4   Formalism

To probe the universal properties of Majorana edge states, the energy scales of the qubit should be much smaller than the cutoff scale of the Ising model, $\varepsilon, \delta \ll \Lambda$. In the weak coupling limit $\varepsilon \gg \delta$, we construct a perturbation theory in δ/ε by separating the Hamiltonian $\mathcal{H}_I = \mathcal{H}_0 + V$ into an unperturbed part and a perturbation

$$\mathcal{H}_0 = H_I - \frac{\varepsilon}{2}\tau^z, \qquad V = -\frac{\delta}{2}\tau^x \mu. \tag{12.25}$$

Without loss of generality we set $\varepsilon > 0$, so that the ground state of the unperturbed qubit is $|0\rangle$. For brevity we omit the spatial coordinate of the μ operator in the following since it is always the same in the setup that we consider.

We use the interaction picture with time-dependent operators

$$\mathcal{O}(t) = e^{i\mathcal{H}_0 t}\mathcal{O}e^{-i\mathcal{H}_0 t}. \tag{12.26}$$

The perturbation $V(t)$ in this picture is given by

$$V(t) = -\frac{\delta}{2}\mu(t)[\tau^+(t) + \tau^-(t)], \tag{12.27}$$

where $\tau^\pm(t) = e^{\mp i\varepsilon t}\tau^\pm$ are the time-dependent raising and lowering operators. The structure of the raising and lowering operators leads to physics similar to the Kondo and Luttinger liquid resonant tunneling problems [182, 237, 266].

In the calculation we need the real-time two-point and four-point correlation functions of μ in the long-time limit $\Lambda|t - t'| \gg 1$. The two-point correlation function is

$$\langle\mu(t)\mu(t')\rangle = \frac{e^{-i\,\mathrm{sgn}(t-t')\pi/8}}{\Lambda^{2\Delta_\mu}|t - t'|^{2\Delta_\mu}}, \tag{12.28}$$

where $\mathrm{sgn}(x)$ denotes the sign of x, and $\Delta_\mu = 1/8$ the scaling dimension of the μ field [251, 252]. The phase shift $\pi/8$ of the two-point correlator is the Abelian part of the statistical angle for the Ising anyons braiding rules [8]. Correlation functions involving combination of multiple fields can be obtained via the underlying Ising conformal field theory or via a bosonization scheme [241, 248, 251, 252]. The expression for the four-point correlation function is given in App. 12.A due to its length. For brevity we will

measure energies in units of Λ and times in units of $1/\Lambda$ in the following calculation and restore the dimensionality in the final result.

We are interested in observables of the flux qubit: the spin expectation values and the spin susceptibilities. We use time-dependent perturbation theory to calculate these quantities [267]. This method is straightforward because of the simple form of the perturbing Hamiltonian (12.27) in terms of raising and lowering operators.

Assuming that the system is in the unperturbed ground state at time $t_0 \to -\infty$, the expectation value of a qubit spin operator $\sigma^\alpha(t)$ is expressed through the S-matrix $S(t, t')$,

$$\langle \sigma^\alpha(t) \rangle = \langle S(t, t_0)^\dagger \sigma^\alpha(t) S(t, t_0) \rangle_0, \tag{12.29}$$

$$S(t, t') = \mathcal{T} \exp\left(-i \int_{t'}^t V(s) ds\right), \; t > t'. \tag{12.30}$$

Here, $\mathcal{T}$ is the time-ordering operator and $\langle \cdot \rangle_0$ is the expectation value with respect to the unperturbed ground state. Similarly, the two-point correlation functions of the qubit spin are given by

$$\langle \sigma^\alpha(t) \sigma^\beta(0) \rangle = \langle S^\dagger(t, t_0) \sigma^\alpha(t) S(t, 0) \sigma^\beta(0) S(0, t_0) \rangle_0. \tag{12.31}$$

The perturbative calculation for both the expectation values and correlation functions is done by expanding the S-matrices in V order by order. This procedure is equivalent to the Schwinger-Keldysh formalism with the expansion of S and $S^\dagger$ corresponding to insertions on the forward and backward Keldysh contour.

According to linear response theory, the susceptibility is given by the Fourier transform of the retarded correlation function of the qubit [267]:

$$\chi_{\alpha\beta}(\omega) = i \int_0^\infty dt \, e^{i\omega t} \langle [\sigma^\alpha(t), \sigma^\beta(0)] \rangle_c$$

$$= -2 \int_0^\infty dt \, e^{i\omega t} \mathrm{Im} \langle \sigma^\alpha(t) \sigma^\beta(0) \rangle_c, \quad (12.32)$$

where $\langle \cdot \rangle_c$ denotes the cumulant,

$$\langle \sigma^\alpha(t) \sigma^\beta(0) \rangle_c = \langle \sigma^\alpha(t) \sigma^\beta(0) \rangle - \langle \sigma^\alpha(t) \rangle \langle \sigma^\beta(0) \rangle, \tag{12.33}$$

and we have used $\langle \sigma^\beta(0) \sigma^\alpha(t) \rangle_c = \langle \sigma^\alpha(t) \sigma^\beta(0) \rangle_c^*$. We see that in order to calculate the susceptibilities only the imaginary part of the correlation functions for $t > 0$ is required.

12.5   Expectation values of the qubit spin

In this section, we calculate the expectation values of the qubit spin due to coupling with the Majorana edge states to the lowest non-vanishing order. Using the identity

$$\sigma^z = 1 - 2\sigma^- \sigma^+, \tag{12.34}$$

we obtain

$$\langle\sigma^z\rangle - \langle\sigma^z\rangle^{(0)} = -2\langle\sigma^-\sigma^+\rangle = -2\langle\tau^-\tau^+\rangle, \tag{12.35}$$

since $\langle\sigma_z\rangle^{(0)} = 1$.

The first non-vanishing correction in the perturbative calculation of $\langle\sigma^-\sigma^+\rangle$ is of second order in V. By expanding S and $S^\dagger$ in Eq. (12.29), we obtain

$$\langle\tau^-\tau^+\rangle^{(2)} = \int_{-\infty}^0 dt_1 \int_{-\infty}^0 dt_2\, I^z, \tag{12.36}$$
$$I^z = \langle V(t_2)\tau^-\tau^+ V(t_1)\rangle_0.$$

The integrand I_z originates from the first order expansion of both S and $S^\dagger$. The second order contributions from the same S- or $S^\dagger$-matrix vanish due to the structure of V in the qubit spin space.

Substituting (12.27) and (12.28) into the integrand I^z yields

$$I^z = \frac{\delta^2 e^{i\varepsilon(t_1-t_2)-i\,\mathrm{sgn}(t_2-t_1)\pi/8}}{4|t_2 - t_1|^{2\Delta_\mu}}. \tag{12.37}$$

By evaluating the integral in Eq. (12.36), we find

$$\langle\sigma^z\rangle^{(2)} = -2\langle\tau^-\tau^+\rangle^{(2)} = -\frac{3\Gamma(\frac{3}{4})\delta^2}{8\varepsilon^{2-2\Delta_\mu}}, \tag{12.38}$$

where $\Gamma(x)$ denotes the Gamma function.

The expectation value of σ^x in the unperturbed ground state vanishes. The first non-vanishing contribution to $\langle\sigma^x\rangle$ arises to first order in δ/ε. Expanding S and $S^\dagger$ in Eq. (12.29) to the first order yields

$$\langle\sigma^x\rangle^{(1)} = \int_{-\infty}^0 dt_1\, I^x, \tag{12.39}$$
$$I^x = -i\langle[\tau^x\mu(0), V(t_1)]\rangle_0 = \frac{\sin(-\varepsilon t_1 + \frac{\pi}{8})\delta}{|t_1|^{2\Delta_\mu}}$$

after substituting σ^x from Eq. (12.24) and employing the two point correlator, Eq. (12.28). Evaluating (12.39), we find

$$\langle\sigma^x\rangle^{(1)} = \frac{\Gamma(\frac{3}{4})\delta}{\varepsilon^{1-2\Delta_\mu}}. \tag{12.40}$$

Finally, $\langle\sigma^y\rangle = 0$ to all orders in perturbation theory since the Hamiltonian is invariant under $\sigma^y \mapsto -\sigma^y$.

12.6 Correlation functions and susceptibilities of the flux qubit spin

Since we are interested in the behavior of susceptibilities at frequencies close to the resonance $\omega \approx \varepsilon$, we only need to obtain the long-time asymptotic of the correlation

functions of the qubit spin. Using (12.24) and (12.28), we immediately obtain that

$$\langle \sigma^x(t)\sigma^x(0)\rangle_c = \frac{e^{-i\varepsilon t - i\pi/8}}{t^{2\Delta_\mu}}, \tag{12.41}$$

is non-vanishing to zeroth order. This is due to the fact that flipping the qubit spin automatically involves creation of an edge vortex, and σ^x is exactly the spin flip operator. In the same manner, one obtains that $\langle \sigma^y(t)\sigma^y(0)\rangle_c = \langle \sigma^x(t)\sigma^x(0)\rangle_c$ to zeroth order.

Concentrating next on the mixed correlator, the relations (12.24) and (12.34) yield

$$\langle \sigma^x(t)\sigma^z(0)\rangle_c = -2\langle \mu(t)\tau^x(t)\tau^-(0)\tau^+(0)\rangle_0. \tag{12.42}$$

The leading non-vanishing term in this correlation function is of first order in δ and given by

$$\langle \sigma^x(t)\sigma^z(0)\rangle_c^{(1)} = -\frac{\delta}{\varepsilon}\langle \sigma^x(t)\sigma^x(0)\rangle_c. \tag{12.43}$$

in the long-time limit.

The leading order contribution to $\langle \sigma^z(t)\sigma^z(0)\rangle_c$ can be evaluated using (12.28) with expansions of S and $S^\dagger$ to second order in δ. In the long-time limit, the leading contribution of the correlation function is given by

$$\langle \sigma^z(t)\sigma^z(0)\rangle_c^{(2)} = \frac{\delta^2}{\varepsilon^2}\langle \sigma^x(t)\sigma^x(0)\rangle_c. \tag{12.44}$$

Correlators containing a single σ^y vanish because of the invariance under $\sigma^y \mapsto -\sigma^y$. We see that all the non-vanishing two-point correlation functions are the same up to overall prefactors. Therefore, we will focus on $\langle \sigma^x(t)\sigma^x(0)\rangle_c$ in the following.

12.6.1 Energy renormalization and damping

The coupling of the flux qubit to the continuum Majorana edge states can be thought of as a two-level system coupled to an environment via the interaction (12.27). This coupling leads to self-energy corrections Σ for the qubit Hamiltonian

$$\mathcal{H}_0 \mapsto \mathcal{H}_0 + \Sigma, \quad \Sigma = \begin{pmatrix} \Sigma_{\uparrow\uparrow} & \Sigma_{\uparrow\downarrow} \\ \Sigma_{\downarrow\uparrow} & \Sigma_{\downarrow\downarrow} \end{pmatrix}, \tag{12.45}$$

that effectively shifts the energy spectrum and can also induce damping [268]. Since we are mainly interested in qubit observables, we neglect the structure of Σ in the space of Ising spins.

To second order, the self-energy correction for two spin states can be written [268] in terms of the perturbed Hamiltonian (12.25) as:

$$\Sigma_{\alpha\beta} = \langle \alpha; 0|V + V(E_\alpha + i0^+ - \mathcal{H}_0)^{-1}V|0; \beta\rangle, \tag{12.46}$$

where E_α is the energy for the spin-α $=\uparrow, \downarrow$ qubit states and $|\alpha; 0\rangle$ indicates that the Ising model is in its ground state with spin-α for the qubit state. Due to the structure of

the Hamiltonian (12.25), the first order correction to the self-energy vanishes. Additionally, the off-diagonal self-energy corrections vanish also to second order.

By inserting a complete set $\sum_{E_I,\beta} |E_I; \beta\rangle\langle\beta; E_I| = 1$ of the Hilbert space of $\mathcal{H}_0$ with E_I denoting the complete set of eigenstates with energy E_I for the Ising sector, the diagonal elements of the self-energy become

$$\Sigma_{\alpha\alpha} = \sum_{E_I,\beta} \frac{\langle\alpha; 0|V|E_I; \beta\rangle\langle\beta; E_I|V|0; \alpha\rangle}{E_\alpha + i0^+ - (E_I + E_\beta)}. \tag{12.47}$$

Because $V = -(\delta/2)\tau_x\mu$, only terms with $\alpha \neq \beta$ give non-vanishing contributions such that

$$\Sigma_{\alpha\alpha} = \frac{\delta^2}{4} \sum_{E_I} \frac{\langle 0|\mu|E_I\rangle\langle E_I|\mu|0\rangle}{\pm\varepsilon - E_I + i0^+}, \tag{12.48}$$

where $+$ corresponds to $\alpha = \downarrow$, and $-$ to $\alpha = \uparrow$. The diagonal elements of the self-energy in Eq. (12.48) can be cast to the form

$$\Sigma_{\alpha\alpha} = -i\frac{\delta^2}{4} \int_0^\infty dt\, e^{\pm i\varepsilon t} e^{-0^+ t} \langle\mu(t)\mu(0)\rangle. \tag{12.49}$$

To see that (12.49) is equal to (12.48), we first insert a complete set of states of the Ising model, then write the time evolution of μ in the Heisenberg picture, and finally evaluate the integral.

Evaluating Eq. (12.49) with Eq. (12.28) yields

$$\Sigma_{\uparrow\uparrow} = -\frac{\delta^2\Gamma(\frac{3}{4})}{4\varepsilon^{1-2\Delta_\mu}}, \quad \Sigma_{\downarrow\downarrow} = e^{-i\pi/4} \frac{\delta^2\Gamma(\frac{3}{4})}{4\varepsilon^{1-2\Delta_\mu}}, \tag{12.50}$$

where we have used $\varepsilon > 0$. The absence of the imaginary part for $\Sigma_{\uparrow\uparrow}$ indicates that the spin-up state is stable. The self-energy thus gives an energy shift to the spin-up state while it gives an energy shift with a damping to the spin-down state,

$$E_\alpha = \pm\frac{\varepsilon}{2} \mapsto \pm\frac{\varepsilon}{2} + \Sigma_{\alpha\alpha}. \tag{12.51}$$

The energy renormalization and damping (12.51) alter the time evolution of the ground state correlation function

$$\langle\tau^+(t)\tau^-(0)\rangle_0 = e^{-i\varepsilon t} \mapsto e^{-i(\varepsilon+\nu)t - \gamma t/2}, \tag{12.52}$$

where the energy renormalization and damping $\nu - i\gamma/2 \equiv \Sigma_{\downarrow\downarrow} - \Sigma_{\uparrow\uparrow}$ are given by

$$\nu = \frac{\cos^2(\frac{\pi}{8})\Gamma(\frac{3}{4})\delta^2}{2\varepsilon^{1-2\Delta_\mu}}, \qquad \gamma = \frac{\Gamma(\frac{3}{4})\delta^2}{2\sqrt{2}\varepsilon^{1-2\Delta_\mu}}. \tag{12.53}$$

At zero temperature, this correlator is the only non-vanishing qubit correlator that enters in the perturbative calculation. Therefore, the effect of the self energy can be captured by replacing

$$\varepsilon \mapsto \varepsilon + \nu - \frac{i}{2}\gamma, \tag{12.54}$$

in the qubit correlation functions computed in the long-time limit excluding the self-energy correction. Using the replacement rule (12.54), one obtains the zero temperature correlator

$$\langle \sigma^x(t)\sigma^x(0)\rangle_c = \frac{e^{-i(\varepsilon+\nu)t-\gamma t/2-i\pi/8}}{t^{2\Delta_\mu}}. \tag{12.55}$$

The energy renormalization and the induced damping (12.51) do not arise explicitly in the lowest-order perturbation and require the resummation of the most divergent contributions to all orders in perturbation theory. In a system where Wick's theorem applies, the resummation for the self-energy can be derived explicitly from a diagrammatic perturbation scheme [267]. Because the correlation functions of multiple μ's do no obey the Wick's theorem (see App. 12.A), the resummation procedure for our system becomes more complicated. In the long time limit, however, the most divergent contributions in all orders can be collected by using the operator product expansion for two μ fields that resembles the structure of the Wick's theorem [241, 248].

12.6.2 Finite temperature

Besides γ, finite temperature is an alternative source of decoherence. The finite temperature correlators of disorder fields are readily obtained from the zero temperature correlators using a conformal transformation [269]:

$$\frac{1}{t^{2\Delta_\mu}} \mapsto \frac{(\pi k_B T)^{2\Delta_\mu}}{[\sinh(\pi k_B T t)]^{2\Delta_\mu}}, \tag{12.56}$$

where T denotes temperature and k_B the Boltzmann constant. The finite temperature correlator $\langle \sigma^x(t)\sigma^x(0)\rangle_c$ in the long-time limit can be obtained by substituting Eq. (12.56) into (12.55) with the proviso $\varepsilon \gg k_B T$ such that the temperature has no direct effect on the qubit dynamics.

12.6.3 Susceptibility

With the correlation functions derived above, we are now in the position to evaluate susceptibilities of the qubit. We should keep in mind that these correlators are valid only in the long-time limit and can only be used to study the behavior of the susceptibilities close to the resonant frequency $\omega \approx \varepsilon$.

Evaluating Eq. (12.32) with Eq. (12.55) yields the susceptibility at zero temperature around the resonance,

$$\chi_{xx}(\omega) = \frac{e^{i3\pi/8}\Gamma(\frac{3}{4})}{[i(\varepsilon+\nu-\omega)+\gamma/2]^{1-2\Delta_\mu}}, \tag{12.57}$$

where ν and γ are given in (12.53). If we neglect ν and γ, which are of higher order in δ/ε, this susceptibility reduces to

$$\chi_{xx}(\omega) = \frac{\Gamma(\frac{3}{4})}{|\omega-\varepsilon|^{1-2\Delta_\mu}} \begin{cases} 1, & \text{for } \omega < \varepsilon, \\ e^{i3\pi/4}, & \text{for } \omega > \varepsilon, \end{cases} \tag{12.58}$$

so it diverges and changes the phase by $3\pi/4$ at the resonant frequency. We can attribute this phase change to the phase shift of the correlator of two disorder fields in Eq. (12.28).

The presence of damping γ in Eq. (12.57) provides a cutoff for the divergence of the response on resonance. The maximal susceptibility is reached at $\omega = \varepsilon + \nu$, and its value is given by

$$|\chi_{xx}(\varepsilon + \nu)| = \frac{2^{1-2\Delta_\mu}\Gamma(\frac{3}{4})}{\gamma^{1-2\Delta_\mu}}. \tag{12.59}$$

Using the proportionality of the correlation functions (12.43) and (12.44), one gets that $\chi_{xz} = \chi_{zx} = -(\delta/\varepsilon)\chi_{xx}$ and $\chi_{zz} = (\delta/\varepsilon)^2\chi_{xx}$. It is interesting to note that when $\delta \to 0$ both χ_{xx} and χ_{xz} are divergent while χ_{zz} vanishes at the resonance.

In Fig. 12.2, the absolute value of the susceptibility $|\chi_{xx}(\omega)|$ close to the resonance is plotted as a function of frequency. The dotted line shows the modulus of Eq. (12.58) for $\nu = \gamma = 0$ while the dashed line shows that of Eq. (12.57). A renormalization of the resonant frequency ν becomes clearly visible when comparing the peak positions of the dashed line to the dotted line.

The conformal dimension of the vortex excitation can be measured in the region with $\varepsilon \gg |\omega - \varepsilon| \gtrsim \gamma$ where

$$|\chi_{xx}(\omega)| = \frac{\Gamma(\frac{3}{4})}{|\omega - \varepsilon|^{1-2\Delta_\mu}}. \tag{12.60}$$

Moreover, both χ_{xz} and χ_{zz} exhibit the same scaling behavior.

The finite temperature susceptibility of $\chi_{xx}(\omega, T)$ can be evaluated from the correlation function (12.55) subjected to the transformation (12.56). The result is plotted as the solid line in Fig. 12.2. An immediate effect of the temperature is that it also introduces a cutoff for the divergence on resonance. For instance, the resonance peak of the susceptibility yields a different scaling behavior with respect to the temperature

$$|\chi_{xx}(\varepsilon + \nu, T)| \propto T^{-(1-2\Delta_\mu)}, \tag{12.61}$$

as long as $\pi k_B T \gg \gamma$. The zero temperature scaling behavior of the resonance peak (12.59) will be masked by a finite temperature with a crossover at $\pi k_B T \approx \gamma$. These scaling and crossover behaviors of the resonance strength are features of the coupling of the Majorana edge states and the flux qubit.

The finite temperature susceptibility shows a resonance at $\varepsilon + \nu$, as shown in Fig. 12.2. Around the resonance, the frequency dependence at finite temperature will be given by the power law (12.60) but with the region constrained by $\pi k_B T$ instead of γ if $\pi k_B T > \gamma$.

12.7   Higher order correlator

So far, we have computed the qubit susceptibilities to their first non-vanishing orders and the lowest order self-energy correction $\varepsilon \mapsto \varepsilon + \nu - i\gamma/2$. As a consequence, we only used the two-point correlation functions $\langle \mu(t)\mu(0) \rangle$ in our evaluations. The next
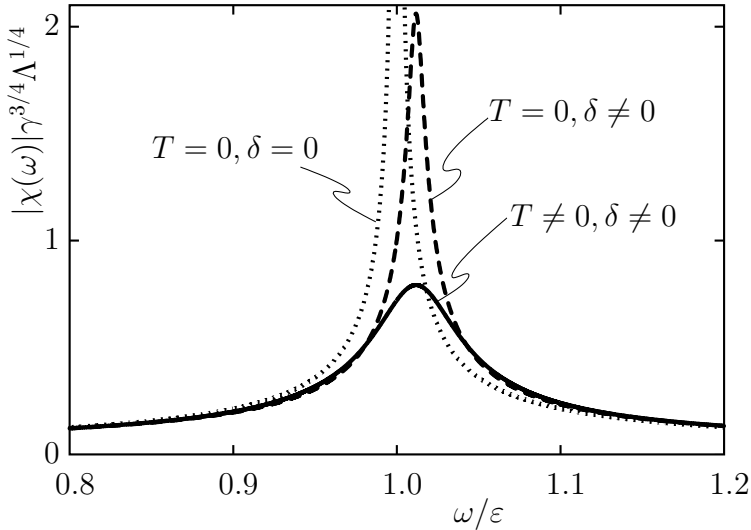
Figure 12.2: Plot of the magnitude of the susceptibility $|\chi_{xx}(\omega)|$ as a function of frequency ω close to resonance ε. The dotted line shows the zero temperature susceptibility in the absence of the damping and energy renormalization while the dashed line shows the result in the presence of the energy shift and the damping in Eq. (12.51). The parameters used for the plot are $\varepsilon = 0.1\Lambda$ and $\delta/\varepsilon = 0.2$. The solid line shows a plot of the finite temperature susceptibility with $k_B T = 0.02\varepsilon$.

nontrivial corrections to the qubit correlators involve the equal position four-point correlator of the disorder fields $\langle \mu(t_1)\mu(t_2)\mu(t_3)\mu(t_4) \rangle$. As discussed in Appendix 12.A, the four-point correlator, in principle, contains information about the non-Abelian statistics of the particles because changing the order of the fields in the correlation function not only alters the phase but can also change the functional form of the correlator [256]. It is thus interesting to go beyond the lowest non-vanishing order. Additionally, doing so allows to check the consistency of the calculation of the self-energy correction done in Sec. 12.6.1.

As an example we focus on the second order correction to the $\langle \sigma^x(t)\sigma^x(0) \rangle_c$ correlator in the long-time limit. The details of the calculation are given in App. 12.B and the result in Eq. (12.108). The dominant correction is a power law divergence

$$\langle \sigma^x(t)\sigma^x(0) \rangle_c^{(2)} \propto e^{-i\pi/8} \frac{e^{-i\varepsilon t}}{t^{2\Delta_\mu}} \left[1 - (i\nu + \frac{\gamma}{2})t \right], \tag{12.62}$$

which is just the second order in δ expansion of the modified correlation function

$$\langle \sigma^x(t)\sigma^x(0) \rangle_c \propto \frac{e^{-i(\varepsilon+\nu)t}e^{-\gamma t/2}e^{-i\pi/8}}{t^{2\Delta_\mu}}. \tag{12.63}$$

Hence, we confirm that the second order perturbative correction is consistent with the the self-energy correction calculation.

The leading correction to the susceptibility χ_{xx} in second order is due to the logarithmic term $\propto t^{-1/4} \log t$ in the correlator (12.108) and has the form

$$\chi_{xx}^{(2)}(\omega) = -\frac{\delta^2(2+\sqrt{2})\Gamma(\tfrac{7}{4})\Gamma(\tfrac{3}{4})e^{i3\pi/8}}{16\varepsilon^{7/4}[i(\varepsilon+\nu-\omega)+\gamma/2)]^{1-2\Delta_\mu}}$$
$$\times \ln\left(\frac{(\gamma/2)^2+(\omega-\varepsilon-\nu)^2}{\varepsilon^2}\right)$$

(12.64)

where we have included the self-energy correction (12.54), and omitted terms without logarithmic divergence. Unfortunately the effects of nontrivial exchange statistics of disorder fields are not apparent in this correction.

12.8   Conclusion and discussion

We have proposed a novel scheme to probe the edge vortex excitations of chiral Majorana fermion edge states realized in superconducting systems utilizing a flux qubit. To analyze the coupling we mapped the Hamiltonian of the Majorana edge states on the transverse-field Ising model, so that the coupling between the qubit and the Majorana edge modes becomes a local operator. In the weak coupling regime $\delta \ll \varepsilon$ we have found that the ground state expectation values of the qubit spin are given by

$$\langle \sigma^x \rangle = \frac{\Gamma(\tfrac{3}{4})\delta}{\varepsilon^{1-2\Delta_\mu}\Lambda^{2\Delta_\mu}}, \ \langle \sigma^y \rangle = 0, \ \langle \sigma^z \rangle = 1 - \frac{3\delta}{8\varepsilon}\langle \sigma^x \rangle.$$

(12.65)

Additionally, the susceptibility tensor of the qubit spin in the basis x, y, z is given by

$$\chi(\omega) = \chi_{xx}(\omega)\begin{pmatrix} 1 & 0 & -\delta/\varepsilon \\ 0 & 1 & 0 \\ -\delta/\varepsilon & 0 & (\delta/\varepsilon)^2 \end{pmatrix},$$

(12.66)

$$\chi_{xx}(\omega) = \frac{e^{i3\pi/8}\Gamma(\tfrac{3}{4})}{[i(\varepsilon+\nu-\omega)+\gamma/2]^{1-2\Delta_\mu}\Lambda^{2\Delta_\mu}},$$

(12.67)

with the real part ν and the imaginary part $\gamma/2$ of the self-energy given by

$$\nu = \frac{\cos^2(\tfrac{\pi}{8})\Gamma(\tfrac{3}{4})\delta^2}{2\varepsilon^{1-2\Delta_\mu}\Lambda^{2\Delta_\mu}}, \qquad \gamma/2 = (\sqrt{2}-1)\nu.$$

(12.68)

We see that all of these quantities acquire additional anomalous scaling $(\varepsilon/\Lambda)^{2\Delta_\mu}$ due to the fact that each spin flip of the qubit spin couples to a disorder field μ. Similar scaling with temperature appears in interferometric setups [260]. but using a flux qubit allows to attribute its origin to the dynamics of vortices much more easily and also gives additional tunability of the strength of the coupling. Unlike anomalous scaling,

the phase change $\delta\phi = 3\pi/4$ of the susceptibility around the resonance probes the Abelian statistical angle of the disorder field, a feature which cannot easily be measured by electronic means to the best of our knowledge.

The long wavelength theory which we used is only applicable when all of the energy scales are much smaller than the cutoff energy of the Majorana modes. This is an important constraint for the flux qubit coupled to the Majorana edge states. In systems where the time-reversal symmetry is broken in the bulk (unlike for topological insulator-based proposals[2]), the velocity of the Majorana edge states can be estimated to be $v_M \propto v_F\Delta/E_F$ and the dispersion stays approximately linear all the way up to Δ. The cutoff of the Majorana modes is related to the energy scale of the Ising model $\Lambda = \Delta \mapsto J$. Equating $J = \Delta$ and $v_M = 2Ja$, we obtain the lattice constant of the Ising model $a = v_F/E_F \equiv \lambda_F$, with λ_F the Fermi wavelength. The Fermi wavelength is typically smaller than any other length scale, and so the long wavelength approximation we have used is well-justified. For a typical flux qubit the tunneling strength δ is indeed much smaller than the superconducting gap, the level splitting ε may vary from zero to quantities much larger than the superconducting gap.

Our proposal provides a way to measure properties of the non-Abelian edge vortex excitations different from the conventional detection scheme that requires fusing vortices into fermion excitations. However, none of our results for the single flux qubit can be directly connected to the non-Abelian statistics of the quasiparticles, even after including higher-order corrections. Thus, it is of interest for future research to investigate a system where the edge vortex excitations are coupled to two qubits such that braiding of vortex excitations can be probed [8]. Another feature of systems with several qubits worth to investigate is the ability of the Majorana edge modes to mediate entanglement between different flux qubits.

12.A Correlation functions of disorder fields

The one-dimensional critical transverse-field Ising model is a conformal field theory (CFT) with central charge $c = 1/2$. This CFT contains the following primary fields: $\mathbb{I}$, $\epsilon = i\psi\bar{\psi}$, s, and μ. Here I is the identity operator, ϵ is the energy field (a product of the right and left moving Majorana fermion fields ψ and $\bar{\psi}$), and s is the Ising spin field with its dual field μ [241, 251, 252]. The dual field μ is also called the disorder field and has the same scaling behavior as the Ising spin field s at the critical point. On the lattice, the disorder fields μ are non-linear combinations of Ising spin fields s and reside on the bonds of lattice Ising model. They are hence not independent of the Ising spin field s.

In the continuum and in imaginary time, the two-point correlation function of disor-

---

[2]For topological insulator-based proposal with time-reversal symmetry in the bulk, cf. Ref. [144], the velocity of Majorana edge modes is further suppressed and is given by $v_M \sim v_F(\Delta/E_F)^2$ when $E_F \gg \Delta$. The cutoff energy for the linear dispersion is constrained to the region $\Lambda \sim \Delta^2/E_F$. In this case, we still get $a = \lambda_F$ the Fermi wavelength.

der fields μ can be obtained from CFT [241]:

$$\langle \mu(z_1, \bar{z}_1)\mu(z_2, \bar{z}_2)\rangle = \frac{1}{[(z_1 - z_2)(\bar{z}_1 - \bar{z}_2)]^{\Delta_\mu}}, \tag{12.69}$$

with $z_i = \tau_i + i x_i$ and $\bar{z}_i = \tau_i - i x_i$.

Following Ref. [256], the real-time correlators can be obtained by analytical continuation $\tau \to \xi + it$. Here $\xi \to 0^+$ is introduced to ensure the correct phase counting and is important for the Abelian part of the statistics. The equal position two-point correlation function is given by

$$\langle \mu(t_1, x_0)\mu(t_2, x_0)\rangle = \frac{1}{(\xi + i(t_1 - t_2))^{2\Delta_\mu}}. \tag{12.70}$$

By using the identity

$$\lim_{\xi \to 0^+} \frac{1}{(\xi + it)^{1/4}} = \frac{e^{-i \, \mathrm{sgn}(t)\pi/8}}{|t|^{1/4}}, \tag{12.71}$$

one obtains the two-point correlation function in the form of Eq. (12.28).

The four-point correlation function of μ's can be obtained in a similar manner. In imaginary time, the correlation function is given by [241]:

$$\langle \mu(z_1, \bar{z}_1)\mu(z_2, \bar{z}_2)\mu(z_3, \bar{z}_3)\mu(z_4, \bar{z}_4)\rangle^2$$
$$= \left| \frac{z_{13}z_{24}}{z_{12}z_{34}z_{14}z_{23}} \right|^{1/2} \left(\frac{1 + |\chi| + |1 - \chi|}{2} \right), \quad (12.72)$$

where $\chi = (z_{12}z_{34}/z_{13}z_{24})$ is the conformally invariant cross ratio, and the absolute values should be understood as $|z_{ij}|^\alpha = (z_{ij}\bar{z}_{ij})^{\alpha/2}$. Because we are interested in tunneling at a single point, we can set $x_i = 0$. In this limit the four-point correlation function can be evaluated to be

$$\langle \mu(z_1)\mu(z_2)\mu(z_3)\mu(z_4)\rangle^2 = \begin{cases} \left| \dfrac{z_{13}z_{24}}{z_{12}z_{34}z_{14}z_{23}} \right|^{1/2} & \text{for} \quad 0 < \chi < 1 \\[2ex] \left| \dfrac{z_{14}z_{23}}{z_{12}z_{34}z_{13}z_{24}} \right|^{1/2} & \text{for} \quad \chi < 0 \\[2ex] \left| \dfrac{z_{12}z_{34}}{z_{14}z_{23}z_{13}z_{24}} \right|^{1/2} & \text{for} \quad \chi > 1 \end{cases} \tag{12.73}$$

The real-time correlation function can be obtained by first taking a square root of

Eq. (12.73) followed by the analytical continuation [256], $\tau_i \to \xi + i t_i$:

$$\langle \mu(t_1)\mu(t_2)\mu(t_3)\mu(t_4)\rangle$$
$$= F_{12}(t_1,t_2,t_3,t_4)\,[\theta(1324) + \theta(1423) + \theta(2413)$$
$$+\theta(2314) + \theta(3241) + \theta(3142) + \theta(4132) + \theta(4231)]$$
$$+ F_{13}(t_1,t_2,t_3,t_4)\,[\theta(1234) + \theta(1432) + \theta(2143) \qquad (12.74)$$
$$+\theta(2341) + \theta(3214) + \theta(3412) + \theta(4123) + \theta(4321)]$$
$$+ F_{14}(t_1,t_2,t_3,t_4)\,[\theta(1243) + \theta(1342) + \theta(2134)$$
$$+\theta(2431) + \theta(3124) + \theta(3421) + \theta(4213) + \theta(4312)],$$

where $\theta(abcd) = 1$ for $t_a > t_b > t_c > t_d$ and is otherwise zero. The corresponding functions F_{ij} are given by

$$F_{12}(t_1,t_2,t_3,t_4) = [\xi + i(t_1 - t_2)]^{1/4}[\xi + i(t_3 - t_4)]^{1/4}[\xi + i(t_1 - t_3)]^{-1/4}$$
$$[\xi + i(t_1 - t_4)]^{-1/4}[\xi + i(t_2 - t_3)]^{-1/4}[\xi + i(t_2 - t_4)]^{-1/4}, \quad (12.75a)$$

$$F_{13}(t_1,t_2,t_3,t_4) = [\xi + i(t_1 - t_3)]^{1/4}[\xi + i(t_2 - t_4)]^{1/4}[\xi + i(t_1 - t_2)]^{-1/4}$$
$$[\xi + i(t_1 - t_4)]^{-1/4}[\xi + i(t_2 - t_3)]^{-1/4}[\xi + i(t_3 - t_4)]^{-1/4}, \quad (12.75b)$$

$$F_{14}(t_1,t_2,t_3,t_4) = [\xi + i(t_1 - t_4)]^{1/4}[v + i(t_2 - t_3)]^{1/4}[\xi + i(t_1 - t_2)]^{-1/4}$$
$$[\xi + i(t_1 - t_3)]^{-1/4}[\xi + i(t_2 - t_4)]^{-1/4}[\xi + i(t_3 - t_4)]^{-1/4}. \quad (12.75c)$$

Here F_{12}, F_{13}, and F_{14} are the three characteristic functions appearing in the fourth-order correlation functions. For an Abelian state, they usually appear in quasi-symmetric combinations and exchanging two of the times alters various phase factors, which is a characteristic of fractional statistics. For the current non-Abelian case, however, exchanging two of the times not only alters phase factors but can also change the form of the correlation function from one of the characteristic functions to another. This is a special feature of non-Abelian statistics [256].

12.B Second order correction to $\langle \sigma^x(t)\sigma^x(0)\rangle_c$

Because our ultimate goal is to compute the qubit susceptibility, we are interested in the correlator with $t > 0$ in the long-time limit $t \to \infty$. Let us first recall the perturbative part of Hamiltonian (12.27) in the interaction picture:

$$V(t, x_0) = -\frac{\delta}{2}\mu(t)[\tau^+(t) + \tau^-(t)]. \qquad (12.76)$$

Since the vortex tunneling in or out of the superconducting ring directly couples to the disorder field of the Ising model $\sigma^x(t) = \mu(t)\tau^x(t)$ in the transformed basis, the
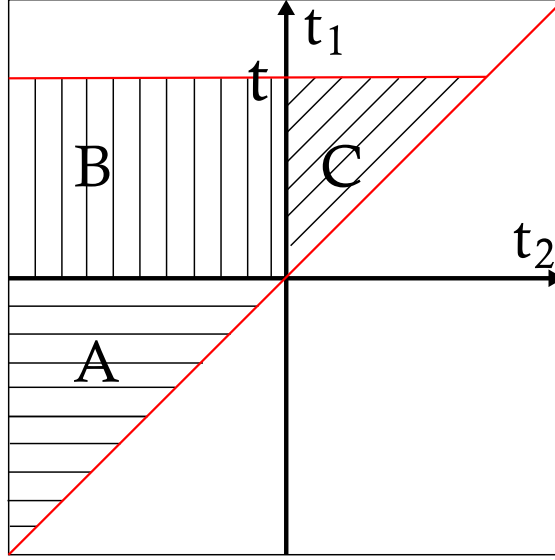
Figure 12.3: The integral domains for regions A, B and C in the t_1 and t_2 coordinates used in Appendix 12.B.

evaluation of the second order correction for the correlator $\langle \sigma^x(t)\sigma^x(0) \rangle$ requires the knowledge of the four-point correlation function derived in Appendix 12.A.

We expand the S and $S^\dagger$-matrices in (12.31) to second order with insertions at times t_1 and t_2. Nonzero contributions to the correlator come from three regions: (A) $t > 0 > t_1 > t_2$, (B) $t > t_1 > 0 > t_2$ and (C) $t > t_1 > t_2 > 0$. These three regions are shown in Fig. 12.3. In what follows, we will evaluate the second order contributions from each region in the long-time limit.

12.B.1   Region A: $t > 0 > t_1 > t_2$

The contribution from region A is given by

$$\langle \sigma^x(t)\sigma^x(0) \rangle_A^{(2)} = (-i)^2 \int_{-\infty}^{0} dt_1 \int_{-\infty}^{t_1} dt_2 I_A, \tag{12.77}$$

with the integrand

$$\begin{aligned} I_A = & + \langle \sigma^x(t)\sigma^x(0)V_1V_2 \rangle_0 + \langle V_2V_1\sigma^x(t)\sigma^x(0) \rangle_0 \\ & - \langle V_2\sigma^x(t)\sigma^x(0)V_1 \rangle_0 - \langle V_1\sigma^x(t)\sigma^x(0)V_2 \rangle_0, \end{aligned} \tag{12.78}$$

where $V_i \equiv V(t_i)$ is a shorthand notation. The plus and minus signs come from the location of the insertions. The plus sign corresponds to having both insertions located

on the same branch (either forward S or backward $S^\dagger$) while the minus sign corresponds to the situation where the two insertions are located on different branches.

Because only certain orderings of insertions of raising and lowering operators τ^+ or τ^-, coming both from the interaction term (12.76) and the τ^x, give non-vanishing contributions, the integrand is given by

$$
\left(\frac{2}{\delta}\right)^2 I_A = + e^{-i\varepsilon t}e^{i\varepsilon(t_2-t_1)}\langle\mu(t)\mu(0)\mu(t_1)\mu(t_2)\rangle
$$
$$
+ e^{-i\varepsilon t}e^{i\varepsilon(t_1-t_2)}\langle\mu(t_2)\mu(t_1)\mu(t)\mu(0)\rangle \tag{12.79}
$$
$$
- e^{+i\varepsilon t}e^{i\varepsilon(t_1-t_2)}\langle\mu(t_2)\mu(t)\mu(0)\mu(t_1)\rangle
$$
$$
- e^{+i\varepsilon t}e^{i\varepsilon(t_2-t_1)}\langle\mu(t_1)\mu(t)\mu(0)\mu(t_2)\rangle.
$$

Here, the four-point correlation function can be read off from Eq. (12.74) and simplified using the identity (12.71). Remarkably, these correlators have the same time dependence function and differ only by phase factors. This feature is characteristic also to regions B and C. After some algebra, the integrand simplifies to

$$
I_A = 2\left(\frac{\delta}{2}\right)^2 e^{-i\pi/8}(e^{-i\varepsilon t} - e^{+i\varepsilon t})
$$
$$
\times \operatorname{Re}\left\{e^{i\varepsilon(t_2-t_1)}\frac{(t-t_1)^{1/4}(-t_2)^{1/4}e^{-i\pi/8}}{t^{1/4}(t-t_2)^{1/4}(-t_1)^{1/4}(t_1-t_2)^{1/4}}\right\}. \tag{12.80}
$$

To evaluate the integral (12.77), we first simplify it by introducing new variables such that $t_1 = -tT$ and $t_2 = -t(T+\tau)$ with the new integrating domain $0 < \tau < \infty$ and $0 < T < \infty$. The second order correction from region A becomes

$$
\langle\sigma^x(t)\sigma^x(0)\rangle_A^{(2)} = it^{3/2}\delta^2 e^{-i\pi/8}\sin(\varepsilon t)
$$
$$
\times \operatorname{Re}\left\{e^{-i\pi/8}\int_0^\infty d\tau\frac{e^{-\varepsilon t(\eta+i)\tau}}{\tau^{1/4}}\int_0^\infty dT\frac{e^{-2\eta\varepsilon tT}(1+T)^{1/4}(T+\tau)^{1/4}}{(1+T+\tau)^{1/4}T^{1/4}}\right\}, \tag{12.81}
$$

where we have introduced a regularization factor $\exp(\varepsilon\eta t_i)$, with $\eta \to 0^+$.

The integral in Eq. (12.81) will not generate any oscillatory dependence but is divergent when both T and τ are large. It is thus convenient to separate the algebraic part of the integrand into three parts

$$
I_{A_1} = \frac{(1+T)^{1/4}(T+\tau)^{1/4}}{(1+T+\tau)^{1/4}(T\tau)^{1/4}} - \frac{1}{\tau^{1/4}} - \frac{\tau^{3/4}}{4(T+\tau)(1+T)},
$$
$$
I_{A_2} = \frac{1}{\tau^{1/4}}, \quad I_{A_3} = \frac{\tau^{3/4}}{4(T+\tau)(1+T)}. \tag{12.82}
$$

Combined with the exponential prefactor, the integration of I_{A_1} is regular, the integral of I_{A_2} diverges linearly while that of I_{A_3} diverges logarithmically.

Integrating I_{A_2} with all the exponential prefactors gives

$$\int \frac{e^{-i\pi/8}e^{-\varepsilon t(\eta+i)\tau}e^{-2\eta\varepsilon tT}}{\tau^{1/4}}d\tau dT = \frac{e^{-i\pi/8}\Gamma(\frac{3}{4})}{2\eta(\varepsilon t)^{7/4}(i+\eta)^{3/4}}$$

$$\propto \frac{1}{(\varepsilon t)^{7/4}}[-i\frac{\Gamma(\frac{3}{4})}{2\eta} + \frac{3\Gamma(\frac{3}{4})}{8} + \mathcal{O}(\eta)], \quad \eta \to 0^+ \quad (12.83)$$

Since the the linear long time divergence is purely imaginary, it does not contribute to the correlation function.

In the long-time limit, the integrals of I_{A_1} and I_{A_3} with all the exponential prefactors can be carried out to the lowest order in $1/(\varepsilon t)$ and are given by

$$\int e^{-i\pi/8}e^{-\varepsilon t(\eta+i)\tau}e^{-2\eta\varepsilon tT}I_{A_1}d\tau dT \sim \frac{\Gamma(\frac{7}{4})(\pi-2(1+\log(8)))}{8(\varepsilon t)^{7/4}}, \quad (12.84)$$

$$\int e^{-i\pi/8}e^{-\varepsilon t(\eta+i)\tau}e^{-2\eta\varepsilon tT}I_{A_3}d\tau dT \sim$$

$$-\frac{\Gamma(\frac{7}{4})\left(3\log(8\varepsilon t)-(3\pi/\sqrt{2})e^{-\frac{i\pi}{4}}+3\gamma-4\right)}{12(\varepsilon t)^{7/4}}. \quad (12.85)$$

We now add the real parts of the three integrals (12.83), (12.84), and (12.85) and then multiply them with the prefactors in (12.81). The result is the leading long-time contribution from region A to the qubit spin correlator:

$$\langle\sigma^x(t)\sigma^x(0)\rangle_A^{(2)} \sim$$
$$\frac{\delta^2 e^{-i\pi/8}(e^{i\varepsilon t}-e^{-i\varepsilon t})}{2t^{1/4}\varepsilon^{7/4}}\left\{\frac{\Gamma(\frac{7}{4})(7+3\pi-3\gamma-18\log(2)-3\log(\varepsilon t))}{12}\right\}. \quad (12.86)$$

In the long-time limit, the leading contribution is given by the term $\propto t^{-1/4}\log(\varepsilon t)$.

12.B.2   Region B: $t > t_1 > 0 > t_2$

The contribution from the region B is given by

$$\langle\sigma^x(t)\sigma^x(0)\rangle_B^{(2)} = (-i)^2 \int_0^t dt_1 \int_{-\infty}^0 dt_2 I_B, \quad (12.87)$$

with the integrand

$$I_B = + \langle\sigma^x(t)V_1\sigma^x(0)V_2\rangle_0 + \langle V_2 V_1\sigma^x(t)\sigma^x(0)\rangle_0$$
$$- \langle V_2\sigma^x(t)V_1\sigma^x(0)\rangle_0 - \langle V_1\sigma^x(t)\sigma^x(0)V_2\rangle_0. \quad (12.88)$$

After ordering the the raising and lowering operators τ^+ or τ^- and using Eq. (12.74), the integrand reads

$$I_B = e^{-i\pi/4} I_{B_1} + e^{+i\pi/4} I_{B_2} - I_{B_1}^* - I_{B_2}^*, \tag{12.89a}$$

where the two integrand functions are given by

$$I_{B_1} = \frac{\delta^2 e^{-i\varepsilon t} e^{i\varepsilon(t_1+t_2)} t^{1/4}(t_1 - t_2)^{1/4}}{4(t - t_1)^{1/4}(t - t_2)^{1/4}(t_1)^{1/4}(-t_2)^{1/4}}, \tag{12.89b}$$

$$I_{B_2} = \frac{\delta^2 e^{-i\varepsilon t} e^{i\varepsilon(t_1-t_2)} t^{1/4}(t_1 - t_2)^{1/4}}{4(t - t_1)^{1/4}(t - t_2)^{1/4}(t_1)^{1/4}(-t_2)^{1/4}}, \tag{12.89c}$$

with x^* denoting complex conjugate of x. Again, the four-point correlators of μ's in region B have the same functional form up to phase factors.

To evaluate the integral of I_{B_1}, we introduce new variables x_1 and x_2 with $t_1 = t(1 - x_1)$ and $t_2 = -tx_2$ such that

$$B_1 = \int I_{B_1} dt_1 dt_2 = \frac{\delta^2 t^{3/2}}{4}$$
$$\times \int_0^1 dx_1 \int_0^\infty dx_2 e^{-i\varepsilon t(x_1+x_2)} \frac{(1 - x_1 + x_2)^{1/4}}{(1 - x_1)^{1/4}(1 + x_2)^{1/4}(x_1)^{1/4}(x_2)^{1/4}}. \tag{12.90}$$

We can then split the integral B_1 into an oscillatory contribution B_1^O and a non-oscillatory one B_1^{NO}.

Since the non-oscillatory contribution from (12.90) is dominated by $x_1 \sim x_2 \approx 0$, we can expand the integrand around this point to get the leading contribution. Because we are interested in the correlator in the long-time limit, we then deform the integration contour in the complex plane such that both x_1 and x_2 change from 0 to $-i\infty$. The leading non-oscillatory contribution is given by

$$B_1^{NO} \sim \frac{\delta^2 t^{3/2}}{4} \int_0^{-i\infty} dx_1 \int_0^{-i\infty} dx_2 e^{-i\varepsilon t(x_1+x_2)} \left(\frac{1}{(x_1 x_2)^{1/4}} + \frac{(x_1 x_2)^{3/4}}{4} \right)$$
$$= \frac{\delta^2 \Gamma(\tfrac{3}{4})^2 e^{i\pi/4}}{4\varepsilon^{3/2}} \left(-1 + \frac{9}{64\varepsilon^2 t^2} \right). \tag{12.91}$$

The oscillatory contribution B_1^O is dominated by $x_1 \approx 1$ and $x_2 \approx 0$, we can thus expand the integrand around this point to get the leading contribution. Again we are interested in the correlator in the long-time limit and thus deform the integration contour such that x_1 varies from $1 - i\infty$ to 1 and x_2 varies from 0 to $-i\infty$. After these

transformations B_1^O evaluates to

$$
B_1^O \sim \frac{\delta^2 t^{3/2} e^{-i\varepsilon t}}{4} \int_{-i\infty}^0 du_1 \int_0^{-i\infty} dx_2 e^{-i\varepsilon t(u_1+x_2)} \frac{(x_2 - u_1)^{1/4}(-u_1)^{1/4}}{u_1 x_2^{1/4}}
$$

$$
= \frac{\delta^2 e^{-i\varepsilon t}}{4\varepsilon^{7/4}} \left(\frac{\cos(\frac{\pi}{8})\Gamma(\frac{5}{8})\Gamma(\frac{3}{4})\Gamma(\frac{7}{4})}{\sqrt{2} t^{1/4}\Gamma(\frac{11}{8})} \right), \quad (12.92)
$$

where $u_1 = x_1 - 1$.

Summing up, the leading contributions to B_1 are

$$
B_1 = \frac{\delta^2}{4\varepsilon^{3/2}} \left\{ \Gamma(\tfrac{3}{4})^2 e^{i\pi/4} \left(\frac{9}{64\varepsilon^2 t^2} - 1 \right) + e^{-i\varepsilon t} \frac{\cos(\frac{\pi}{8})\Gamma(\frac{5}{8})\Gamma(\frac{3}{4})\Gamma(\frac{7}{4})}{\sqrt{2}\Gamma(\frac{11}{8})(\varepsilon t)^{1/4}} \right\}. \quad (12.93)
$$

The leading non-oscillatory contribution of B_1 is a constant while the leading oscillatory contribution has a power law decay $\propto t^{-1/4}$.

To integrate I_{B_2}, we again use the variables $t_1 = t(1 - x_1)$ and $t_2 = -t x_2$ such that

$$
B_2 = \int I_{B_2} dt_1 dt_2 = \frac{\delta^2 t^{3/2}}{4}
$$

$$
\times \int_0^1 dx_1 \int_0^\infty dx_2 e^{-i\varepsilon t(x_1-x_2)} \frac{(1 - x_1 + x_2)^{1/4}}{(x_1)^{1/4}(1 + x_2)^{1/4}(1 - x_1)^{1/4}(x_2)^{1/4}}. \quad (12.94)
$$

Once again, the non-oscillatory contribution is dominated by $x_1 \sim x_2 \approx 0$. We expand the algebraic part of the integrand around $x_1 = x_2 = 0$, deform the integration contour such that x_1 runs from 0 to $-i\infty$ and x_2 from 0 to $i\infty$, and get

$$
B_2^{NO} \sim \frac{\delta^2 t^{3/2}}{4} \int_0^{-i\infty} dx_1 \int_0^{i\infty} dx_2 e^{-i\varepsilon t(x_1-x_2)} \left\{ \frac{1}{x_1^{1/4} x_2^{1/4}} + \frac{x_1^{3/4} x_2^{3/4}}{4} \right\}
$$

$$
= \frac{\delta^2 \Gamma(\frac{3}{4})^2}{4\varepsilon^{3/2}} \left(1 + \frac{9}{64\varepsilon^2 t^2} \right). \quad (12.95)
$$

To evaluate the oscillatory part B_2^O of B_2, we expand the integrand around $x_1 = 1$ and $x_2 = 0$ for the leading contribution. The necessary deformation of the integration contour is now given by x_1 changing from $1 - i\infty$ to 1 and x_2 from 0 to $i\infty$. The leading oscillatory contribution from Eq. (12.94) is now given by

$$
B_2^O \sim \frac{\delta^2 t^{3/2}}{4} e^{-i\varepsilon t} \int_{-i\infty}^0 du_1 \int_0^{i\infty} dx_2 e^{-i\varepsilon t(u_1-x_2)} \left\{ -\frac{(x_2 - u_1)^{1/4}(-u_1)^{1/4}}{u_1 x_2^{1/4}} \right\}
$$

$$
= \frac{\delta^2 \Gamma(\frac{3}{4})^2}{4\varepsilon^{7/4}} \frac{2\Gamma(\frac{7}{4})}{\sqrt{\pi} t^{1/4}} e^{i\frac{7\pi}{8}} e^{-i\varepsilon t}, \quad (12.96)
$$

with $u_1 = x_1 - 1$.

The final expression for B_2 is

$$B_2 = \frac{\delta^2\Gamma(\frac{3}{4})^2}{4\varepsilon^{3/2}}\left(1 + \frac{9}{64\varepsilon^2t^2} + \frac{2\Gamma(\frac{7}{4})e^{i\frac{7\pi}{8}}}{\sqrt{\pi}(\varepsilon t)^{1/4}}e^{-i\varepsilon t}\right). \tag{12.97}$$

Similarly to B_1, the leading non-oscillatory contribution of B_2 is a constant, while the leading oscillatory contribution has a power law decay $\sim t^{-1/4}$.

From Eq. (12.87) and (12.89), the leading contributions to the qubit spin correlation function from region B is given by

$$\langle\sigma^x(t)\sigma^x(0)\rangle_B^{(2)} = -\left(e^{-i\pi/4}B_1 + e^{i\pi/4}B_2 - B_1^* - B_2^*\right)$$

$$= \frac{\delta^2\Gamma(\frac{3}{4})^2}{2\varepsilon^{3/2}}\left(1 - \cos(\pi/4) - \frac{9i\sin(\pi/4)}{64\varepsilon^2t^2} + \right.$$

$$\left. \frac{3\cos(\frac{\pi}{8})\Gamma(\frac{5}{8})}{8\sqrt{2}\Gamma(\frac{11}{8})(\varepsilon t)^{1/4}}(e^{i\varepsilon t} - e^{-i(\varepsilon t+\pi/4)}) + \frac{\Gamma(\frac{7}{4})e^{i\pi/8}}{\sqrt{\pi}(\varepsilon t)^{1/4}}(e^{-i\varepsilon t} - e^{i\varepsilon t})\right). \tag{12.98}$$

12.B.3   Region C: $t > t_1 > t_2 > 0$

The integral in region C reads

$$\langle\sigma^x(t)\sigma^x(0)\rangle_C^{(2)} = (-i)^2\int_0^t dt_1\int_0^{t_1} dt_2 I_C. \tag{12.99}$$

We calculate the integrand I_C in a similar way to regions A and B. We get

$$I_C = (e^{-i\pi/4} + 1)(I_{C_1} - I_{C_2}), \tag{12.100a}$$

with the two integrand functions being

$$I_{C_1} = \frac{\delta^2 e^{-i\varepsilon t}e^{i\varepsilon(t_1-t_2)}(t-t_2)^{1/4}(t_1)^{1/4}}{4(t-t_1)^{1/4}(t)^{1/4}(t_2)^{1/4}(t_1-t_2)^{1/4}}, \tag{12.100b}$$

$$I_{C_2} = \frac{\delta^2 e^{i\varepsilon t}e^{-i\varepsilon(t_1+t_2)}(t-t_2)^{1/4}(t_1)^{1/4}}{4(t-t_1)^{1/4}(t)^{1/4}(t_2)^{1/4}(t_1-t_2)^{1/4}}. \tag{12.100c}$$

To integrate I_{C_1}, we make the variable transformation: $t_1 = t(T + 1/2 + \tau/2)$ and $t_2 = t(T + 1/2 - \tau/2)$. In terms of the new variables, the integral of I_{C_1} reads

$$C_1 = \frac{\delta^2 t^{3/2}e^{-i\varepsilon t}}{4}\int_0^1 d\tau\frac{e^{i\varepsilon t\tau}}{\tau^{1/4}}\int_{-1/2+\tau/2}^{1/2-\tau/2} dT$$

$$\times\frac{(1/2 - T + \tau/2)^{1/4}(1/2 + T + \tau/2)^{1/4}}{(1/2 - T - \tau/2)^{1/4}(1/2 + T - \tau/2)^{1/4}}. \tag{12.101}$$

The integration over T can be carried out exactly with the result

$$C_1 = \frac{\delta^2 t^{3/2} e^{-i\varepsilon t}}{4} \frac{2\sqrt{\pi}\,\Gamma(\frac{3}{4})}{\Gamma(\frac{1}{4})}$$
$$\int_0^1 d\tau \frac{e^{i\varepsilon t\tau}}{\tau^{1/4}} \sqrt{1-\tau^2}\; {}_2F_1\left(-\frac{1}{4}, \frac{1}{2}; \frac{5}{4}; \left(\frac{1-\tau}{1+\tau}\right)^2\right), \quad (12.102)$$

where ${}_2F_1(\alpha, \beta; \gamma; x)$ is the Gaussian hypergeometric function [270].

We deform the integration contour in Eq. (12.102) such that τ goes from 0 to $+i\infty$ and then back from $1 + i\infty$ to 1. The leading contribution in the long-time limit is dominated by the region near the real axis. The expansion around $x = 0$ leads to an oscillatory contribution while the expansion around $x = 1$ leads to a non-oscillatory contribution. To the lowest few orders, the asymptotic behavior in the long-time limit is given by

$$C_1 \sim +\frac{\delta^2 \Gamma(\frac{3}{4})^2 e^{i\pi/4}}{4\varepsilon^{3/2}}\left(-1 + \frac{9}{64\varepsilon^2 t^2}\right) + \frac{\delta^2 e^{-i\varepsilon t}}{4}\left\{\frac{e^{3i\pi/8}\Gamma(\frac{3}{4})t^{3/4}}{\varepsilon^{3/4}}\right.$$
$$\left. + \frac{e^{7i\pi/8}\Gamma(\frac{7}{4})(6\log(\varepsilon t) - (6+3i)\pi + 6\gamma - 14 + 36\log(2))}{12\varepsilon^{7/4}t^{1/4}}\right\}. \quad (12.103)$$

The oscillatory contribution contains a power-law divergent $t^{3/4}$ term. As we discuss later, this term contributes to the shift of the resonant frequency and to the damping for the $\langle\sigma^+(t)\sigma^-(0)\rangle$ correlation function.

To integrate I_{C_2}, we first change the integration variables to τ and T defined by $t_1 = t(T + \tau/2)$ and $t_2 = t(T - \tau/2)$ such that the integral separates into two parts

$$C_2 = \frac{\delta^2 t^{3/2} e^{i\varepsilon t}}{4}\left\{\int_0^{1/2} dT \int_0^{2T} d\tau + \int_{1/2}^1 dT \int_0^{2-2T} d\tau\right\}$$
$$\times \left(e^{-i2\varepsilon tT}\frac{(1-T+\tau/2)^{1/4}(T+\tau/2)^{1/4}}{(1-T-\tau/2)^{1/4}(T-\tau/2)^{1/4}(\tau)^{1/4}}\right). \quad (12.104)$$

After changing $T \to 1 - T$ in the second integral and then introducing $X = 2T$, this equation simplifies to

$$C_2 = \frac{\delta^2 t^{3/2}}{4} \times$$
$$\text{Re}\left\{e^{i\varepsilon t}\int_0^1 dX e^{-i\varepsilon tX}\int_0^X d\tau \frac{(2-X+\tau)^{1/4}(X+\tau)^{1/4}}{(2-X-\tau)^{1/4}(X-\tau)^{1/4}(\tau)^{1/4}}\right\}. \quad (12.105)$$

Again, we deform the integration contour in the integral over X with X changing from 0 to $-i\infty$ and then from $1-i\infty$ to 1. Now the oscillatory contribution comes from

$X \sim 0$ while the non-oscillatory one from $X \sim 1$. By expanding the integrand around these two points, we get the leading contributions:

$$C_2 = \frac{\delta^2 \Gamma(\frac{3}{4})^2}{4\varepsilon^{3/2}}\left(1 + \frac{9}{64\varepsilon^2 t^2} - \right.$$
$$\left. \frac{\left(e^{i\varepsilon t}e^{i\pi/8} + e^{-i\varepsilon t}e^{-i\pi/8}\right) {}_2F_1\left(-\frac{1}{4}, \frac{3}{4}; \frac{3}{2}; -1\right)\Gamma(\frac{7}{4})}{\varepsilon^{1/4}t^{1/4}} \frac{}{\sqrt{\pi}}\right). \quad (12.106)$$

The Gaussian hypergeometric function evaluates to ${}_2F_1\left(-\frac{1}{4}, \frac{3}{4}; \frac{3}{2}; -1\right) \approx 1.102$.

From Eqs. (12.99) and (12.100), we obtain contribution to the qubit correlation function from the region C:

$$\langle \sigma^x(t)\sigma^x(0)\rangle_C^{(2)} =$$
$$- (e^{-i\pi/4} + 1)(C_1 - C_2) \sim \frac{\delta^2 \Gamma(\frac{3}{4})^2}{2\varepsilon^{3/2}}\left(1 + \cos(\frac{\pi}{4}) - \frac{9i\,\sin(\frac{\pi}{4})}{64\varepsilon^2 t^2}\right)$$
$$+ \left(e^{-i\pi/8}\frac{e^{-i\varepsilon t}}{t^{1/4}}\right)\frac{\delta^2\Gamma(\frac{3}{4})}{4\varepsilon^{7/4}}(1 + e^{-i\pi/4})(-i\varepsilon t)$$
$$+ \frac{\delta^2 e^{-i\varepsilon t}e^{-i\pi/8}(e^{-i\pi/4} + 1)}{4\varepsilon^{7/4}t^{1/4}}\left\{\frac{\Gamma(\frac{7}{4})(6\log(\varepsilon t) - (6 + 3i)\pi + 6\gamma - 14 + 36\log(2))}{12}\right\}$$
$$+ \frac{\delta^2 \Gamma(\frac{3}{4})^2(e^{-i\pi/4} + 1)\left(e^{i\varepsilon t}e^{i\pi/8} + e^{-i\varepsilon t}e^{-i\pi/8}\right) {}_2F_1\left(-\frac{1}{4}, \frac{3}{4}; \frac{3}{2}; -1\right)\Gamma(\frac{7}{4})}{4\varepsilon^{7/4}t^{1/4} \sqrt{\pi}}.$$
$$(12.107)$$

12.B.4   Final result for $\langle \sigma^x(t)\sigma^x(0)\rangle_c^{(2)}$

The second order correction to the correlation function $\langle \sigma^x(t)\sigma^x(0)\rangle_c^{(2)}$ can be obtained by adding up the contributions from all the three regions, given by Eqs. (12.86), (12.98) and (12.107) and then subtracting $\langle \sigma^x\rangle^2$ as calculated in Eq. (12.40). The full expression

for the correlator in the long-time limit is

$$
\begin{aligned}
\langle \sigma^x(t)\sigma^x(0)\rangle_c^{(2)} = \\
-i\,\frac{9\delta^2\Gamma(\tfrac{3}{4})^2}{64\varepsilon^{3/2}}\frac{\sin(\tfrac{\pi}{4})}{\varepsilon^2 t^2} + e^{-i\pi/8}\frac{e^{-i\varepsilon t}}{t^{1/4}}\frac{\delta^2\Gamma(\tfrac{3}{4})}{4\varepsilon^{7/4}}(1+e^{-i\pi/4})(-i\varepsilon t) \\
+\frac{\delta^2\Gamma(\tfrac{7}{4})\log(\varepsilon t)e^{-i\pi/8}}{8\varepsilon^{7/4}t^{1/4}}\left\{(2+e^{-i\pi/4})e^{-i\varepsilon t}-e^{i\varepsilon t}\right\} \\
-\frac{\delta^2\Gamma(\tfrac{7}{4})e^{-i\pi/8}e^{-i\varepsilon t}}{4\varepsilon^{7/4}t^{1/4}}\left\{(2+e^{-i\pi/4})\frac{(7+3\pi-3\gamma-18\log(2))}{6}+(e^{i\pi/4}+e^{i\pi/2})\frac{\pi}{4}\right\} \\
+\frac{\delta^2\Gamma(\tfrac{3}{4})^2\Gamma(\tfrac{7}{4})e^{-i\varepsilon t}}{4\varepsilon^{7/4}t^{1/4}}\left(\frac{2e^{i\pi/8}}{\sqrt{\pi}}-\frac{3\cos(\tfrac{\pi}{8})\Gamma(\tfrac{5}{8})e^{-i\pi/4}}{4\sqrt{2}\Gamma(\tfrac{11}{8})\Gamma(\tfrac{7}{4})}\right. \\
\left.+\frac{{}_2F_1\left(-\tfrac{1}{4},\tfrac{3}{4};\tfrac{3}{2};-1\right)(e^{-i3\pi/8}+e^{-i\pi/8})}{\sqrt{\pi}}\right) \\
+\frac{\delta^2\Gamma(\tfrac{3}{4})^2 e^{i\varepsilon t}}{4\varepsilon^{7/4}t^{1/4}}\left\{\frac{[7+3\pi-3\gamma-18\log(2)]e^{-i\pi/8}}{8\Gamma(\tfrac{3}{4})}+\frac{3\cos(\tfrac{\pi}{8})\Gamma(\tfrac{5}{8})}{4\sqrt{2}\Gamma(\tfrac{11}{8})}\right. \\
\left.-\frac{2\Gamma(\tfrac{7}{4})e^{i\pi/8}}{\sqrt{\pi}}+\frac{2\cos(\tfrac{\pi}{8})\,{}_2F_1\left(-\tfrac{1}{4},\tfrac{3}{4};\tfrac{3}{2};-1\right)\Gamma(\tfrac{7}{4})}{\sqrt{\pi}}\right\}.
\end{aligned}
\tag{12.108}
$$

This result agrees well with numerical evaluation of the integral. A power law divergence $\sim t^{3/4}$ and a logarithmic contribution $\sim \log(\varepsilon t)/t^{1/4}$ dominate the long-time behavior of the correlator. However, this logarithmic contribution will be cut off either by the induced damping or by a finite temperature.

A heuristic way to see that the term diverging as $t^{3/4}$ corresponds to self-energy correction is to add it to the zeroth order correlator of $\langle\sigma^x(t)\sigma^x(0)\rangle$ given by (12.41). The sum of these two terms equals to

$$
\begin{aligned}
e^{-i\pi/8}\frac{e^{-i\varepsilon t}}{t^{1/4}}\left(1-i\,\frac{\delta^2\Gamma(\tfrac{3}{4})}{4\varepsilon^{3/4}}(2\cos^2(\tfrac{\pi}{8})-i\,\frac{1}{\sqrt{2}})t\right) \\
=e^{-i\pi/8}\frac{e^{-i\varepsilon t}}{t^{1/4}}\left(1-i(\nu-i\tfrac{\gamma}{2})t\right),
\end{aligned}
\tag{12.109}
$$

with ν and γ the same as in Eq. (12.51). It then becomes apparent that (12.109) is exactly the expansion of the renormalized correlator (12.55) to the second order in δ

$$
\frac{e^{-i\pi/8}}{t^{1/4}}e^{-i(\varepsilon+\nu)t-\gamma t/2}.
\tag{12.110}
$$

We thus conclude that the explicit evaluation of the higher order correction gives a result consistent with the self-energy calculation.

12.B.5 Comments on leading contributions of higher orders

The leading contribution to the second order corrections comes from region C with integration of C_1 when the integration variable τ is around $\tau = 0$, cf. Eq. (12.101). Since $\tau = (t_1 - t_2)/t$, this expansion to the zeroth order is equivalent to making an operator product expansion of $\mu(t_1)\mu(t_2)$ for $t_1 \approx t_2$ in the four-point correlation function of μ operators [241]. In the nth order of perturbation theory with insertion times $t_1, \ldots, t_n$, we expect that the most divergent contribution arises when all the insertion times belong to the interval $[0, t]$. By ordering the times $t_1 > t_2 > \cdots > t_n$ and using the operator product expansion for the pairs $\mu_{t_{2i-1}}\mu_{t_{2i}}$ for $i = 1, \ldots, n/2$, we get a perturbative structure resembling Wick's theorem. The resummation of these terms would give the contributions for the self energy which we calculated in Sec. 12.6.1.

Chapter 13

Anyonic interferometry without anyons: How a flux qubit can read out a topological qubit

13.1 Introduction

A topological quantum computer makes use of a nonlocal way of storing quantum information in order to protect it from errors [8, 9]. One promising way to realize the nonlocality is to store the information inside the Abrikosov vortices that form when magnetic field lines penetrate a superconductor. Abrikosov vortices can trap quasiparticles within their normal core [135], which in special cases are anyons having non-Abelian statistics [6, 139]. For this to happen, the vortex should have a midgap state of zero excitation energy, known as a Majorana bound state. While vortices in a conventional s-wave superconductor lack Majorana bound states, they are expected to appear [129–131, 257] in the chiral p-wave superconductors that are currently being realized using topological states of matter.

The method of choice to read out a nonlocally encoded qubit is interferometry [175, 176]. A mobile anyon is split into a pair of partial waves upon tunneling, which interfere after encircling an even number of stationary anyons. (There is no interference if the number is odd.) The state of the qubit encoded in the stationary anyons can be read out by measuring whether the interference is constructive or destructive. The superconducting implementation of this anyonic interferometry has been analyzed in different setups [144–146, 261], which suffer from one and the same impediment: Abrikosov vortices are massive objects that do not readily tunnel or split into partial waves.

The mass of an Abrikosov vortex is much larger than the bare electron mass because it traps a large number of quasiparticles. (The enhancement factor is $k_F^3 \xi^2 d$, with d the thickness of the superconductor along the vortex, ξ the superconducting coherence length, and k_F the Fermi wave vector [271].) There exist other ways to make Majorana bound states in a superconductor (at the end-points of a semiconducting wire or electrostatic line defect [132, 134, 207, 208]), but these also involve intrinsically classical objects. If indeed Majorana bound states and classical motion go hand in hand, it would seem that anyonic interferometry in a superconductor is ruled out — which would be

bad news indeed.

Here we propose an alternative way to perform the interferometric read out, using quantum Josephson vortices instead of classical Abrikosov vortices as the mobile particles. A Josephson vortex is a 2π twist of the phase of the order parameter, at constant amplitude. Unlike an Abrikosov vortex, a Josephson vortex has no normal core so it does not trap quasiparticles. Its mass is determined by the electrostatic charging energy and is typically less than 1% of the electron mass [272]. Quantum tunneling and interference of Josephson vortices have been demonstrated experimentally [273, 274]. This looks promising for anyonic interferometry, but since the Josephson vortex itself is not an anyon (it lacks a Majorana bound state), one might object that we are attempting anyonic interferometry without anyons. Let us see how this can be achieved, essentially by using a non-topological flux qubit [275, 276] to read out the topological qubit.

We consider a Josephson junction circuit (see Fig. 13.1) which can exist in two degenerate states $|L\rangle$, $|R\rangle$, distinguished by the phases ϕ_i^L, ϕ_i^R of the order parameter on the islands. The supercurrent flows to the left or to the right in state $|L\rangle$ and $|R\rangle$, so the circuit forms a flux qubit (or persistent current qubit). This is a non-topological qubit.

13.2   Analysis of the setup

The topological qubit is formed by a pair of non-Abelian anyons in a superconducting island, for example the midgap states in the core of a pair of Abrikosov vortices. The two states $|0\rangle$, $|1\rangle$ of the topological qubit are distinguished by the parity of the number n_p of particles in the island. For n_p odd there is a zero-energy quasiparticle excitation shared by the two midgap states. This qubit is called topological because it is insensitive to local sources of decoherence (since a single vortex cannot tell whether its zero-energy state is filled or empty).

To measure the parity of n_p, and hence read out the topological qubit, we make use of the suppression of macroscopic quantum tunneling by the Aharonov-Casher (AC) effect [276, 277]. Tunneling from $|L\rangle$ to $|R\rangle$ requires quantum phase slips. If the tunneling can proceed along two path ways, distinguished by a 2π difference in the value of ϕ_1^R, then the difference between the two tunneling paths amounts to the circulation of a Josephson vortex around the island containing the topological qubit (dashed arrows in Fig. 13.1).

According to the Aharonov-Casher (AC) effect, a vortex encircling a superconducting island picks up a phase increment $\psi_{AC} = \pi q/e$ determined by the total charge q coupled capacitively to the superconductor [278]. (The charge may be on the superconducting island itself, or on a nearby gate electrode.) If q is an odd multiple of the electron charge e, the two tunneling paths interfere destructively, so the tunnel splitting vanishes, while for an even multiple the interference is constructive and the tunnel splitting is maximal. A microwave measurement of the splitting of the flux qubit thus reads out the topological qubit.

Since we only need to distinguish maximal from minimal tunnel splitting, the flux qubit does not need to have a large quality factor (limited by $1/f$ charge noise from
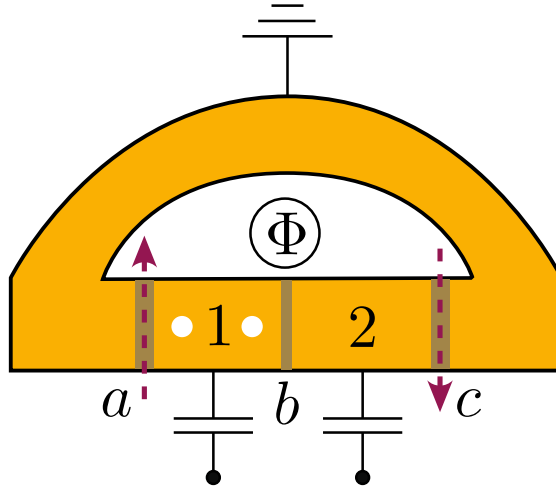
Figure 13.1: Circuit of three Josephson junctions a, b, c, two superconducting islands $1, 2$, and a superconducting ring (enclosing a flux Φ). A persistent current can flow clockwise or counterclockwise. This flux qubit can read out the state of a topological qubit stored in one of the two islands (white discs). Dashed arrows indicate the Josephson vortex tunneling events that couple the two states of the flux qubit, leading to a tunnel splitting that depends on the state of the topological qubit.

the gate electrodes). Moreover, the read out is insensitive to sub-gap excitations in the superconductor — since these do not change the fermion parity n_p and therefore do not couple to the flux qubit. This *parity protection* against sub-gap excitations is the key advantage of flux qubit read-out [279].

Following Ref. [276] we assume that the ring is sufficiently small that the flux generated by the supercurrent can be neglected, so the enclosed flux Φ equals the externally applied flux. Junctions a and c are assumed to have the same critical current $I_{\rm crit}$, while junction b has critical current $\alpha I_{\rm crit}$. Because the phase differences across the three junctions a, b, c sum to $\delta\phi_a + \delta\phi_b + \delta\phi_c = 2\pi\Phi/\Phi_0$ (with $\Phi_0 = h/2e$ the flux quantum), we may take $\delta\phi_a$ and $\delta\phi_c$ as independent variables. The charging energy $E_C = e^2/2C$ of the islands (with capacitance C) is assumed to be small compared to the Josephson coupling energy $E_J = \Phi_0 I_{\rm crit}/2\pi$, to ensure that the phases are good quantum variables. The phase on the ring is pinned by grounding it, while the phases on the islands can change by Josephson vortex tunneling events (quantum phase slips).

The superconducting energy of the ring equals

$$U_J = -E_J[\cos\delta\phi_a + \cos\delta\phi_c$$
$$+ \alpha\cos(2\pi\Phi/\Phi_0 - \delta\phi_a - \delta\phi_c)]. \qquad (13.1)$$

The states $|L\rangle$ and $|R\rangle$ correspond in the potential energy landscape of Fig. 13.2 to the minima indicated by red and blue dots, respectively. Because phases that differ by 2π
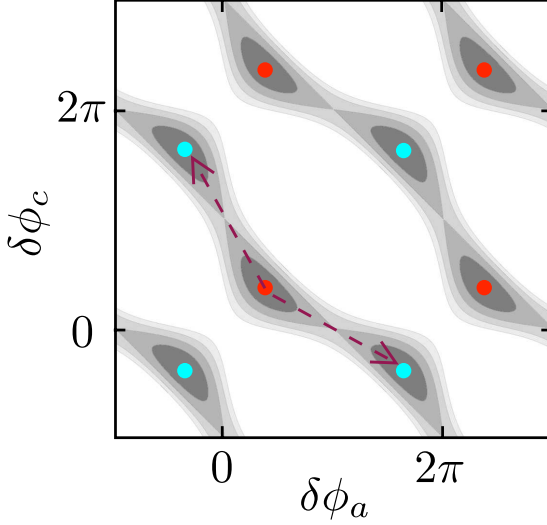
Figure 13.2: Contour plot of the potential energy (13.1) of the flux qubit for $\alpha = 1.3$ and $\Phi = \Phi_0/2$ (white is high potential, black is low potential). The red and blue dots indicate the minima of clockwise or counterclockwise persistent current. All red dots and all blue dots are equivalent, because the phase differences $\delta\phi_a, \delta\phi_c$ across the Josephson junctions are defined modulo 2π. Tunneling between two inequivalent minima occurs predominantly along the two pathways indicated by the arrows.

are equivalent, all red dots represent equivalent states and so do all blue dots. For $\alpha > 1$ the minima are connected by two tunneling paths (arrows), differing by an increment of $+2\pi$ in $\delta\phi_a$ and -2π in $\delta\phi_c$. The difference amounts to the circulation of a Josephson vortex around both islands 1 and 2. The two interfering tunneling paths have the same amplitude, because of the left-right symmetry of the circuit. Their phase difference is $\psi_{AC} = \pi q/e$, with $q = \sum_{i=1,2}(e n_p^{(i)} + q_{ext}^{(i)})$ the total charge on islands and gate capacitors.

The interference produces an oscillatory tunnel splitting of the two levels $\pm\frac{1}{2}\Delta E$ of the flux qubit,

$$\Delta E = E_{tunnel}\big|\cos(\psi_{AC}/2)\big|. \tag{13.2}$$

Tiwari and Stroud [276] have calculated $E_{tunnel} \approx 100\,\mu\text{eV} \simeq 1\,\text{K}$ for parameter values representative of experimentally realized flux qubits [275] ($E_J = 800\,\mu\text{eV}$, $E_C = 10\,\mu\text{eV}$). They conclude that the tunnel splitting should be readily observable by microwave absorption at temperatures in the 100 mK range.

To read out the topological qubit one would first calibrate the charge $q_{ext}^{(1)} + q_{ext}^{(2)}$ on the two gate capacitors to zero, by maximizing the tunnel splitting in the absence of vortices in the islands. A vortex pair in island 1 can bind a quasiparticle in the midgap state, allowing for a nonzero $n_p^{(1)}$ (while $n_p^{(2)}$ remains zero without vortices in island
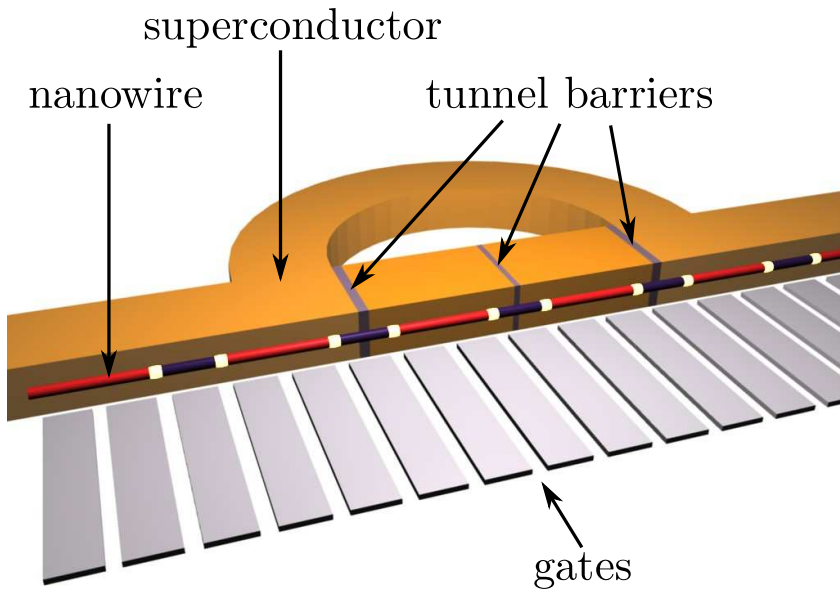
Figure 13.3: Register of topological qubits, read out by a flux qubit in a superconducting ring. The topological qubit is encoded in a pair of Majorana bound states (white dots) at the interface between a topologically trivial (blue) and a topologically nontrivial (red) section of an InAs wire. The flux qubit is encoded in the clockwise or counterclockwise persistent current in the ring. Gate electrodes (grey) can be used to move the Majorana bound states along the wire.

2). A measurement of the tunnel splitting then determines the parity of $n_p^{(1)}$ (vanishing when $n_p^{(1)}$ is odd), and hence reads out the topological qubit.

13.3 Discussion

To implement this read-out scheme the absence of low-energy excitations near the Josephson junction is desirable in order to minimize decoherence of the Josephson vortex as it passes along the junction. The metallic edge states of a topological superconductor are a source of low-energy excitations that one would like to keep away from the junction. So for the flux qubit we would choose a conventional (non-topological) *s*-wave superconductor such as Al or Nb.

Since a vortex in a non-topological superconductor has no Majorana bound states, we turn to one of the vortex-free alternatives [132, 134, 207, 208]. The "Majorana wire" [207, 208] seems particularly suitable: A single-mode semiconducting InAs nanowire

in a weak (0.1 T) parallel magnetic field is driven into a chiral p-wave superconducting state by the interplay of spin-orbit coupling, Zeeman effect, and the proximity to an s-wave superconductor. A pair of Majorana bound states is formed at the end points of the wire, provided it is long compared to ξ. For that reason Nb ($\xi \lesssim 40$ nm) is to be preferred over Al as superconducting substrate.

A long InAs wire running through a Josephson junction circuit could conveniently form a register of topological qubits, as illustrated in Fig. 13.3. Gate electrodes (grey) deplete sections of the wire (blue) such that they enter a topologically trivial phase, producing a pair of Majorana bound states (white dots) at the end points of the topologically nontrivial sections (red). Each pair encodes one topological qubit, which can be reversibly moved back and forth along the wire by adjusting, the gate voltage. (The wire is not interrupted by the tunnel barriers, of thickness $\ll \xi$.) Once inside the circuit, the tunnel splitting of the flux qubit measures the state of the topological qubit.

For a universal quantum computation the flux qubit read-out discussed here should be combined with the ability to exchange adjacent Majorana bound states, using two parallel registers [210]. This is the topologically protected part of the computation. In addition, one needs to perform single-qubit rotations, which as a matter of principle lack topological protection [8]. In the Appendix we show how the flux qubit can be used for parity protected single-qubit rotations (by slowly increasing the flux through the ring from zero to a value close to $\Phi_0/2$ and back to zero).

In comparison with existing read-out schemes [9, 130, 144–146, 261, 280], there are two key differences with the flux qubit read-out proposed here. Firstly, unlike proposals based on the fusion of vortices, our scheme is nondestructive — meaning that the topological qubit remains available after the measurement (necessary for the realization of a two-qubit CNOT gate, see the Appendix).

Secondly, our use of *coreless* vortices to perform the interferometry provides protection against subgap excitations. This parity protection is essential because the operating temperature would otherwise be restricted to unrealistically small values (below 0.1 mK for a typical Abrikosov vortex [135]). The characteristic temperature scale for flux qubit read-out is larger by up to three orders of magnitude.

13.A   How a flux qubit enables parity-protected quantum computation with topological qubits

13.A.1   Overview

In the main text we discussed the read out of a topological qubit by coupling it to a flux qubit through the Aharonov-Casher effect. This read out is nondestructive (the topological qubit remains available after the read out) and insensitive to subgap excitations (since these do not change the fermion parity). In this Appendix we show, in Sec. 13.A.3, how flux qubit read-out supplemented by braiding operations [210] provides the topologically protected part of a quantum computation (in the form of a CNOT gate acting on a pair of qubits).

For a universal quantum computer, one needs additionally to be able to perform single qubit rotations of the form

$$|0\rangle + |1\rangle \mapsto e^{-i\theta/2}|0\rangle + e^{i\theta/2}|1\rangle. \tag{13.3}$$

(Such a rotation over an angle θ is also called a $\theta/2$ phase gate.) In general (for θ not equal to a multiple of $\pi/2$), this part of the quantum computation is not topologically protected. A more limited protection against subgap excitations, which do not change the fermion parity, is still possible [279]. We will show in Sec. 13.A.4 how the flux qubit provides a way to perform parity-protected rotations.

In order to make this Appendix self-contained, we first summarize in Sec. 13.A.2 some background information on topological quantum computation with Majorana fermions [8]. Then we discuss the topologically protected CNOT gate and the parity-protected single-qubit rotation.

13.A.2 Background information

Encoding of a qubit in four Majorana fermions

In the main text we considered a qubit formed out of a pair of Majorana bound states. The two states $|0\rangle$ and $|1\rangle$ of this elementary qubit differ by fermion parity, which prevents the creation of a coherent superposition. For a quantum computation we combine two elementary qubits into a single logical qubit, consisting of four Majorana bound states. Without loss of generality we can assume that the joint fermion parity is even. The two states of the logical qubit are then encoded as $|00\rangle$ and $|11\rangle$. These two states have the same fermion parity, so coherent superpositions are allowed.

The four Majorana operators γ_i ($i = 1, 2, 3, 4$) satisfy $\gamma_i^\dagger = \gamma_i$, $\gamma_i^2 = \frac{1}{2}$, and the anticommutation relation $\{\gamma_i, \gamma_j\} = \delta_{ij}$. They can be combined into two complex fermion operators,

$$a_1 = \frac{\gamma_1 + i\gamma_2}{\sqrt{2}}, \quad a_2 = \frac{\gamma_3 + i\gamma_4}{\sqrt{2}}, \tag{13.4}$$

which satisfy $\{a_i, a_j^\dagger\} = \delta_{ij}$. The fermion parity operator

$$2a_1^\dagger a_1 - 1 = 2i\gamma_1\gamma_2 \tag{13.5}$$

has eigenvalues -1 and $+1$ in states $|0\rangle$ and $|1\rangle$, respectively.

Pauli operators in the computational basis $|00\rangle, |11\rangle$ can be constructed as usual from the $a, a^\dagger$ operators, and then expressed in terms of the γ operators as follows:

$$\sigma_x = -2i\gamma_2\gamma_3, \quad \sigma_y = 2i\gamma_1\gamma_3, \quad \sigma_z = -2i\gamma_1\gamma_2. \tag{13.6}$$

Measurement in the computational basis

An arbitrary state $|\psi\rangle$ of the logical qubit has the form

$$|\psi\rangle = \alpha|00\rangle + \beta|11\rangle, \quad |\alpha|^2 + |\beta|^2 = 1. \tag{13.7}$$

A measurement in the computational basis projects $|\psi\rangle$ on the states $|00\rangle$ or $|11\rangle$. This is a fermion parity measurement of one of the two fundamental qubits that encode the logical qubit.

Referring to the geometry of Fig. 13.3, one would perform such a nondestructive projective measurement (called a quantum nondemolition measurement) by moving the Majorana fermions γ_1, γ_2 along the InAs wire into the Josephson junction circuit, while keeping the Majorana fermions γ_3, γ_4 outside of the circuit. Read out of the flux qubit would then measure the fermion parity of the first fundamental qubit, thereby projecting the logical qubit onto the states $|00\rangle$ or $|11\rangle$.

Braiding of Majorana fermions

The Majorana bound states in the geometry of Fig. 13.3 are separated by insulating regions on a single InAs wire, so they cannot be exchanged. The exchange of Majorana fermions, called "braiding" is needed to demonstrate their non-Abelian statistics. It is also an essential ingredient of a topologically protected quantum computation. In order to be able to exchange the Majorana bound states one can use a second InAs wire, running parallel to the first and connected to it by side branches. Braiding of Majorana fermions in this "railroad track" geometry has been studied recently by Alicea *et al.* [210]. We refer to their paper for the details of this implementation and in the following just assume that adjacent Majorana bound states can be exchanged as needed.

The counterclockwise exchange of Majorana fermions $j < j'$ implements the operator [6, 139]

$$\rho_{jj'} = 2^{-1/2}(1 - 2\gamma_j \gamma_{j'}) = e^{(i\pi/4)(2i\gamma_j \gamma_{j'})}. \tag{13.8}$$

Using Eq. (13.6), we conclude that braiding generates the operations $\exp[\pm(i\pi/4)\sigma_k]$ ($k = x, y, z$). These $\pi/2$ rotations (or $\pi/4$ phase gates) are the only single-qubit operations that can be generated in a topologically protected way [8].

13.A.3   Topologically protected CNOT gate

The controlled-not (CNOT) two-qubit gate can be carried out in a topologically protected way by the combination of braiding and fermion parity measurements, along the lines set out by Bravyi and Kitaev [281].

The computational basis, constructed from the first logical qubit formed by Majorana operators $\gamma_1, \gamma_2, \gamma_3, \gamma_4$ and the second logical qubit $\gamma_5, \gamma_6, \gamma_7, \gamma_8$, consists of the four states

$$|00\rangle|00\rangle, \quad |00\rangle|11\rangle, \quad |11\rangle|00\rangle, \quad |11\rangle|11\rangle. \tag{13.9}$$

The first and second kets represent the first and second logical qubits, respectively, and the two states within each ket represent the two fundamental qubits. In this basis, the

CNOT gate has the matrix form

$$\text{CNOT} = \begin{pmatrix} 1 & 0 & 0 & 0 \\ 0 & 1 & 0 & 0 \\ 0 & 0 & 0 & 1 \\ 0 & 0 & 1 & 0 \end{pmatrix}. \tag{13.10}$$

In words, the second logical qubit (the target) is flipped if the first logical qubit (the control) is in the state $|11\rangle$, otherwise it is left unchanged.

For a topologically protected implementation one needs an extra pair of Majorana fermions γ_9, γ_{10} (ancilla's), that can be measured jointly with the Majorana fermions $\gamma_1, \ldots \gamma_8$. The CNOT gate can be constructed from $\pi/2$ rotations (performed by braiding), together with measurements of the fermion parity operator $(2i \gamma_i \gamma_j)(2i \gamma_k \gamma_l)$ of sets of four Majorana fermions [281]. Because the measurements include Majorana fermions from the computational set $\gamma_1, \ldots \gamma_8$ (not just the ancilla's), it is essential that they are nondestructive.

Referring to Fig. 13.3, such a nondestructive joint parity measurement can be performed by moving the four Majorana bound states i, j, k, l into the Josephson junction circuit. (The double wire geometry of Ref. [210] would be used to bring the bound states in the required order.) Read out of the flux qubit then projects the system onto the two eigenstates of $(2i \gamma_i \gamma_j)(2i \gamma_k \gamma_l)$ of definite joint parity.

13.A.4 Parity-protected single-qubit rotation

From topological protection to parity protection

There is a relatively small set of unitary operations that one needs in order to be able to perform an arbitrary quantum computation. One needs the CNOT two-qubit gate, which can be done in a topologically protected way by braiding and read out as discussed in Sec. 13.A.3. One needs $\pi/2$ single-qubit rotations ($\pi/4$ phase gates), which can also be done with topological protection by braiding (Sec. 13.A.2). These socalled Clifford gates can be efficiently simulated on a classical computer, and are therefore not sufficient.

One more gate is needed for a quantum computer, the $\pi/4$ single-qubit rotation ($\pi/8$ phase gate). This operation cannot be performed by braiding and read out — at least not without changing the topology of the system during the operation [282, 283] and incurring both technological and fundamental obstacles[1] [284]. As an alternative to full topological protection, we propose here a parity-protected $\pi/4$ rotation.

Braiding and read out are topologically protected operations, which means firstly that they are insensitive to local sources of decoherence and secondly that they can be

---

[1] As first shown by Bravyi and Kitaev (2001, unpublished) in an abstract formulation, a topologically protected $\pi/4$ rotation of a single qubit can be performed in higher genus topologies (like a torus). To use this approach in condensed matter systems is problematic for obvious technological reasons, but also because of a more subtle and fundamental obstacle: Topolgical superconductors and Moore-Read quantum Hall phases of a higher genus lack a degenerate ground state [284].

carried out exactly. (As discussed in Sec. 13.A.2, exchange of two Majorana fermions rotates the qubit by exactly $\pi/2$.) The $\pi/4$ rotation lacks the second benefit of topological protection, so it is an approximate operation, but the first benefit can remain to a large extent if we use a flux qubit to perform the rotation in a parity protected way, insensitive to subgap excitations.

The straightforward approach to single-qubit rotations is partial fusion, which lacks parity protection: One would bring two vortices close together for a short time t, and let the tunnel splitting δE impose a phase difference $\theta = t\delta E/\hbar$ between the two states $|0\rangle$ and $|1\rangle$. The result is the rotation (13.3), but only if the vortices remain in the ground state. The minigap in a vortex core is smaller than the bulk superconducting gap Δ_0 by a large factor $k_F\xi$, so this is a severe restriction (although there might be ways to increase the minigap[2] [137, 285]). An alternative to partial fusion using edge state interferometry has been suggested [286] in the context of the Moore-Read state of the $\nu = 5/2$ quantum Hall effect [5], where parity protection may be less urgent.

Like the parity-protected read-out discussed in the main text, our parity-protected $\pi/4$ rotation uses the coupling of a flux qubit to the topological qubit. The coupling results from the Aharonov-Casher effect, so it is insensitive to any any other degree of freedom of the topological qubit than its fermion parity. The operation lacks topological protection and is therefore not exact (the rotation angle is not exactly $\pi/4$). It can be combined with the distillation protocol of Bravyi and Kitaev [287, 288], which allows for error correction with a relatively large tolerance (error rates as large as 10% are permitted).

Method

As explained in Sec. 13.A.2, we start from a logical qubit encoded as $|00\rangle$, $|11\rangle$ in the four Majorana fermions $\gamma_1, \gamma_2, \gamma_3, \gamma_4$. We bring the Majorana bound states 1 and 2 into the Josephson junction circuit, keeping 3 and 4 outside. The effective Hamiltonian of the Josephson junction circuit is

$$H = -\tfrac{1}{2}\varepsilon\,\tau_z + \tfrac{1}{2}\Delta E\,\tau_x, \qquad (13.11)$$

with energy levels

$$E_\pm = \pm\tfrac{1}{2}\sqrt{\varepsilon^2 + \Delta E^2}. \qquad (13.12)$$

The Pauli matrices τ_i act on the two states $|L\rangle$, $|R\rangle$ of the flux qubit (states of clockwise and counterclockwise circulating persistent current). In the absence of tunneling between these two states, their energy difference $\varepsilon = \varepsilon_0(\Phi/\Phi_0 - 1/2)$ (with $\varepsilon_0 = 4\pi E_J\sqrt{1 - 1/4\alpha^2}$) vanishes when the flux Φ through the ring equals half a flux quantum $\Phi_0 = h/2e$. Tunneling leads to a splitting ΔE given by Eq. (13.2).

---

[2]In a semiconductor-superconductor multilayer there may be ways to increase the minigap, if one can somehow control the strength of the proximity effect and the work function difference between the semiconductor and the superconductor [137]. In p-wave superfluids the minigap may be increased by going to the regime of small chemical potential, near the transition to a strongly paired phase [285].

Parity protection means that the Majorana bound states 1 and 2 appear in H only through their fermion parity n_p, which determines $\Delta E = \Delta E(n_p)$ through the Aharonov-Casher phase. Subgap excitations preserve fermion parity, so they do not enter into H and cannot cause errors.

To perform the single-qubit rotation, we start at time $t = 0$ from a flux Φ far from $\Phi_0/2$, when $|\varepsilon| \gg \Delta E$. Then the state $|L\rangle$ is the ground state of the flux qubit and the coupling to the topological qubit is switched off. The flux $\Phi(t)$ is changed slowly to values close to $\Phi_0/2$ at $t = t_f/2$ and then brought back to its initial value at time $t = t_f$. The variation of Φ should be sufficiently slow (adiabatic) that the flux qubit remains in the ground state, so its final state is $|L\rangle$ times a dynamical phase $e^{i\varphi(n_p)}$ dependent on the fermion parity of the first of the two topological qubits that encode the logical qubit.

The initial state $|\Psi_i\rangle = (\alpha|00\rangle + \beta|11\rangle)|L\rangle$ of flux qubit and logical qubit is therefore transformed into

$$|\Psi_i\rangle \mapsto |\Psi_f\rangle = \left(e^{i\varphi(0)}\alpha|00\rangle + e^{i\varphi(1)}\beta|11\rangle\right)|L\rangle. \tag{13.13}$$

By adjusting the variation of $\Phi(t)$ we can ensure that $\varphi(1) - \varphi(0) = \pi/8$, thereby realizing the desired $\pi/4$ rotation.

Example

As an example, we vary the flux linearly in time according to

$$\frac{\Phi(t)}{\Phi_0} - \frac{1}{2} = -\frac{E_0 + \lambda|t - t_f/2|}{\varepsilon_0}, \tag{13.14}$$

$$\Rightarrow E_\pm = \pm\frac{1}{2}\sqrt{(E_0 + \lambda|t - t_f/2|)^2 + \Delta E^2}. \tag{13.15}$$

We assume $q_{ext} = 0$, so $\Delta E(1) = 0$ and $\Delta E(0) = E_{tunnel}$. We take $E_0 \gg E_{tunnel}$, for weak coupling between flux qubit and topological qubit. The condition for the adiabatic approximation [289] then takes the form

$$\left|\frac{\hbar}{2E_-^2}\frac{dE_-}{dt}\right|_{t=t_f/2} \approx \frac{\hbar\lambda}{E_0^2} \ll 1. \tag{13.16}$$

From time $t = 0$ to $t = t_f$, the flux qubit accumulates the dynamical phase factor

$$\varphi(n_p) = \hbar^{-1}\int_0^{t_f} dt\, E_-(t, n_p). \tag{13.17}$$

To leading order in the small parameter E_{tunnel}/E_0 we find

$$\phi(1) - \phi(0) = \frac{E_{tunnel}^2}{2\hbar\lambda}\ln(1 + \lambda t_f/2E_0). \tag{13.18}$$

By choosing

$$t_f = \frac{2E_0}{\lambda}\left[\exp\left(\tfrac{1}{4}\pi\hbar\lambda/E_{tunnel}^2\right) - 1\right] \tag{13.19}$$

we implement a $\pi/4$ rotation.

In order to maximally decouple the flux qubit from the topological qubit at the start and at the end of the operation, we take $\Phi(t) = 0$ at $t = 0$ and $t = t_f$. In view of Eq. (13.14), this requires $\lambda t_f = \varepsilon_0 - 2E_0$. Substitution into Eq. (13.19) gives the desired optimal value of λ,

$$\lambda_{\text{opt}} = (4/\pi\hbar)E_{\text{tunnel}}^2 \ln(\varepsilon_0/2E_0), \qquad (13.20)$$

still consistent with the adiabaticity requirement (13.16). For $E_{\text{tunnel}} \ll E_0 \ll \varepsilon_0$ the entire operation then has a duration of order $\hbar\varepsilon_0/E_{\text{tunnel}}^2$, up to a logarithmic factor. The quality factor of the flux qubit should thus be larger than $(\varepsilon_0/E_{\text{tunnel}})^2 \simeq E_J/E_C$ (typically $\simeq 10^2$).

References

[1] P. R. Wallace, Phys. Rev. **71**, 622 (1947).

[2] H. P. Boehm, A. Clauss, G. O. Fischer, and U. Hofmann, Z. anorg. allg. Chemie **316**, 119 (1962).

[3] K. S. Novoselov, A. K. Geim, S. V. Morozov, D. Jiang, Y. Zhang, S. V. Dubonos, I. V. Grigorieva, and A. A. Firsov, Science **306**, 666 (2004).

[4] E. Majorana, Nuovo Cimento **9**, 335 (1932).

[5] G. Moore and N. Read, Nucl. Phys. B **360**, 362 (1991).

[6] N. Read and D. Green, Phys. Rev. B **61**, 10267 (2000).

[7] G. E. Volovik and V. M. Yakovenko, J. Phys. **1**, 5263 (1989).

[8] C. Nayak, S. H. Simon, A. Stern, M. Freedman, and S. Das Sarma, Rev. Mod. Phys. **80**, 1083 (2008).

[9] A. Y. Kitaev, Ann. Phys. **303**, 2 (2003).

[10] I. Tamm, Phys. Zh. Sov. U. **1**, 733 (1932).

[11] W. Shockley, Phys. Rev. **56**, 317 (1939).

[12] A. Altland and M. R. Zirnbauer, Phys. Rev. B **55**, 1142 (1997).

[13] E. H. Lieb, Phys. Rev. Lett. **62**, 1201 (1989).

[14] P. G. De Gennes, *Superconductivity of Metals and Alloys* (Benjamin, New York, 1966).

[15] S. Datta and P. F. Bagwell, Superlatt. Microstruct. **25**, 1233 (1999).

[16] S. Ryu, A. P. Schnyder, A. Furusaki, and A. W. W. Ludwig, New J. Phys. **12**, 065010 (2010).

[17] D. P. Di Vincenzo and E. J. Mele, Phys. Rev. B **29**, 1685 (1984).

[18] Y.-W. Son, M. L. Cohen, and S. G. Louie, Nature **444**, 347 (2006).

[19] E. McCann and V. I. Fal'ko, J. Phys. **16**, 2371 (2004).

[20] A. R. Akhmerov and C. W. J. Beenakker, Phys. Rev. Lett. **98**, 157003 (2007).

[21] L. Brey and H. A. Fertig, Phys. Rev. B **73**, 235411 (2006).

[22] M. Ezawa, Phys. Rev. B **73**, 045432 (2006).

[23] M. V. Berry and R. J. Mondragon, Proc. R. Soc. London A **412**, 53 (1987).

[24] Z. Chen, Y. Lin, M. Rooks, and P. Avouris, Physica E **40**, 228 (2007).

[25] M. Y. Han, B. Özyilmaz, Y. Zhang, and P. Kim, Phys. Rev. Lett. **98**, 206805 (2007).

[26] K. Nakada, M. Fujita, G. Dresselhaus, and M. S. Dresselhaus, Phys. Rev. B **54**, 17954 (1996).

[27] I. Martin and Y. M. Blanter, Phys. Rev. B **79**, 235132 (2009).

[28] A. Rycerz and C. W. J. Beenakker, arXiv:0709.3397 (2007).

[29] A. Rycerz, Phys. Stat. Sol. A **205**, 1281 (2008).

[30] K. S. Novoselov, A. K. Geim, S. V. Morozov, D. Jiang, M. I. Katsnelson, I. V. Grigorieva, S. V. Dubonos, and A. A. Firsov, Nature **438**, 197 (2005).

[31] Y. Zhang, Y. Tan, H. L. Stormer, and P. Kim, Nature **438**, 201 (2005).

[32] L. Brey and H. A. Fertig, Phys. Rev. B **73**, 195408 (2006).

[33] D. A. Abanin, P. A. Lee, and L. S. Levitov, Phys. Rev. Lett. **96**, 176803 (2006).

[34] H. Takayanagi and T. Akazaki, Physica B **249-251**, 462 (1998).

[35] T. D. Moore and D. A. Williams, Phys. Rev. B **59**, 7308 (1999).

[36] D. Uhlisch, S. G. Lachenmann, T. Schäpers, A. I. Braginski, H. Lüth, J. Appenzeller, A. A. Golubov, and A. V. Ustinov, Phys. Rev. B **61**, 12463 (2000).

[37] J. Eroms, D. Weiss, J. de Boeck, G. Borghs, and U. Zülicke, Phys. Rev. Lett. **95**, 107001 (2005).

[38] Y. Takagaki, Phys. Rev. B **57**, 4009 (1998).

[39] H. Hoppe, U. Zülicke, and G. Schön, Phys. Rev. Lett. **84**, 1804 (2000).

[40] Y. Asano and T. Yuito, Phys. Rev. B **62**, 7477 (2000).

[41] N. M. Chtchelkatchev, JETP Lett. **73**, 94 (2001).

[42] F. Giazotto, M. Governale, U. Zülicke, and F. Beltram, Phys. Rev. B **72**, 054518 (2005).

[43] C. W. J. Beenakker, Phys. Rev. Lett. **97**, 067007 (2006).

[44] E. Prada, P. San-Jose, B. Wunsch, and F. Guinea, Phys. Rev. B **75**, 113407 (2007).

[45] M. Titov and C. W. J. Beenakker, Phys. Rev. B **74**, 041401(R) (2006).

[46] G. E. Blonder, M. Tinkham, and T. M. Klapwijk, Phys. Rev. B **25**, 4515 (1982).

[47] H. B. Heersche, P. Jarillo-Herrero, J. B. Oostinga, L. M. K. Vandersypen, and A. F. Morpurgo, Nature **446**, 56 (2007).

[48] A. Shailos, W. Nativel, A. Y. Kasumov, C. Collet, M. Ferrier, S. Guéron, R. Deblock, and H. Bouchiat, Europhys. Lett. **79**, 57008 (2007).

[49] T. Ando, T. Nakanishi, and R. Saito, J. Phys. Soc. Jap. **67**, 2857 (1998).

[50] K. Wakabayashi and T. Aoki, Int. J. Mod. Phys. B **16**, 4897 (2002).

[51] A. Rycerz, J. Tworzydło, and C. W. J. Beenakker, N. Phys. **3**, 172 (2007).

[52] S. A. Wolf, D. D. Awschalom, R. A. Buhrman, J. M. Daughton, S. von Molnár, M. L. Roukes, A. Y. Chtchelkanova, and D. M. Treger, Science **294**, 1488 (2001).

[53] J. Tworzydło, I. Snyman, A. R. Akhmerov, and C. W. J. Beenakker, Phys. Rev. B **76**, 035411 (2007).

[54] V. V. Cheianov and V. I. Fal'ko, Phys. Rev. B **74**, 041403(R) (2006).

[55] N. M. R. Peres, A. H. Castro Neto, and F. Guinea, Phys. Rev. B **73**, 195411 (2006).

[56] F. Sols, F. Guinea, and A. H. Castro Neto, Phys. Rev. Lett. **99**, 166803 (2007).

[57] K. S. Novoselov, D. Jiang, F. Schedin, T. J. Booth, V. V. Khotkevich, S. V. Morozov, and A. K. Geim, Proc. Natl. Acad. Sci. **102**, 10451 (2005).

[58] A. K. Geim and K. S. Novoselov, N. Mat. **6**, 183 (2007).

[59] P. Avouris, Z. Chen, and V. Perebeinos, N. Nanotech. **2**, 605 (2007).

[60] A. H. Castro Neto, F. Guinea, N. M. R. Peres, K. S. Novoselov, and A. K. Geim, Rev. Mod. Phys. **81**, 109 (2009).

[61] D. J. Klein, Chem. Phys. Lett. **217**, 261 (1994).

[62] M. Fujita, K. Wakabayashi, K. Nakada, and K. Kusakabe, J. Phys. Soc. Jap. **65**, 1920 (1996).

[63] A. R. Akhmerov and C. W. J. Beenakker, Phys. Rev. B **77**, 085423 (2008).

[64] E. V. Castro, N. M. R. Peres, J. M. B. L. dos Santos, A. H. Castro Neto, and F. Guinea, Phys. Rev. Lett. **100**, 026802 (2008).

[65] B. Sahu, H. Min, A. H. MacDonald, and S. K. Banerjee, Phys. Rev. B **78**, 045404 (2008).

[66] E. V. Castro, N. M. R. Peres, and J. M. B. L. dos Santos, Europhys. Lett. **84**, 17001 (2008).

[67] Y. Niimi, T. Matsui, H. Kambara, K. Tagami, M. Tsukada, and H. Fukuyama, Appl. Surf. Sci. **241**, 43 (2005).

[68] Y. Kobayashi, K. Fukui, T. Enoki, K. Kusakabe, and Y. Kaburagi, Phys. Rev. B **71**, 193406 (2005).

[69] Y. Niimi, T. Matsui, H. Kambara, K. Tagami, M. Tsukada, and H. Fukuyama, Phys. Rev. B **73**, 085421 (2006).

[70] K. Nakada, M. Igami, and M. Fujita, J. Phys. Soc. Jap. **67**, 2388 (1998).

[71] J. Fernández-Rossier and J. J. Palacios, Phys. Rev. Lett. **99**, 177204 (2007).

[72] M. Ezawa, Phys. Rev. B **76**, 245415 (2007).

[73] O. V. Yazyev and M. I. Katsnelson, Phys. Rev. Lett. **100**, 047209 (2008).

[74] M. Wimmer, I. Adagideli, S. Berber, D. Tománek, and K. Richter, Phys. Rev. Lett. **100**, 177207 (2008).

[75] B. Wunsch, T. Stauber, and F. Guinea, Phys. Rev. B **77**, 035316 (2008).

[76] B. Wunsch, T. Stauber, F. Sols, and F. Guinea, Phys. Rev. Lett. **101**, 036803 (2008).

[77] I. Romanovsky, C. Yannouleas, and U. Landman, Phys. Rev. B **79**, 075311 (2009).

[78] L. A. Ponomarenko, F. Schedin, M. I. Katsnelson, R. Yang, E. W. Hill, K. S. Novoselov, and A. K. Geim, Science **320**, 356 (2008).

[79] J. Güttinger, C. Stampfer, S. Hellmüller, F. Molitor, T. Ihn, and K. Ensslin, Appl. Phys. Lett. **93**, 212102 (2008).

[80] C. Stampfer, J. Güttinger, F. Molitor, D. Graf, T. Ihn, and K. Ensslin, Applied Physics Letters **92**, 012102 (2008).

[81] J. Güttinger, C. Stampfer, F. Libisch, T. Frey, J. Burgdörfer, T. Ihn, and K. Ensslin, Phys. Rev. Lett. **103**, 046810 (2009).

[82] S. Schnez, F. Molitor, C. Stampfer, J. Güttinger, I. Shorubalko, T. Ihn, and K. Ensslin, Appl. Phys. Lett. **94**, 012107 (2009).

[83] J. Güttinger, T. Frey, C. Stampfer, T. Ihn, and K. Ensslin, Phys. Rev. Lett. **105**, 116801 (2010).

[84] N. Shima and H. Aoki, Phys. Rev. Lett. **71**, 4389 (1993).

[85] T. G. Pedersen, C. Flindt, J. Pedersen, N. A. Mortensen, A.-P. Jauho, and K. Pedersen, Phys. Rev. Lett. **100**, 136804 (2008).

[86] M. Vanević, V. M. Stojanović, and M. Kindermann, Phys. Rev. B **80**, 045410 (2009).

[87] J. A. Fürst, J. G. Pedersen, C. Flindt, N. A. Mortensen, M. Brandbyge, T. G. Pedersen, and A.-P. Jauho, New J. Phys. **11**, 095020 (2009).

[88] T. Shen, Y. Q. Wu, M. A. Capano, L. P. Rokhinson, L. W. Engel, and P. D. Ye, Appl. Phys. Lett. **93**, 122102 (2008).

[89] J. Eroms and D. Weiss, New J. Phys. **11**, 095021 (2009).

[90] J. Bai, X. Zhong, S. Jiang, Y. Huang, and X. Duan, N. Nanotech. **5**, 190 (2010).

[91] R. Balog, B. Jørgensen, L. Nilsson, M. Andersen, E. Rienks, M. Bianchi, M. Fanetti, E. Lægsgaard, A. Baraldi, S. Lizzit, Z. Sljivancanin, F. Besenbacher, B. Hammer, T. G. Pedersen, P. Hofmann, and L. Hornekaer, N. Mat. **9**, 315 (2010).

[92] L. G. Cancado, M. A. Pimenta, B. R. A. Neves, M. S. S. Dantas, and A. Jorio, Phys. Rev. Lett. **93**, 247401 (2004).

[93] A. L. V. de Parga, F. Calleja, B. Borca, M. C. G. Passeggi, J. J. Hinarejos, F. Guinea, and R. Miranda, Phys. Rev. Lett. **100**, 056807 (2008).

[94] X. Jia, M. Hofmann, V. Meunier, B. G. Sumpter, J. Campos-Delgado, J. M. Romo-Herrera, H. Son, Y. Hsieh, A. Reina, J. Kong, M. Terrones, and M. S. Dresselhaus, Science **323**, 1701 (2009).

[95] Ç. Ö. Girit, J. C. Meyer, R. Erni, M. D. Rossell, C. Kisielowski, L. Yang, C.-H. Park, M. F. Crommie, M. L. Cohen, S. G. Louie, and A. Zettl, Science **323**, 1705 (2009).

[96] Z. Liu, K. Suenaga, P. J. F. Harris, and S. Iijima, Phys. Rev. Lett. **102**, 015501 (2009).

[97] C. Casiraghi, A. Hartschuh, H. Qian, S. Piscanec, C. Georgi, A. Fasoli, K. S. Novoselov, D. M. Basko, and A. C. Ferrari, Nano Lett. **9**, 1433 (2009).

[98] Y.-J. Xu and J.-Q. Li, Chem. Phys. Lett. **400**, 406 (2004).

[99] D. Jiang, B. G. Sumpter, and S. Dai, J. Phys. Chem. B **110**, 23628 (2006).

[100] F. Cervantes-Sodi, G. Csányi, S. Piscanec, and A. C. Ferrari, Phys. Rev. B **77**, 165427 (2008).

[101] B. Huang, F. Liu, J. Wu, B. Gu, and W. Duan, Phys. Rev. B **77**, 153411 (2008).

[102] S. Schnez, K. Ensslin, M. Sigrist, and T. Ihn, Phys. Rev. B **78**, 195427 (2008).

[103] M. Ezawa, Physica E **42**, 703 (2010).

[104] A. R. Akhmerov, J. H. Bardarson, A. Rycerz, and C. W. J. Beenakker, Phys. Rev. B **77**, 205416 (2008).

[105] K. Sasaki, S. Murakami, and R. Saito, Appl. Phys. Lett. **88**, 113110 (2006).

[106] K. Sasaki, Y. Shimomura, Y. Takane, and K. Wakabayashi, Phys. Rev. Lett. **102**, 146806 (2009).

[107] R. Peierls, Zeit. Phys. **80**, 763 (1933).

[108] E. R. Mucciolo, A. H. Castro Neto, and C. H. Lewenkopf, Phys. Rev. B **79**, 075407 (2009).

[109] E. Anderson, Z. Bai, C. Bischof, S. Blackford, J. Demmel, J. Dongarra, J. Du Croz, A. Greenbaum, S. Hammarling, A. McKenney, and D. C. Sorensen, *LAPACK Users' Guide* (Society for Industrial Mathematics, 1987), 3 edn.

[110] N. E. Gibbs, J. Poole, and P. K. Stockmeyer, SIAM J. Num. Anal. **13**, 236 (1976).

[111] R. B. Lehoucq, D. C. Sorensen, and C. Yang, *Arpack User's Guide: Solution of Large-Scale Eigenvalue Problems With Implicitly Restorted Arnoldi Methods* (Soc for Industrial & Applied Math, 1998).

[112] P. R. Amestoy, I. S. Duff, J.-Y. L'Excellent, and J. Koster, SIAM J. Mat. Anal. and Appl. **23**, 15 (2001).

[113] K. Sasaki, K. Sato, R. Saito, J. Jiang, S. Onari, and Y. Tanaka, Phys. Rev. B **75**, 235430 (2007).

[114] D. A. Bahamon, A. L. C. Pereira, and P. A. Schulz, Phys. Rev. B **79**, 125414 (2009).

[115] S. C. Kim, P. S. Park, and S.-R. E. Yang, Phys. Rev. B **81**, 085432 (2010).

[116] R. J. Bell and P. Dean, Disc. Far. Soc. **50**, 55 (1970).

[117] R. J. Bell, Rep. Prog. Phys. **35**, 1315 (1972).

[118] F. Libisch, S. Rotter, J. Güttinger, C. Stampfer, and J. Burgdörfer, Phys. Rev. B **81**, 245411 (2010).

[119] J. Wurm, A. Rycerz, I. Adagideli, M. Wimmer, K. Richter, and H. U. Baranger, Phys. Rev. Lett. **102**, 056806 (2009).

[120] F. Libisch, C. Stampfer, and J. Burgdörfer, Phys. Rev. B **79**, 115423 (2009).

[121] M. L. Mehta, *Random Matrices* (Elsevier, Amsterdam, 2004).

[122] K. Harigaya, Chem. Phys. Lett. **340**, 123 (2001).

[123] K. Harigaya and T. Enoki, Chem. Phys. Lett. **351**, 128 (2002).

[124] L. Brey, H. A. Fertig, and S. Das Sarma, Phys. Rev. Lett. **99**, 116802 (2007).

[125] J. Martin, N. Akerman, G. Ulbricht, T. Lohmann, J. H. Smet, K. von Klitzing, and A. Yacoby, N. Phys. **4**, 144 (2008).

[126] E. H. Lee, K. Balasubramanian, R. T. Weitz, M. Burghard, and K. Kern, N. Nanotech. **3**, 486 (2008).

[127] S. Heydrich, M. Hirmer, C. Preis, T. Korn, J. Eroms, D. Weiss, and C. Schüller, arXiv:1006.2067 (2010).

[128] H. de Raedt and M. I. Katsnelson, JETP Lett. **88**, 607 (2009).

[129] G. E. Volovik, JETP Lett. **70**, 609 (1999).

[130] L. Fu and C. L. Kane, Phys. Rev. Lett. **100**, 096407 (2008).

[131] J. D. Sau, R. M. Lutchyn, S. Tewari, and S. Das Sarma, Phys. Rev. Lett. **104**, 040502 (2010).

[132] A. Y. Kitaev, Physics-Uspekhi **44**, 131 (2001).

[133] L. Fu and C. L. Kane, Phys. Rev. B **79**, 161408(R) (2009).

[134] M. Wimmer, A. R. Akhmerov, M. V. Medvedyeva, J. Tworzydło, and C. W. J. Beenakker, Phys. Rev. Lett. **105**, 046803 (2010).

[135] C. Caroli, P. G. De Gennes, and J. Matricon, Phys. Lett. **9**, 307 (1964).

[136] Y. E. Kraus, A. Auerbach, H. A. Fertig, and S. H. Simon, Phys. Rev. Lett. **101**, 267002 (2008).

[137] J. D. Sau, R. M. Lutchyn, S. Tewari, and S. Das Sarma, Phys. Rev. B **82**, 094522 (2010).

[138] L. Fu, Phys. Rev. Lett. **104**, 056402 (2010).

[139] D. A. Ivanov, Phys. Rev. Lett. **86**, 268 (2001).

[140] A. Stern, F. von Oppen, and E. Mariani, Phys. Rev. B **70**, 205338 (2004).

[141] N. Read, Phys. Rev. B **79**, 045308 (2009).

[142] V. Gurarie and L. Radzihovsky, Ann. Phys. **322**, 2 (2007).

[143] F. Hassler, A. R. Akhmerov, C.-Y. Hou, and C. W. J. Beenakker, New J. Phys. **12**, 125002 (2010).

[144] L. Fu and C. L. Kane, Phys. Rev. Lett. **102**, 216403 (2009).

[145] A. R. Akhmerov, J. Nilsson, and C. W. J. Beenakker, Phys. Rev. Lett. **102**, 216404 (2009).

[146] E. Grosfeld, B. Seradjeh, and S. Vishveshwara, arXiv:1004.2295 (2010).

[147] S. Das Sarma, C. Nayak, and S. Tewari, Phys. Rev. B **73**, 220502(R) (2006).

[148] S. Tewari, S. Das Sarma, C. Nayak, C. Zhang, and P. Zoller, Phys. Rev. Lett. **98**, 010506 (2007).

[149] P. Ghaemi and F. Wilczek, arXiv:0709.2626 (2007).

[150] D. L. Bergman and K. Le Hur, Phys. Rev. B **79**, 184520 (2009).

[151] G. W. Semenoff and P. Sodano, J. Phys. B **40**, 1479 (2007).

[152] C. J. Bolech and E. Demler, Phys. Rev. Lett. **98**, 237002 (2007).

[153] S. Tewari, C. Zhang, S. Das Sarma, C. Nayak, and D. Lee, Phys. Rev. Lett. **100**, 027001 (2008).

[154] J. M. Byers and M. E. Flatté, Phys. Rev. Lett. **74**, 306 (1995).

[155] S. G. den Hartog, C. M. A. Kapteyn, B. J. van Wees, T. M. Klapwijk, and G. Borghs, Phys. Rev. Lett. **77**, 4954 (1996).

[156] T. Martin, Phys. Lett. A **220**, 137 (1996).

[157] J. Cayssol, Phys. Rev. Lett. **100**, 147001 (2008).

[158] C. Benjamin and J. K. Pachos, Phys. Rev. B **78**, 235403 (2008).

[159] M. König, S. Wiedmann, C. Brüne, A. Roth, H. Buhmann, L. W. Molenkamp, X.-L. Qi, and S.-C. Zhang, Science **318**, 766 (2007).

[160] M. König, H. Buhmann, L. W. Molenkamp, T. Hughes, C.-X. Liu, X.-L. Qi, and S.-C. Zhang, J. Phys. Soc. Jap. **77**, 031007 (2008).

[161] D. Hsieh, D. Qian, L. Wray, Y. Xia, Y. S. Hor, R. J. Cava, and M. Z. Hasan, Nature **452**, 970 (2008).

[162] L. Fu, C. L. Kane, and E. J. Mele, Phys. Rev. Lett. **98**, 106803 (2007).

[163] J. E. Moore and L. Balents, Phys. Rev. B **75**, 121306(R) (2007).

[164] R. Roy, Phys. Rev. B **79**, 195322 (2009).

[165] A. Y. Kasumov, O. V. Kononenko, V. N. Matveev, T. B. Borsenko, V. A. Tulin, E. E. Vdovin, and I. I. Khodos, Phys. Rev. Lett. **77**, 3029 (1996).

[166] Y. M. Blanter and M. Büttiker, Phys. Rep. **336**, 1 (2000).

[167] M. J. M. de Jong and C. W. J. Beenakker, Phys. Rev. B **49**, 16070 (1994).

[168] M. P. Anantram and S. Datta, Phys. Rev. B **53**, 16390 (1996).

[169] H.-J. Kwon, Low Temp. Phys. **30**, 613 (2004).

[170] A. L. Fauchére, G. B. Lesovik, and G. Blatter, Phys. Rev. B **58**, 11177 (1998).

[171] I. P. Radu, J. B. Miller, C. M. Marcus, M. A. Kastner, L. N. Pfeiffer, and K. W. West, Science **320**, 899 (2008).

[172] M. Dolev, M. Heiblum, V. Umansky, A. Stern, and D. Mahalu, Nature **452**, 829 (2008).

[173] R. L. Willett, L. N. Pfeiffer, and K. W. West, Proc. Natl. Acad. Sci. **106**, 8853 (2009).

[174] S. Das Sarma, M. Freedman, and C. Nayak, Phys. Rev. Lett. **94**, 166802 (2005).

[175] A. Stern and B. I. Halperin, Phys. Rev. Lett. **96**, 016802 (2006).

[176] P. Bonderson, A. Y. Kitaev, and K. Shtengel, Phys. Rev. Lett. **96**, 016803 (2006).

[177] P. Bonderson, M. Freedman, and C. Nayak, Ann. Phys. **324**, 787 (2008).

[178] M. Greiter, X. G. Wen, and F. Wilczek, Nucl. Phys. B **374**, 567 (1992).

[179] H. Zhang, C.-X. Liu, X.-L. Qi, X. Dai, Z. Fang, and S.-C. Zhang, N. Phys. **5**, 438 (2009).

[180] Y. Xia, D. Qian, D. Hsieh, L. Wray, A. Pal, H. Lin, A. Bansil, D. Grauer, Y. S. Hor, R. J. Cava, and M. Z. Hasan, N. Phys. **5**, 398 (2009).

[181] J. Nilsson, A. R. Akhmerov, and C. W. J. Beenakker, Phys. Rev. Lett. **101**, 120403 (2008).

[182] P. Fendley, M. P. A. Fisher, and C. Nayak, Phys. Rev. B **75**, 045317 (2007).

[183] J. E. Mooij and Y. V. Nazarov, N. Phys. **2**, 169 (2006).

[184] G. Koren, Y. Mor, A. Auerbach, and E. Polturak, Phys. Rev. B **76**, 134516 (2007).

[185] B. I. Halperin, Phys. Rev. B **25**, 2185 (1982).

[186] M. Büttiker, Phys. Rev. B **38**, 9375 (1988).

[187] T. Senthil, J. B. Marston, and M. P. A. Fisher, Phys. Rev. B **60**, 4245 (1999).

[188] T. Senthil and M. P. A. Fisher, Phys. Rev. B **61**, 9690 (2000).

[189] A. Vishwanath, Phys. Rev. Lett. **87**, 217004 (2001).

[190] M. Matsumoto and M. Sigrist, J. Phys. Soc. Jap. **68**, 994 (1999).

[191] H.-J. Kwon, V. M. Yakovenko, and K. Sengupta, Synth. Met. **133-134**, 27 (2003).

[192] J. R. Kirtley, C. Kallin, C. W. Hicks, E.-A. Kim, Y. Liu, K. A. Moler, Y. Maeno, and K. D. Nelson, Phys. Rev. B **76**, 014526 (2007).

[193] C. Kallin and A. J. Berlinsky, J. Phys. **21**, 164210 (2009).

[194] A. P. Schnyder, S. Ryu, A. Furusaki, and A. W. W. Ludwig, Phys. Rev. B **78**, 195125 (2008).

[195] M. Sato, Y. Takahashi, and S. Fujimoto, Phys. Rev. Lett. **103**, 020401 (2009).

[196] P. A. Lee, arXiv:0907.2681 (2009).

[197] M. Sigrist and D. F. Agterberg, Prog. Theor. Phys. **102**, 965 (1999).

[198] A. Bouhon and M. Sigrist, New J. Phys. **12**, 043031 (2010).

[199] Y. S. Barash, A. M. Bobkov, and M. Fogelström, Phys. Rev. B **64**, 214503 (2001).

[200] H.-J. Kwon, K. Sengupta, and V. M. Yakovenko, Euro. Phys. J. B **37**, 349 (2003).

[201] M. Stone and R. Roy, Phys. Rev. B **69**, 184511 (2004).

[202] B. Béri, J. N. Kupferschmidt, C. W. J. Beenakker, and P. W. Brouwer, Phys. Rev. B **79**, 024517 (2009).

[203] K. T. Law, P. A. Lee, and T. K. Ng, Phys. Rev. Lett. **103**, 237001 (2009).

[204] B. Béri, Phys. Rev. B **79**, 245315 (2009).

[205] B. Béri, Phys. Rev. B **79**, 214506 (2009).

[206] H. Nobukane, A. Tokuno, M. Toyoki, and S. Tanda, arXiv:0906.3644 (2009).

[207] R. M. Lutchyn, J. D. Sau, and S. Das Sarma, Phys. Rev. Lett. **105**, 077001 (2010).

[208] Y. Oreg, G. Refael, and F. von Oppen, Phys. Rev. Lett. **105**, 177002 (2010).

[209] G. E. Volovik, JETP Lett. **66**, 522 (1997).

[210] J. Alicea, Y. Oreg, G. Refael, F. von Oppen, and M. P. A. Fisher, arXiv:1006.4395 (2010).

[211] J. D. Sau, S. Tewari, and S. Das Sarma, Phys. Rev. A **82**, 052322 (2010).

[212] J. A. van Dam, Y. V. Nazarov, E. P. A. M. Bakkers, S. De Franceschi, and L. P. Kouwenhoven, Nature **442**, 667 (2006).

[213] J. Linder, Y. Tanaka, T. Yokoyama, A. Sudbø, and N. Nagaosa, Phys. Rev. Lett. **104**, 067001 (2010).

[214] V. Shivamoggi, G. Refael, and J. E. Moore, Phys. Rev. B **82**, 041405 (2010).

[215] T. Neupert, S. Onoda, and A. Furusaki, Phys. Rev. Lett. **105**, 206404 (2010).

[216] K. Flensberg, Phys. Rev. B **82**, 180516 (2010).

[217] M. Z. Hasan and C. L. Kane, Rev. Mod. Phys. **82**, 3045 (2010).

[218] X.-L. Qi and S.-C. Zhang, arXiv:1008.2026 (2010).

[219] F. Merz and J. T. Chalker, Phys. Rev. B **65**, 054425 (2002).

[220] M. Bocquet, D. Serban, and M. R. Zirnbauer, Nucl. Phys. B **578**, 628 (2000).

[221] P. W. Brouwer, A. Furusaki, I. A. Gruzberg, and C. Mudry, Phys. Rev. Lett. **85**, 1064 (2000).

[222] P. W. Brouwer, A. Furusaki, and C. Mudry, Phys. Rev. B **67**, 014530 (2003).

[223] O. Motrunich, K. Damle, and D. A. Huse, Phys. Rev. B **63**, 224204 (2001).

[224] I. A. Gruzberg, N. Read, and S. Vishveshwara, Phys. Rev. B **71**, 245124 (2005).

[225] F. Evers and A. D. Mirlin, Rev. Mod. Phys. **80**, 1355 (2008).

[226] M. Wimmer and K. Richter, J. Comp. Phys. **228**, 8548 (2009).

[227] R. M. Lutchyn, T. Stanescu, and S. Das Sarma, arXiv:1008.0629 (2010).

[228] A. C. Potter and P. A. Lee, Phys. Rev. Lett. **105**, 227003 (2010).

[229] M. Büttiker and T. M. Klapwijk, Phys. Rev. B **33**, 5114 (1986).

[230] C. Benjamin and J. K. Pachos, Phys. Rev. B **81**, 085101 (2010).

[231] C. de C. Chamon, D. E. Freed, S. A. Kivelson, S. L. Sondhi, and X. G. Wen, Phys. Rev. B **55**, 2331 (1997).

[232] E. Fradkin, C. Nayak, A. M. Tsvelik, and F. Wilczek, Nucl. Phys. B **516**, 704 (1998).

[233] W. Bishara, P. Bonderson, C. Nayak, K. Shtengel, and J. K. Slingerland, Phys. Rev. B **80**, 155303 (2009).

[234] G. E. Volovik, *The Universe in a Helium Droplet* (Oxford University Press, 2003).

[235] A. L. Fetter and J. D. Walecka, *Quantum Theory of Many-Particle Systems* (Dover, New-York, 1972).

[236] H. U. Baranger and A. D. Stone, Phys. Rev. B **40**, 8169 (1989).

[237] C. L. Kane and M. P. A. Fisher, Phys. Rev. B **46**, 15233 (1992).

[238] M. Oshikawa, C. de C. Chamon, and I. Affleck, J. Stat. Mech. **2006**, P02008 (2006).

[239] R. Guyon, P. Devillard, T. Martin, and I. Safi, Phys. Rev. B **65**, 153304 (2002).

[240] E.-A. Kim, M. J. Lawler, S. Vishveshwara, and E. Fradkin, Phys. Rev. B **74**, 155324 (2006).

[241] P. Di Francesco, P. Mathieu, and D. Sénéchal, *Conformal field theory* (Springer, 1997).

[242] B. Rosenow, B. I. Halperin, S. H. Simon, and A. Stern, Phys. Rev. Lett. **100**, 226803 (2008).

[243] B. J. Overbosch and X. G. Wen, arXiv:0706.4339 (2007).

[244] B. Rosenow, B. I. Halperin, S. H. Simon, and A. Stern, Phys. Rev. B **80**, 155305 (2009).

[245] W. Bishara and C. Nayak, Phys. Rev. B **80**, 155304 (2009).

[246] J. B. Zuber and C. Itzykson, Phys. Rev. D **15**, 2875 (1977).

[247] A. O. Gogolin, A. A. Nersesyan, and A. M. Tsvelik, *Bosonization and strongly correlated systems* (Cambridge University Press, 2004).

[248] D. Allen and D. Sénéchal, Phys. Rev. B **61**, 12134 (2000).

[249] J. von Delft and H. Schoeller, Ann. Phys. **7**, 225 (1998).

[250] A. A. Belavin, A. M. Polyakov, and A. B. Zamolodchikov, Nucl. Phys. B **241**, 333 (1984).

[251] P. Ginsparg, arXiv:hep-th/9108028 (1989).

[252] E. Brezin, *Fields, Strings and Critical Phenomena* (Elsevier Science & Technology, 1989).

[253] C. Nayak and F. Wilczek, Nucl. Phys. B **479**, 529 (1996).

[254] C. de C. Chamon, D. E. Freed, and X. G. Wen, Phys. Rev. B **53**, 4033 (1996).

[255] K.-H. Rehren and B. Schroer, Phys. Lett. B **198**, 84 (1987).

[256] C. Bena and C. Nayak, Phys. Rev. B **73**, 155335 (2006).

[257] J. Alicea, Phys. Rev. B **81**, 125318 (2010).

[258] M. Duckheim and P. W. Brouwer, arXiv:1011.5839 (2010).

[259] S. B. Chung, H.-J. Zhang, X.-L. Qi, and S.-C. Zhang, arXiv:1011.6422 (2010).

[260] J. Nilsson and A. R. Akhmerov, Phys. Rev. B **81**, 205110 (2010).

[261] J. D. Sau, S. Tewari, and S. Das Sarma, arXiv:1004.4702 (2010).

[262] Y. Makhlin, G. Schön, and A. Shnirman, Rev. Mod. Phys. **73**, 357 (2001).

[263] S. Sachdev, *Quantum Phase Transitions* (Cambridge University Press, 2000).

[264] E. Fradkin and L. Susskind, Phys. Rev. D **17**, 2637 (1978).

[265] J. B. Kogut, Rev. Mod. Phys. **51**, 659 (1979).

[266] C. L. Kane and M. P. A. Fisher, Phys. Rev. B **46**, 7268 (1992).

[267] G. D. Mahan, *Many particle physics, Third edition* ([Indiana Univ., Dept. of Physics], 1980).

[268] C. Cohen-Tannoudji, J. Dupont-Roc, and G. Grynberg, *Atom-Photon Interactions: Basic Processes and Applications* (Wiley-Interscience, 1998).

[269] R. Shankar, Int. J. Mod. Phys. B **4**, 2371 (1990).

[270] M. Abramowitz and I. A. Stegun, *Handbook of Mathematical Functions: with Formulas, Graphs, and Mathematical Tables* (Dover Publications, 1965).

[271] G. E. Volovik, JETP Lett. **65**, 217 (1997).

[272] R. Fazio and H. van der Zant, Phys. Rep. **355**, 235 (2001).

[273] A. Wallraff, A. Lukashenko, J. Lisenfeld, A. Kemp, M. V. Fistul, Y. Koval, and A. V. Ustinov, Nature **425**, 155 (2003).

[274] W. J. Elion, J. J. Wachters, L. L. Sohn, and J. E. Mooij, Phys. Rev. Lett. **71**, 2311 (1993).

[275] C. H. van der Wal, A. C. J. ter Haar, F. K. Wilhelm, R. N. Schouten, C. J. P. M. Harmans, T. P. Orlando, S. Lloyd, and J. E. Mooij, Science **290**, 773 (2000).

[276] R. P. Tiwari and D. Stroud, Phys. Rev. B **76**, 220505(R) (2007).

[277] J. R. Friedman and D. V. Averin, Phys. Rev. Lett. **88**, 050403 (2002).

[278] A. Stern, Ann. Phys. **323**, 204 (2008).

[279] A. R. Akhmerov, Phys. Rev. B **82**, 020509(R) (2010).

[280] M. Stone and S. B. Chung, Phys. Rev. B **73**, 014505 (2006).

[281] S. B. Bravyi and A. Y. Kitaev, Ann. Phys. **298**, 210 (2002).

[282] M. Freedman, C. Nayak, and K. Walker, Phys. Rev. B **73**, 245307 (2006).

[283] P. Bonderson, S. Das Sarma, M. Freedman, and C. Nayak, arXiv:1003.2856 (2010).

[284] Y. Ran, P. Hosur, and A. Vishwanath, arXiv:1003.1964 (2010).

[285] G. Möller, N. R. Cooper, and V. Gurarie, arXiv:1006.0924 (2010).

[286] P. Bonderson, D. J. Clarke, C. Nayak, and K. Shtengel, Phys. Rev. Lett. **104**, 180505 (2010).

[287] S. B. Bravyi and A. Y. Kitaev, Phys. Rev. A **71**, 022316 (2005).

[288] S. B. Bravyi, Phys. Rev. A **73**, 042313 (2006).

[289] L. D. Landau and L. M. Lifshitz, *Quantum Mechanics Non-Relativistic Theory, Third Edition: Volume 3* (Butterworth-Heinemann, 1981).

Summary

The rising sun creates a narrow strip of light at the horizon, separating the earth from the sky — regardless of the profile of the horizon. Similarly, the electronic states studied in this thesis appear at the edge of a material not because of a particular structure of the edge, but because of a fundamental difference between the material inside and empty space outside.

The first part of the thesis is dedicated to edge states in graphene, a single sheet of graphite with carbon atoms on a honeycomb lattice. It was originally thought that only a particular type of boundary, the zigzag edge, has states confined to the edge. However the analysis of chapter two shows that, instead, edge states appear generically whenever the honeycomb lattice is terminated. The key ingredient of this analysis is the formulation of the most general boundary condition of the Dirac equation (which was unknown, although the Dirac equation entered physics early in the 20th century).

The remainder of the first part addresses observable consequences of edge states. In the third chapter we show how to use a combination of superconductivity and strong magnetic fields to probe the elusive valley polarization of an edge state. (The band structure of graphene has two valleys, related by time reversal symmetry.) Next, in chapter four, we present an analytical theory of the current switching effect (known as the "valley valve"), which had been discovered in computer simulations. This analysis revealed an unexpected difference between zigzag and anti-zigzag nanoribbons, which cannot be described by the Dirac equation. Finally in chapter five, we propose a method for direct detection of edge states in a graphene quantum dot, including also the perturbing effects of disorder and next-nearest-neighbor hopping.

In the second part of the thesis the focus shifts from edge states in graphene to Majorana edge states in superconductors. Both types of edge states appear from fundamental considerations, regardless of the microscopic properties of the edge. The special property of Majorana particles is that they are their own antiparticles, and consequently are chargeless and spinless. Majorana edge states are predicted to appear in superconductors with an unusual "chiral p-wave" pairing symmetry. Conventional s-wave superconductors can be used as well, in combination with materials having strong spin-orbit coupling (topological insulators). Majorana particles are in demand because they are predicted to have very long coherence times. Our goal in this part of the thesis is to identify experimental signatures of Majorana edge states, as well as to investigate their potential for quantum computation.

In the sixth chapter we analyze the reasons for the protection against decoherence of Majorana particles and show that the key principle is conservation of particle number parity. Contrary to concerns raised in the literature, thermal excitations do not lead to decoherence. This is of crucial importance, since suppression of thermal excitations would require unrealistically low temperatures of 10^{-4} K. In the following two chapters we propose methods for detection of Majorana edge states. Since they are charge neutral, the central problem is how to couple them to an electrical current. In chapter seven we show that a Cooper pair is split into two electrons when it is injected through a pair of Majorana states. In the next chapter we propose a "Dirac-to-Majorana" converter, which reversibly transforms an electrical current carried by ordinary (Dirac) electrons into a neutral current carried by Majorana edge states. (The charge deficit is absorbed by the superconducting condensate.) This idea was independently proposed by Liang Fu and Charles Kane, and appeared in an episode of the American sitcom *The Big Bang Theory*.

In chapter nine we apply these ideas to chiral *p*-wave superconductors. We predict that if two domains of opposite chirality are brought into close contact, their joint edge starts conducting electrical current even though a single edge carries only a charge-neutral current. In chapter ten we study the topological phase transition into a phase which supports Majorana states. We find that the transition point in a wire geometry is signaled by a peak of quantized thermal conductance and quantized electrical shot noise — without any of the finite size effects that usually accompany a phase transition. In chapters eleven and twelve we use a formal correspondence with the Ising model in a transverse field to analyze the non-Abelian statistics of Majorana particles. (These are the technically most involved chapters of the thesis.) Finally, in chapter thirteen we present a new scheme for quantum computation with Majorana particles, based on the Aharonov-Casher effect (the dual of the more familiar Aharonov-Bohm effect). The advantage of this new scheme over earlier proposals is that it is insensitive to thermal excitations (in accord with the findings of chapter six).

Samenvatting

De opgaande zon creëert een smalle band van licht aan de horizon, die de aarde scheidt van de lucht — ongeacht het profiel van de horizon. Op een soortgelijke wijze, verschijnen de elektronische toestanden die in dit proefschrift onderzocht worden aan de rand van een materiaal, niet omdat die rand een bijzondere structuur zou hebben, maar omdat er een fundamenteel verschil is tussen het materiaal binnen en de lege ruimte buiten.

Het eerste deel van het proefschrift is gewijd aan randtoestanden in grafeen, een enkele laag grafiet met koolstofatomen op een honingraatrooster. Het was oorspronkelijk gedacht dat alleen een speciaal type begrenzing, de zigzagrand, toestanden aan de rand kan binden. Echter, de analyse in hoofdstuk twee toont aan, dat randtoestanden in het algemeen verschijnen waar het honingraatrooster eigdigt. Het kernpunt van deze analyse is de formulering van de meest algemene randvoorwaarde van de Diracvergelijking (die onbekend was, hoewel de Diracvergelijking al vroeg in de 20ste eeuw haar intrede deed in de natuurkunde).

De rest van het eerste deel behandelt waarneembare consequenties van randtoestanden. In het derde hoofdstuk laten we zien hoe een combinatie van supergeleiding en sterke magneetvelden de verborgen "valley" polarisatie van een randtoestand kan onthullen. (De bandstructuur van grafeen heeft twee "valleys", gerelateerd door tijdsomkeersymmetrie.) Vervolgens, in hoofdstuk vier, presenteren we een analytische theorie van een stroomschakeleffect (bekend als de "valley valve"), dat in computersimulaties ontdekt was. Deze analyse onthulde een onverwacht verschil tussen zigzag en anti-zigzag nanodraden, wat niet met de Diracvergelijking beschreven kan worden. Tenslotte, in hoofdstuk vijf, stellen we een methode voor om randtoestanden direct te detecteren in een quantum dot in grafeen, rekening houdend met de verstorende effecten van wanorde en tweede-naaste-buur koppelingen.

In het tweede deel van het proefschrift verschuift de focus van randtoestanden in grafeen naar Majorana randtoestanden in supergeleiders. Beide typen van randtoestanden verschijnen ten gevolge van fundamentele overwegingen, ongeacht de microscopische eigenschappen van de rand. De bijzondere eigenschap van Majorana deeltjes is dat zij hun eigen antideeltje zijn, en dientengevolge geen lading of spin hebben. Majorana randtoestanden zijn voorspeld in supergeleiders met een ongebruikelijke "chirale p-golf" paarsymmetrie. Gewone s-golf supergeleiders kunnen ook gebruikt worden, in combinatie met materialen die een sterke spin-baan koppeling hebben (topologische isolatoren). Majorana deeltjes zijn aantrekkelijk omdat ze naar verwachting een zeer lange

coherentie-tijd hebben. Ons doel in dit deel van het proefschrift is om experimentele signalen van Majorana randtoestanden te identificeren, alsook om hun potentieel te onderzoeken voor quantumcomputers.

In hoofdstuk zes analyseren we de redenen voor de bescherming tegen decoherentie van Majorana deeltjes. We laten zien dat het sleutelprincipe het behoud is van de pariteit van het deeltjesaantal. In tegenstelling tot bezorgde verwachtingen in de literatuur, leiden thermische excitaties niet tot decoherentie. Dit is van cruciaal belang, omdat het onderdrukken van thermische excitaties een onrealistisch lage temperatuur van 10^{-4} K zou vereisen. In de volgende twee hoofdstukken stellen we methodes voor om Majorana randtoestanden te detecteren. Aangezien zij ladingsneutraal zijn, is het centrale probleem hoe ze te koppelen aan een elektrische stroom. In hoofdstuk zeven laten we zien dat een Cooper-paar zich opslitst in twee elektronen als het geïnjecteerd wordt in een tweetal Majorana toestanden. In het volgende hoofdstuk stellen we een "Dirac-tot-Majorana" converter voor, die op reversibele wijze een elektrische stroom van gewone (Dirac) elektronen transformeert in een neutrale stroom van Majorana randtoestanden. (Het ladingstekort wordt geabsorbeerd door het supergeleidende condensaat.) Dit idee is ook voorgesteld door Liang Fu en Charles Kane, en verscheen in een aflevering van de Amerikaanse sitcom *The Big Bang Theory*.

In hoofdstuk negen passen we deze ideeën toe op chirale p-golf supergeleiders. We voorspellen dat als twee domeinen van tegengestelde chiraliteit in contact worden gebracht, hun gezamenlijke rand een elektrische stroom geleidt — terwijl de afzonderlijke randen slechts een ladingsneutrale stroom kunnen dragen. In hoofdstuk tien bestuderen we de topologische fase-overgang naar een fase die Majorana toestanden bevat. We vinden dat het overgangspunt in een draad-geometrie gekenmerkt wordt door een piek van gequantiseerde thermische geleiding en gequantiseerde elektrische hagelruis — zonder de effecten van een eindige afmeting die gewoonlijk een fase-overgang vergezellen. In hoofdstukken elf en twaalf benutten we een formele overeenkomst met het Ising-model in een transversaal veld om de niet-Abelse statistiek te analyseren van Majorana deeltjes. (Dit zijn de twee technisch meest ingewikkelde hoofdstukken van het proefschrift.) Tenslotte, in hoofdstuk dertien, presenteren we een nieuw schema voor een quantum computer gebaseerd op Majorana deeltjes, gebruik makend van het Aharonov-Casher effect (het duale van het meer bekende Aharonov-Bohm effect). Het voordeel van dit nieuwe schema is dat het ongevoelig is voor thermische excitaties (in overeenstemming met de bevindingen van hoofdstuk zes).

List of Publications

1. *Universal temperature dependence of the conductivity of a strongly disordered granular metal,* A. R. Akhmerov and A. S. Ioselevich, JETP Letters **83**, 251 (2006).

2. *Pseudo-diffusive conduction at the Dirac point of a normal-superconductor junction in graphene,* A. R. Akhmerov and C. W. J. Beenakker, Phys. Rev. B **75**, 045426 (2007).

3. *Detection of valley polarization in graphene by a superconducting contact,* A. R. Akhmerov and C. W. J. Beenakker, Phys. Rev. Lett. **98**, 157003 (2007) [Chapter 3].

4. *Valley-isospin dependence of the quantum Hall effect in a graphene p-n junction,* J. Tworzydło, I. Snyman, A. R. Akhmerov, and C. W. J. Beenakker, Phys. Rev. B **76**, 035411 (2007).

5. *Correspondence between Andreev reflection and Klein tunneling in bipolar graphene,* C. W. J. Beenakker, A. R. Akhmerov, P. Recher, and J. Tworzydło, Phys. Rev. B **77**, 075409 (2008).

6. *Boundary conditions for Dirac fermions on a terminated honeycomb lattice,* A. R. Akhmerov and C. W. J. Beenakker, Phys. Rev. B **77**, 085423 (2008) [Chapter 2].

7. *Theory of the valley-valve effect in graphene nanoribbons,* A. R. Akhmerov, J. H. Bardarson, A. Rycerz, and C. W. J. Beenakker, Phys. Rev. B **77**, 205416 (2008) [Chapter 4].

8. *Splitting of a Cooper pair by a pair of Majorana bound states,* J. Nilsson, A. R. Akhmerov, and C. W. J. Beenakker, Phys. Rev. Lett. **101**, 120403 (2008) [Chapter 7].

9. *Nonalgebraic length dependence of transmission through a chain of barriers with a Levy spacing distribution,* C. W. J. Beenakker, C. W. Groth, and A. R. Akhmerov, Phys. Rev. B **79**, 024204 (2009).

10. *Electrically detected interferometry of Majorana fermions in a topological insulator,* A. R. Akhmerov, J. Nilsson, and C. W. J. Beenakker, Phys. Rev. Lett. **102**, 216404 (2009) [Chapter 8].

11. *Quantum Goos-Hänchen effect in graphene,* C. W. J. Beenakker, R. A. Sepkhanov, A. R. Akhmerov, and J. Tworzydło, Phys. Rev. Lett. **102**, 146804 (2009).

12. *Pseudodiffusive transmission of nodal Dirac fermions through a clean d-wave superconductor,* J. K. Asbóth, A. R. Akhmerov, A. C. Berceanu, and C. W. J. Beenakker, Phys. Rev. B **80**, 224517 (2009).

13. *Theory of the topological Anderson insulator,* C. W. Groth, M. Wimmer, A. R. Akhmerov, J. Tworzydło, and C. W. J. Beenakker, Phys. Rev. Lett. **103**, 196805 (2009).

14. *Switching of electrical current by spin precession in the first Landau level of an inverted-gap semiconductor,* A. R. Akhmerov, C. W. Groth, J. Tworzydło, and C. W. J. Beenakker, Phys. Rev. B **80**, 195320 (2009).

15. *Domain wall in a chiral p-wave superconductor: a pathway for electrical current,* I. Serban, B. Béri, A. R. Akhmerov, and C. W. J. Beenakker, Phys. Rev. Lett. **104**, 147001 (2010) [Chapter 9].

16. *Theory of non-Abelian Fabry-Perot interferometry in topological insulators,* J. Nilsson and A. R. Akhmerov, Phys. Rev. B **81**, 205110 (2010) [Chapter 11].

17. *Absence of a metallic phase in charge-neutral graphene with a random gap,* J. H. Bardarson, M. V. Medvedyeva, J. Tworzydło, A. R. Akhmerov, and C. W. J. Beenakker, Phys. Rev. B **81**, 121414(R) (2010).

18. *Majorana bound states without vortices in topological superconductors with electrostatic defects,* M. Wimmer, A. R. Akhmerov, M. V. Medvedyeva, J. Tworzydło, and C. W. J. Beenakker, Phys. Rev. Lett. **105**, 046803 (2010).

19. *Flat-lens focusing of electrons on the surface of a topological insulator,* F. Hassler, A. R. Akhmerov, and C. W. J. Beenakker, Phys. Rev. B **82**, 125423 (2010).

20. *Robustness of edge states in graphene quantum dots,* M. Wimmer, A. R. Akhmerov, and F. Guinea, Phys. Rev. B **82**, 045409 (2010) [Chapter 5].

21. *Geodesic scattering by surface deformations of a topological insulator,* J. P. Dahlhaus, C.-Y. Hou, A. R. Akhmerov, and C. W. J. Beenakker, Phys. Rev. B **82**, 085312 (2010).

22. *Topological quantum computation away from the ground state with Majorana fermions,* A. R. Akhmerov, Phys. Rev. B **82**, 020509(R) (2010) [Chapter 6].

23. *Anyonic interferometry without anyons: How a flux qubit can read out a topological qubit,* F. Hassler, A. R. Akhmerov, C.-Y. Hou, and C. W. J. Beenakker, New J. Phys. **12**, 125002 (2010) [Chapter 13].

24. *Quantized conductance at the Majorana phase transition in a disordered super-conducting wire,* A. R. Akhmerov, J. P. Dahlhaus, F. Hassler, M. Wimmer, and C. W. J. Beenakker, Phys. Rev. Lett. **106**, 057001 (2011) [Chapter 10].

25. *Random-matrix theory of Andreev reflection from a topological superconductor,* C. W. J. Beenakker, J. P. Dahlhaus, M. Wimmer, and A. R. Akhmerov, Phys. Rev. B **83**, 085413 (2011).

26. *Effects of disorder on the transmission of nodal fermions through a d-wave super-conductor,* J. K. Asbóth, A. R. Akhmerov, M. V. Medvedyeva, and C. W. J. Been-akker, Phys. Rev. B. **83**, 134519 (2011).

27. *Probing Majorana edge states with a flux qubit,* C.-Y. Hou, F. Hassler, A. R. Akh-merov, and J. Nilsson, submitted to Phys. Rev. B [Chapter 12].

28. *Scattering formula for the topological quantum number of a disordered multi-mode wire,* I. C. Fulga, F. Hassler, A. R. Akhmerov, and C. W. J. Beenakker, Phys. Rev. B **83**, 155429 (2011).

29. *Quantum point contact as a probe of a topological superconductor,* M. Wimmer, A. R. Akhmerov, J. P. Dahlhaus, and C. W. J. Beenakker, accepted to New J. Phys.

30. *Majorana fermions in equilibrium and driven cold atom quantum wires,* L. Jiang, T. Kitagawa, J. Alicea, A. R. Akhmerov, D. Pekker, G. Refael, J. I. Cirac, E. Dem-ler, M. D. Lukin, and P. Zoller, submitted to Phys. Rev. Lett.

31. *Spin-triplet supercurrent carried by quantum Hall edge states through a Joseph-son junction,* J. A. M. van Ostaay, A. R. Akhmerov, and C. W. J. Beenakker, accepted to Phys. Rev. B.

Curriculum Vitæ

I was born on the 30th of December 1984 in Krasnoobsk, a small Siberian town not far from Novosibirsk. My primary and middle school was the Ecological Gymnasium 13 of Krasnoobsk. I received my secondary education in the years 1999-2001 at the boarding school specialized in physics and mathematics, affiliated with Novosibirsk State University. During these years I participated in the Russian physics olympiad, winning it twice at the national level.

After finishing high school I moved to Moscow to study physics at the Moscow Institute for Physics and Technology. My Bachelor thesis, which I finished in 2005 under supervision of prof. Alexey Ioselevich, is entitled "Universal temperature dependence of the conductivity of a strongly disordered granular metal". My Master's education is split equally between the Landau Institute for Theoretical Physics, where I studied for one year, and Leiden University, where I studied for another year under supervision of prof. Carlo Beenakker. The results of my master's research are reported in my master's thesis "Pseudo-diffusive conduction at the Dirac point of a normal-superconductor junction in graphene". Since my graduation in the Summer of 2007 I am employed by the Foundation for Fundamental Research on Matter (FOM), as a member of the Delft–Leiden focus group on "Solid-State Quantum Information Processing", doing doctoral studies in the group of prof. Beenakker. Part of the research I performed during these years is presented in this thesis.

During my Bachelor studies I coached the Russian team for the international physics olympiad. In Leiden I taught exercise classes in electrodynamics. I was an invited participant of the workshop "Progress in spintronics and graphene research" held in 2010 at the Kavli institute for theoretical physics in Beijing and presented my work at several international conferences.